



**HAL**  
open science

# Development of a SHM system by elastic guided waves applied to aeronautic structures

Andrii Kulakovskiy

► **To cite this version:**

Andrii Kulakovskiy. Development of a SHM system by elastic guided waves applied to aeronautic structures. Signal and Image Processing. Université Paris Saclay (COMUE), 2019. English. NNT : 2019SACLX021 . tel-02271270

**HAL Id: tel-02271270**

**<https://theses.hal.science/tel-02271270>**

Submitted on 26 Aug 2019

**HAL** is a multi-disciplinary open access archive for the deposit and dissemination of scientific research documents, whether they are published or not. The documents may come from teaching and research institutions in France or abroad, or from public or private research centers.

L'archive ouverte pluridisciplinaire **HAL**, est destinée au dépôt et à la diffusion de documents scientifiques de niveau recherche, publiés ou non, émanant des établissements d'enseignement et de recherche français ou étrangers, des laboratoires publics ou privés.

# Développement d'un système SHM pour aéronef par ondes élastiques guidées

Thèse de doctorat de l'Université Paris-Saclay  
préparée à Ecole Polytechnique

Ecole doctorale n°580 Sciences et Technologies de l'Information et de la  
Communication (STIC)

Spécialité de doctorat : Traitement du signal et des images

Thèse présentée et soutenue à Saclay, le 27/05/2019, par

**ANDRII KULAKOVSKYI**

Composition du Jury :

Michel Castaings, Professeur Bordeaux INP	Président
Emmanuel Moulin, Professeur Université Valenciennes, IEMN	Rapporteur
Patrice Masson, Professeur Université de Sherbrooke, GAUS	Rapporteur
Bing Tié, HDR CentraleSupélec, MSSMat	Examineur
Marc Rébillat, Maître de conférence Ecole Nationale Supérieure d'Arts et Métiers, PIMM	Examineur
Alain Lhémy, Directeur de recherche CEA, LIST	Directeur de thèse
Bastien Chapuis, Expert senior CEA, LIST	Invité
Olivier Mesnil, Expert CEA, LIST	Invité
Oscar d'Almeida, Expert Safran SA, TCA	Invité



# Résumé

Depuis l'origine de l'industrie aérospatiale, l'ambition inhérente d'améliorer la performance des systèmes aérospatiaux a été à l'origine du développement de matériaux de hautes performances. Les alliages d'aluminium et les composites constituent deux grandes catégories de ces matériaux et jouent un rôle important dans les applications aérospatiales actuelles et futures. Avec un certain nombre de propriétés bénéfiques par rapport à d'autres alliages métalliques, les alliages d'aluminium sont souvent utilisés pour créer des fuselages. Les matériaux composites sont particulièrement intéressants pour les applications aérospatiales en raison de leurs propriétés mécaniques directionnelles, la légèreté et la résistance à la corrosion. Ils sont généralement faits de fibres relativement fortes et rigides, souvent de carbone ou de verre, encapsulées dans une matrice de résine dure (abréviation en anglais CFRP et GFRP pour Carbon et Glass Fiber Reinforced Polymer).

Il existe également des dérivés des matériaux susmentionnés, tels qu'une structure sandwich composite en nid d'abeille (abréviation en anglais HCSS pour HoneyComb Sandwich Structure). Il s'agit de matériaux composites fabriqués en attachant deux plaques minces mais rigides (ce sont généralement de multicouches en CFRP ou GFRP) au cœur léger mais épais en nid d'abeille en aluminium. L'épaisseur relativement élevée du panneau sandwich assure une rigidité élevée à la flexion, tandis que la densité globale du panneau reste faible. La structure interne fixe (abréviation en anglais IFS pour Inner Fixed Structure) d'une nacelle d'avion est une structure composée de panneaux HCSS et CFRP. La nacelle est un complément indispensable au moteur de l'avion. La nacelle, et l'IFS en particulier, remplit plusieurs fonctions, telles que la tenue du moteur, l'optimisation et le guidage du flux d'air secondaire, la protection du moteur contre l'agression mécanique et environnementale, et l'atténuation du bruit acoustique.

Malgré ses propriétés mécaniques excellentes, cette structure est susceptible d'endommagement après une période longue de service dans un environnement opérationnel hostile, à l'apparition de défaut à cause de chocs ou à une utilisation non conforme de la structure.

En termes plus généraux, l'endommagement peut être défini comme une modification des propriétés du matériau et / ou de la géométrie de la structure, qui affecte négativement la capacité de la structure à fonctionner de manière optimale. En particulier les structures composites HCSS tel que la nacelle d'aéronef, sont susceptibles de souffrir des défauts suivants : le délaminage des couches composites, le décollement de la feuille centrale et / ou la corrosion du cœur aluminium. De tels défauts se produisent dans la structure, ce qui les rend difficilement voire non détectables à l'œil nu, mais ils peuvent s'étendre de manière interne sur des volumes importants. Comme la structure continue de fonctionner selon certains scénarios de chargement, ces défauts peuvent se développer jusqu'à atteindre un point où le système n'est plus en mesure de fonctionner normalement et peut mener à une défaillance.

Ces dernières années, les systèmes d'inspection des dommages ont suscité un intérêt croissant. En conséquence, différentes techniques de contrôle non destructives (CND), telles que les tests par ultrasons, les tests électromagnétiques, la tomographie, les tests rayons X, les tests par

ressuage, les tests par particules magnétiques, etc., ont été développées. Par exemple, le contrôle par ultrasons est devenu une méthode fiable et largement utilisée pour l'inspection des structures. Il est en effet possible d'exciter des ondes ultrasonores dans l'IFS et d'examiner le champ d'ondes résultant pour identifier les défauts internes. Cependant, l'inspection par ultrasons et les autres techniques classiques de CND sont souvent intrusives, longues et coûteuses. Ils nécessitent une intrusion humaine et perturbent le fonctionnement normal d'une structure. Par exemple, un aéronef doit être partiellement démonté afin de fournir un accès à l'IFS de la nacelle de l'aéronef pour des inspections régulières.

De nos jours, de nombreuses recherches ont été orientées vers le domaine de Structural Health Monitoring (SHM) qui permettra surpasser les limitations susmentionnées. Compte tenu des avancées technologiques dans le domaine de transducteurs embarqués et de méthodes de traitement du signal, le SHM envisage un paradigme différent de l'évaluation non destructive, dans lequel les transducteurs sont embarqués en permanence à la structure pour effectuer la détection et l'identification des endommagements in situ.

Un tel système informerait un utilisateur de l'intégrité de la structure sur une base de temps continu ou périodique sans certaines des contraintes imposées par les techniques classiques de CND. Les données collectées par les transducteurs au cours de la durée de vie de la structure peuvent être inspectées afin de détecter tout endommagements naissant et de décrire l'évolution de défauts existants. Si les endommagements ont été détectés par un système SHM, une inspection plus approfondie peut être effectuée à l'aide des méthodes CND classiques.

Dans cette perspective, le contrôle par ondes guidées (abréviation en anglais GW pour Guided Waves) est apparu comme une option importante pour le système SHM. Dans une structure en forme de plaque, ces ondes sont également appelées ondes de Lamb, du nom d'un mathématicien, Horace Lamb, qui a publié le premier ouvrage sur le calcul et l'analyse des GW en 1917. Même si les avantages potentiels de l'utilisation de GW pour l'évaluation des CND ont été reconnus dans les années 1950, il a fallu plusieurs décennies avant de pouvoir mettre en pratique cette technique, puisqu'il fallait mener des recherches approfondies sur les phénomènes d'excitation de GW, de propagation modale de GW, et leur interaction avec les défauts. De nos jours, les GWs sont utilisés dans de nombreuses méthodologies de détection et de caractérisation des endommagements, notamment l'imagerie par des ondes guidées (abréviation en anglais GWI pour Guided Wave Imaging).

Dans le secteur l'aéronautique, le SHM devient de plus en plus demandé, principalement pour les raisons suivantes. Premièrement, l'application de méthodes SHM permet de garantir l'intégrité structurelle et la fiabilité. La durée de la vie de la structure peut ainsi être prolongée à mesure que l'initiation d'endommagements peut être détectée et la maintenance nécessaire peut être anticipée afin d'empêcher la dégradation de la structure. Deuxièmement, la procédure de la maintenance régulière, qui nécessite le désassemblage de l'aéronef, peut être remplacée par une maintenance conditionnelle, c'est-à-dire que, lorsqu'un dommage est détecté, le système SHM envoie un signal d'alerte de manière à ce que le travail de réparation puisse être planifié en avance et que les actions correspondantes puissent être planifiées. Un système SHM peut également surveiller des zones inaccessibles pour les techniques de contrôle non destructif classiques et ne perturbe pas le fonctionnement normal d'un aéronef. Cela permet d'éviter des pertes économiques causées par des temps d'arrêt imprévus. Des inférences statistiques peuvent être tirées des données fournies par des systèmes SHM similaires afin de prédire l'évolution de l'intégrité de la structure. Enfin, un système SHM peut potentiellement réduire une marge de sécurité de conception. Tous ces facteurs entraînent un avantage économique significatif pour un utilisateur de la structure.

Le sujet de cette thèse vise à développer un système SHM basé sur GWs pour la détection, la localisation et la caractérisation de dommages dans des structures en plaques en alliages

d'aluminium, CFRP / GFRP et HCSS, et à les traduire en structures composites complexes, telles que une nacelle d'avion. Cette thèse présente les travaux menés dans le but de développer un système de SHM par ondes guidées capable de détecter, localiser et dimensionner efficacement les défauts dans des structures aéronautiques assimilables à des plaques, en matériaux composites ou en aluminium. Des simulations et des méthodes d'apprentissage sont utilisées pour déterminer les caractéristiques principales des ondes guidées propagées, notamment les vitesses de phase et de groupe ainsi que la fonction de Green 3D. Celles-ci sont ensuite utilisées pour traiter les signaux des ondes guidées afin de produire des images représentant l'intégrité des structures étudiées. Ce travail comprend également une étude approfondie des algorithmes d'imagerie DAS, MV et Excitelet, les plus prometteurs parmi ceux de la littérature, une évaluation de leurs performances par analyse statistique sur une grande base de données de résultats de simulation d'imagerie par ondes guidées et propose une méthode d'imagerie parcimonieuse. Alors que la détection et la localisation des défauts à partir de l'analyse des images est aisée, le dimensionnement du défaut est un problème plus complexe en raison de sa forte dimensionnalité et de sa non-linéarité. Il est démontré que ce problème peut être résolu par des méthodes d'apprentissage automatique sur une grande base de données de résultats de simulation d'imagerie par ondes guidées. Ces méthodes d'imagerie nécessitent cependant une référence, mesurée sur la structure dans un état supposé sain. Elles sont efficaces dans des conditions opérationnelles stationnaires mais sont sensibles aux variations de l'environnement et notamment aux fluctuations de température. Ce travail présente donc l'étude de la robustesse face aux effets thermiques des méthodes d'imagerie par ondes guidées et propose un modèle de détection de défauts capable d'analyser des résultats d'imagerie détériorés. Plusieurs techniques de compensation des effets thermiques sont étudiées et des améliorations sont proposées. Leur efficacité est validée pour les plaques d'aluminium mais des améliorations supplémentaires sont nécessaires pour les étendre aux plaques de composites.

# Table of Contents

<b>Remerciements</b>	<b>iii</b>
<b>Table of Contents</b>	<b>vii</b>
<b>1 Introduction</b>	<b>1</b>
1.1 Background	1
1.2 Structural Health Monitoring	5
1.2.1 Introduction to SHM	5
1.2.2 SHM methods	5
1.2.3 Guided waves-based SHM	7
1.2.3.1 General overview of GWs-based SHM system	7
1.2.3.2 Advantages and challenges	8
1.2.3.3 A brief review on GW-based SHM methods	9
1.3 Objectives of thesis	11
1.4 Thesis outline	11
<b>2 Guided waves propagation in composite structures</b>	<b>13</b>
2.1 Introduction to guided waves	14
2.2 Guided wavefield analysis	17
2.3 Guided waves modeling	18
2.3.1 Semi-analytical finite elements modeling	20
2.3.2 Modal expansion method	21
2.3.3 Homogenization model for HCSS	22
2.3.4 Validation of simulation results	25
2.4 Data driven approach for Guided Waves modeling	31
2.4.1 Bayesian Framework for Guided waves spectra processing	31
2.4.1.1 Bayesian Inference	31
2.4.1.2 Gaussian process	32
2.4.1.3 Overlapping Mixtures of Gaussian Processes	33
2.4.2 Determination of 3D Green's function	35
2.5 Chapter summary	43
<b>3 Defect detection and localization using Guided Waves Imaging</b>	<b>45</b>
3.1 Guided Waves Imaging	46
3.2 Defect imaging algorithms	47
3.2.1 Delay-And-Sum algorithm	48
3.2.2 Minimum Variance algorithm	49
3.2.3 Excitelet algorithm	50

3.3	Defect imaging results	53
3.3.1	Aluminum plate	53
3.3.2	Multilayer CFRP plate	55
3.3.3	HCSS	62
3.4	Statistical studies on localization accuracy	65
3.4.1	Guided waves simulation framework	65
3.4.2	Database description	66
3.4.3	Defect localization error analysis	67
3.5	Sparse defect imaging	74
3.5.1	Bayesian optimization of Gaussian process for sparse defect imaging	74
3.5.2	Sparse imaging results	75
3.6	Chapter summary	79
<b>4</b>	<b>Defect sizing using Guided Wave Imaging</b>	<b>81</b>
4.1	Inversion problem formulation	82
4.2	Machine learning for defect sizing	84
4.2.1	Supervised learning approach	84
4.2.2	Defect sizing using Deep Learning	84
4.2.2.1	Introduction to CNN	85
4.2.2.2	Database generation	87
4.2.2.3	Inversion of simulation results	88
4.2.2.4	Inversion of experimental results	92
4.2.2.5	Inversion model interpretation	93
4.3	Chapter summary	95
<b>5</b>	<b>Robustness of GWs-based SHM</b>	<b>97</b>
5.1	Effects of temperature variations on GWI	98
5.1.1	Temperature effect on GWs propagation	98
5.1.2	Defect detection under temperature variations	99
5.1.2.1	Database generation	101
5.1.2.2	Damage detection model	101
5.2	Methods for temperature effect compensation	105
5.2.1	Conventional approach for baseline correction	105
5.2.1.1	Optimal Baseline Selection	105
5.2.1.2	Baseline Signal Stretch	105
5.2.2	Dynamic Time Warping for baseline correction	106
5.2.3	Defect imaging results under varying temperature	109
5.3	Chapter summary	118
	<b>Conclusions</b>	<b>119</b>
	<b>Recommendation for future work</b>	<b>123</b>
	<b>References</b>	<b>125</b>
<b>A</b>	<b>Appendix</b>	<b>137</b>
A.1	Maximum likelihood for the normal distribution	137
A.2	GW profiles	139
A.3	DTW Local cost computation	140
A.4	List of communications	141

# Introduction

## Outline of the current chapter

<b>1.1 Background</b>	<b>1</b>
<b>1.2 Structural Health Monitoring</b>	<b>5</b>
1.2.1 Introduction to SHM . . . . .	5
1.2.2 SHM methods . . . . .	5
1.2.3 Guided waves-based SHM . . . . .	7
1.2.3.1 General overview of GWs-based SHM system . . . . .	7
1.2.3.2 Advantages and challenges . . . . .	8
1.2.3.3 A brief review on GW-based SHM methods . . . . .	9
<b>1.3 Objectives of thesis</b>	<b>11</b>
<b>1.4 Thesis outline</b>	<b>11</b>

This chapter provides an introduction to the field of Guided Waves-based Structural Health monitoring (GW-SHM) starting with motivation and basic concepts of structural integrity evaluation. Then, it delves into constitutive parts and into operational principle of a GW-SHM system and provides a brief literature review. Afterwards, advantages and challenges are pointed out, and research objectives are formulated.

## 1.1 Background

From the very origin, airspace industry is intended to use lightweight and high-performance materials in order to increase the reliability and profitability of aircraft. From this perspective, aluminum alloys and composites are particularly attractive. They constitute two major classes of widely used materials and play a significant role in current and future aerospace applications.

Aluminum alloys are beneficial in comparison with other metallic alloys, and they are often used in aircraft frame designs. Composite materials are particularly attractive to aerospace applications due to their exceptional directional mechanical properties, lightweightness and corrosion resistance. Such materials typically consist of relatively strong and rigid fibers encapsulated in a tough resin matrix, as schematically shown in Figure 1.1a. The most eminent composite

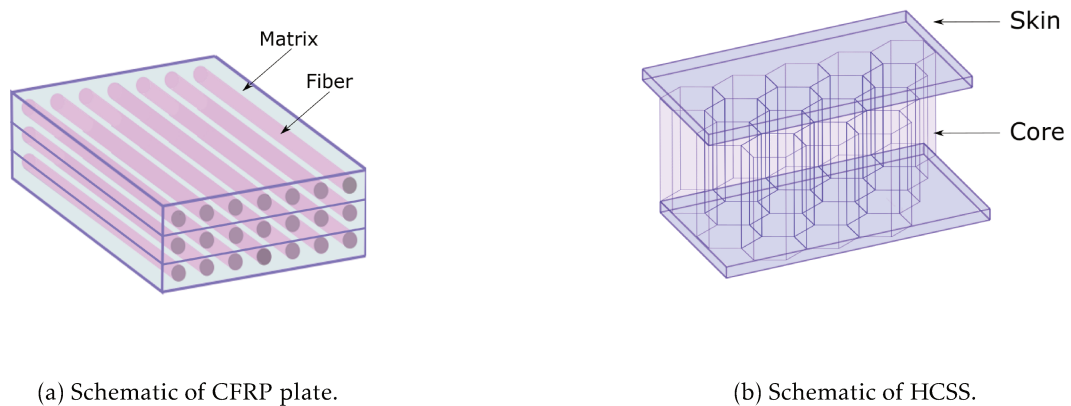


Figure 1.1 – Schematic of composite structures typically used in the aerospace industry.

materials used in aerospace and other industries are Carbon- and Glass-Fibers-Reinforced Polymers (CFRP and GFRP respectively) which consist of carbon and glass fibers, both of them are stiff and strong (for their density) but brittle in a polymer matrix, which is tough but neither particularly stiff nor strong. In general, these polymer plies are sequentially stacked to form either unidirectional or multidirectional composite laminates, as shown in Figure 1.1a.

There also exist derivatives of above-mentioned materials, such as a Honeycomb Composite Sandwich Structure (HCSS), schematically shown in Figure 1.1b. This is a special class of composite materials that are manufactured by attaching two thin but stiff plates typically made of multilayer CFRP or GFRP to a lightweight but thick aluminum honeycomb core. Comparatively high thickness of a sandwich panel ensures relatively high bending stiffness, while the overall panel density remains low. Top and bottom face sheets carry most of in-plane and bending loads, whereas the core mostly contributes to bending stiffness, out-of-plane shear and compressive strength [1].

Multilayer composite plates and HCSS panels have been largely employed in airspace industry. Their excellent mechanical properties, lightweight and corrosion resistance make them very attractive to be used in severe operational environment. For example, an aircraft nacelle's Inner Fixed Structure (IFS), shown in Figure 1.2, is a typical structure made of these components. A nacelle is an essential complement to an aircraft engine; in assembly, they constitute an aircraft's propulsion system. The nacelle, and IFS in particular, perform several functions, such as optimizing and guiding the primary and secondary airflows, protecting the engine from any aggression and temperature differences, and damping of acoustic noise.

Despite outstanding mechanical properties of these materials, defects such as corrosion, fractures, composite fiber breakage, plies delamination or core-sheet debonding can appear because of thermo-mechanical aging in a hostile working environment or impact forces due to the improper use of a structure. For instance, the X-ray tomography<sup>1</sup> of fiber breakage in a CFRP plate is shown in Figure 1.3. This defect is produced by an impact force perpendicular to the surface so that the integrity of a plate is violated as demonstrated from the top and bottom views as well as in through defect profiles. It is worth noting that such defects can also occur within the structure. While being barely detectable to the naked eye on the composite surface, they can

<sup>1</sup>The image is provided by SAFRAN Composites.



Figure 1.2 – Aircraft nacelle’s Inner Fixed Structure.

expand internally to large volumes and decrease significantly the reliability of the structure.

In recent years, there has been an increasing interest to structural integrity evaluation systems in many industries, and aerospace in particular. It is envisaged that such systems would apprise manufacturers, end-users, and maintenance teams of the structure’s integrity and inform about any incipient damage on a frequent or continuous time basis. It would also allow estimating and extending the Remaining Useful Life of structures, but a high level of knowledge is necessary to guarantee both structures availability and reliability.

A number of Non-Destructive Evaluation (NDE) techniques have been developed to evaluate the integrity of such structures [2, 3]. Currently, this is a primary approach for the aerospace structures inspection, but these techniques have certain drawbacks: they are usually expensive, time-consuming and often disturb a structure from normal operation. Moreover, such structures are often hardly accessible to maintenance teams, so an aircraft disassembly might be required. Manufacturers introduce a safety margin design to resist accidental impacts and structure aging, but this leads to additional weight of the structure and to consequent economic shortcomings.

In light of this, Structural Health Monitoring (SHM) can contribute significantly towards enhancing the reliability and profitability of engineering structures [4, 5]. More details on basics, principles of operation and brief overview of SHM methods are provided in the following section.

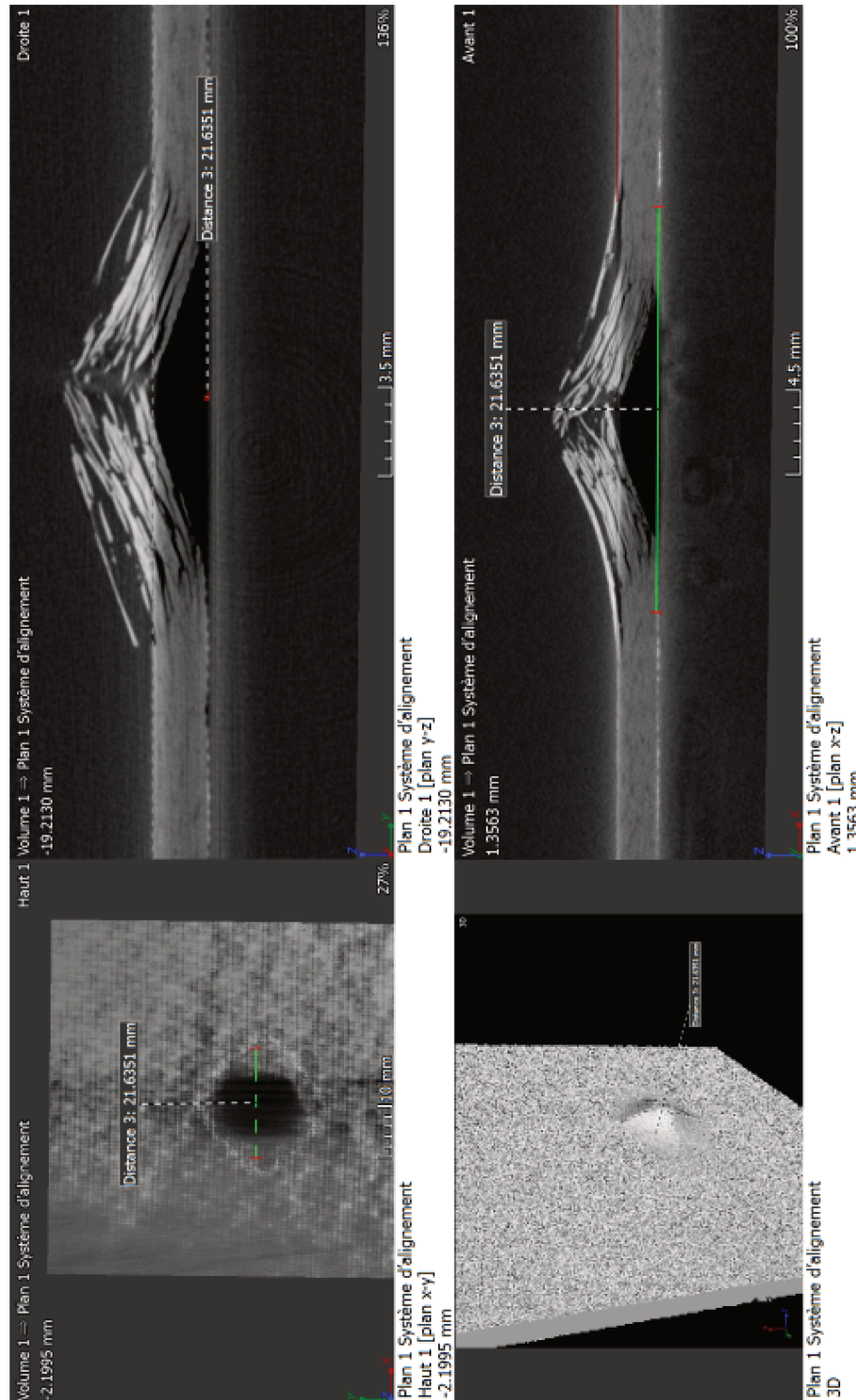


Figure 1.3 – X-ray tomography of fiber breakage in the CFRP plate due to the impact force.

## 1.2 Structural Health Monitoring

### 1.2.1 Introduction to Structural Health Monitoring

A number of industries, including the aerospace, are interested in damage detection in their products, as well as in their manufacturing infrastructure at the earliest possible stage. General practice for damage detection requires performing some form of regular structural integrity monitoring (NDE or SHM) and is motivated by potential life-safety and economic impact of this process. Both NDE and SHM aim to evaluate the integrity of a studied structure using non-destructive methods. These fields are very close intrinsically and can overlap to a greater or lesser extent.

NDE can be referred to the assessment of structural integrity using removable transducers and instrumentation. It is usually scheduled, requires human intrusion and disturbs structures from normal operation. In general, NDE measurements are interpreted by the qualified staff on a one-off basis, meaning that current inspection results are not compared with those obtained previously [6].

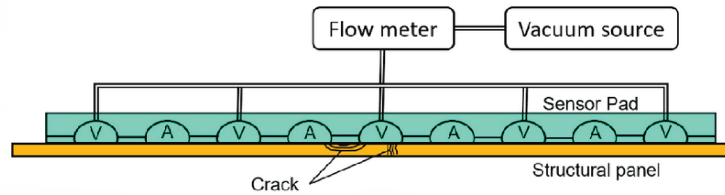
In contrast to NDE, SHM relies on permanently embedded transducers that are typically used for measuring a structural dynamic response either in a passive or active way. As the SHM system is an integrated one, inspection can be conducted anytime and generally presumes periodical structure observations. Knowledge-based methods, i.e., signal processing algorithms [7, 8], are then used for damage-sensitive features extraction and analysis to determine the current state of structure health.

In a long-term perspective, SHM provides periodically updated information regarding the ability of the structure to operate and perform its intended functions taking into consideration inevitable thermo-mechanical aging and fatigue accumulation [9]. In case of extreme events, such as unanticipated blast loading or impact forces due to improper use of the structure, SHM is used for rapid integrity screening. Such inspection aims at providing the real-time information about structural performance and quality reduction, and its current ability to meet a user's requirements. However, SHM system also imposes additional constraints such as system integration and robustness against hardware aging.

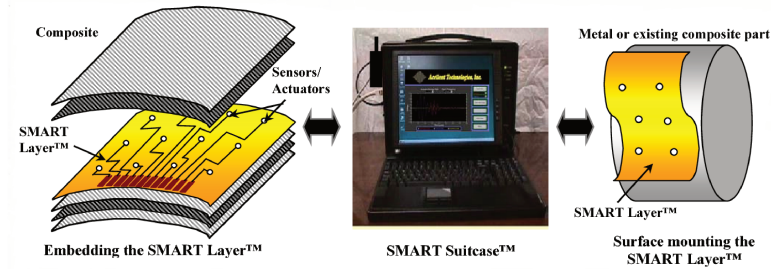
### 1.2.2 Primary methods in Structural Health Monitoring for aerospace structures

A number of methods have been developed for SHM applications, some of them are presented below. These methods can be broadly classified into two categories: active and passive, respectively [10]. Active approaches require actuation, i.e. excitation, of the structure and then measurements of the resulting responses [11], while passive ones are aimed only at structure observation and do not require any type of actuation. Sensors are used for capturing perturbations directly caused by a defect such as a rapid release of acoustics energy, heat or strain measurement. Passive SHM methods have been studied for a long time and are relatively mature. They might be attractive due to low energy consumption of the SHM system, but they are constrained only to listening to the structure and do not interact with a defect. Therefore, passive methods might be susceptible to miss the damage event.

Among passive methods, perhaps, the most prominent is a Comparative Vacuum Monitoring (CVM) [12]. This SHM technique based on the comparison of vacuum and atmospheric pressure in fine tubes within a simple manifold that is adhered to the surface of a structure [13]. It is efficiently used for real-time monitoring of crack initiation and/or propagation, and therefore, was adapted for SHM of aeronautic structures [14, 15]. It is worth noting that for now this is



(a) Schematic of comparative vacuum monitoring [13].



(b) Schematic of Smart Layer made by Acellent [16].

Figure 1.4 – Schematic representation of SHM techniques.

the single technique which has been successfully tested, certified and installed on aircraft, but in practice it allows monitoring only small surfaces. The schematic of comparative vacuum monitoring is shown in Figure 1.4a.

Another mature passive SHM technique is acoustic emission monitoring [17, 18], where transducers listen to transient elastic waves generation by sudden strain energy releases due to fractures, delamination, fiber breakage and any other types of defects [2]. Smart Layer developed by Acellent One is another well-known SHM technique [16, 19]. This is a thin dielectric film with an embedded network of distributed piezoelectric transducers, which can be either integrated within composite structures or attached to the surface, see Figure 1.4b. This film is used for generating and sensing diagnostic signals that can be interpreted for determining structural integrity.

Obviously, there are many other SHM techniques, but they are currently under development and a higher level of maturity is required in order to translate them to the industry. For example, natural frequencies observation [21, 22] is a passive method used for monitoring intrinsic modes of the structure. If damage occurs, a frequency shift can be detected. This technique is usually applied to rotating machinery. Local strain monitoring is another passive SHM technique that can be implemented using strain gauges [23] or fiber Bragg grating (FBG) sensors [24]. The latter is basically a fiber-optic cable with optical interference patterns generated by a laser, see Figure 1.5. Any local strain causes a slight change in the sensor's light transmitted/reflected wavelength. Acousto-ultrasonics [25–27] can be attributed to active SHM methods. This SHM technique implements structural vibration observation where low-frequency acoustic pulses are sent through the structure and a damage can be detected if reflected acoustic energy is changed. Another active and, perhaps, one of the most well-known SHM methods is ultrasonic guided elastic waves testing [28, 29]. It implements damage detection and characterization in the structure using the capability of guided waves to interact with defects in the vicinity of their

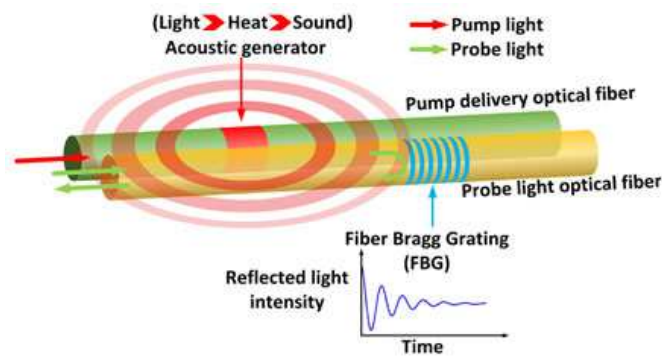


Figure 1.5 – Schematic of Fiber Bragg gratings sensor [20].

path [30]. These waves are usually actuated and sensed by a set of piezoelectric transducers. However, hybrid models have been recently developed [31], where piezoelectric transducers are used for actuation, and FBG sensors are used for guided waves sensing, respectively. Such a configuration allows partial integration of the SHM system into the structure.

Active SHM methods are currently of great interest due to their ability to interrogate a structure when required in prescribed and repeatable manner. It appears that ultrasonic Guided Waves (GWs) inspection is the most prominent among them [7, 28], but the complexity of GWs signals often requires sophisticated processing and analysis tools for correct interpretation [29].

### 1.2.3 Guided waves-based Structural Health Monitoring

Since plate-like structures are widely used in different industries and aerospace in particular, this work is mainly focused on the use of GWs for SHM. This is arguably one among a few detection mechanisms that combines both reasonable sensitivity to damage and significant propagation distance in plate-like structures [32]. Therefore, a relatively small number of transducers are required to monitor large and hardly accessible structures such as IFS.

Although, the first application of GWs for structure monitoring was proposed by Worlton in 1961 [33], it is still under development. Historically, the first industrial application of GWs for defect detection was proposed for petroleum and chemical industries, namely for pipelines inspection [34, 35], but, nowadays, this method is increasingly used in other industries, including the aerospace.

#### 1.2.3.1 General overview of GWs-based SHM system

These days, GWs are increasingly used in SHM systems [32, 36, 37] for damage detection, localization and sizing in plate-like structures. They excite whole structures cross-section and, under certain conditions, can propagate over significant distances while being sensitive to both surface and subsurface defects [38]. Therefore, only a limited number of sensors are required to monitor efficiently large and often inaccessible for human intrusion structures. The schematic of GWs-based SHM system is shown in Figure 1.6 [39]. It is worth noting that GWs are multi-modal and dispersive, thus they require advanced post-processing techniques to extract defect signatures from the collected data. More details on GWs properties are provided in Chapter 2.

There exist a number of methods to excite and sense GWs [40]. A significant amount of efforts has been devoted to design lightweight, low energy consuming and sensitive transducers capable of delivering modal and directional purity of GWs excitation and sensing, respectively

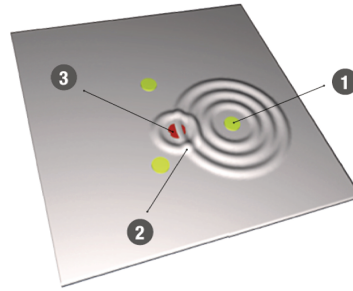


Figure 1.6 – Schematic of GWs-based SHM process. Transducers are denoted by 1, GWs are shown by 2 and structural flaw is represented by 3.

[32]. In the current work, SHM system relies on sparse arrays of circular Lead Zirconate Titanate  $Pb[Zr_xTi_{1-x}]O_3$  (PZT) transducers bonded to a structure [41].

Typically, each transducer in this array is used for driving in turn the structure with impulsive excitation, while the others are used for recording corresponding GWs signals. The wavepacket positions in these signals in the time domain can be related to inter-transducers locations, as well as to structural features, e.g. rivets, flanges, welds. Therefore, any wavepacket that cannot be related to known structural features is assumed to be a defect. It is worth noting that GWs signals interpretation is a complex problem and somewhat fundamentally limited to geometrically simple structures with low density of features. As the number of structural features becomes higher, GWs signals merge together obscuring scattered signals from defects.

There are two types of approaches for GWs signals processing: baseline and baseline-free. The baseline approaches [42] are based on the comparison of reference signals (measured when the structure was defect-free) and current signals (when state of the structure is unknown). If a damage occurs, GWs propagation is disturbed by a defect in the vicinity of the GW path, and the defect response can be revealed by such a comparison including signals subtraction or correlation. The baseline-free approaches, in contrast, do not require any form of GWs signals as compared to reference signals and allow the direct determination of the defect response [43]. The baseline-free methods are very attractive and somewhat promising for future SHM applications as they are not vulnerable to environmental effects and to any other form of GWs signals modification and corruption, but, for now, they are premature and their application is limited to specific and often simple structural shapes.

### 1.2.3.2 Advantages and challenges

As stated above, a SHM system can contribute significantly towards increasing the reliability and profitability of engineering structures. Continuous monitoring allows detecting structural flaws at the early stage as well as replacing regularly scheduled maintenance by the one on-demand. GWs-based SHM inspection is generally fast, it can be conducted at any convenient time, and does not require human intrusion. This permits decreasing the maintenance cost of the structure, time and efforts.

Another potential benefit of SHM, that mostly concerns the aerospace industry, is a weight saving, which is possible due to safety margins reduction in some structural components of aircraft. Therefore, fuel consumption can be lowered and a flying range of the aircraft can be increased. GW-based SHM can provide an operator with information on structure areas that are remote and inaccessible. Since SHM relies on embedded transducers, a large amount of time is

thus saved instead of being spent on disassembling and reassembling the aircraft in order to conduct conventional NDE.

With a number of benefits, GWs-based SHM arises as a prominent technology for intelligent structures, but it also has drawbacks that should be mentioned. First, such a system is an integrated one, therefore, significant effort has to be dedicated to design reliable hardware that supports high resolution acquisition of GWs signals and does not degrade with time in harsh environment. Among different types of GWs transducers, PZT transducers are standing out as a mature and reliable technology with service time that can last dozens of years. However, these transducers have to be surely integrated using special glues, and require cabling that, in total, is heavy and takes room. It is worth noting that for the next generation of GWs-based SHM it could be possible to use FBG sensors for GWs measurements. Apart from other benefits, this technology can decrease significantly the total weight of sensors.

The following drawbacks of a GWs-based SHM system are rather due to the complexity of GWs propagation in both isotropic and anisotropic structures. As mentioned above, they can propagate over long distances and are sensitive to structural inhomogeneities, but they are also multi-modal, dispersive, and their propagation can be adversely affected by environmental effects and operational conditions. The damage response is often overlapped and obscured by incident GWs and corresponding reflections from structural features that can lead to false alarms of the SHM system.

### 1.2.3.3 A brief review on GW-based SHM methods

As mentioned above, GWs are multi-modal and dispersive. They are complex for straightforward interpretation and usually require sophisticated and intelligent methods for analysis and patterns recognition. The main goal of these methods is to remove noise and non-relevant information, and to enhance weak but informative features that can be used to assess the integrity of a structure. Obviously, there are no universal physical or statistical features and signal processing methods that will be always efficient. Many research efforts have been devoted to adapt existing and to develop new signal processing methods in order to overcome difficulties associated with physical understanding of GWs propagation. Some of these methods are presented below.

Among the fundamental methods for GWs signal analysis, frequency domain analysis is, perhaps, the most prominent. Alleyne et al. [44] applied a two-dimensional Fourier transform to decompose GWs signals into frequencies and wavenumbers that make it up and to estimate the strength of each modal component. Afterwards, they proposed to use a reflection coefficient of each guided mode [38] as an indicator of the damage size. Later on, the determination of damage-sensitive features became of a great interest in GWs-SHM community. For example, Michaels et al. [45] demonstrated that a combination of differential features in both time and frequency domains can be used to discriminate damage in GWs signals. They also proposed [46] to consider local temporal coherence between a measured signal and reference signals as a tool for damage detection under temperature variations. Later, Xu et al. [47] used the Hilbert-Huang transform to decompose GWs signals into intrinsic modes (empirical mode decomposition) and to assess the instantaneous phase and frequency in order to build damage sensitive features. Chen et al. [48] applied a wavelet transform using a novel mother wavelet in order to build a damage sensitive indicator. Samaratunga et al. [49] developed a wavelet spectral finite element method for transverse cracks detection in composite plates. This method assumes the comparison of measured signals with model predictions so that the defect location can be determined through the time-of-flight of scattered GWs. Ghrib et al. [50] developed a method for non-linear signal based features extraction and applied support vector machine (SVM) for damage type classification and severity quantification in CFRP plates.

Over the last decade, data-driven methods have become increasingly popular for SHM, and for GWs-based SHM in particular [51]. Data driven feature-based inference plays a key role in solving inverse problems and is widely adopted for damage characterization tasks [52]. These statistical and machine learning methods are often used for completing challenging tasks such as automatic feature generation, classification and regression.

Perhaps, the most widely used statistical tool in SHM community is principal component analysis (PCA) [53]. It has been successfully applied for removing environmental effects on the observed damage sensitive features [54]. Kernel tricks, namely kernel-PCA, have been applied for non-linear patterns recognition in GWs signals. These patterns have a better discriminative power as compared to linear methods [22]. Dynamic Time Warping [55] has also been used to build features that distinguish damaged states from pristine ones of structures under varying environmental conditions. Finally, a Gaussian Mixture Model (GMM) [56] has been used to suppress time-varying influence from GWs signals and to determine time-independent damage features.

These physical and statistical features can be used in robust regression and classification analysis in order to determine the integrity of the structure and characterize defects, as proposed in following works: [50, 56, 57]. However, being effective for damage detection and discrimination, such features generally lack interpretation. In addition, their calibration might require an expert intrusion which is somewhat limiting for automatic SHM systems.

With the purpose of overcoming these limitations, GWs imaging techniques have been proposed. For example, Memmolo et al. [58] presented a GWs imaging technique focused on impact damage detection in composite plates. Druet et al. [43, 59] proposed a noise cross-correlation technique for passive GWs tomography of extended defects such as corrosion using an array of piezoelectric (PZT) transducers for GWs actuation and sensing. Wang et al. [60] proposed a synthetic time-reversal method, in which the energy of GWs signals is mapped to the image representing the integrity of the structure. This approach has been improved to the different extent by a number of researchers and now exists in several modifications [61–63]. Some of them incorporate the knowledge of a defect diffraction pattern [64], and some take into account complex paths of GWs propagation after several reflections [65]. Quaegebeur et al. [66, 67] proposed a more advanced GWs imaging technique that is based on the correlation coefficient calculation between experimental and theoretically computed signals assuming that the defect is a perfect reflector.

Recently, compressed sensing has been actively used for analyzing GWs signals [68–70]. Harley et al. [71] used a matching field model based on the sparse wavenumber analysis to reconstruct images representing structural integrity. Mesnil et al. [72] demonstrated that a guided wavefield can be reconstructed over significant area using only several measurement points so that defect location and size can be determined from the full-field analysis.

All the presented methods have their strengths and weaknesses. In general, they are effective for damage detection and localization, but, as of today, defect characterization remains challenging.

## 1.3 Objectives of thesis

Many engineering structures, including IFS shown in Figure 1.2, are exposed to harsh environment or improper use so that structural flaws might appear. As mentioned above, SHM is a technology that implements on-line damage detection and identification strategy in order to increase life-safety and profitability of engineering structures.

The research topic of this work is aimed at developing a GWs-based SHM system for damage detection, localization, and characterization in plate-like structures made of aluminum alloys, CFRP/GFRP and HCSS that could be eventually translated to complex composite structures, such as an aircraft nacelle. From this perspective, objectives of the thesis are formulated as follows:

1. The first objective of this work is to identify state-of-the art methods for GWs signals interpretation that allow structural integrity evaluation. Then, improve and test them in the multiple configurations relevant to the use-case of this thesis.
2. The second objective comprises extending GWs-based SHM system capabilities and enhancing its robustness against operational effects so that it would be capable of performance under realistic conditions.

## 1.4 Thesis outline

In this work, a prototype of a GWs-based SHM system has been developed in order to detect, localize and characterize structural damages in plates made of aluminum alloys, multi-layered monolithic plate-like composites and HCSS panels. The research objectives are accomplished in the order of appearance and the thesis is composed as follows.

Chapter two reports on general properties of GWs, analysis of their propagation and damage interaction. A semi-analytical finite element method coupled to a modal expansion method and a honeycomb homogenization model as well as a data driven method are used for determining principal characteristics of GWs and for modeling their propagation in the studied structures.

Chapter three reports on damage detection and localization using GWs imaging. Three defect imaging algorithms are implemented, tested and adapted to the large structures through the sparse sampling. In addition, exhaustive statistical study has been conducted in order to evaluate their localization accuracy.

Chapter four presents results on damage size evaluation using GWI results. An extensive database of GWI results is processed by means of machine learning methods, including a support vector machine and convolution neural networks in order to build an inversion model capable of defect size estimation in mono- and multi-frequency inspection modes.

Chapter five reports on methods for GWs-based SHM system robustness enhancement. Temperature effects on GWs propagation, defect detection, localization and characterization are studied. The Modified Dynamic Time Warping method is proposed for compensating this effect and for enhancing defect imaging capabilities of the GWs-based SHM system.

Finally, conclusions for this work are drawn and perspectives on further developments are discussed. The progress of this research work has been presented in eight national and international conferences and three papers are currently under preparation. They are listed in Appendix A.

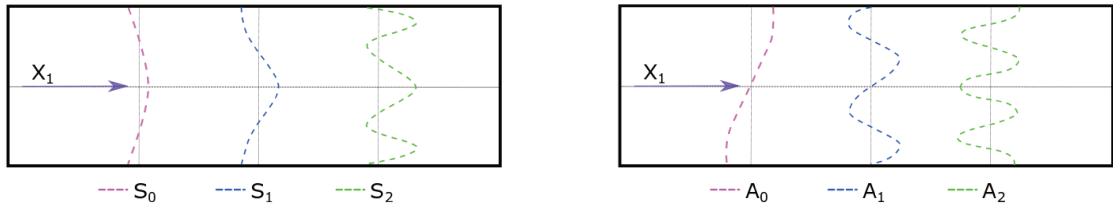


# Guided waves propagation in composite structures

## Outline of the current chapter

<b>2.1 Introduction to guided waves</b>	<b>14</b>
<b>2.2 Guided wavefield analysis</b>	<b>17</b>
<b>2.3 Guided waves modeling</b>	<b>18</b>
2.3.1 Semi-analytical finite elements modeling	20
2.3.2 Modal expansion method	21
2.3.3 Homogenization model for HCSS	22
2.3.4 Validation of simulation results	25
<b>2.4 Data driven approach for Guided Waves modeling</b>	<b>31</b>
2.4.1 Bayesian Framework for Guided waves spectra processing	31
2.4.1.1 Bayesian Inference	31
2.4.1.2 Gaussian process	32
2.4.1.3 Overlapping Mixtures of Gaussian Processes	33
2.4.2 Determination of 3D Green's function	35
<b>2.5 Chapter summary</b>	<b>43</b>

Guided elastic waves for metallic and composite material inspection, including Lamb waves, have come a long way since their discovery. A lot of research has been done in this field to overcome difficulties and challenges of understanding complex phenomena of GWs excitation/sensing, propagation in the structure and interaction with the defect. They are especially interesting for SHM as they can travel at large distances in structures with only a small attenuation. Hence, SHM of large areas is possible. In this chapter, general properties and principles of GWs are presented as well as corresponding theoretical and experimental methods for dispersion curves and 3D Green's function determination.



(a) Schematic of the first three symmetric mode shapes.

(b) Schematic of the first three antisymmetric mode shapes.

Figure 2.1 – Schematic of displacement profiles across the thickness of the plate. GWs propagate in  $X_1$  direction.

## 2.1 Introduction to guided waves

Consider an infinite isotropic medium that is subjected to dynamic loading so that elastic waves are generated. Being excited at any point in this medium, they transfer energy through it, but the medium itself does not move as a whole. Two types of elastic waves can be found: longitudinal waves, also known as pressure waves, and transverse waves, known as shear waves. If the medium is constrained with boundary(-ies), the propagation of elastic waves is modified due to the refraction and reflection phenomena, and guided waves (GWs) can appear. In contrast to conventional ultrasonic waves, they can travel on greater propagation distances because they use the structure itself as a waveguide by exploiting the resonance between the boundaries. GWs can be classified into different families with respect to the geometry and elastic properties of the structure. For example, Lamb waves, Rayleigh waves and Stoneley waves are GWs that exist in infinite plates, semi-infinite plates and at the interface of two structures, respectively. Further details can be found in the following works [3, 52].

Since plate-like structures are widely used in different industries and aerospace in particular, this work is mainly focused on the use of Lamb waves. They were initially described by an English mathematician Horace Lamb in 1917 [73], and experimentally observed by Worlton [33]. Lamb waves have several advantageous properties; for instance, they can travel over long distances, exhibit a low attenuation, especially in metallic structures, and interact with structural inhomogeneities. It is worth noting that there can be an infinite number of modes, and their propagation characteristics depend on an entry angle, excitation frequency and structural geometry. Although the traveling distance is more limited in composite structures, i.e. CFRP, GFRP plates, and even more in HCSS, Lamb waves are still highly attractive for damage detection techniques used in SHM.

In isotropic plate, an infinite number of Lamb wave modes exist. Except for the fundamental modes, i.e. zero-order modes, each of them has a certain nascent frequency, often called cut-off frequency. Lamb waves can be categorized into two families, namely symmetric  $S_i$  modes and antisymmetric  $A_i$  modes. This classification can be done regarding the through-thickness displacement profile, while the waves travel along the neutral axis  $X_1$  of the plate, as schematically shown in Figure 2.1. At the cut-off frequency, the symmetric modes are predominantly characterized by in-plane particles displacement, whereas the antisymmetric ones are mostly characterized by out-of-plane displacement. Such propagation particularities allow describing symmetric guided modes as compressional, where the thickness of the structure

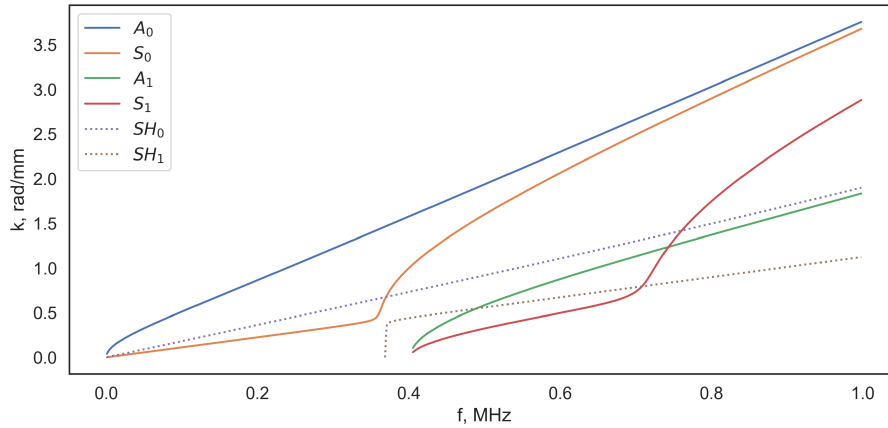


Figure 2.2 – Lamb and shear waves dispersion curves in  $0^\circ$  direction for 2.2 mm thick CFRP plate consisting of 8 orthotropic plies placed symmetrically as follows  $[0^\circ, 45^\circ, \dots, 45^\circ, 0^\circ]$ .

contracts and expands while the S-modes propagate. In contrast, the anti-symmetric modes can be referred to as flexural waves, where the structure bends while it propagates. In practice, two fundamental modes  $S_0$  and  $A_0$  are used in SHM applications. It is worth noting that additionally to Lamb waves, an infinite number of shear waves  $SH_i$  can be observed in the isotropic plate-like structure. The shear waves can also be either symmetric or anti-symmetric with respect to the neutral axis of the plate.

However, in anisotropic plates the distinction between types of wave modes is somewhat artificial since all the three types of guided modes are coupled [39, 74]. In practice, symmetric laminates are often used in the design of composite structures, and the Lamb waves in such structures can be classified into symmetric and antisymmetric modes [75]. Symmetric modes consist of two subclasses, namely quasi-extensional and quasi-horizontal shear waves, whereas antisymmetric modes consist of quasi-flexural and quasi-horizontal shear waves. For the sake of simplicity, the prefix quasi is omitted unless stated otherwise.

One of the most important characteristics of the GWs is that they are dispersive, meaning that their phase and energy (group) velocities, depend on the frequency, often in non-linear manner. The dispersion curves reveal the relationship between the frequency and phase or group velocity for different wave modes. Equivalently, this information can be expressed as wavenumber - frequency dependence. The dispersion curves of the eight-layer orthotropic CFRP plate in the  $0^\circ$  direction of GWs propagation are given as an example in Figure 2.2.

The GWs dispersion is often considered as an undesirable limitation in SHM applications, because interpretation and processing of GWs signals become complicated. For example, if the structure is excited with a tone burst, the measured GWs signals will generally contain multiple overlapped and spread wave packets. GWs dispersion leads to the loss of temporal resolution.

In isotropic plates, GWs propagate with identical velocities and amplitudes in all directions, therefore the corresponding wavefield has a circular symmetry. On the other hand, in anisotropic materials, e.g. CFRP, GFRP, and HCSS, velocities and amplitudes of guided modes depend on the direction of propagation [76]. This phenomenon is related to the directional dependence of elastic parameters, such as Young's moduli  $E_x, E_y, E_z$ , Poisson's ratios  $\nu_{yz}, \nu_{zx}, \nu_{xy}$ , and shear moduli  $G_{yz}, G_{zx}, G_{xy}$ .

In various NDT and SHM applications, there is a strong interest in analytical computation of GWs signals over the region of interest (ROI) of the structure. For example, our SHM system prototype relies on processing such signals that are generated by an elastic pulse induced by piezoelectric transducers. As shown in Figure 2.5a, the PZT can be modeled as a distributed force acting on the upper surface of the plate, i.e.  $x_3 = 0$ . The GWs signals can be expressed in terms of the elastodynamic 3D Green's function [36, 77–79], and a particle displacement field can be obtained using double integration of the 3D Green's function convolved with the excitation function. It can be expressed as follows:

$$u(x_1, x_2, x_3, t) = \int \int G^{3D}(x_1 - x'_1, x_2 - x'_2, x_3) \times f(x_1 - x'_1, x_2 - x'_2) dx'_1 dx'_2, \quad (2.1)$$

where  $u(x_1, x_2, x_3, t)$  is the displacement field,  $G^{3D}(x_1 - x'_1, x_2 - x'_2, x_3)$  is the 3D Green's function,  $f(x_1 - x'_1, x_2 - x'_2)$  is the harmonic force applied to the surface.

The 3D Green's function can be either modeled or experimentally determined. The analytical modeling, including semi-analytical modeling (SAFE) [80] method coupled to the modal expansion method (MEM) [36, 81–83], has been widely used as it allows computing the 3D Green's function for isotropic and anisotropic layered structures. The honeycomb core homogenization model can be applied to replace a periodic core of HCSS, and it allows retaining the same modeling framework. On the other hand, the 3D Green's function can be experimentally determined using spectral filters. This approach makes it possible to overcome limitations of analytical modeling, such as 3D Green's function modifications by structural features. Both methods are developed in the following section.

## 2.2 Guided wavefield analysis

To study the guided waves propagation in CFRP and HCSS plates, the following experimental laser-based set-up has been used. As demonstrated in Figure 2.3, the plate of interest is equipped with piezoelectric transducers of different diameters in order to generate GWs. The normal displacement at the surface of the plate is measured using a laser scanning Doppler velocimeter (LSVD), which converts the velocity of the surface displacement into the corresponding magnitude. The LSVD is mounted on a movable carriage, so it can reach any point of the plate to measure the GWs time series of the length  $T$ . If the ROI is defined as  $(X \times Y)$ , then the dictionary of size  $(X \times Y \times T)$ , representing the GWs wavefield, can be reconstructed by collecting signals from each acquisition point. In practice, such a region is often covered with a reflecting foil for improving optical reflectivity of the surface, and at each point, the measurement is averaged  $n$  times to improve the signal-to-noise ratio. At low frequencies, the  $A_0$  mode, in contrast to the  $S_0$  mode, is mainly formed by the out-of-plane displacement of the surface, so the major drawback of LSVD measurements is that the recorded guided wavefield mainly contains  $A_0$  mode. Phenyl salicylate, e.g salol, is often used as an adhesive to bound PZT to the surface of the plate, as it has a low melting point of  $41.5^\circ\text{C}$  and a relatively high cooling rate. This adhesive, being solidified, conducts better elastic perturbation induced by PZT than regular couplant gel. Collected data can be post-processed in both time-space and frequency–wavenumber domains to extract fundamental metrics of the guided modes, such as phase and group velocities, dispersion curves, attenuation, and anisotropy of the propagation.

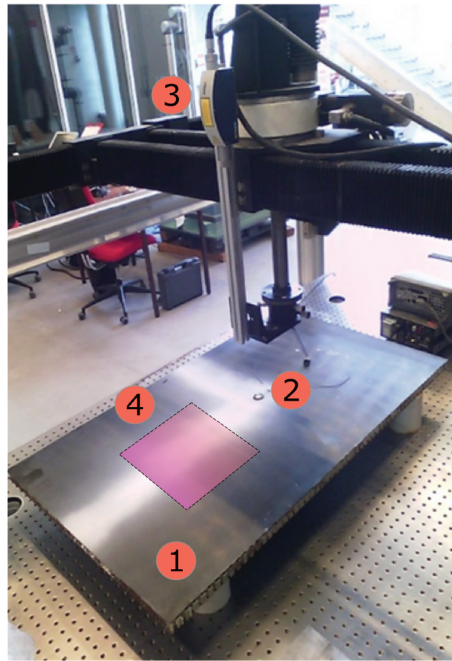


Figure 2.3 – Experimental setup used to characterize GWs propagation in composite plates. The studied plate is shown by (1), the PZT is denoted by (2), the LSVD is represented by (3), and ROI is shown by (4).

It has been mentioned in Chapter 1 that IFS of an aircraft nacelle is a principal structure of interest in this study. It mainly consists of HCSS, so this structural element has been selected to

study the GWs propagation.

Yu et al. [84] have demonstrated that at low frequencies, where the wavelengths are larger than the honeycomb cell size, the guided wavefield is global and GWs excite the entire sandwich. In this case, the HCSS can be considered as a single waveguide, and interact with honeycomb cells. At higher frequencies, where the wavelengths are comparable to the cell size, the mixture of global and partial guided wavefields can be observed. At this frequency, GWs start to interact with honeycomb cells, and, as a result, the energy of propagating GWs is partially trapped in the cellular, hence standing waves are formed. At even higher frequency, where the wavelengths are smaller than the honeycomb cell size, it becomes difficult to interpret the guided wavefield, as GWs propagate the skins and in the core. In addition, a complex speckle pattern of the guided wavefield is observed due to complex deformation modes of the honeycomb core cell walls. For the sake of simplicity and interpretability, it was agreed to inspect the structure using GWs generated at low frequencies, as they are still capable of interacting with defects such as fiber breakage, plies delamination or core-sheet debonding.

For example, a guided wavefield in the HCSS generated at 30 kHz by a piezoelectric transducer, 18 mm in diameter and 0.5 mm thick, is shown in Figure 2.4. Figures 2.4a and 2.4b compare the measured guided wavefields in the pristine HCSS at 332  $\mu\text{s}$  and 372  $\mu\text{s}$ , respectively. It can be observed that the reconstructed guided wavefield mainly consists of  $A_0$  mode, as the LSVD is much more sensitive to the normal displacement measurements. The  $S_0$  mode is mostly governed by the in-plane particle motion, so that it is almost not measured by LSVD. The guided wavefield is capable of propagating over long distances in coherent wavepackets and is affected by the anisotropy of the material. GWs propagate faster along  $X$  and  $Y$  axes than in the direction of  $45^\circ$ , and exhibit  $90^\circ$  symmetry.

GWs capability to interact with defects can be demonstrated using a simplified defect model, see Figure 2.4c, where the structural flaw is simulated by a teflon plate insertion in the skin layer of HCSS between the CFRP laminates. The guided wavefield is modified in the damaged region of the structure in comparison with the pristine region. Besides the GWs reflection from the defect, as shown in Figure 2.4c, a part of the energy is trapped and standing waves are formed inside the defect. The displacement amplitude of GWs signals is increased in the flawed zone, so that the energy trapping by the defect can be observed by computing an energy map. It is obtained by taking a root-mean-square (RMS) of the GWs signals, as shown in Figure 2.4d. While the HCSS excitation is centered at 30 kHz, a part of the spectrum corresponds to wavelengths that are small enough to interact with the periodic cellular structure of the core layer. Figure 2.4d also presents the evidence of standing waves formation, i.e. energy trapping, in the pristine region of the structure. A periodic honeycomb pattern can be observed on the energy map, meaning that the skin layer acted as a vibrating membrane due to the standing waves inside each honeycomb cell.

### 2.3 Guided waves modeling

Poisson's and Kirchhoff's theories accurately describe extensional and flexural motions in the isotropic plate at low frequencies [3]. However, for CFRP plates and HCSS, more sophisticated modeling tools are required. They must take into account the angular dependency of phase and group velocities and energy focusing factor, i.e. Maris factor, caused by the anisotropy of the structure [36, 82]. Here, we describe the modal expansion method coupled with the semi-analytical finite element (SAFE) modeling. This method allows linear decomposition of the 3D wavefield on propagating modes, so that each mode can be independently used for defect imaging in the structure.

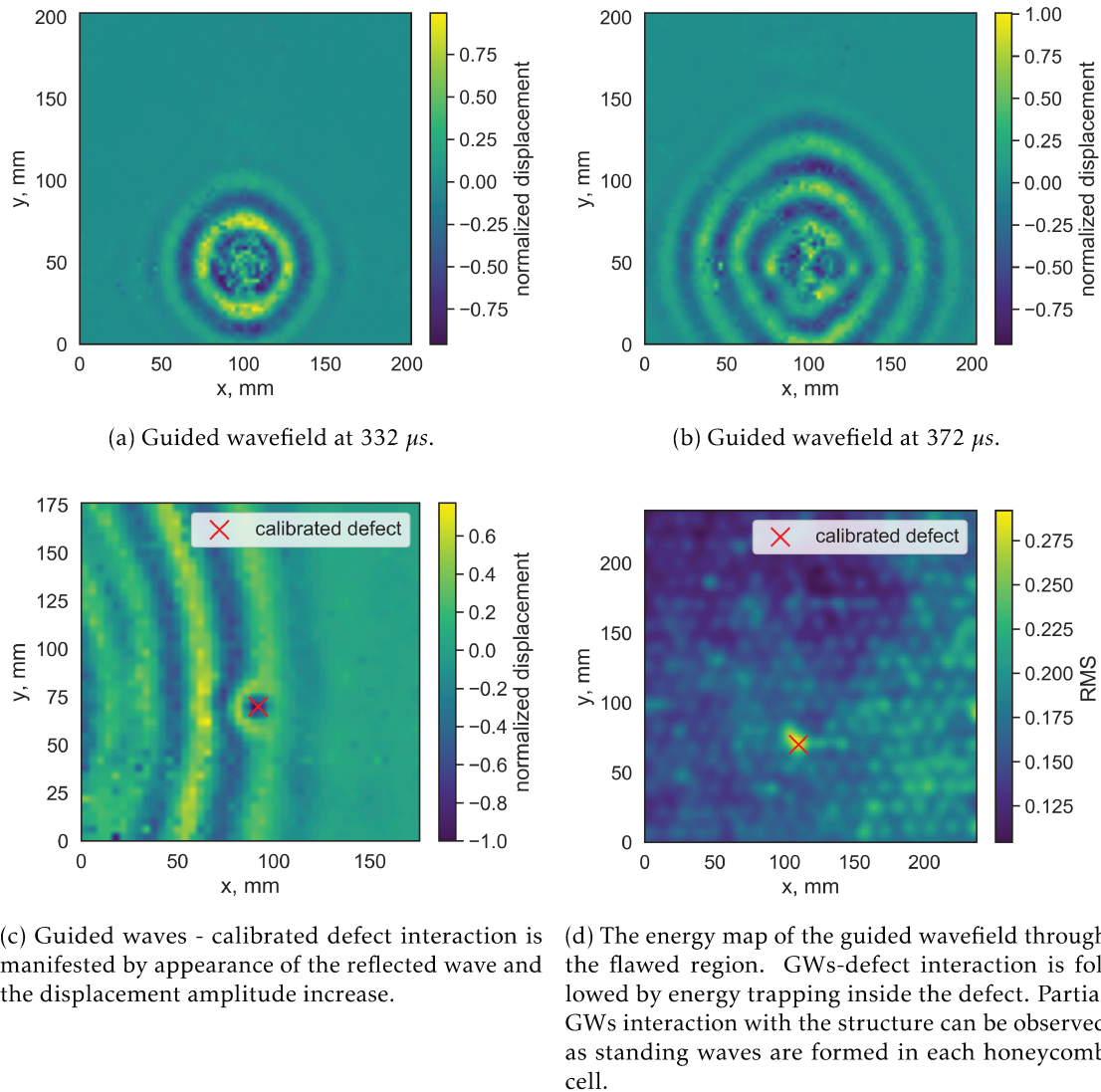
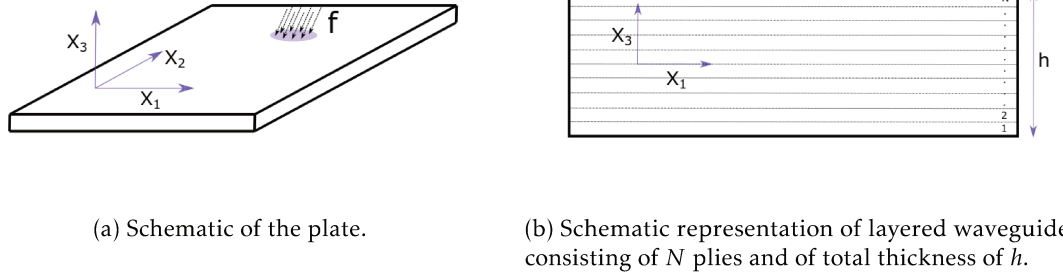


Figure 2.4 – Guided wavefield in the HCSS. The structure is excited at 30 kHz using PZT 18 mm in diameter and 0.5 mm thick. The PZT is bounded to the structure surface using salol adhesive.



(a) Schematic of the plate.

(b) Schematic representation of layered waveguide consisting of  $N$  plies and of total thickness of  $h$ .

Figure 2.5 – Plate geometry.

### 2.3.1 Semi-analytical finite elements modeling

Assuming linearity, wave fields in the structure can be decomposed into guided modes (i.e. modal decomposition) [3]. The SAFE method is employed to compute modes in layered composite plates. This method presumes waveguide discretization in the transverse direction  $x_3$ , while the GW propagation in the direction  $x_1$  is expressed analytically [39, 85], as demonstrated in Figure 2.5b.

A two-dimensional Fourier transform according to the  $x_1$  and  $t$  variables is applied to the equilibrium equation, while the  $x_3$  direction is discretized following the usual Finite Element (FE) method. It results in the following matrix eigenproblem:

$$(k^2 A_2 + ikA_1 + A_0 - \omega^2 M)U = 0, \quad (2.2)$$

where  $A_0, A_1, A_2$  are decompositions of the global stiffness matrix in powers of  $k$ ,  $M$  is the mass matrix, and  $U$  is the nodal displacement vector. These matrices are constructed from elementary matrices, which are computed for each element during the FE discretization procedure. Owing to the introduction of an auxiliary variable, the quadratic eigenproblem (2.2) is transformed into the linear eigenproblem (2.3), which can be solved by standard solvers for sparse matrices:

$$(A - kB)\underline{Q} = 0, \quad (2.3)$$

$$\underline{Q} = \begin{pmatrix} U \\ kU \end{pmatrix}, \quad (2.4)$$

where

$$A = \begin{pmatrix} 0 & I \\ \omega^2 M - A_0 & -iA_1 \end{pmatrix}, \quad (2.5)$$

$$B = \begin{pmatrix} I & 0 \\ 0 & A_2 \end{pmatrix}. \quad (2.6)$$

Eigenvalues and eigenvectors obtained by solving equation (2.3) correspond to wavenumbers and modal displacements of guided modes. Solutions are obtained for both directions of propagation  $x_1$  and  $-x_1$ , so the modes corresponding to the positive direction of propagation  $x_1$  have to be extracted. Further filtering has to be applied to eliminate evanescent modes, for which the wavenumber is purely imaginary, i.e.  $\Re(k) = 0 \text{ rad/mm}$ , and rapidly decaying ones, for which

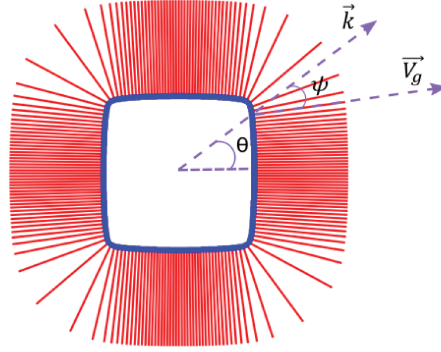


Figure 2.6 – Schematic of anisotropic propagation of GWs in layered composite plate.

the wavenumber has a significant imaginary part.

### 2.3.2 Modal expansion method

Once modes in the current waveguide are computed, the Poynting vector (2.7) and consequently the 2D Excitability matrix (2.8) for one given mode  $m$  can be obtained from corresponding eigenvalues and eigenvectors for the angle  $\psi_m$  as follows [82]:

$$P_m(\theta) = \frac{\omega}{2} (\text{imag}(\underline{U}_m^\dagger(\theta)(ikA_2 + A_4))\underline{U}_m(\theta)), \quad (2.7)$$

$$E_m^{2D}(\theta) = \frac{i\omega}{4P_m} \underline{U}_m \underline{U}_m^\dagger, \quad (2.8)$$

It has been shown that a far-field asymptotic expression of the 3D Green's function in composite plates can be written in terms of the modal expansion. It allows reconstructing the 3D theoretical signal using 2D modal solutions computed by SAFE. The relation between 2D and 3D formulations of the guided waves is the following:

$$E_m^{3D}(\alpha, z) = B_m(\psi_m)A^{-1}(\psi_m)E_m^{2D}(\psi_m)A(\psi_m), \quad (2.9)$$

where  $B_m(\psi_m)$  is the propagation factor of the mode  $m$  in the direction  $\psi_m$ ,  $A(\psi_m)$  is the rotation matrix, and  $\psi_m$  is the steering angle of the guided mode  $m$  as schematically shown in Figure 2.6 [39].

Equation 2.9 shows that the far-field solution for the mode  $m$  in the  $\alpha$  direction is related to the appropriate 2D modal solution for the same mode in the  $\psi_m$  direction. The 3D Green's function for the structure of interest can be expressed as follows:

$$G^{3D}(r, \alpha, z) = \frac{1}{\sqrt{r}} \sum_m E_m^{3D}(\alpha, z) e^{irk_m(\psi_m)\cos\psi_m - \alpha}. \quad (2.10)$$

In order to compute modal components of the 3D Green's function, it is necessary to track each mode for the frequency range of interest. A useful property of guided modes is that they form an orthogonal basis of the solutions in the waveguide section for a given frequency. This basis

can be obtained from the orthogonality matrix:

$$O = \begin{pmatrix} A_1 - \omega^2 M & 0 \\ 0 & -A_3 \end{pmatrix}, \quad (2.11)$$

which represents a scalar product on a specific basis. Hence, the modal displacements obtained for the formulation 2.2 have to be expressed in this specific basis. The basis change is done through the unitary transformation matrix  $T$ . More specifically, the matrix  $T$  is diagonal, where all off-diagonal elements are equal to zero. The diagonal elements are equal to one, except for elements corresponding to the particle displacements in the  $x_1$  direction, which are equal to the imaginary unit  $i$ . Therefore, the modal displacement vector can be reformulated as follows:

$$\underline{\hat{Q}} = T \underline{Q}. \quad (2.12)$$

Orthogonality relation states that for the frequency  $\omega$  all existing modes are orthogonal, and this yields the following:

$$\underline{\hat{Q}}_m^\dagger(\omega) O_m(\omega) \underline{\hat{Q}}_m(\omega) = 0. \quad (2.13)$$

Consequently, it can be assumed that orthogonality relation still approximately holds for the solutions that are quite close in the frequency domain, which gives:

$$\begin{cases} \underline{\hat{Q}}_n^\dagger(\omega) O_m(\omega) \underline{\hat{Q}}_m(\omega + \delta\omega) \approx 0 \\ \underline{\hat{Q}}_m^\dagger(\omega) O_m(\omega) \underline{\hat{Q}}_m(\omega + \delta\omega) \neq 0, \end{cases} \quad (2.14)$$

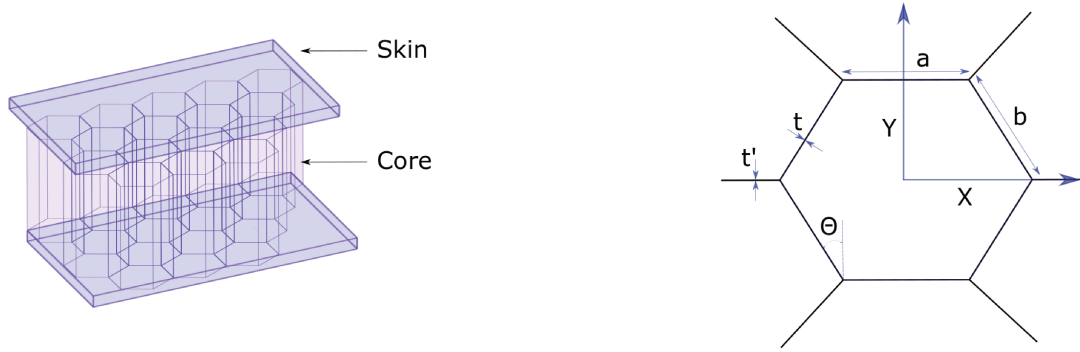
where  $\delta\omega \ll \omega$ . Orthogonality terms have to be calculated between the current eigenvector  $\underline{\hat{Q}}_m(\omega)$  that corresponds to the mode  $m$  at frequency  $\omega$  and all other existing solutions for adjacent frequency  $\underline{\hat{Q}}_m(\omega + \delta\omega)$ . The correct mode tracking is achieved by minimizing the orthogonality term and imposing the mode continuity constrains.

### 2.3.3 Homogenization model for HCSS

The honeycomb sandwich structure consists of an aluminum honeycomb core bonded to layered composite skins, as shown in Figure 2.7. Hence, such a complex structure cannot be straightforwardly modeled using SAFE formulation. Song et al. [86], Smelyanskiy et al. [87] and Sikdar et al. [88] showed that by replacing the honeycomb core with an equivalent orthotropic plate, it is possible to model static and low-frequency dynamics of the HCSS. This approach provides acceptable results when the wavelengths of propagating GWs are larger than the size of an elementary cell. Effective elastic properties of an equivalent plate can be obtained using various analytical and numerical homogenization models.

From the numerical point of view, a homogenization model is much less time consuming and computationally demanding than the models that describe all the micro-structures of honeycomb cells. It has been demonstrated by Tian et al. [89] and Florens [1] that in the high frequency range, where the wavelengths are comparable to the size of the honeycomb cell, the interactions between GWs and the core layer become noticeable. Such interactions result in complex deformation modes of the honeycomb cell. They are also responsible for several phenomena, including structural resonances, where standing waves are formed in the single cell, and the appearance of energy band gaps.

On the basis of the analysis of GWs propagation in HCSS [1], it was agreed to monitor the structure using low-frequency excitation, so the wavelength of propagating guided modes are



(a) Schematic representation of a honeycomb sandwich structure. The skin of the HCSS consists of multi-layered CFRP and GFRP composites. Adhesive is used to attach an aluminum honeycomb core to the skins.

(b) Geometric parameters of the unit honeycomb cell. The side lengths of the cell are defined by  $a$  and  $b$ , while the single wall and double wall thicknesses are defined by  $t$  and  $t'$ , respectively.

Figure 2.7 – Schematic of the honeycomb composite sandwich structure.

larger than the honeycomb cell size. This constraint is aimed at avoiding GWs interaction with the honeycomb core layer, while preserving the capability of GWs to interact with structural flaws. Hence, HCSS can be modeled as a classical multi-layered composite enabling the use of the 2D SAFE formulation.

The Gibson and Ashby's model [90] is considered as a reference work for the honeycomb core homogenization. It permits computing nine elastic effective parameters (Young moduli, shear moduli and Poisson ratios) of an equivalent orthotropic plate. This analytical model requires the geometric parameters of the honeycomb cell, shown in Figure 2.7b, and the elastic properties of the constituting material. However, this model ignores vertices at the intersection of horizontal and inclined walls of the cell and neglects the double thickness of the walls in the X direction. Consequently, it does not agree well with measurements for increasing value of the relative density of the core.

In their recent work, Malek and Gibson [91] overcame this problem by considering honeycomb cell vertices and by introducing an effective bending length of cell walls, which resulted in a more accurate analytical model. Therefore, this model has been chosen for this study. The relative density of the core layer can be computed as follows:

$$\frac{\rho^*}{\rho_s} = 1 - \frac{l \cos \theta (h_b + l \sin \theta)}{(l \cos \theta + t)(h + l \sin \theta)}, \quad (2.15)$$

where  $\rho^*$  and  $\rho$  are the effective and constitutive material densities,  $l_b = l - t/(2 \cos \theta)$ , and  $h_b = h - t(1 - \sin \theta)/\cos \theta$  are the bending lengths of the inclined and horizontal cell walls under an in-plane load. The cell wall thickness and angle between inclined and horizontal walls are denoted by  $t$  and  $\theta$ , respectively, see Figure 2.7b.

The in-plane and out-of-plane Young effective moduli of the homogenized core layer can be computed as follows:

$$E_1 = E_s \left(\frac{t}{l_b}\right)^3 \frac{\cos \theta}{(h/l + \sin \theta) \sin^2 \theta} \frac{1}{1 + (2.4 + 1.5\nu_s + \cot^2 \theta)(t/l_b)^2}, \quad (2.16)$$

$$E_2 = E_s \left(\frac{t}{l_b}\right)^3 \frac{h/l + \sin \theta}{\cos^3 \theta} \frac{1}{1 + (2.4 + 1.5\nu_s + \tan^2 \theta + \frac{h_b/l_b}{\cos^2 \theta})(t/l_b)^2}, \quad (2.17)$$

$$E_3 = E_s \frac{\rho^*}{\rho_s}, \quad (2.18)$$

where  $E_1, E_2, E_3$  denote effective Young moduli,  $E_s$  and  $\nu_s$  correspond to the constitute material Young modulus and Poisson ratio, respectively. The effective shear moduli can be obtained as follows:

$$G_{12} = E_s \frac{h/l + \sin \theta}{(h_b/l_b)^2 \cos \theta} \frac{1}{C}, \quad (2.19)$$

$$G_{13} = G_s \frac{t/l}{(h/l + \sin \theta)(\cos \theta + t/l)} \left[ \cos^2 \theta \left(\frac{l_b}{l}\right) + 2 \left(\frac{t}{l}\right) \tan\left(\frac{\pi}{4} - \frac{\theta}{2}\right) \right], \quad (2.20)$$

$$G_{23} = G_s \frac{t/l}{(h/l + \sin \theta)(\cos \theta + t/l)} \left[ \sin^2 \theta \left(\frac{l_b}{l}\right) + \frac{h}{l} + \frac{t}{l} \tan\left(\frac{\pi}{4} - \frac{\theta}{2}\right) \right], \quad (2.21)$$

with

$$C = 1 + 2(h_b/l_b) + (t/l_b)^2 \left( \frac{2.4 + 1.5\nu_s}{h_b/l_b} (4 + h/l + \sin \theta) + \frac{h/l + \sin \theta}{(h_b/l_b)^2} [(h/l + \sin \theta) \tan^2 \theta + \sin \theta] \right), \quad (2.22)$$

where  $G_s$  denotes a shear modulus of the constitutive material. Finally, effective in-plane and out-of-plane Poisson ratios can be computed as follows:

$$\nu_{12} = \frac{\cos^2 \theta}{(h/l + \sin \theta) \sin \theta} \left[ \frac{1 + (1.4 + 1.5\nu_s) \left(\frac{t}{l_b}\right)^2}{1 + (2.4 + 1.5\nu_s + \cot^2 \theta) \left(\frac{t}{l_b}\right)^2} \right], \quad (2.23)$$

$$\nu_{21} = \frac{\sin \theta (h/l + \sin \theta)}{\cos^2 \theta} \left[ \frac{1 + (1.4 + 1.5\nu_s) \left(\frac{t}{l_b}\right)^2}{1 + (2.4 + 1.5\nu_s + \tan^2 \theta + \frac{2(h_b/l_b)}{\cos^2 \theta}) \left(\frac{t}{l_b}\right)^2} \right], \quad (2.24)$$

$$\nu_{31} = \nu_{32} = \nu_s, \quad (2.25)$$

where  $\nu_s$  denotes the Poisson ratio of the constitute material. It is worth noting that once all the three effective Young's moduli, namely  $E_1, E_2, E_3$ , are obtained, other Poisson's ratios can be determined using reciprocal relation. Having analyzed effective elastic properties formulations, it can be concluded that the in-plane effective parameters vary as a function of  $(\frac{t}{l})^3$ , while the out-of-plane parameters exhibit linear behavior with respect to  $\frac{t}{l}$ . It has been shown that the effective shear moduli  $G_{13}$  and  $G_{23}$  of the core and the Young modulus of the skins have the highest impact on the HCSS dynamics.

Such an analytical honeycomb homogenization model takes into account the effect of nodes at the intersection of the cell walls and introduces an effective bending length. Hence, an accurate HCSS modeling in a low frequency range becomes possible. The validation of the modeling results is presented in the section 2.2. It is noteworthy that this homogenization model is physically consistent only in low frequency range (which is currently sufficient for defect detection in IFS). However, as Tie et al. [92, 93] demonstrated, it lacks of accuracy for

	$E_1 = E_2, MPa$	$E_3, MPa$	$\nu_{12}$	$\nu_{13} = \nu_{23}$	$G_{12}, MPa$	$G_{13} = G_{23}, MPa$	$\rho, kg/mm^3$
<b>CFRP</b>	65700	4500	0.03	0.3	5100	2500	1760
<b>GFRP</b>	72400			0.255		28800	2100
<b>Core</b>	0.4	1131.3	0.8	0.00013	0.1	207.2	67

Table 2.1 – Elastic parameters of the CFRP, GFRP and effective elastic parameters of the honeycomb core.

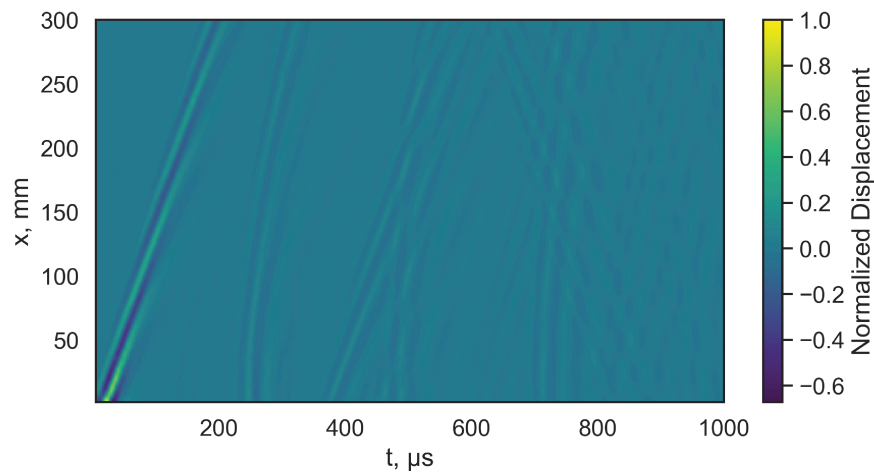
higher frequencies range where wavelengths are of the same size as the honeycomb cell and meso-scale interactions become important. Therefore, further improvements of this method might consist in coupling SAFE method with Bloch's function formulation in order to deliver fast and reliable GWs modeling tool that would be valid for higher frequencies.

### 2.3.4 Validation of simulation results

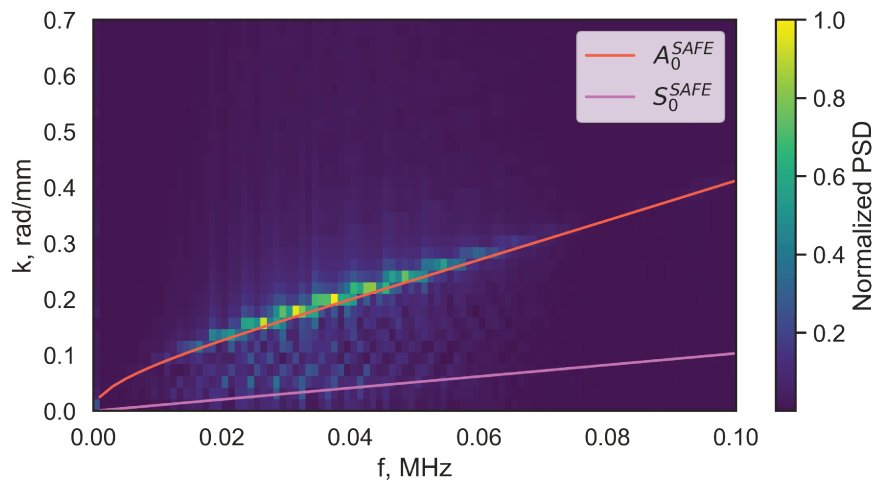
GWs propagation can be equidistantly recorded in a 2D dictionary along the line of observation which passes through the PZT. Such a collection represents a time-distance domain mapping of GWs or so-called b-scan measurements. Alleyne and Cawley [44] demonstrated that the 2D Fourier transform, along the time and space axes, can be applied to the B-scan measurements in order to transform the time-space domain into the wavenumber-frequency domain. There are several advantages of such transformation, but the main one is that it is capable of decomposing overlapped and superposed guided wavepackets into guided modes. Such a technique is often used to validate GWs modeling, as theoretical modal solutions can be compared to experimental dispersion curves in order to evaluate wavenumber computation accuracy for the frequency range of interest.

For example, GWs B-scan and corresponding dispersion curves for orthotropic CFRP plate are shown in Figure 2.8. The CFRP plate consists of twenty one woven-ply laminates, each 0.275 mm thick, which are oriented 0° with respect to the carbon fiber direction. The elastic parameters are tabulated in Table 2.1. The GWs are generated using PZT 18 mm in diameter and 0.5 mm thick, and the excitation function contains two Hanning modulated cycles centered at 40 kHz. The modal solution obtained with SAFE modeling method are superimposed over the experimental dispersion curves. By analyzing the results, it can be concluded that the SAFE model presented in section 2.3.1 provides an accurate solution for the  $A_0$  mode. Unfortunately, theoretical solution of  $S_0$  mode cannot be compared with experimental ones due to measurement set-up limitations.

As described in section 2.3, once wavenumbers and associated displacement vectors are obtained from the 2D SAFE formulation, the 3D Green's function can be computed using the far-field approximation. Consequently, the displacement field generated by the harmonic point force applied to the surface of the multi-layered composite plate can be obtained. The MEM formulation stipulates that the global 3D displacement field is computed as a sum of 3D displacement fields related to each mode. The magnitude of the 3D displacement field of the specific mode depends on the corresponding 3D excitability matrix. The latter can be computed from the 2D excitability matrix depending on 2D modal displacement vectors. Taking into account that the wavenumber solutions have been previously validated, the associated modal displacement vectors can be considered correct and the 3D Green's function and the displacement field can be computed. The real part of the 3D Green's function for the same composite plate is shown in Figure 2.9.

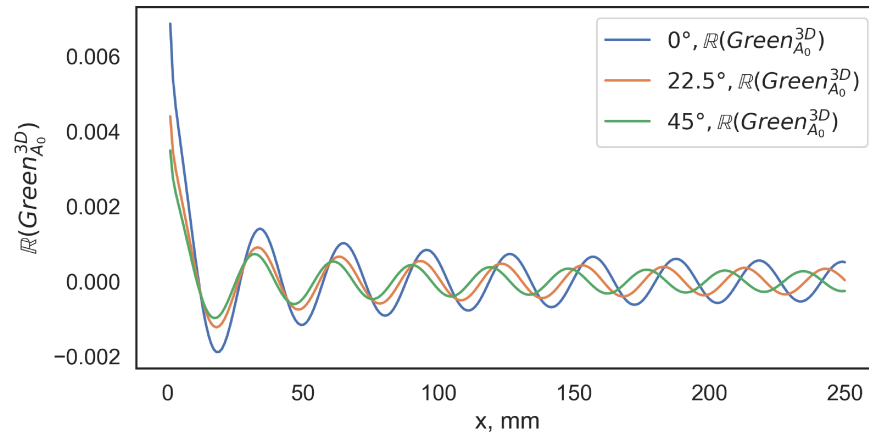


(a) Time-distance domain mapping, i.e. B-scan, of the GWs. It can be observed that the time duration of the wave packets corresponding to a single guided mode increases with a propagating distance due to the dispersion phenomena.

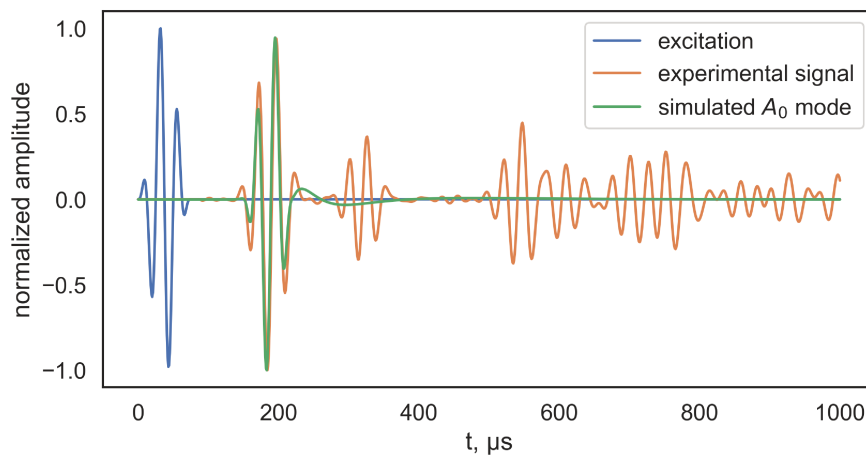


(b) Wavenumber-frequency domain mapping of the GWs superposed to the theoretical dispersion curve of the simulated  $A_0$  mode, which is computed using SAFE modeling method. Comparison of simulation and experiment shows a good agreement. The  $S_0$  mode is not tractable on experimental dispersion pattern as the LSVD is more sensitive to the out-of-plane than to the in-plane surface displacements.

Figure 2.8 – GWs propagation in  $0^\circ$  direction in the composite plate consisting of twenty one orthotropic CFRP laminates, each  $0.275\text{ mm}$  thick. The excitation function is a Hanning modulated two-cycle tone burst with a central frequency set to  $40\text{ kHz}$ . The PZT transducer,  $18\text{ mm}$  in diameter and  $0.5\text{ mm}$  thick, is selected to generate GWs in the structure.



(a) The real part of 3D Green's function computed at 40 kHz for 0°, 22.5°, and 45° direction.



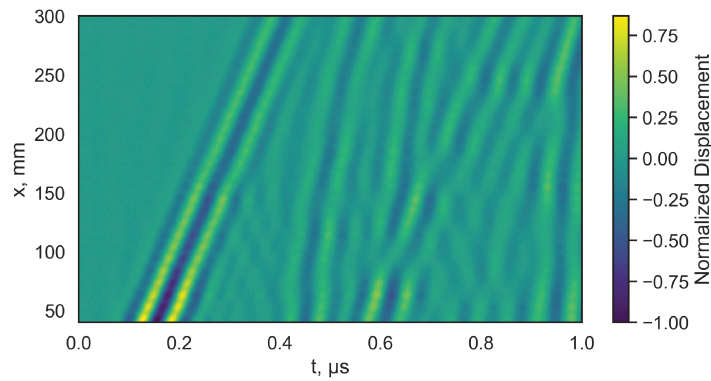
(b) Modeled GWs signal validation in CFRP plate at 40 kHz. The experimental signal measured by LSVD is compared with the theoretically propagated  $A_0$  mode on 250 mm in the 0° direction.

Figure 2.9 – The 3D Green function and GWs signal validation in multi-layered CFRP composite. The CFRP consists of twenty one woven-ply orthotropic laminates, each 0.275 mm thick, where all the plies are oriented in 0° direction with respect to the carbon fibers placement.

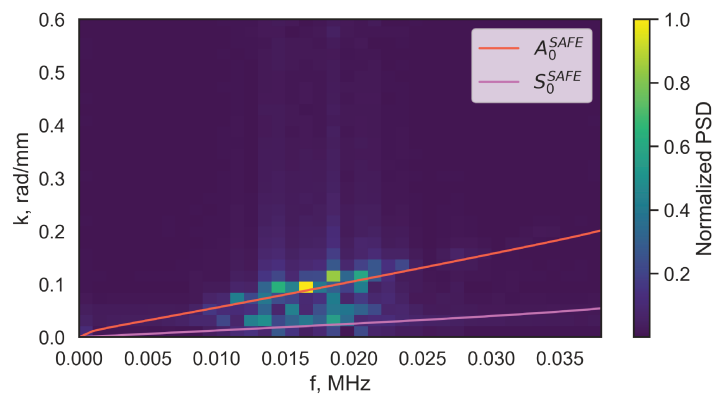
In the current research, it was chosen to inspect the structure using low frequencies, where the wavelength is larger than the honeycomb cell size in order to avoid GWs-HCSS core layer interaction, while preserving the capability of GWs to interact with structural flaws. Under these constraints, the HCSS can be considered as a classical multi-layered composite consisting of different orthotropic plies. For example, to model GWs propagation in such a structure a 20 mm thick HCSS has been selected. Its top skin panel consists of a three-layer CFRP plate attached to the GFRP ply, whereas the bottom skin is composed of GFRP ply attached to a five-layer CFRP plate. All the plies comply with the following orientation  $0^\circ, 45^\circ, 0^\circ, 0^\circ$ , and  $0^\circ, 0^\circ, 45^\circ, 0^\circ, 45^\circ, 0^\circ$  in the top and bottom skins, respectively. Each ply is 0.275 mm thick, and the elastic parameters are tabulated in Table 2.1.

To simulate GWs propagation in HCSS, the Malek-Gibson homogenization model has been applied (as presented in Section 2.3.3). Obviously, this model is less time-consuming and computationally demanding than those which describe all the micro-structures of honeycomb cells of the core layer. However, it is worth noting that the homogenized model is correct in describing static or low frequency dynamic behaviors of the HCSS, but it fails to provide an accurate solution for higher frequencies. It has been demonstrated that for the high frequency range, where wavelengths are comparable to the size of the honeycomb cell, it is no more reasonable to consider the core layer as homogeneous, since interactions between waves and honeycomb cells become noticeable. Low frequency GWs wavenumbers modeling results for  $0^\circ$  direction are presented in Figure 2.10. The theoretical solutions are superimposed with the experimental ones, and show a good agreement.

Eigenvectors obtained from the SAFE modeling, while the honeycomb core has been homogenized, cannot be considered as real modal displacements, rather pseudo modal displacements. Even though, wavenumber solutions exhibit a good agreement with an experiment even above 50 kHz, these solutions are no more reliable, as they do not take into account GWs-core layer interactions. Hence, the 3D Green's function can be computed only in the low frequency range, as associated modal characteristics, e.g. Poynting vector, Maris factor etc., require displacement vectors to be computed. Figure 2.11a presents a real part of the 3D Green's function for the HCSS in the  $0^\circ, 22.5^\circ, 45^\circ$  directions. The 3D Green's function has been used to compute an analytical signal, which contains  $A_0$  mode propagated on the 150 mm, see Figure 2.11b.

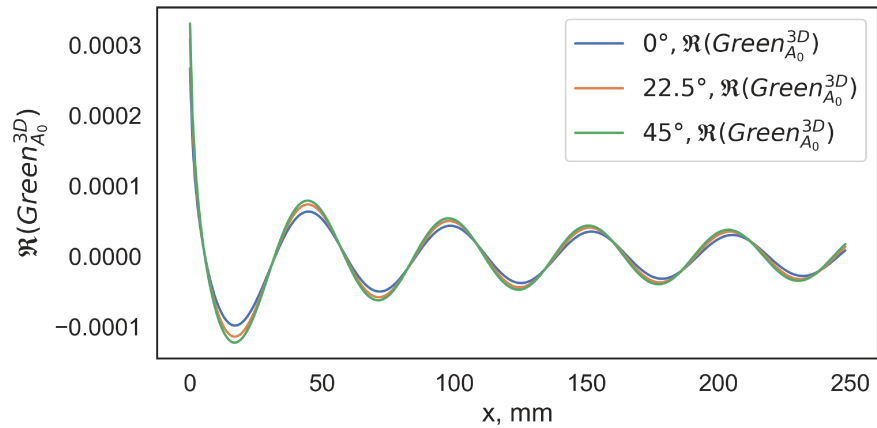


(a) Time-distance domain mapping, i.e. B-scan, of the GWs.

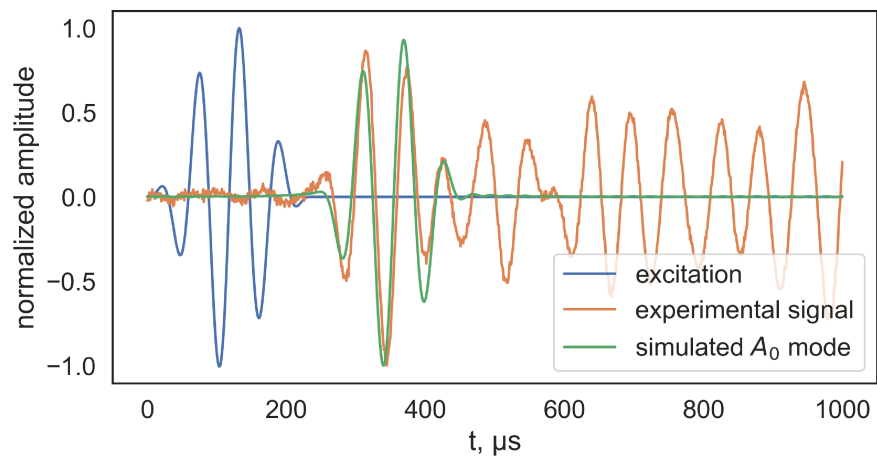


(b) Wavenumber-frequency domain mapping of the GWs superposed to the theoretical dispersion curve of the simulated  $A_0$  mode, which is computed using SAFE modeling method. Comparison of simulation and experiment shows a good agreement. The  $S_0$  mode is barely tractable in the experimental dispersion pattern as the LSVD is more sensitive to the out-of-plane than to the in-plane surface displacements.

Figure 2.10 – GWs propagation in  $0^\circ$  direction in the HCSS. The excitation function is a Hanning modulated four-cycle tone burst with a central frequency set to  $20\text{ kHz}$ . The PZT transducer,  $24\text{ mm}$  in diameter and  $0.5\text{ mm}$  thick, is selected to generate GWs in the structure.



(a) The real part of the  $A_0$  modal component of the 3D Green's function computed at 20 kHz for  $0^\circ$ ,  $22.5^\circ$ , and  $45^\circ$  direction.



(b) Comparison of experimental signal and theoretically propagated  $A_0$  mode on 270 mm in the  $0^\circ$  direction.

Figure 2.11 – The 3D Green function and GWs signal validation in HCSS.

## 2.4 Data driven approach for Guided Waves modeling

For simple shape structures, e.g. plates, pipes, rails, the 3D Green's function can be computed for each guided mode using analytical modeling methods, such as SAFE or GMM. However, real-life structures are often equipped with stiffeners or joints, which introduce additional complexity to GWs propagation. Such structural features modify the 3D Green's function of each propagating mode, so analytical determination is no longer possible. On the other hand, a classical finite element modeling (FEM) method can be used to model structures of any complexity, but it requires a tedious meshing procedure and significant computation time. To partially overcome this limitation, a hybrid SAFE/FE method has also been developed to deal with stiffened composite plates where the propagation through the stiffener is computed by FE whereas the propagation elsewhere is computed using the SAFE method [94]. However, this method is barely adapted to real aerospace structures that are large and often equipped with multiple structural features.

For the sake of overcoming this limitation, an experimental approach for the 3D Green's function determination in composite plates is discussed in this section. The proposed technique is generic and, therefore, can be applied to any structure regardless complexity of the geometry or constitutive materials. Alleyne and Cawley [44] demonstrated that the 2D Fourier transform could be used for obtaining experimental dispersion curves of propagating GWs. In the wavenumber - frequency domain, i.e., Fourier space, the GWs are well-discriminated, unlike the time-distance domain [95]. Therefore, modal components of the 3D Green's function can be deconvolved from the spectrum. Such a filter can be constructed using machine learning techniques, including overlapping mixtures of Gaussian processes, in order to preserve information relevant to the guided mode of interest and discard the rest.

### 2.4.1 Bayesian Framework for Guided waves spectra processing

The overlapping mixtures of Gaussian processes (OMGPs) algorithm [96] has been proven effective for data association problems. It is based on Gaussian processes (GPs) and is capable of clustering mixed data into different trajectories that can come close and even cross each other. In the following section, theoretical foundations of Bayesian inference, GP and OMGP are provided.

#### 2.4.1.1 Bayesian Inference

Data modeling problems occur in different fields of research, including SHM. In the Bayesian framework, a model of a particular phenomenon can be designed using prior knowledge, and when the data are considered, the model can be adapted to new information. In this framework, knowledge can be formulated in terms of probability distributions. For example, given the 2D spectrum of the GWs in a plate-like structure and the corresponding model describing the dispersion curves by curvilinear lines, the spectrum data can be element-wise associated with different dispersion curves with certain probability. It is worth noting that the model choice plays a key role in this framework.

Firstly formulated by Bernoulli in 1713, this probabilistic framework was then developed by Bayes in 1763, Laplace in 1812, and Jeffreys in 1939. Consider a model  $\mathbb{H}_i$  with parameters  $\theta_i$ , which is used to describe some data  $D$ . Bayesian inferences can thus be made using a two step procedure. The first step consists of inferring parameters  $\theta_i$  of the model using the data, and the second one involves selecting the best model among counterparts [97].

The prior belief about models  $\mathbb{H}$  can be expressed in terms of probability distribution over all possible models,  $P(\mathbb{H}_i)$ . The prior belief about parameters can be also described as probability

distribution,  $P(\theta_i|\mathbb{H}_i)$ . Each model is characterized by a distinct set of parameters  $\theta_i$ , therefore, parameters distribution is conditional on  $\mathbb{H}_i$ .

Consider the first step of the framework and the data. Parameters have to be inferred for each model conditioning on the data. In other words, each model makes a prediction about how likely the data  $D$  were generated using  $\mathbb{H}_i$  and parameters  $\theta_i$ , which results in corresponding probability distribution  $P(D|\theta_i, \mathbb{H}_i)$ . The Bayes' theorem can be used for updating the prior distribution of the parameters,  $P(\theta_i|\mathbb{H}_i)$ , using the knowledge that was just gained from the data  $P(D|\theta_i, \mathbb{H}_i)$ . The updated, i.e. posterior, distribution of parameters can be expressed as follows:

$$P(\theta_i|D, \mathbb{H}_i) = \frac{P(D|\theta_i, \mathbb{H}_i)P(\theta_i|\mathbb{H}_i)}{P(D|\mathbb{H}_i)}, \quad (2.26)$$

where  $P(\theta_i|D, \mathbb{H}_i)$  is the posterior distribution of parameters,  $P(D|\theta_i, \mathbb{H}_i)$  is the likelihood describing the gain of information from the data,  $P(\theta_i|\mathbb{H}_i)$  is the prior parameter distribution, and  $P(D|\mathbb{H}_i)$  is the evidence or marginal likelihood. The latter term describes the probability of the data for a given model, so the best model from the hypothesis space can be chosen as the one with the largest  $P(D|\mathbb{H}_i)$ . For instance, the information gain and therefore parameters selection for a toy model, which complies with Gaussian distribution, is provided in Appendix A.1.

The second step of the Bayesian framework consists in selecting the best model using the evidence from the equation (2.26). The Bayes' theorem can be applied once again to compute the credibility of the model  $\mathbb{H}_i$ . It can be expressed as follows:

$$P(\mathbb{H}_i|D) = \frac{P(D|\mathbb{H}_i)P(\mathbb{H}_i)}{P(D)}, \quad (2.27)$$

where  $P(\mathbb{H}_i|D)$  is the probability distribution of the model  $\mathbb{H}_i$  while describing the dataset  $D$ . It allows estimating the plausibility of the model. The  $P(D)$  is the probability distribution of the data.

It should be noted that the Bayesian framework operates in a closed hypothesis space. Therefore, it is important to choose a good set of models for describing the data, so that they are flexible enough to capture features of the data, and simple enough to avoid over-fitting. The parameters  $\theta_i$ , which are inferred from the data, introduce an additional complexity when it comes to compare models from the hypothesis space. The marginal-likelihood  $P(D|\mathbb{H}_i)$  can be evaluated, thus the best model can be chosen as follows:

$$P(D|\mathbb{H}_i) = \int P(D|\theta_i, \mathbb{H}_i)P(\theta_i, \mathbb{H}_i)d\theta_i, \quad (2.28)$$

where the likelihood  $P(D|\theta_i, \mathbb{H}_i)$  and the priors  $P(\theta_i, \mathbb{H}_i)$  are in general non-linear functions. The integral (2.28) is often analytically intractable, except for the linear models, where the likelihood complies with the Gaussian distribution. Such a linear model is specified by a number of basis functions, and is named the Gaussian process.

#### 2.4.1.2 Gaussian process

The Gaussian process (GP) [98], a flexible Bayesian nonparametric model, has been widely used in a multitude of applications for data analysis due to its remarkable analytical properties and exceptional performance in regression tasks. Assume the data set of  $N$  elements  $D \equiv \{x_i, y_i\}_{i=1}^N$ , where  $x$  and  $y$  denote inputs and corresponding outputs. The regression problem can be formulated as follows: for a given new input  $x_*$ , derive a predictive distribution for the corresponding output  $y_*$  using  $D$ .

The GP regression model supposes that the observation  $y$  differs from the function values  $f(x)$  by an additive noise  $\epsilon$ . The noise complies with the independent and identically distributed Gaussian distribution with zero mean and variance  $\sigma$  that specifies the noise power. Thus, the regression problem can be expressed as follows:

$$y = f(x) + \epsilon, \quad (2.29)$$

where the function  $f(x)$  describes variables  $x$  as the Gaussian distribution  $N$  with the mean  $\mu$ , often set to 0 by subtracting the sample mean from the data set  $\{y(x_n)\}_{n=1}^m$ , and the covariance function  $K(x, x')$ , also known as kernel. One of the most well-known covariance functions [99] is a squared exponential:

$$K(x, x') = \sigma_0 \exp\left(-\frac{1}{2} x^T \Lambda^{-1} x'\right), \quad (2.30)$$

where  $\sigma_0$  is the signal power and  $\Lambda$  is the length scale that controls the decay rate of the correlation between outputs. From now on, all kernel parameters will be referred to as  $\theta$ .

Hence, for all available and forthcoming observations, the GP regression problem can be formulated as follows:

$$\begin{pmatrix} y \\ y_* \end{pmatrix} \sim N\left(\mu, \begin{pmatrix} K + \sigma^2 I & K_* \\ K_*^T & K_{**} \end{pmatrix}\right), \quad (2.31)$$

where  $K = K(x, x')$ ,  $K_* = K(x, x'_*)$ , and  $K_{**} = K(x'_*, x'_*)$ .  $I$  denotes the identity matrix. The predictive distribution for  $y_*$  is obtained from equation 2.31 conditioned on the available dataset  $D$  using the Bayes' theorem:

$$P_{GP}(y_* | x_*, D) = N(y_* | \mu_{GP_*}, \sigma_{GP_*}^2), \quad (2.32)$$

where the expected mean value  $\mu_{GP_*}$  and expected variance  $\sigma_{GP_*}^2$  for unknown output  $y_*$  are computed as follows:

$$\mu_{GP_*} = K_*^T (K + \sigma^2 I)^{-1} y \quad (2.33)$$

$$\sigma_{GP_*}^2 = \sigma^2 + K_{**} - K_*^T (K + \sigma^2 I)^{-1} K_*. \quad (2.34)$$

It is evident that the GP regression model performance highly depends on the hyperparameters  $\{\theta, \sigma\}$ , which specify the kernel and independent noise in the model. Optimal parameters can be obtained by maximizing the marginal likelihood, while fitting the model on the dataset  $D$ . In practice, a log of marginal likelihood is maximized due to computational reasons. It can be expressed as follows:

$$\log(P(y|\theta, \sigma)) = -\frac{1}{2} y^T (K + \sigma^2 I)^{-1} y - \frac{1}{2} |K + \sigma^2 I| - \frac{N}{2} \log(2\pi). \quad (2.35)$$

The kernel is often constructed so that the analytical derivative of (2.35) is available. Thus, the optimization gradient methods can be efficiently used for selecting optimal hyperparameters.

### 2.4.1.3 Overlapping Mixtures of Gaussian Processes

GPs constitute building blocks for the OMGP [96], which assumes that there are  $M$  different trajectories in the data set  $D$ , and each trajectory can be associated with a corresponding latent function from the dictionary  $F = \{f^m(x)\}_{m=1}^M$ . It is worth noting that each latent function can be specified by different covariance functions  $K^m$ , and every output  $y$  can be evaluated using only one of these functions and by adding an independent noise to it. Hence, the binary  $N \times M$  data association matrix  $Z$  can be constructed for the dataset  $D$ , where each matrix element  $z_{n,m}$

designates that the observation  $y_n$  was generated using  $f^m(x_n)$  and belongs to the trajectory  $m$ .

Regarding the previously mentioned description of GP, the OMGP model's likelihood can be formulated using every observed element  $n$  as follows:

$$P(y|f^m, Z) = \prod_{n=1, m=1}^{M, N} N(y_n | f^m(x_n), \sigma^2)^{z_{n,m}}, \quad (2.36)$$

where the prior probability distributions for the association matrix  $Z$  and latent functions  $f^m$  are defined as follows:

$$P(Z) = \prod_{n=1, m=1}^{M, N} \Upsilon^{z_{n,m}}, \quad (2.37)$$

$$P(f^m|x) = \prod_{n=1, m=1}^{M, N} N(f^m(x_n) | 0, K^m), \quad (2.38)$$

where in the multinomial distribution  $\rho(z)$  the hyperparameters  $\Upsilon^{z_{n,m}}$  satisfy the following expression:  $\sum_{m=1}^M \Upsilon^{z_{n,m}} = 1, \forall_n$  and the independent Gaussian process is associated with each trajectory  $m$ .

In general form, the marginal likelihood is defined as an integral of the likelihood times the prior distribution. Unlike a single GP, an analytical computation of the posterior distribution (2.36) for OMGP model is intractable, so the approximation techniques based on the evaluation of the Kullback-Leibler (KL)-corrected variational bound are used. Taking into account that the marginal likelihood is a convex function, the Jensen's inequality can be used for obtaining its lower bound:

$$\begin{aligned} \log \rho(y|x) &= \log \int P(y|f^m, Z) P(Z) \prod_{m=1}^M P(f^m|x) d(f^m) dZ \\ &\geq \int q(f^m, Z) \log \frac{P(y|f^m, Z) P(Z) \prod_{m=1}^M P(f^m|x)}{q(f^m, Z)} d(f^m) dZ =: \zeta_{VB}, \end{aligned} \quad (2.39)$$

where the  $\zeta_{VB}$  is a lower bound on log marginal likelihood  $\log P(y|x)$  for any variational distribution  $q(f^m, Z)$ . For the equation (2.39), the equality is reached if and only if variational distribution becomes a true posterior distribution of OMGP, i.e.  $q(f^m, Z) = P(Z, f^m|x, y)$ . It is also assumed that the variation distribution consists of linearly independent distributions, so it can be factorized as follows:

$$q(f^m, Z) = q(f^m)q(Z). \quad (2.40)$$

Consider that the probability distribution over trajectories  $q(f^m)$  is given, then the lower bound on log-marginal likelihood  $\zeta_{VB}$  can be maximized with respect to the  $q(Z)$ . Similarly, assuming that  $q(Z)$  is given, it allows maximization of  $\zeta_{VB}$  with respect to  $q(f^m)$ . Therefore, distributions  $q(f^m)$  and  $q(Z)$  initialized from their priors (2.37) and (2.38), respectively, are iteratively updated following such a twofold optimization procedure. The convergence can be guaranteed as both distributions are increasingly ameliorated, and for each optimization step the lower bound can be computed as follows:

$$\zeta_{VB} = \log P(Y|F^m, Z)_{q(f^m, Z)} - KL(q(F^m || p(F^m))) - KL(q(Z) || p(Z)), \quad (2.41)$$

where

$$\log P(Y|F^m, Z)_{q(f^m, Z)} = \sum_{n,m}^{N,M} \Upsilon_{n,m} a_{nm}, \quad (2.42)$$

with

$$a_{nm} = -\frac{1}{2\sigma^2}((y_n - \mu_m)^2 + \Sigma_{n,n}^m - \frac{1}{2} \log 2\pi\sigma^2), \quad (2.43)$$

and

$$\Sigma^m = (K^{-1,m} + B^m)^{-1}, \quad (2.44)$$

$$\mu^m = \Sigma^m B^m y^m, \quad (2.45)$$

where  $B^m$  is a diagonal matrix containing  $[\Upsilon_{1,m}/\sigma^2 \dots \Upsilon_{N,m}/\sigma^2]$  elements. KL denotes the Kullback-Leibler divergence, that is a measure of how approximate posterior distribution is different from the prior. For arbitrary discrete probability distributions  $P$  and  $Q$ , it can be computed as follows:

$$KL(P||Q) = \sum_i P(i) \log \frac{Q(i)}{P(i)}. \quad (2.46)$$

The  $KL$  divergence is used for quantifying the information gain that can be obtained if  $Q$  is used instead of  $P$ . In other words, it denotes an amount of information lost when distribution  $Q$  is used for approximating distribution  $P$ .

While for a human observer a little effort is required to attribute a part of the spectrum to a specific guided mode, from an algorithmic point of view this problem is more complex. In the current research, the OMGP algorithm has been applied to process wavenumber - frequency, i.e., spectrum, data, so the guided modes and noise can be decomposed into different trajectories  $f^m(\omega)$ . The latter can be used to construct a filter that will preserve a guided mode of interest and discard non-relevant information. The mean values of the filters along the frequency axis can be defined by the corresponding  $f^m(\omega)$  trajectory, while the width of the filter along wavenumber axis can be modulated by Gaussian distribution, it can be expressed as follows:

$$F^m(k(\omega), f^m(\omega)) = \frac{1}{\sqrt{2\pi\xi^2}} \exp \frac{-(k(\omega) - f^m(\omega))^2}{2\xi^2}, \quad (2.47)$$

where  $F^m(k(\omega), f^m(\omega))$  is a spectral filter,  $k(\omega)$  is a wavenumber of the GWs,  $f^m(\omega)$  is an OMGP trajectory of the mode  $m$ ,  $\omega$  is frequency, and  $\xi$  denotes the width of the filter and it is typically derived from experimental measurements. More details on the principle of operation and examples of validation are given in the following section.

### 2.4.2 Determination of 3D Green's function

In this section, the data driven approach presented above is used for processing GWs spectrum in an aluminum plate, CFRP plate and HCSS. Both simulated and experimental data are processed in order to extract dispersion curves and modal components of the 3D Green's function. Real and imagery parts of extracted modal components are then compared with the ones obtained using modeling tools presented in the Section 2.3. The data-driven approach can be summarized as follows:

1. Directional guided wavefield measurements;
2. Wavenumber-frequency filtering using OMGP to isolate guided mode of interest;

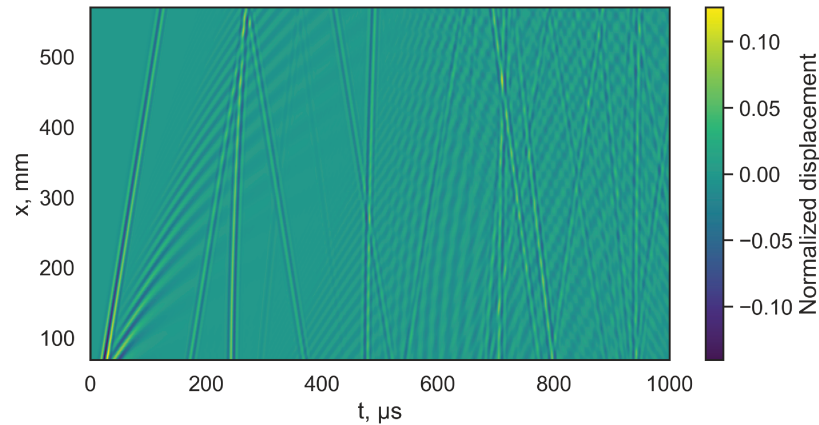


Figure 2.12 – Simulated B-scan at 80 kHz in the aluminum plate 1400 mm × 1250 mm × 3 mm in dimension.

3. Temporal windowing of the GWs signals to extract incident wave, and the 3D Green's function deconvolution.

Each step of this approach is described in detail below.

The OMGP model and spectral filter are first applied to the FE simulated data. The main reason for using simulated data is to overcome the limitation of LSVD, where the acquisition process is biased towards out-of-plane displacement measurements so that asymmetric modes are more prominent. Therefore, model's capability of determining several modal components of the 3D Green's function can be assessed.

The studied structure is an aluminum plate 1400 mm × 1250 mm × 3 mm in dimension. It is equipped with a PZT transducer 18 mm in diameter, which is driven with two-cycle Hanning modulated tone burst centered at 80 kHz. Such a short excitation function generates broadband GWs in the structure. The so-called B-scan of GWs propagation is shown in Figure 2.12.

The GWs data is transformed to the wavenumber-frequency domain using the 2D Fourier transform, see Figure 2.13. While in the time-space domain it is barely possible to decompose GWs signals in constitutive modes, in the wavenumber-frequency domain the spectral filtering can be efficiently applied to isolate guided modes and discard non-relevant information.

It has been mentioned in 2.1 that the wavenumber-frequency dependence of the guided mode is a non-linear function. Hence, such a filter has to be steady to the curvilinear shapes of guided modes to insure continuity of the mode, and to be able to distinguish several possible modes, even if they approach or cross each other. The frequency-wise processing of the spectral data is a natural way to track guided modes. For example, Rose [3] and Lowe [100] followed this routine in the mode sorting procedures. In this work, an alternative approach has been proposed, where the spectral data are collected in a single batch, and the sorting procedure is performed using probabilistic models in the Bayesian framework. Therefore, a part of the spectrum can be associated with a single guided mode with certain probability.

Over the past decades, the Gaussian process presented in 2.4, has been proven effective for nonlinear regression problems, and even for processing noisy data but only for a single trajectory. The overlapping mixtures of Gaussian processes have been proposed to separate the data into different trajectories. This algorithm is adapted to process the power spectrum of the GWs,

so it can be decomposed into different parts: trajectories associated with guided modes and non-relevant noise.

Then, the spectral filter can be constructed as follows. First, the power spectrum is transformed to the log-scale, so the low energy components become noticeable. The negative part of the wavenumber-frequency distribution that corresponds to the reflected GWs is discarded, so only incident waves are preserved. The Sobel–Feldman operator is then applied to the power spectrum in  $f$  and  $k$  directions to emphasize edges. This is a discrete differentiation operator, which computes the approximation of the gradient of intensity distribution. It consists of two  $(3 \times 3)$  kernels convolved with the power spectrum. It can be expressed as follows:

$$G_f = \begin{pmatrix} 1 & 0 & -1 \\ 2 & 0 & -2 \\ 1 & 0 & -1 \end{pmatrix} * PS, \quad (2.48)$$

$$G_k = \begin{pmatrix} 1 & 2 & 1 \\ 0 & 0 & 0 \\ -1 & -2 & -1 \end{pmatrix} * PS, \quad (2.49)$$

where  $G_f$  and  $G_k$  are derivative approximations of power spectrum in the  $f$  and  $k$  directions, respectively. The power spectrum is denoted by  $PS$ . Hence, resulting gradient approximations can be computed as follows:

$$G = \sqrt{G_f^2 + G_k^2}, \quad (2.50)$$

where  $G$  is a combined gradient magnitude of the power spectrum. This filter allows enhancing the contours of the power spectrum, and dispersion curves become more perceptible.

The 2D post-processed spectrum data are transformed to the two vectors  $f$  and  $k$ , respectively. From Figure 2.13, it can be deduced that the OMGP model has to be specified in such a way that three trajectories could be reconstructed. The first two trajectories represent guided modes, and the third one describes the independent noise. The rational quadratic and white kernels have been selected. The model's hyperparameters optimization is performed by maximizing a modified lower variation bound of the log-marginal likelihood as described in section 2.4.1.3.

Trajectories of the OMGP model that correspond to  $A_0$  and  $S_0$  guided modes are shown by red and black crosses while the noise component is discarded. The power spectrum values  $(f, k)$  associated with this trajectory are fitted to the polynomial function using the least square regression. This procedure allows determining the filter mean wavenumber values over the frequency range of interest; they are shown in Figure 2.13 by blue and orange lines, respectively. Following the frequency-wise sampling, the spectral filter is then constructed for each guided mode using equation (2.47).

This filter is then applied to the spectrum of the GWs, so only a single guided mode is preserved at once. The inverse 2D Fourier transform is used for re-projecting filtered spectrum into the time-space domain. From now on, the filtered B-scan contains only temporally separated wave packets of a single guided mode. Consider a single signal from the filtered B-scan, the first wavepacket corresponds to the incident guided mode, whereas others represent reflections from the opposite border of the plate. The guided wave dispersion and attenuation phenomena result in progressive decrease of the GWs amplitude with propagation distance. Hence, the first propagated wavepacket can be determined from the signal envelope analysis. The envelope can be computed using the Hilbert transform as follows:

$$\hat{u}(t) = \sqrt{(u(t))^2 + (iH(u(t)))^2}, \quad (2.51)$$

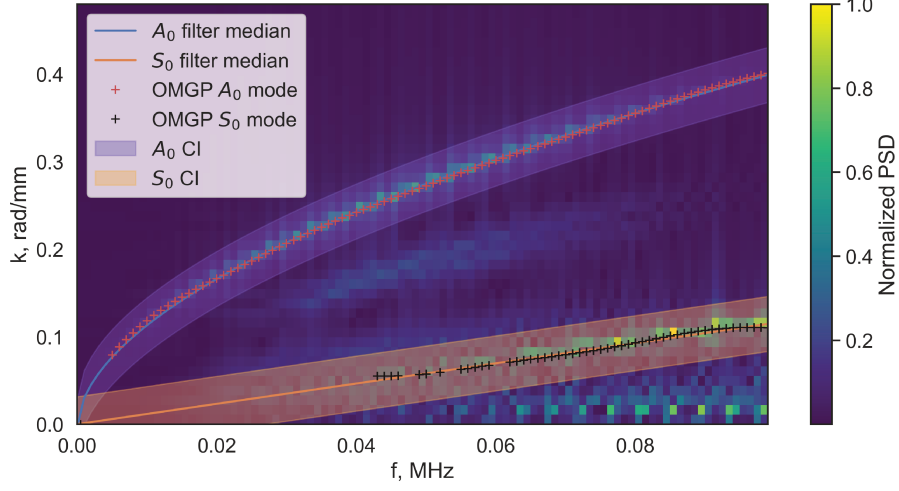


Figure 2.13 – OMGP processing of the GWs spectrum in aluminum plate.

where  $\hat{u}(t)$  is a signal envelope of the real-valued signal  $u(t)$ , and  $H$  denotes the Hilbert transform.

The boundaries of the first propagated packet can be determined through the calculation of the gradient sign change, while moving to the left and to the right from the maximum of the corresponding envelope. Once the incident wavepacket is filtered, as shown in Figure 2.14, the 3D Green's function for the current position can be determined as follows:

$$G^m(r, \theta, \omega) = \frac{\tilde{u}(r, \theta, \omega)p(0, \omega)^\dagger}{|p(0, \omega)^\dagger|}, \quad (2.52)$$

where  $\tilde{u}(r, \theta, \omega)$  is the filtered packet of the mode  $m$  propagated on the distance  $r$  and angle  $\theta$  at the  $\omega$  circular frequency, and  $p(0, \omega)$  represents the excitation function.

This deconvolution procedure is iteratively repeated for each signal in the B-scan  $R \in [50, 300] \Delta R = 1, mm$ , and corresponding modal components of the 3D Green's function are collected. Figure 2.15 presents the comparison of OMGP determined and semi-analytically simulated  $A_0$  modal components at 40 kHz; a good agreement is observed for both real and imaginary parts.

Once the data-driven approach has been tested on the simulated data, the experimental validation in CFRP plate and HCSS is conducted. The same CFRP plate as described in section 2.3.4 is chosen to be studied first. It is equipped with a PZT transducer, 18 mm in diameter and 0.5 mm thick, to generate GWs in the structure. The surface of the composite is covered with an aluminum reflective foil in order to enhance the surface reflectivity as GWs measurements are performed using LSVD set-up, shown in Figure 2.3.

A polar coordinated system  $(R, \theta)$  with a transducer in the origin has been chosen for this acquisition. The polar axis is aligned with the carbon fibers direction. In such a plate, which consists of orthotropic woven plies all aligned in the same direction, the guided wavefield has a 45° symmetry with respect to fiber direction. Hence, directional propagations of GWs, e.g. B-scans, were collected for  $\theta \in [0, 45] \Delta\theta = 1^\circ$  and  $R \in [0, 300] \Delta R = 1, mm$ . The excitation function is an two-cycle tone burst centered at 40 kHz.

Unlike FE simulation, the experimental GWs measurements by means of LSVD are mainly constrained to the acquisition of out-of-plane displacement so that the  $A_0$  mode is dominant in

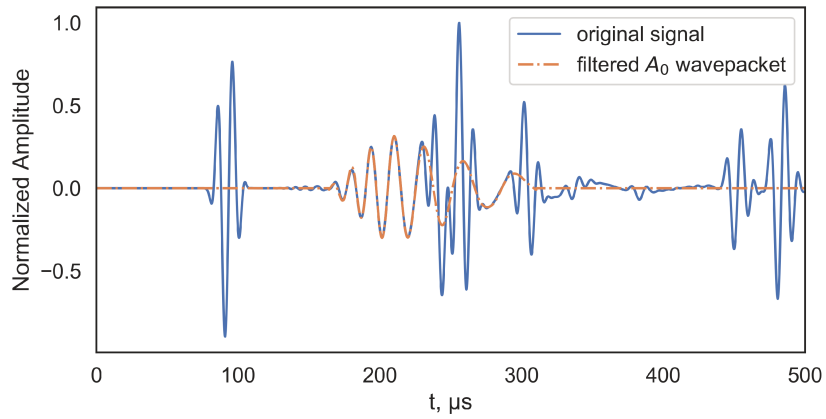
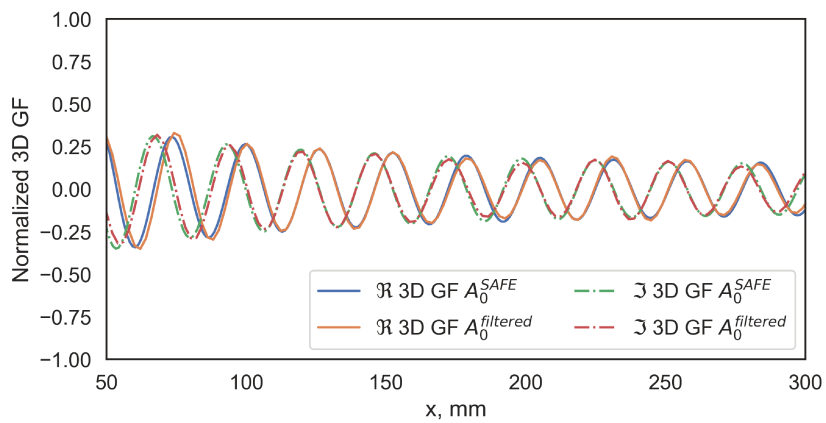


Figure 2.14 – GWs signal filtering in aluminum plate.

Figure 2.15 – Real and imaginary parts of the  $A_0$  modal component of the 3D Green's function in aluminum plate at 40 kHz.

the spectrum. Therefore, OMGP model is configured in such a way that two trajectories could be reconstructed. The first trajectory represents the guided mode, and the second one describes the independent noise. Spectrum processing results are presented in Figure 2.16a. Red crosses denote spectral values associated with  $A_0$  mode. The blue line, and shadowed region denote the mean trajectory of the spectral filter and the confidence interval, respectively.

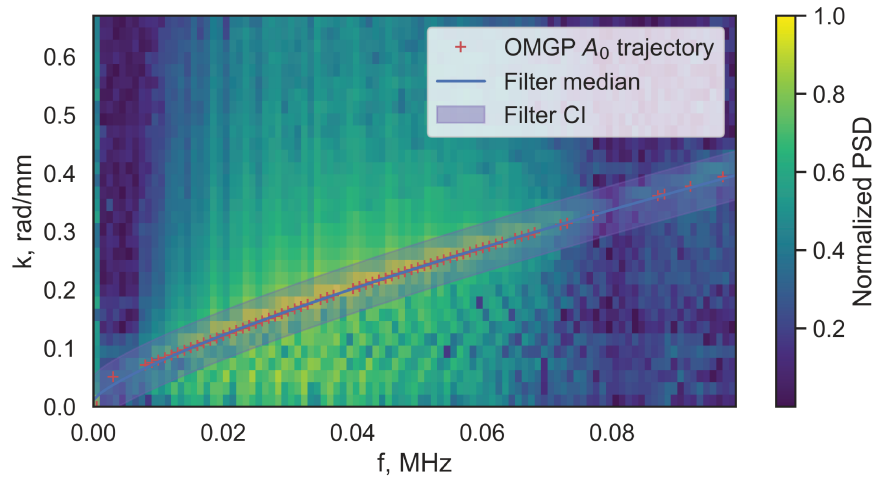
This filter is applied to the spectrum of the GWs in order to isolate  $A_0$  modal component of the 3D Green's function. The inverse 2D Fourier transform is then used to re-project data into the time-space domain and the windowing technique is applied to filter incident wavepacket. The  $A_0$  modal component of the 3D Green's function in the CFRP plate is obtained using Eq. (2.52). This procedure is iteratively repeated for each signal  $\theta \in [0, 45]_{\Delta\theta = 1^\circ}$  and  $R \in [0, 300]_{\Delta R = 1, mm}$ , so the 3D Green's function is collected over the ROI.

For the sake of comparability between data-driven approach and simulation method that is presented in Section 2.3, experimental real and imaginary parts of  $A_0$  modal component of the 3D Green's function are plotted against the ones computed using SAFE and MEM modeling framework, as shown in Figure 2.17a.

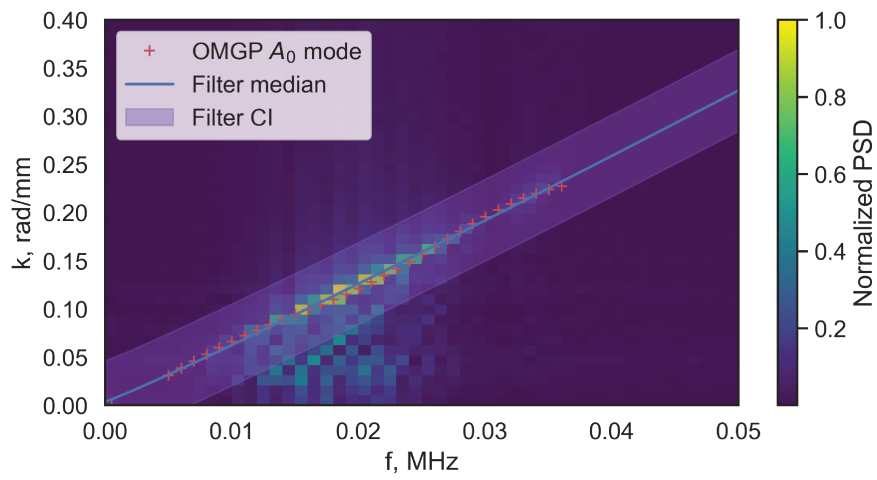
The last studied structure is HCSS. This is the same structure as the one that was used for modeling results validation in Section 2.3.4. The panel is equipped with a PZT transducer 18 mm in diameter. It is excited with a two-cycle Hanning modulated tone burst centered at 15 kHz to generate GWs that are collected using the same LSVD set-up. As for CFRP plate, this HCSS has a 90° symmetry of GWs propagation, therefore GWs are collected in polar coordinate system for the ROI that is defined as follows  $\theta \in [0, 45]_{\Delta\theta = 1^\circ}$  and  $R \in [0, 300]_{\Delta R = 1, mm}$ .

As in the previous case, the GWs spectrum mainly consists of  $A_0$  mode, therefore, OMGP model is specified to search for one modal trajectory and the independent noise. Corresponding trajectory, filter and corresponding confidence interval are shown in Figure 2.16b. Red crosses denote output of the OMGP model for the modal trajectory, blue line corresponds to spectral mean values and shadowed region represents filter's confidence interval. The deconvolution technique is applied to obtain  $A_0$  modal component of the 3D Green's function in HCSS. Both real and imaginary parts of it are presented and compared to the simulated counterparts in Figure 2.17b.

The presented deconvolution method was successfully applied to determine the  $A_0$  modal component of the approximate 3D Green's function in aluminum plate, CFRP plate and HCSS. This method involves filtering in both wavenumber-frequency and time domains. Spectral filter based on the OMGP model can be efficiently applied to isolate guided modes of interest and to extract corresponding modal components of the 3D Green's function. The main advantage of such a filter, is that it allows an approximate determination of dispersion curves and approximate modal components of the 3D Green's function without any knowledge of GWs propagation in the studied structure.

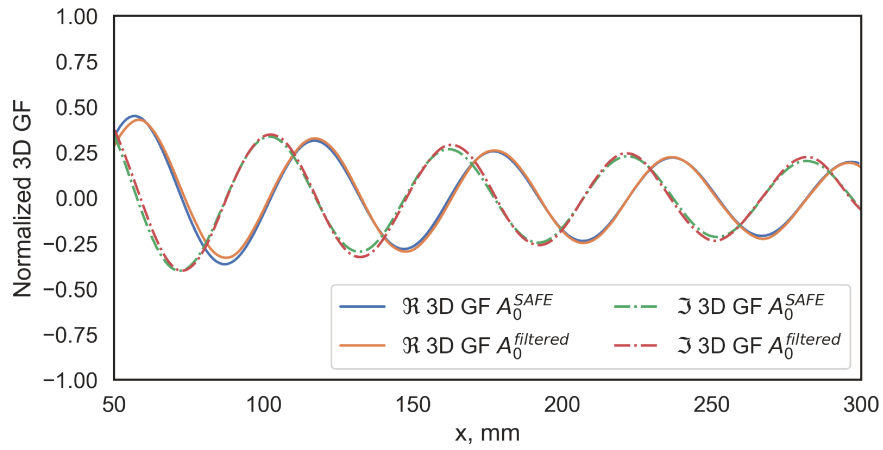


(a) OMGP processing of the GWs spectra in CFRP plate.

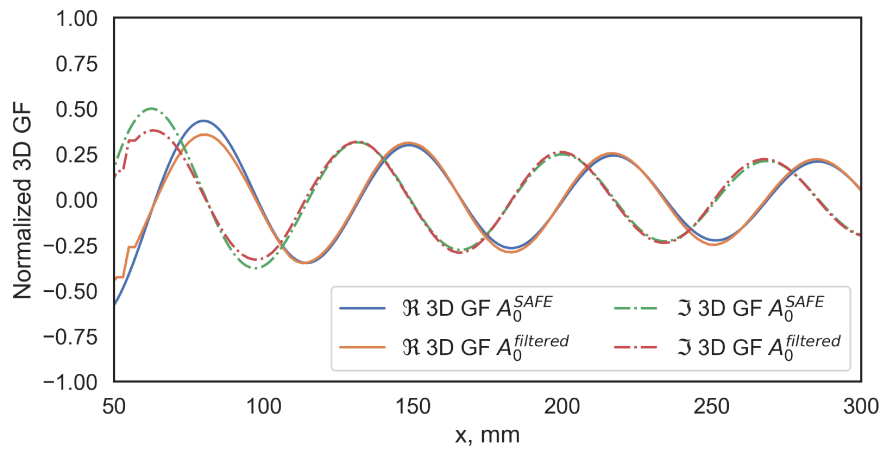


(b) OMGP processing of the GWs spectra in HCSS.

Figure 2.16 – Guided modes spectral filtering using OMGP in  $0^\circ$  direction of propagation.



(a) Real and imaginary parts of the  $A_0$  modal component of the 3D Green's function in CFRP plate.



(b) Real and imaginary parts of the  $A_0$  modal component of the 3D Green's function in HCSS.

Figure 2.17 – Comparison of  $A_0$  modal components of 3D Green's functions in the CFRP plate and HCSS in  $0^\circ$  direction of propagation at 15 kHz.

## 2.5 Chapter summary

This chapter reports on general properties of GWs actuation, propagation, defect interaction and sensing. Among different families of GWs that can exist in a waveguide, Lamb waves are the most attractive for SHM applications. One of the most important properties of the GWs is that they can be linearly decomposed into modal components. There can be found an infinite number of corresponding guided modes in the finite waveguide, and all of them, apart from only fundamental modes, have a specific cut-off frequency. In general, the frequency range that is below the first cut-off frequency is used for structural monitoring, as for higher frequencies GWs signal processing becomes much more complicated.

In isotropic metallic materials, e.g. aluminum alloys, the GWs propagation is omni-directional and is barely attenuated, whereas in anisotropic materials, e.g. CFRP, GFRP composite plates and HCSS, it is heavily affected. In composite structures, some preferential directions for GWs propagation can be found. In general, they coincide with constitutive material directionality. For example, in CFRP composite plate the energy is guided along the fibers' direction, and in HCSS it is guided towards the main axes of the honeycomb core layer. Such an anisotropy of composite structures results in directional dependence of phase and group velocities of guided modes, excitability and attenuation. Hence, more sophisticated modeling methods have to be used for modeling the GWs propagation in anisotropic structures rather than in isotropic ones. Taking into account that GWs can be expressed in terms of the elastodynamic 3D Green's function, a semi-analytical finite element modeling method coupled to a modal expansion method has been used to compute the 3D Green's function of the structure and the corresponding guided wavefield. While this modeling framework is developed to model classical multi-layered composites, the HCSS modeling requires certain modifications due to the periodic core layer. The honeycomb layer homogenization model can be applied to replace it with an equivalent orthotropic plate, for which effective elastic parameters can be computed. Such a model provides a reliable result in the low frequency range, where wavelengths are larger than the honeycomb cell size, but fails to provide accurate solution for higher frequencies, where interactions between GWs and a honeycomb cell become noticeable.

It is worth noting that presented simulation tools are limited to ideal plate-like structures, but, in reality, such structures are often equipped with rivets and other structural features that modify the elastodynamic 3D Green's function. In order to overcome this limitation, a probabilistic data-driven approach has been developed. It is based on the use of overlapping mixtures of Gaussian processes and allows determining modal components of the 3D Green's function from the measured GWs wavefield. This method has been tested on an aluminum plate, CFRP plate and HCSS panel, and demonstrates a good agreement with GWs modeling methods.

Application of computed 3D Green's functions for layered-composite structures, including CFRP, GFRP plates and HCSS, is not limited to the modeling of the guided wavefield in such structures. In the following chapter, it will be demonstrated that they can be used for defect detection, localization, and sizing in plate-like structures. Such a defect detection and characterization strategy is based on the guided waves imaging methodology. It requires a limited number of transducers arranged in the sparse grid around the structure, and thus it is attractive for SHM applications.



# Defect detection and localization using Guided Waves Imaging

## Outline of the current chapter

<b>3.1 Guided Waves Imaging</b>	<b>46</b>
<b>3.2 Defect imaging algorithms</b>	<b>47</b>
3.2.1 Delay-And-Sum algorithm . . . . .	48
3.2.2 Minimum Variance algorithm . . . . .	49
3.2.3 Excitelet algorithm . . . . .	50
<b>3.3 Defect imaging results</b>	<b>53</b>
3.3.1 Aluminum plate . . . . .	53
3.3.2 Multilayer CFRP plate . . . . .	55
3.3.3 HCSS . . . . .	62
<b>3.4 Statistical studies on localization accuracy</b>	<b>65</b>
3.4.1 Guided waves simulation framework . . . . .	65
3.4.2 Database description . . . . .	66
3.4.3 Defect localization error analysis . . . . .	67
<b>3.5 Sparse defect imaging</b>	<b>74</b>
3.5.1 Bayesian optimization of Gaussian process for sparse defect imaging	74
3.5.2 Sparse imaging results . . . . .	75
<b>3.6 Chapter summary</b>	<b>79</b>

As previously mentioned, GWs have been proven effective for large plate-like structures inspection in comparison with conventional ultrasonic testing. The latter can be both expensive and time-consuming as a transducer has to be moved over the surface to scan each point of it. GWs, in contrast, can be excited at one point on the structure and propagate over a considerable distance. Thus, a relatively small number of transducers are required to perform SHM over a large structure.

At any excitation frequency, at least two fundamental modes are generated and propagated with different velocities. Hence, measured signals are complex, and typically contain multiple

overlapping wavepackets that correspond to incident GWs as well as their boundary reflections. GWs are also dispersive, so the shape of wavepackets changes with propagating distance. Both phenomena make interpretation of GWs signals difficult and require sophisticated tools and methods for processing.

This chapter provides a methodology and methods for GWs signals processing that can be used for damage detection and localization in both isotropic and anisotropic plate-like structures. These methods rely on propagation characteristics of GWs that can be determined using simulation and data-driven methods presented in Chapter 2. Experimental results are demonstrated for different defect types in aluminum plates, CFRP plates and HCSS. Furthermore, a statistical study is conducted in order to determine the best performing method and to assess its defect localization performance. Finally, a method for sparse defect imaging is presented that allows accelerating GWs-based SHM of large structures.

### 3.1 Guided Waves Imaging

A number of research works, Alleyne et al. [38] in particular, have demonstrated the interest in using GWs for defect detection and localization in plate-like structures. Many methods have been proposed to process GWs signals, some of them are presented in Chapter 1.

As stated in Section 1.2.3, they can be broadly classified into two categories: baseline and baseline-free methods. The baseline-free methods are very attractive, but they have not been well-developed yet. For example, Druet et al. [43] developed a baseline-free GWs tomography technique, but it has several constraints such as a large number of transducers required around damaged area and its application is limited to simple geometry structures.

Baseline methods, in contrast, are relatively mature and well-studied. In general, they are implemented as follows. First, GWs signals are collected when the structure is defect-free, i.e., the baseline is measured. If a damage occurs, its presence can be highlighted by comparing the baseline to the current state of the structure. Such comparison can be done in several ways, including subtraction in order to obtain residual signals and correlation in order to estimate a degree of similarity between two states. It is worth noting that baseline methods are often vulnerable to environmental and operational conditions; therefore, some sort of GWs signal compensation has to be applied at preprocessing stage. More details are provided in Chapter 5, where the robustness of a GWs-based SHM system is discussed.

Among different categories of GWs processing methods, the Guided Waves Imaging (GWI) is standing out. A number of research works, Wang et al. [60] and Michaels et al. [62] in particular, have demonstrated that information from multiple transducers can be processed and combined in order to compute an image that represents the integrity of the structure. Main advantages of this approach are its robustness to signal corruption and that it provides visually interpretable results as compared to non-imaging methods.

A schematic of the GWI process is represented in Figure 3.1. The grid of pixels discretizes the region of interest (ROI) of the structure so that each pixel is mapped to a corresponding elementary portion of the studied specimen. For each pair of transducers, the defect imaging algorithm computes an elementary image relying on the knowledge of GWs propagation. Elementary images are then fused to construct a final image, where each pixel contains a Damage Index (DI) value that can be related to the probability of structural flaw.

The defect's presence, location and size can be deduced by analyzing the spatial intensity distribution in the image. It is worth noting that the defect sizing should rather be considered as an inverse problem, which requires sophisticated solvers, including machine learning based regressors.

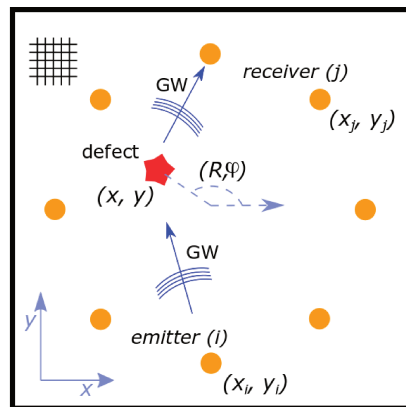


Figure 3.1 – Schematic representation of the Guided waves imaging methodology. Orange circles and a red pentagon define piezoelectric transducers and damage locations respectively. Blue arrows represent GW propagation in the structure.

A common practice is to collect GWs signals using a spatially distributed array of PZT transducers. In comparison with other transducers' arrangement, this disposition is advantageous as it allows interrogating the defect from different angles and provides more information about it. Following the round-robin process [101], each transducer acts as a transmitter and as a receiver to generate and record GWs signals in turn.

### 3.2 Defect imaging algorithms

A number of GWI algorithms have been proposed in the literature. Perhaps, the most representative among them is the delay-and-sum (DAS) proposed by Wang et al. [60] in 2004. This is a synthetic time-reversal imaging method that back-propagates residual signals to the corresponding location using the knowledge of GW group velocity. Michaels et al. [62] improved this algorithm by computing DI values as a square of an averaged shifted residual signal. Hall et al. [64] proposed the energy mapping method, the so-called minimum variance distortionless response (MVDR) or simply (MV), which takes into account a defect scattering pattern and phase information. This algorithm allows the imaging quality improvement by decreasing the number of artifacts as compared to DAS. Then, this algorithm was optimized [63] and became computationally attractive for SHM applications. Furthermore, Hall et al. [65] have proposed a multipath GWI algorithm, which is an advanced version of MV. It can process a large number of echoes and reverberations present in residual GWs signals even in geometrically complex structures such as an aircraft fuselage. Recently, Chehemi et al. [102] developed passive baseline approach for defect detection and localization that relies on the time reversal method. They also proposed to use DORT technique in order to filter correlation matrices of GWs signals' spectra that allows reducing noise and the number of defect imaging artifacts.

While the previous group of GWI algorithms is aimed at mapping residual signals, the following one is aimed at computing images on the basis of correlation analysis between damaged and pristine states of the structure. For example, Gao et al. [103] proposed an imaging method that maps a signal difference coefficient in 2005. This coefficient is computed as  $1 - \rho$ , where  $\rho$  is the correlation coefficient between the two signals compared. The difference coefficient does not take into consideration the amplitude temporal dependence, and rather considers the overall

amplitude variation. Mal et al. [104] proposed an algorithm that computes DI values comparing the frequency response functions of pristine and damaged state signals. Zhao et al. [105] developed the reconstruction algorithm for probabilistic inspection of defects (RAPID). This algorithm attributes DI values by computing the correlation coefficients between the baseline and current state of the structure in the vicinity of GWs path. The defect location is then determined from the severity of signal changes in GWs signals from different sensor pairs. This algorithm is simple, often performs well and does not require any knowledge about GWs propagation in the structure, but it is occasionally prone to false alarms as noise or other form of GWs signals variation cannot be distinguished from scattered signals.

In 2011, Quaegebeur et al. [67] proposed a correlation based imaging algorithm named Excitelet (EXC). For each pixel of an image, it computes a DI value as a correlation coefficient between residual and analytical signals. The latter describes the GW traveling from the emitter to the point of observation and on to the receiver. In comparison with the previously mentioned algorithms, Excitelet requires much more a priori knowledge about GWs propagation in the structure, namely the 3D Green's function and transducers dynamics, but it provides more accurate and better-resolved images.

Having analyzed the above mentioned GWI algorithms, DAS, MV and Excitelet have been chosen for this research as they are well-developed and progressively incorporate the knowledge about GWs propagation in the structure. For each pair of sensors, all the three algorithms process residual signals that are obtained by subtracting the current state of the structures from the baseline. If the only difference between two states is a damage, then residual signals contain echoes coming from it as well as border reflections. It is worth noting that if in addition to the damage there are other variations such as electronic noise or environmental effects, then the defect response can be barely distinguishable. For a single transducer pair, these algorithms map a defect response to an ellipse with foci at transducers' locations.

### 3.2.1 Delay-And-Sum algorithm

Consider a set of  $N$  PZT distributed over the structure. Following the round-robin process, they are driven with impulsive excitation to generate GWs in the structure. In total  $N \times (N - 1)$  signals are collected, and residual signals are obtained by subtracting the current state from the baseline. Then, the envelopes of residual signals are obtained using the Hilbert transform:

$$r_{i,j}(t) = \sqrt{u_{i,j}(t)^2 + H(u_{i,j}(t))^2}, \quad (3.1)$$

where  $r_{i,j}(t)$  is an envelope of the residual signal,  $u_{i,j}(t)$  is a residual signal measured by  $i, j$  pair of piezoelectric transducers and operator  $H$  denotes the Hilbert transform.

Following the standard routine of the GWI procedure, the ROI of the structure is represented by the grid of pixels. Then, a distance matrix is computed for each pair of transducers, where each element of this matrix contains the distance that a GW travels from the emitting transducer to the point of observation and on to the receiving transducer. The knowledge of directional group velocity is used for computing the time of flight of the GW as follows:

$$t_{i,j}(x,y) = \frac{\sqrt{(x-x_i)^2 + (y-y_i)^2}}{C_g} + \frac{\sqrt{(x-x_j)^2 + (y-y_j)^2}}{C_g}, \quad (3.2)$$

where  $t_{i,j}(x,y)$  is the time of flight of the GW that propagates with a group velocity  $C_g$  from the transmitting transducer  $i$  located at  $(x_i, y_i)$  to the inspected point  $(x, y)$  and from the latter to

the receiving transducer  $j$  at  $(x_j, y_j)$ . As opposed to isotropic materials, in anisotropic ones the group velocity depends on the angle of propagation. It can be determined either theoretically or experimentally. Various methods such as SAFE [39] or Radon [106] transform have been proven effective for determining theoretical and experimental  $C_g$ , respectively.

The residual signal is delayed by the corresponding amount of time, so that each point of the elementary image can be associated with a part of the envelope. Finally, all elementary images are summed up to form an image that represents the integrity of the structure, and DI values are computed as follows:

$$DI^{DAS}(x, y) = \sum_{i=1}^{N-1} \sum_{j=i+1}^N r_{i,j}(t_{i,j}(x, y)). \quad (3.3)$$

DAS algorithm implements a single mode imaging. However, several modes can be used sequentially, but have to be generated or measured separately, and the final image can be obtained by combining corresponding results. Since guided waves are dispersive, this algorithm is convenient for imaging defects that are not remote from the transducers network as temporal resolution of the guided waves degrades with propagating distance. A narrow-band signal could be used to limit dispersion effects but this might reduce the size range of detectable defects. Therefore, a compromise is to be found in practice.

### 3.2.2 Minimum Variance algorithm

Hall et al. [64] proposed the Minimum Variance algorithm, which can be considered as an advanced version of DAS. It takes into account a diffraction pattern of GWs scattered by a defect in order to improve the resolution of an image. For each pixel, a vector of time-delayed signals is constructed as follows:

$$\vec{r}(x, y, t) = \left[ \left| \tilde{r}_{1,2}\left(t + \frac{d_{1,2}(x, y)}{C_g}\right) \right|, \dots, \left| \tilde{r}_{N-1,N}\left(t + \frac{d_{N-1,N}(x, y)}{C_g}\right) \right| \right]^T \quad (3.4)$$

where  $\vec{r}(x, y, t)$  is a vector of time-delayed signals,  $d_{i,j}(x, y)$  denotes the distance to the pixel  $(x, y)$  for the  $i, j$  pair of transducers, and  $C_g$  is a group velocity of the guided mode. A correlation matrix, which is identical to the DAS DI mapping [63], is then computed for each pixel  $(x, y)$  as follows:

$$R(x, y) = \sum_{t=t_1}^{t_2} \vec{r}(x, y, t) \vec{r}^\dagger(x, y, t), \quad (3.5)$$

where  $\dagger$  denotes a complex conjugate,  $t_1$  and  $t_2$  are temporal limits of the wave packet. A weighting vector  $\vec{W}(x, y)$  is constructed in order to minimize a false alarm that may be present in the original DAS map. Specifically, elements of this vector are selected to satisfy the following optimization problem:

$$\vec{W}_{i,j}(x, y) = \operatorname{argmin}(\vec{w}_{i,j}^\dagger R_{i,j}(x, y) \vec{w}_{i,j}), \quad (3.6)$$

with

$$\vec{w}_{i,j}^\dagger \vec{e}_{i,j}(x, y) = 1, \quad (3.7)$$

where  $\vec{e}(x, y)$  is an unit vector, which describes the directional relation between GWs signals and  $\vec{w}$  represents a weight vector. In order to obtain  $\vec{w}$ , the unit vectors  $\vec{e}(x, y)$  are computed as

follows:

$$\vec{e}_{i,j}(x,y) = \left[ \frac{\phi_{1,2}}{\sqrt{d_{1,2}(x,y)}}, \dots, \frac{\phi_{N-1,N}}{\sqrt{d_{N-1,N}(x,y)}} \right] \quad (3.8)$$

where the denominators represent the product of the distance traveled by the wavepacket while propagating from the emitter at  $(x_i, y_i)$  to the observation point  $(x, y)$  and to the receiver located at  $(x_j, y_j)$ . The corresponding numerators  $\phi_{i,j}$  represent scattering coefficients that characterize the amount of energy scattered by a defect at the location  $(x, y)$  for a given  $(i, j)$  PZT pair. Optimal values for the  $\phi_{i,j}$  depend on the shape of the defect and its orientation. Unless assumptions can be made regarding a type, shape and orientation of the defect, common practice is to assume the defect is omnidirectional, that is  $\phi_{i,j} = 1$  for all pairs of transducers. The next step consists in minimizing the DI value to the defect free zone, while preserving DI values of the flawed zone. Finally, the DI is computed as follows:

$$DI^{MV}(x,y) = \vec{W}_{i,j}(x,y)^\dagger R(x,y) \vec{W}_{i,j}(x,y). \quad (3.9)$$

It is worth mentioning that this method suffers from the same weakness as the previous algorithm as it also relies on the single value of the wave speed for a given direction of propagation.

### 3.2.3 Excitelet algorithm

Quaegebeur et al. [67] have presented an algorithm called Excitelet. For each pixel of the image, it attributes DI values using a correlation between experimental residual signals and theoretical signals that represent dispersed versions of the excitation signal. In general, a GWs dispersion phenomenon complicates a defect imaging procedure, as wave-packets in the residual signal can overlap and enlarge their limits while propagating. However, Excitelet uses theoretical signals that are computed by considering their dispersion in the medium [107]. Thus, the structure can be excited over a large bandwidth, which allows processing a damage response in a large frequency range.

Consider a plate-like structure, schematically shown in Figure 3.1. Each transducer is driven by an excitation function  $f_{exc}(t)$ , and a dictionary of experimental residual signals  $u_{i,j}(t)$  is collected for each  $(i, j)$  pair of transducers. To calculate a DI value for location  $(x, y)$ , the theoretical signal  $s_{i,j}(x, y, t)$  has to be constructed. For each guided mode it can be obtained by convolving the excitation function with transducer frequency response and the corresponding modal component of the 3D Green's function that corresponds to the path of the GW propagation from the emitting transducer  $i$  located at  $(x_i, y_i)$  to the location  $(x, y)$  and on to the receiving transducer  $j$  located at  $(x_j, y_j)$ . Hence, the theoretical signal can be expressed as follows [67]:

$$s_{i,j}(x,y,t) = \left( \int_{-\infty}^{\infty} \Gamma_m(\omega) G_m(x-x_i, y-y_i, \omega) G_m(x-x_j, y-y_j, \omega) \exp(-j\omega t) d\omega \right) * f_{exc}(t), \quad (3.10)$$

where  $\Gamma_m(\omega)$  denotes a transducer frequency response for the guided mode  $m$ ,  $G_m(x-x_i, y-y_i, \omega)$  and  $G_m(x-x_j, y-y_j, \omega)$  represent modal components of the 3D Green's function. In general, the first term of convolution (3.10) is called a modal transfer function. For isotropic plate-like structures, it can be approximated and expressed analytically as follows:

$$s_{i,j}(x,y,t) = \left( \int_{-\infty}^{\infty} -\frac{2j\Gamma_m(\omega)}{\pi} \frac{\exp-jk_m(\omega)r_1}{\sqrt{k_m(\omega)r_1}} \frac{\exp-jk_m(\omega)r_2}{\sqrt{k_m(\omega)r_2}} \exp(-j\omega t) d\omega \right) * f_{exc}(t), \quad (3.11)$$

where  $k_m(\omega)$  is a wavenumber of the guided mode,  $r_1$  and  $r_2$  are the distances from the emitting

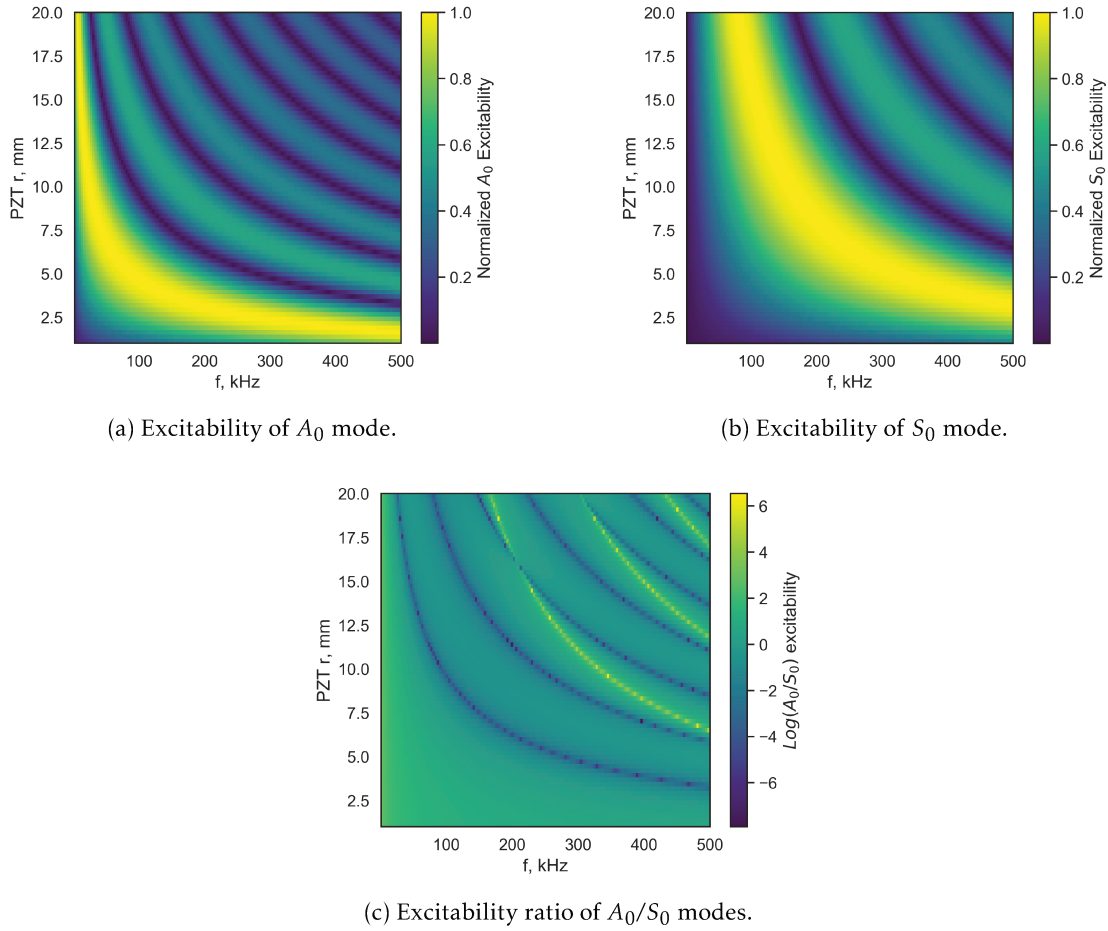


Figure 3.2 – Excitability maps of a thin circular PZT transducer bounded to the surface of a 3 mm thick aluminum plate.

transducer to the point of observation and from the latter to the receiving transducer, respectively.

Transducers' dynamics  $\Gamma_m(\omega)$  has been a subject of intensive research as it is an essential part in GWs signals computation. There are several factors that influence guide modes generation, including transducers' geometry and excitation frequency. Among various shapes, circular piezoelectric transducers are the most frequently used. Consider a PZT transducer bounded to the surface of a plate, if its acoustic impedance is much smaller than the one of the plate, then the modal generation is modulated approximately as follows [39]:

$$\Gamma_m(\omega) \approx |J_1(k_m(\omega), r)|, \quad (3.12)$$

where  $k_m(\omega)$  is a dispersion curve of the mode  $m$ ,  $r$  is a transducer's radius, and  $J_1$  is the first order of the Bessel Function of the first kind. For example, excitabilities of the  $A_0$  and  $S_0$  mode with respect to the transducer's radius and excitation frequency are shown in Figure 3.2. The relative  $A_0/S_0$  excitability, presented in Figure 3.2c can be used for maximizing or equalizing the amplitude ratio of the guided modes.

Unfortunately, for composite materials the expression 3.10 is no longer valid due to the

anisotropy of structures; more sophisticated modeling methods, such as SAFE or Global Matrix Method [80, 100, 108, 109] are required for computing modal components of the transfer function.

Once theoretical signals are computed over the ROI, the structural integrity can be evaluated as follows. For each pixel  $(x, y)$ , Excitelet calculates a normalized coefficient of correlation (3.13) between an experimental residual signal and an analytically propagated guided mode from the transmitting transducer  $i$  located at  $(x_i, y_i)$  to the inspected point at  $(x, y)$  and on to the receiving transducer  $j$  at  $(x_j, y_j)$ . The DI value is computed as follows:

$$DI^{EXC}(x, y) = \sum_{i=1}^{N-1} \sum_{j=i+1}^N \left| \frac{\int u_{i,j}(t) s_{i,j}(x, y, t) dt}{\left| \int u_{i,j}(t) dt \right| \left| \int s_{i,j}(x, y, t) dt \right|} \right|. \quad (3.13)$$

It should be mentioned that Excitelet presumes imaging of a point-like defect, so the wavelength of inspecting GW should be at least twice larger than the defect size.

### 3.3 Defect imaging results

In this section, GWI results on damage detection and localization in an aluminum plate, a CFRP multilayer plate and HCSS are presented for multiple configurations. Each plate is instrumented with a sparse array of PZT transducers that are used for both GWs excitation and sensing. The GWs-defect interaction depends on several factors, including ultrasonic frequency, a GWs incident angle, defects' shape and size. The sparse arrangement of transducers is advantageous in comparison with the dense arrays as it allows interrogating a damage from different angles, and increases the probability of defect detection, as the damage response might be weak in certain directions. It is worth noting that while the sparse transducers' arrangement is advantageous, it is not required to be regular. For complex shape structures, the transducers' arrangement can often take irregular forms in order to maximize the information gain about the integrity of the structure.

In this work, three types of a damage are investigated, namely a simulated defect, a transverse hole and calibrated delamination. It has been demonstrated that GWs propagation can be disturbed by a load locally applied to the surface of the structure. Therefore, a defect can be simulated by attaching a mass to a free boundary. Obviously, the simulated defect is not fully representative of a real defect, but it can be used for testing and comparing imaging algorithms, and for calibrating a SHM system without introducing a real damage to the structure.

An advantageous property of the simulated defect is that it mainly interacts with the  $A_0$  mode so that residual signals are less complex to be processed. The transverse hole is more representative than the simulated defect. It introduces a structural discontinuity so that all generated guided modes interact with it, which results in a complex defect response signal, including a guided mode conversion phenomenon. Finally, the calibrated delamination is the last studied defect. It is the most realistic damage that fully replicates a structural flaw, which can be observed in reality.

Hanning modulated tone burst excitations are widely used in imaging methods, including DAS, MV and Excitelet. Alleyne et al.[38] demonstrated that optimal GWs-defect interaction occurs when the wavelength of an inspecting mode is of the same order as the size of the defect. In general, both size and location of the defect are unknown, therefore, a broadband excitation is often used for detecting and locating the damage efficiently.

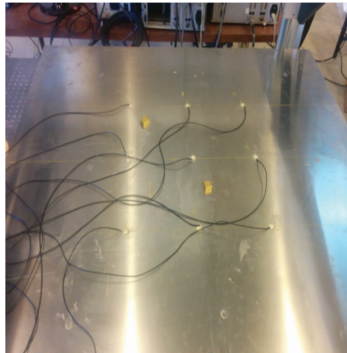
#### 3.3.1 Aluminum plate

The aluminum plate  $1400\text{ mm} \times 1250\text{ mm} \times 3\text{ mm}$  is studied at first. It is instrumented with nine PZT transducers  $18\text{ mm}$  in diameter and  $0.5\text{ mm}$  thick, as shown in Figure 3.3a. Transducers are arranged in four adjacent squares, each  $250\text{ mm}$  in length, and they allow interrogating defects from different directions.

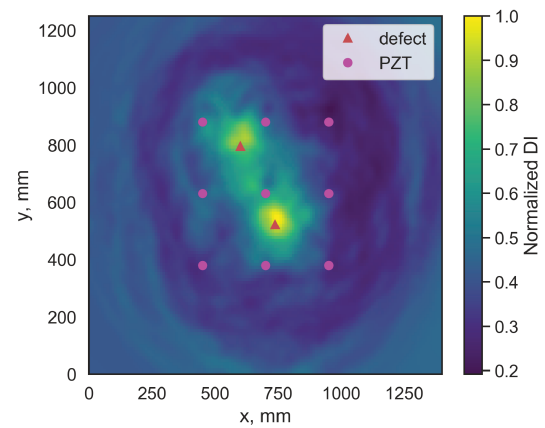
Each pair of transducers is driven in turn with the two-cycles Hanning modulated tone burst centered at  $40\text{ kHz}$  in order to generate broadband GWs. The baseline signals are collected by examining a pristine plate. Then, two attached masses are placed on the surface of the plate to simulate a damaged state, and the corresponding signals are measured.

The GWI is performed by means of DAS, MV and Excitelet algorithms, and are presented in Figure 3.3b, 3.3c and 3.3b, respectively. All the three algorithms are capable of detecting defects, but the imaging quality differs. DAS reconstructs well the lower defect, but barely locates the upper one. The MV is capable of reconstructing both defects, but the localization is not precise. On the other hand, Excitelet is effective for both reconstructing and localizing of two defects.

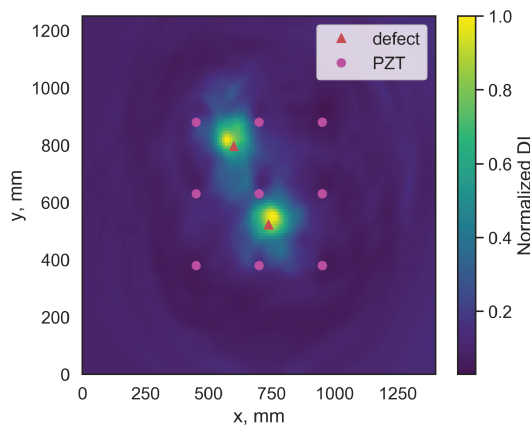
The following study consists in transverse hole imaging in the aluminum plate  $600\text{ mm} \times 600\text{ mm} \times 3\text{ mm}$ . This plate is instrumented with eight PZT transducers  $18\text{ mm}$  in diameter



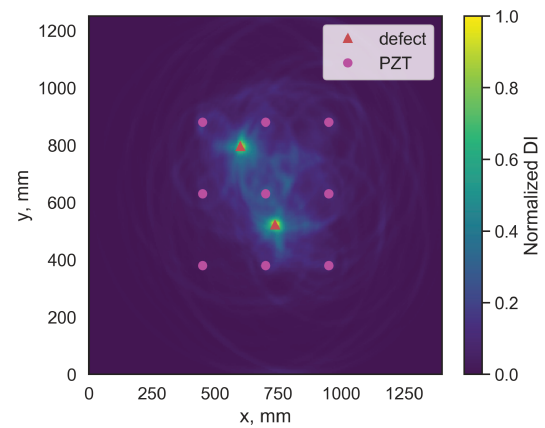
(a) Set-up photo.



(b) DAS GWI result of two attached masses.



(c) MV GWI result of two attached masses.



(d) EXC GWI result of two attached masses.

Figure 3.3 – Defect imaging algorithms comparison.

and 0.5 mm thick. They are regularly arranged over a circle of 150 mm in radius, forming an octagon. The excitation function is a two-cycle Hanning modulated tone burst centered at 25 kHz. Following the round robin process, GWs signals are measured for pristine and damaged states, where a transverse hole represents the defect. The GWI is performed by means of Excitelet algorithm using  $A_0$  mode. While retaining the same location, the size of the hole increased progressively from 6 mm to 17 mm in diameter. Imaging results of transverse holes 6 mm, 8 mm, 10 mm and 15 mm in diameter are presented in Figures 3.4a, 3.4b, 3.4c, 3.4d, respectively. The wavelength of  $A_0$  mode at 25 kHz is about of 35.4 mm, so the defect localization improves progressively with the defect size. From Figure 3.4e analysis, it can be concluded that the best damage localization and image resolution is obtained for the transverse hole 17.7 mm in diameter, where the maximum of diffraction is achieved, i.e.,  $\lambda_{25kHz}^{A_0}/2 \approx 17$  mm.

DI profiles through the defect location are shown in Figure 3.4e in order to demonstrate Excitelet's sensitivity to the defect size. It can be observed that through defect image profiles sharpen with the hole size, and the maximum of them approach the true location of the center of the transverse hole. For a given GWI configuration, DI values grow progressively with the transverse hole size, and the corresponding spatial distribution can be used as a damage size indicator. To achieve a progressive sensitivity, the excitation frequency has to be high enough, so the guided mode remains sensitive to the damage, and, at the same time, the corresponding wavelength has to be twice larger than the possible expected damage.

### 3.3.2 Multilayer CFRP plate

The next studied structure is an orthotropic CFRP plate 1000 mm  $\times$  600 mm  $\times$  5.775 mm consisting of 21 woven plies. All plies are placed in 0° direction with respect to fibers' placement, and each ply is 0.275 mm thick. The CFRP plate is equipped with eight PZTs transducers 8 mm in diameter and 0.5 mm thick, as shown in Figure 3.5a. To verify and calibrate SHM set-up, an attached mass is imaged first, see Figure 3.5b. The GWI is performed by means of Excitelet algorithm using  $A_0$  mode.

A more realistic structural damage is represented by transverse holes growing progressively in size from 5 mm to 25 mm with the step of 5 mm. The plate is inspected using four excitation functions that consist of two-cycle Hanning modulated bursts centered at 20 kHz, 40 kHz, 60 kHz and 80 kHz, respectively. The wavelengths associated with central frequencies are the following:  $\lambda_{A_0}^{20kHz} = 29.59$ , mm,  $\lambda_{A_0}^{40kHz} = 17.91$ , mm,  $\lambda_{A_0}^{60kHz} = 13.23$ , mm and  $\lambda_{A_0}^{80kHz} = 9.73$ , mm.

The GWI results obtained at 20 kHz are demonstrated in Figure 3.6. It can be observed that small transverse holes, namely 5 mm and 10 mm, are undetectable due to the large wavelength of the  $A_0$  mode. However, larger holes, i.e., 15 mm, 20 mm and 25 mm, are detectable, but the image resolution is low. The GWI sensitivity to the damage size is shown in Figure 3.6f. It can be observed that the through defects DI spatial distribution is indifferent for holes 5 mm and 10 mm, it increases progressively and sharpens for larger defects.

Furthermore, at this frequency, images are noisy and contain imaging artifacts that can be misinterpreted and would result in false alarms of a SHM system. More specifically, for 5 mm and 10 mm defects, imaging artifacts are located outside the PZT octagon, and have blurred and stretched out contours. For larger defects, namely 15 mm, 20 mm and 25 mm, imaging results are better. While images are still noisy, there are less artifacts: only a small outstretching of the spot that corresponds to the damage towards the nearest PZTs.

Figure 3.7 presents GWI results obtained at 40 kHz. It can be observed that of all the five sizes of defects are detectable, and images' resolution is increased. The transverse hole localization is more precise than at 20 kHz, the noise of the images decreased, and DI values spatial intensity distribution sharpened, as demonstrated in Figure 3.7f. However, it is no longer increasing

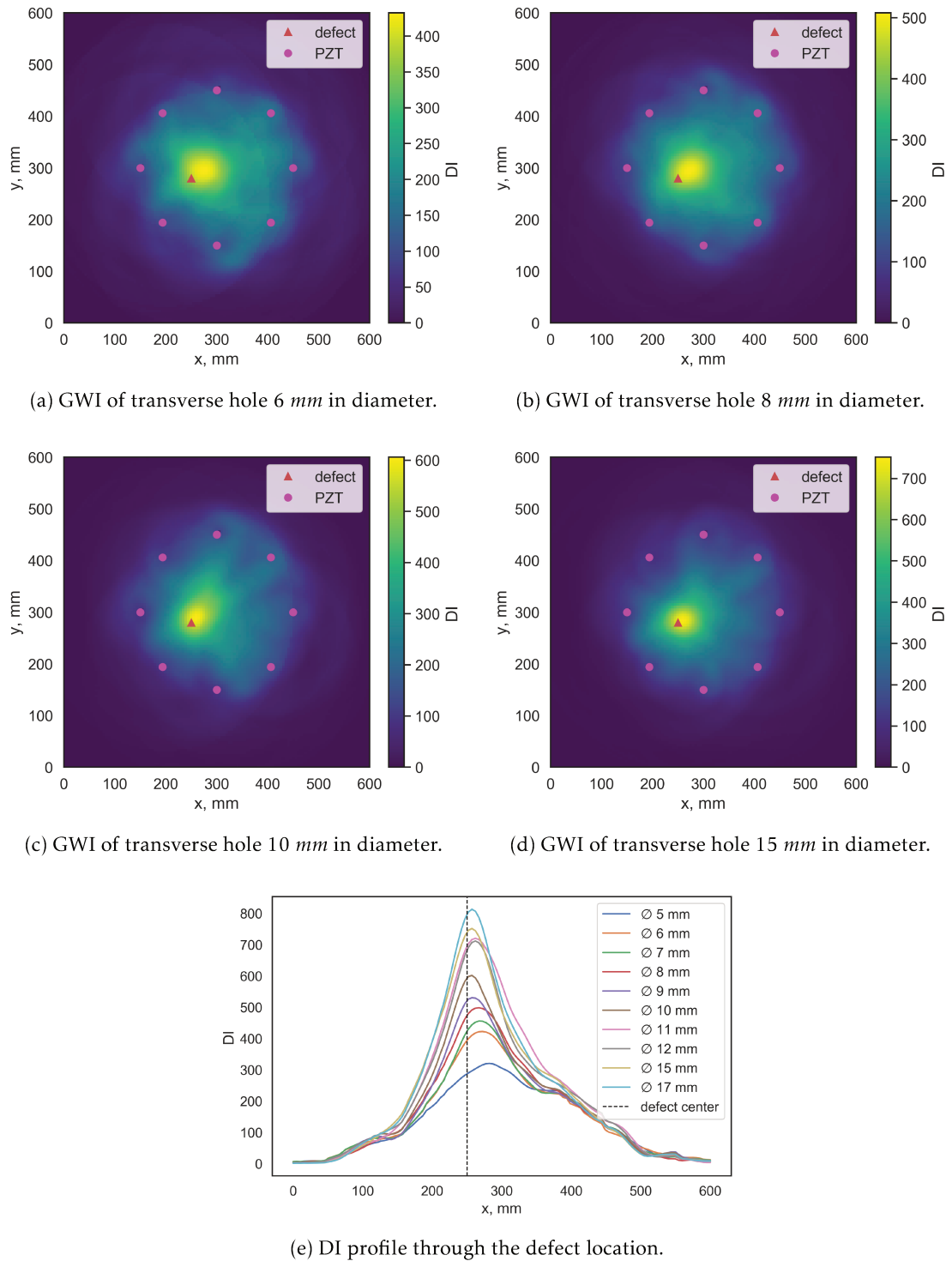
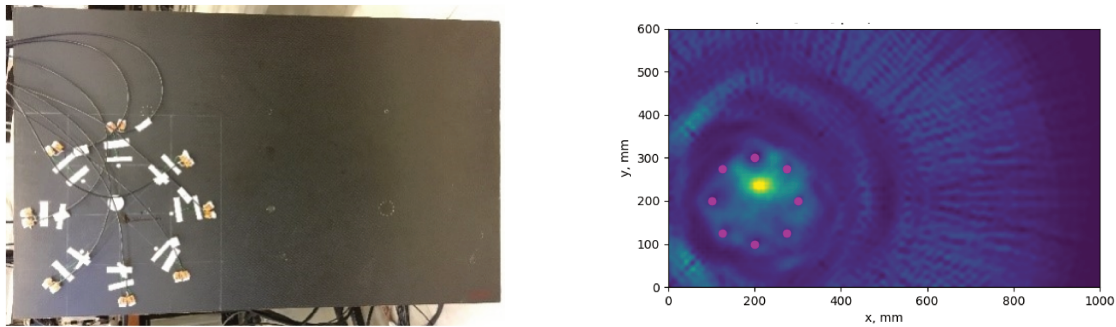


Figure 3.4 – Transverse hole imaging in aluminum plate at 25 kHz.



(a) Photo of the instrumented CFRP plate. The defect is simulated by two magnets attached from both sides of the plate.

(b) Simulated defect imaging result in CFRP plate at 40 kHz.

Figure 3.5 – Experimental instrumentation of a CFRP plate for defect imaging.

progressively: DI values increase with the hole size from 5 mm to 15 mm, and then decrease for defects from 15 mm to 25 mm in size. At 40 kHz, the half wavelength of  $A_0$  mode is of about 16.5 mm, so the maximum of GWs diffraction is observed for the hole of the same size. For smaller and larger defects, the DI decreases and increases, as GWs approach and distance the maximum of diffraction, respectively. There are imaging artifacts in GWI results of the hole 5 mm in diameter. They are of the same shape as at 20 kHz, but they are less intense so that the spot corresponding to the defect is abundantly detectable. For larger defects, namely 10 mm, 15 mm, 20 mm and 25 mm artifacts intensity is even smaller and does not disturb image interpretation.

GWI results obtained at 60 kHz and 80 kHz are presented in Figure 3.8 and Figure 3.9, respectively. At these frequencies, the wavelength of the inspecting mode is smaller than that at 40 kHz so that the defect localization is more accurate than in previous cases. However, imaging artifacts are more intensive. At these frequencies, the amplitude of  $S_0$  mode is more noticeable than at 20 kHz or 40 kHz. The correlation coefficient between  $S_0$  mode in the residual signal and  $A_0$  in theoretical signal is low, but the GWs-damage interaction is often followed by the guided mode conversion phenomenon. While interrogating the defect, the  $S_0$  mode is partially converted into the  $A_0$  mode, which provides a more important correlation coefficient with theoretical signal and, consequently, results in imaging artifacts. However, unlike the real damage, these artifacts have rather elongated shape, and thus do not complicate much the interpretation of GWI results.

Furthermore, distributions of DI values are less sensitive to the transverse hole sizes, as DI values are very close to each other, as shown in Figure 3.8f and 3.9f. It is worth denoting that at 80 kHz the wavelength is small enough to interact with walls of the transverse hole, so the assumption of a point-like damage is violated and DI values profiles are not smooth any more.

Exposed to the real operational environment, CFRP plates are prone to damage such as plies' delamination. This structural flaw often appears due to an impact or thermo-mechanical degradation. Being barely detectable to the naked eye, such defects can expand internally to large volumes decreasing mechanical properties of the structure. The response of these defects on GWs excitation is more complicated than the response on an attached mass and a transverse hole [110].

Under laboratory conditions, such defects can be reproduced using a drop tower [110],

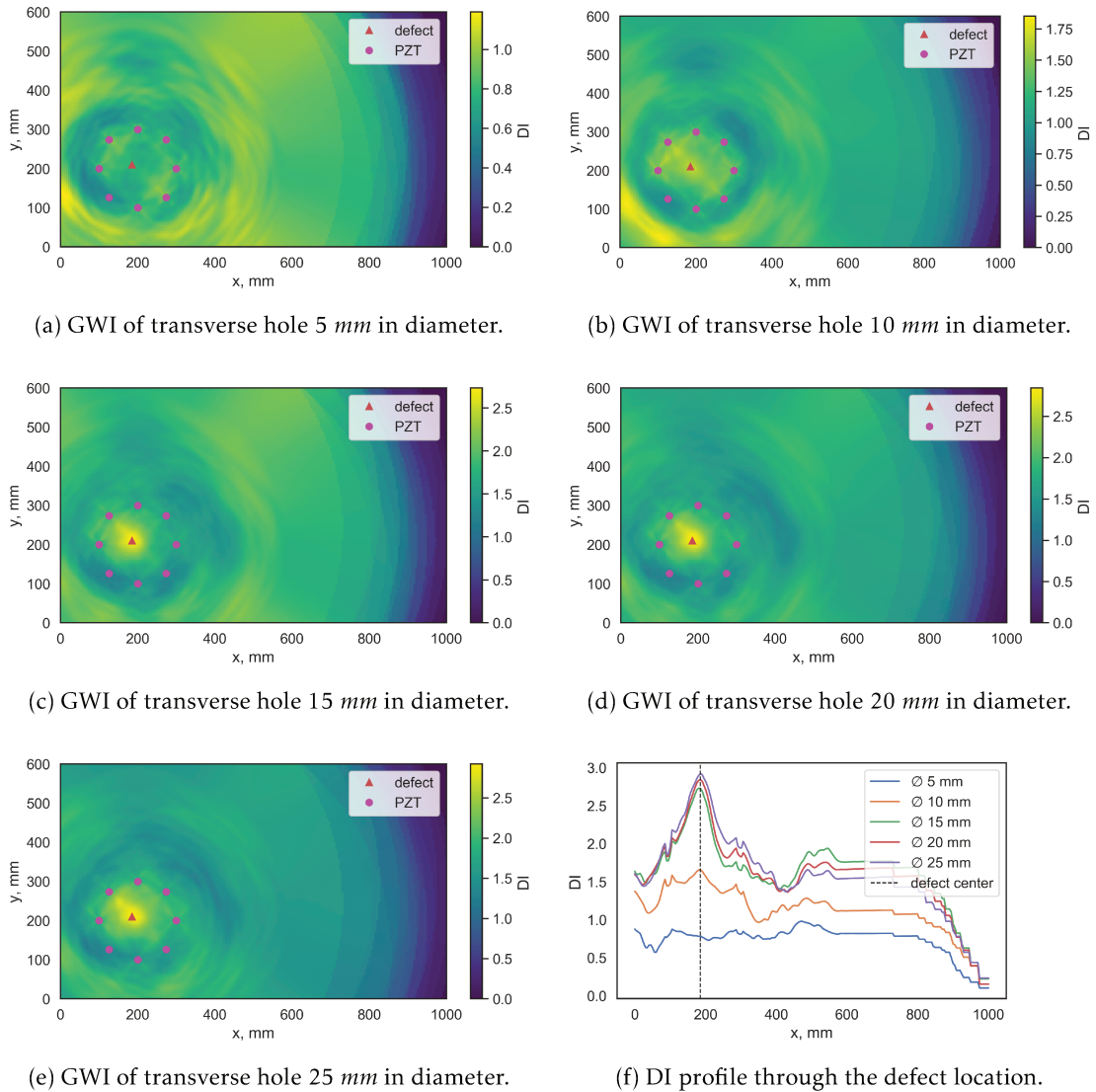


Figure 3.6 – Transverse hole imaging in CFRP plate at 20 kHz.

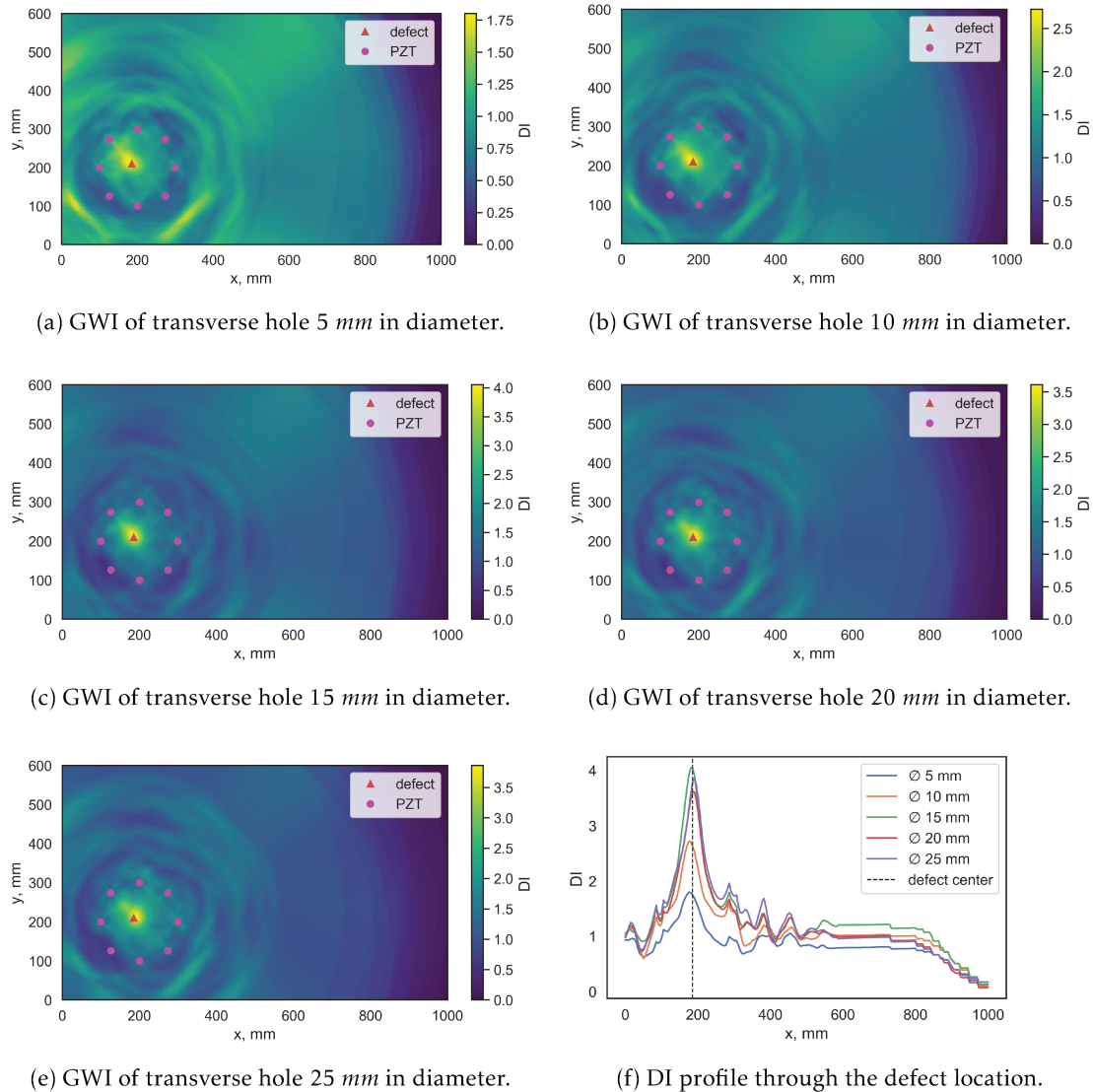


Figure 3.7 – Transverse hole imaging in CFRP plate at 40 kHz.

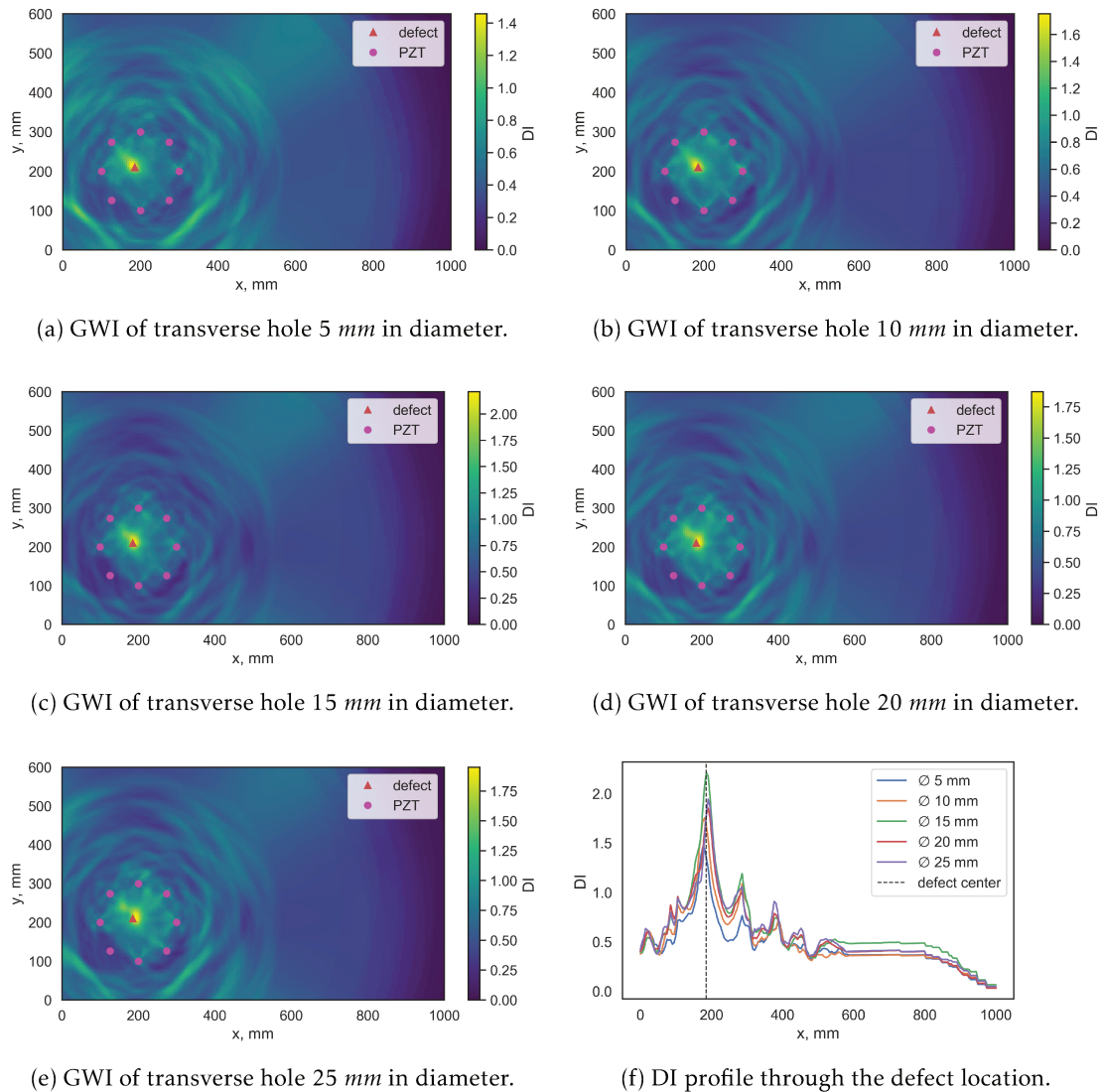


Figure 3.8 – Transverse hole imaging in CFRP plate at 60 kHz.

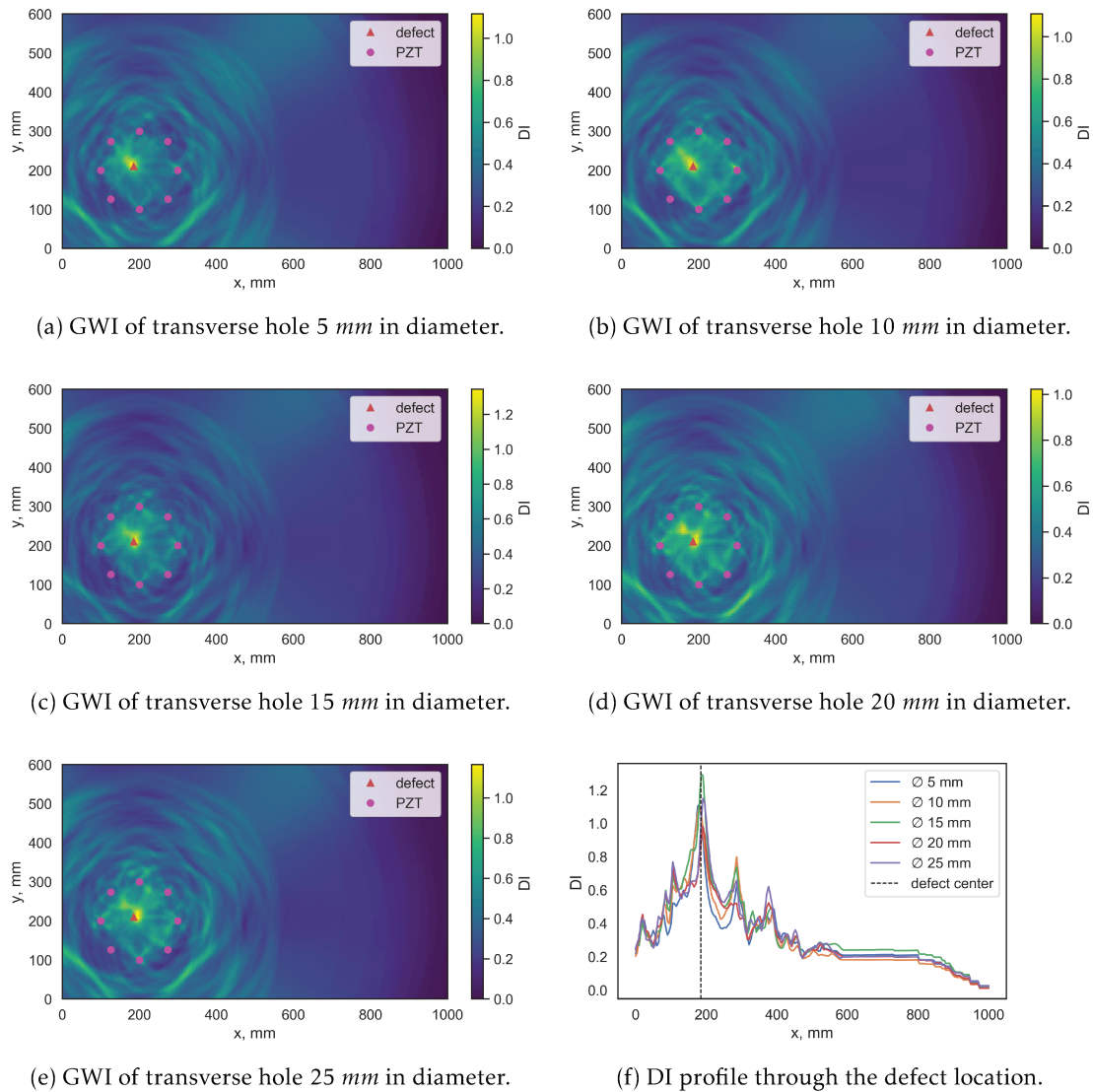


Figure 3.9 – Transverse hole imaging in CFRP plate at 80 kHz.

schematically shown in Figure 3.10. The set-up mainly consists of a calibrated mass  $m$  that can be released from the height  $h$ , a steel sphere and a composite plate. Once dropped, the mass hits a steel sphere, prior placed at the desired impact location, and introduces a damage by delivering the impact energy  $E = mgh$ , where  $g$  is a gravitational constant. Different in size steel spheres can be used for customizing the size of the defect. This approach allows creating calibrated but realistic structural flaws such as delamination or fracture.

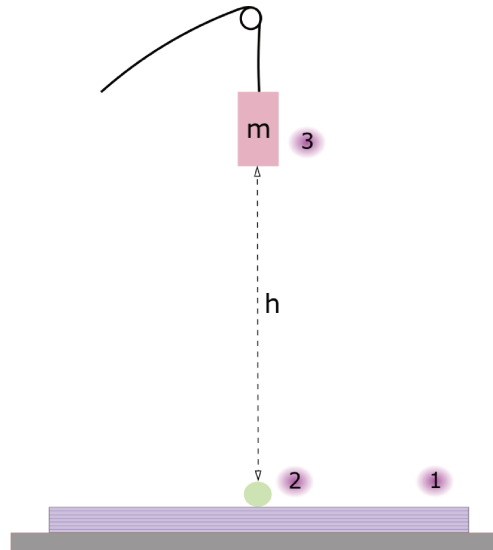


Figure 3.10 – Schematic of the drop tower used for creating impacts in composite structures. A composite plate is represented by 1, a steel sphere is shown by 2, and a mass is denoted by 3.

The following study consists in delamination imaging in an orthotropic CFRP plate. The plate is  $400\text{ mm} \times 400\text{ mm} \times 3\text{ mm}$  in dimension and consists of eight woven-ply, each  $0.275\text{ mm}$  thick. Plys are placed symmetrically with respect to the neutral axis center of the plate as follows  $[0^\circ, 45^\circ \dots 45^\circ, 0^\circ]$ .

The drop tower and steel sphere  $16\text{ mm}$  in diameter are used for introducing delamination by delivering impact energy of  $5\text{ J}$ . The plate is instrumented with eight PZTs  $20\text{ mm}$  in diameter and  $0.5\text{ mm}$  thick. They are driven with a two-cycle Hanning modulated tone burst centered at  $40\text{ kHz}$ ,  $60\text{ kHz}$ ,  $80\text{ kHz}$  and  $100\text{ kHz}$  in order to generate GWs in the structure. The GWI is performed by means of Excitelet algorithm using  $A_0$  mode, and the results are presented in Figure 3.11.

This impact energy is sufficient to create a damage  $7\text{ mm} \times 8\text{ mm}$  in size, which was verified using classical ultrasonic testing. While the flaw is detectable and imaging noise is low for all the four excitation frequencies, the best localization accuracy is achieved at  $40\text{ kHz}$ . This experiment is essential for proving the GWI capability of detecting realistic structural flaws.

### 3.3.3 HCSS

The next studied structure is HCSS  $600\text{ mm} \times 1000\text{ mm} \times 20.7\text{ mm}$  in dimension. Its top skin panel consists of a three-layer CFRP plate attached to a GFRP ply, whereas a bottom skin

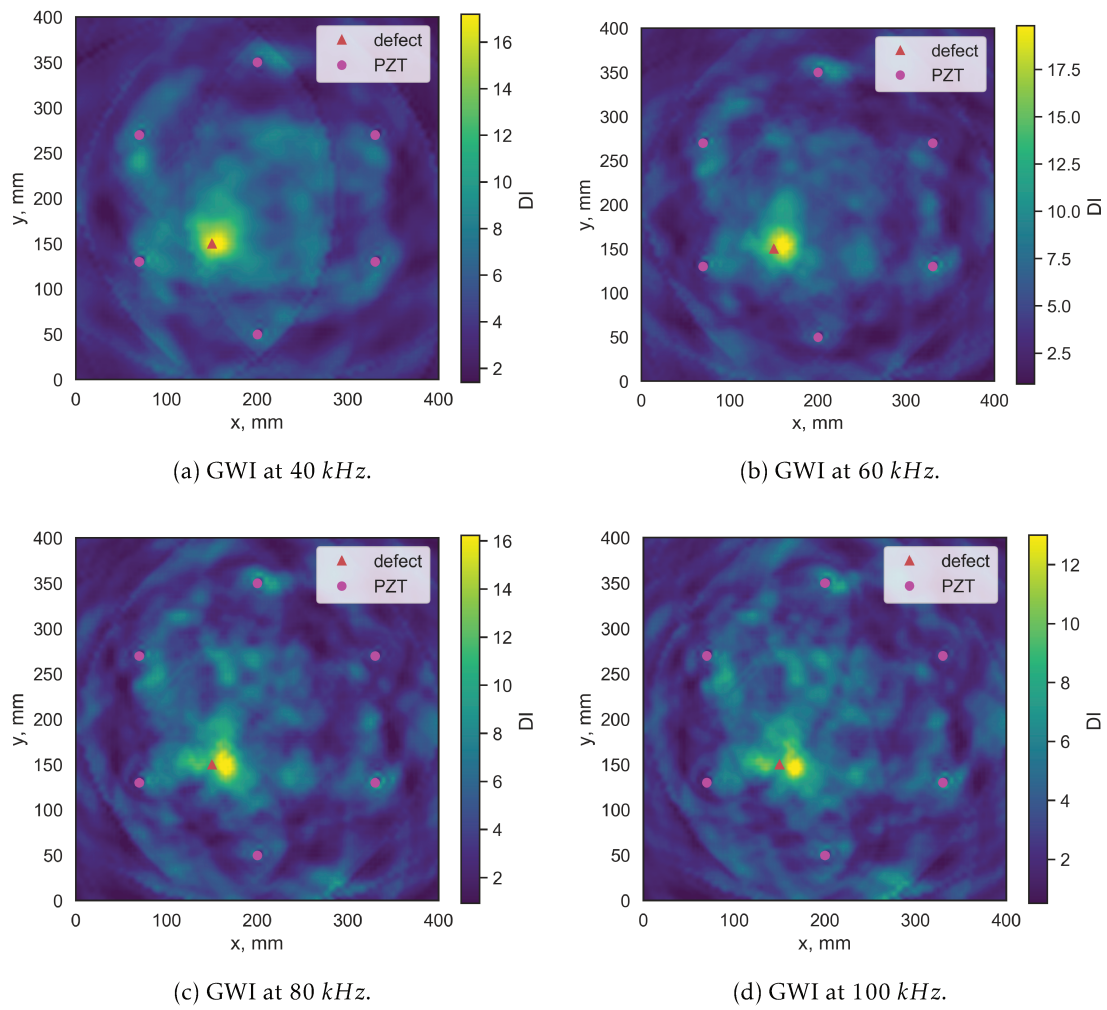
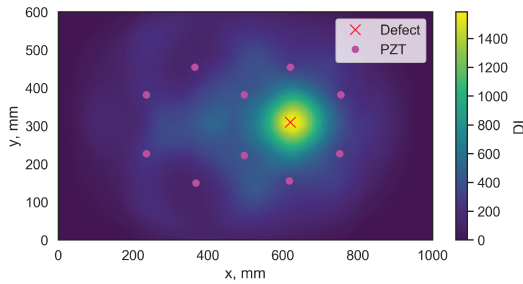


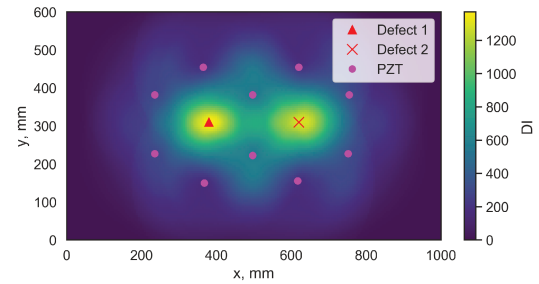
Figure 3.11 – GWI of delamination in CFRP plate induced by delivering impact energy of 5 J.



(a) Photo of HCSS instrumentation.



(b) GWI of attached mass.



(c) GWI of two attached masses.

Figure 3.12 – Experimental instrumentation of HCSS plate and imaging result of simulated by an attached mass defects. GWI is performed by means of Excitelet algorithm at  $15\text{kHz}$  using  $A_0$  mode.

is composed of a GFRP ply attached to a five-layer CFRP plate. All the plies are placed as follows  $0^\circ, 45^\circ, 0^\circ, 0^\circ,$  and  $0^\circ, 0^\circ, 45^\circ, 0^\circ, 45^\circ, 0^\circ$  in the top and bottom skins, respectively. As shown in Figure 3.12a, HCSS is equipped with ten PZT transducers  $20\text{ mm}$  in diameter and  $0.5\text{ mm}$  thick that are used for GWs excitation and sensing. The structure is inspected with a three-cycle Hanning modulated tone burst centered at  $15\text{ kHz}$ . Such a low excitation frequency is chosen with respect to the guided wavefield analysis presented in Section 2.2 and the frequency limitation on the 3D Green's function computation using the proposed in Section 2.3 modeling framework.

The structural damage is simulated by an attached masses. GWI is performed by means of Excitelet algorithms using  $A_0$  mode. The results of simultaneous imaging of one and two attached masses are presented in Figures 3.12b and 3.12c, respectively. It can be observed that Excitelet is capable of detecting defects in either case but the GWI resolution decreased in comparison with the one in CFRP plate, see Figure 3.5. The flawed zone appears larger and more blurred than in a multi-layered CFRP plate due to the larger wavelength of the guided mode, which is directly related due to the overall thickness of the plate, but it is still satisfactory for efficient image analysis.

The same experimental stand has been used to perform GWI of impact-induced damage but, unfortunately, this experiment has failed due to technical reasons. Therefore, further work will comprise validation of this approach for realistic damage imaging in HCSS. It is worth noting that by analogy with delamination imaging in CFRP plate, there are no perceivable limitations that can restrain Excitelet application for defect imaging in such structures.

### 3.4 Statistical studies on localization accuracy of defect imaging algorithms

The reliability of a SHM system has to be estimated before its deployment. It involves the evaluation of several metrics such as robustness to environmental effects, the Probability of Detection (PoD) and the Probability of False Alarm (PoFA) of the system [6, 111]. In GW-SHM, different PoD and PoFA methods [112–115] have been proposed in the literature to evaluate damage detection performance.

Localization performance of a defect imaging algorithm constitutes an essential part of a SHM process. To our knowledge, GWI results have been reported either experimentally or numerically only for a limited number of specimens. Consequently, limitations and performance of GWI algorithms have not been thoroughly studied yet. Such limitations must be evaluated by means of statistical analysis, which requires an extensive database of GWI specimens. However, the cost of generating an extensive experimental database is prohibitive due to the large number of specimens required. Hence, numerical tools can be considered as a proper solution for the generation of large datasets, but until recently, the computation cost was too high. A newly developed finite elements tool for GWs simulation enables the creation of massive databases at a reasonable computation cost [116].

In this section, a statistical study on the defect localization performance is presented for various imaging algorithms and interrogating frequencies. In order to draw statistical inferences, all the three presented algorithms, namely DAS, MV and Excitelet, have been applied to an extensive database of simulated signals, which have been generated using the SHM simulation package of CIVA software. Each database sample is a simulated aluminum plate with a randomly distributed defect size and location.

#### 3.4.1 Guided waves simulation framework

A large database of GWI results is necessary to conduct a statistical analysis on localization accuracy of the above mentioned defect imaging algorithms. GWs simulations using Finite Element (FE) methods are usually time-consuming due to a small element's size and time step requirements [117]. A recent benchmark [118] compares the efficiency of four different FE software, namely in-house EFIT code, Abaqus, Comsol and Ansys, on a specific use case, which represents GWs propagation in a carbon fiber reinforced polymer plate from a piezoelectric transducer over a delaminated region. The performance results of this benchmark are presented in terms of computational time required for this single simulation, which varies from 20 to 90 hours, with memory footprints from tens of GB to hundreds of GB. Such performance makes the generation of an extensive database for statistical studies impossible.

In the present work, CIVA is used to generate an extensive database of GWI samples. It relies on the full three-dimensional Spectral Finite Element (SFE) solution of elastodynamic equations [116]. The SFE code uses two main concepts to speed up the simulation time. First, a high order spectral finite element method is implemented to significantly reduce the number of elements [119]. Second, a macro-element pre-meshing strategy is implemented to optimize global mesh considering its identical regions and implicit element orientation. This leads to significant reduction of CPU load and memory footprint. The simulation configuration used in the benchmark [118] was reproduced with computational time of about 10 minutes on a regular desktop computer and a memory footprint of about 100 MB for quantitatively identical results [120]. The reduction of both memory load and computational time allows running multiple simulations either in parallel or sequentially and enable the creation of an extensive database of simulated GWI results in a reasonable amount of time.

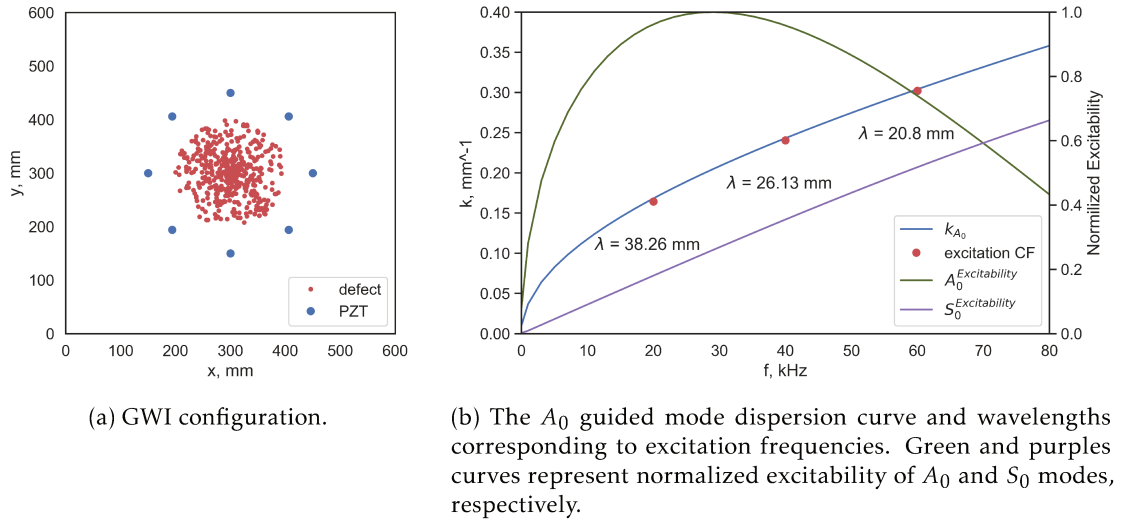


Figure 3.13 – Schematic representation of simulated database configuration.

### 3.4.2 Database description

The studied configuration is an aluminum plate  $600\text{ mm} \times 600\text{ mm} \times 3\text{ mm}$ , which is instrumented with eight identical circular PZT transducers  $18\text{ mm}$  in diameter. The piezoelectric load is modeled as a radial force applied to the surface. In this simulation, it is assumed that excitation is purely radial because of a low-frequency range [121]. In total, 500 simulations were run for three inspecting frequencies.

Each simulated sample contains a transverse hole of varying size and position. Holes are distributed within a circle of  $100\text{ mm}$  in radius with the origin at the center of a plate. The distribution of defects is represented by red circles in Figure 3.13a. This configuration ensures that the distance between defects and PZT transducers is at least of one wavelength of the inspecting mode. Damage radii vary from  $2.5\text{ mm}$  to  $7.5\text{ mm}$  and comply with random uniform distribution.

An aluminum plate is inspected with two-cycle Hanning modulated bursts. Excitation central frequencies are set to  $20\text{ kHz}$ ,  $40\text{ kHz}$ , and  $60\text{ kHz}$  in order to generate only two fundamental guided modes, namely  $A_0$  and  $S_0$ .

The  $A_0$  mode is selected for imaging for two main reasons. Firstly, the corresponding wavelength is smaller than that of the  $S_0$  mode, which results in enhanced GWI resolution. Secondly, in the studied frequency range, the amplitude of  $A_0$  mode measured by a transducer is higher than that of the  $S_0$  mode, as shown in Figure 3.13b. Wavelengths associated with the excitation central frequencies of the  $A_0$  mode are the following:  $\lambda_{A_0}^{20\text{kHz}} = 37.9\text{ mm}$ ,  $\lambda_{A_0}^{40\text{kHz}} = 26.24\text{ mm}$  and  $\lambda_{A_0}^{60\text{kHz}} = 21.19\text{ mm}$ .

Each database sample is processed with three previously described algorithms. For illustrative purposes, images obtained with DAS, MV and Excitelet are presented in Figure 3.14. Their resolution is directly related to the wavelength of a propagating guided mode: the increase of a wavelength leads to the decrease of resolution capability of imaging algorithms. Intuitively, the inspection of a structure at higher frequencies should lead to better defect localization results. However, it is not necessarily true, and it will be demonstrated that for a given GWI configuration an optimal inspection frequency can be identified.

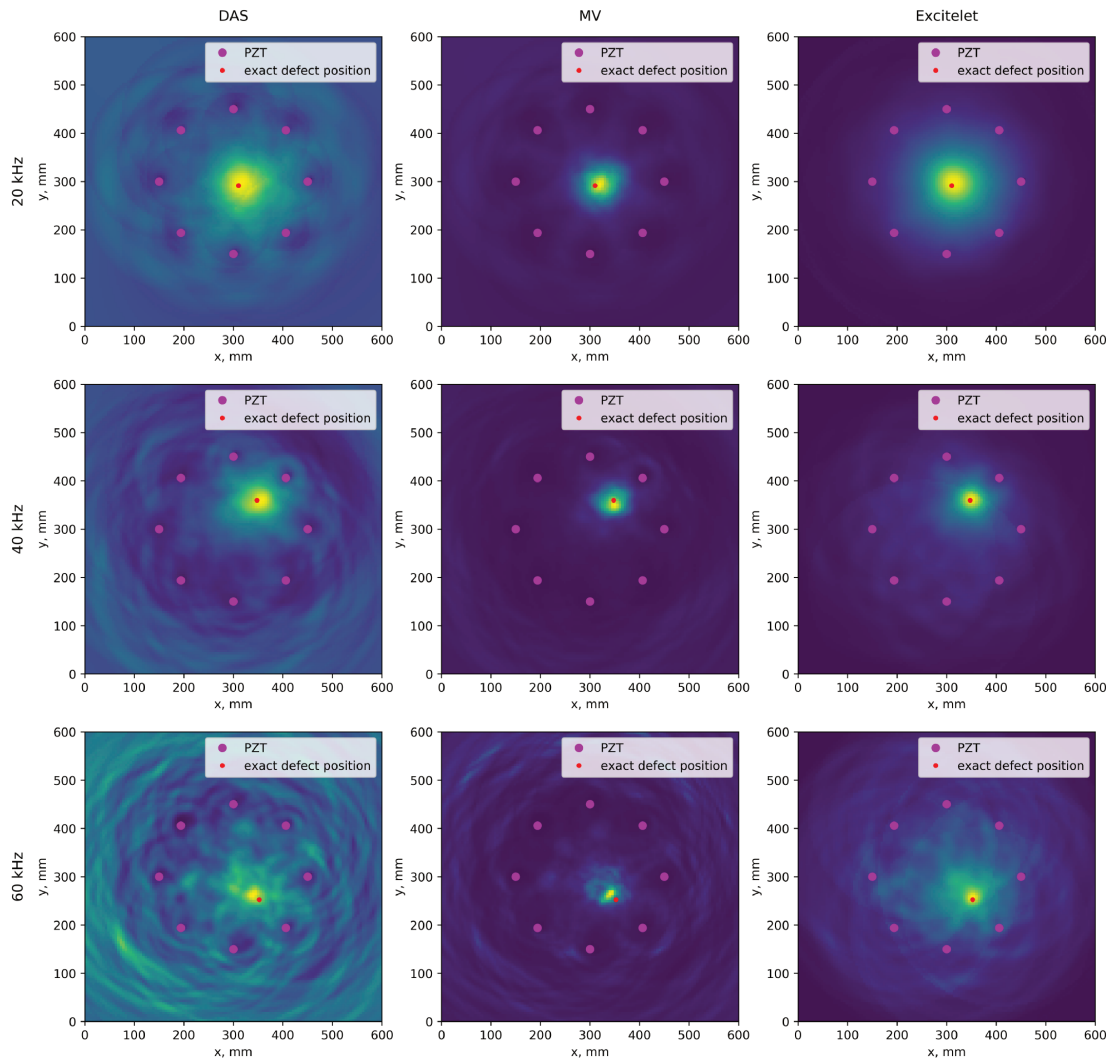


Figure 3.14 – Defect maps computed with DAS (left column), MV (middle column), and Excitelet (right column) with inspection central frequency of 20 kHz (top line), 40 kHz (mid line) and 60kHz (bottom line).

### 3.4.3 Defect localization error analysis

In this section, GWI results obtained with DAS, MV and Excitelet algorithms are discussed. Predicted defect coordinates are compared to their reference values, and localization errors are evaluated. From this analysis, the best combination of an imaging algorithm and inspection frequency are determined.

In GWI, it was demonstrated in [122] that DI spatial distribution complies with Gaussian distribution over damage position. Considering that there is only one defect per simulated dataset instance, the corresponding defect location is obtained by searching the location of maximum in the image.

From now on, defect locations are transformed to the polar coordinate system  $(R, \phi)$  with the

origin at the center of a plate. Each family of observations that corresponds to the combination of an imaging algorithm and excitation frequency is plotted in Figure 3.15 against each other and their reference values in order to estimate defect localization accuracy.

At 20 *kHz*, all the three algorithms suffer from considerable localization errors due to the large wavelength of the inspecting mode ( $\lambda_{A_0}^{20kHz} = 37.9 \text{ mm}$ ) with respect to transducers' inter-distances. The largest distance between transducers approximately corresponds to four wavelengths of the inspecting mode, so the wave packets corresponding to  $A_0$  and  $S_0$  modes in the residual signal are heavily overlapped. Among the three algorithms, Excitelet (represented by green triangles) demonstrates the best coherence between observed defect coordinates and their true values. For this algorithm, there is systematic localization underestimation for the defects remote more than 10 *mm* from the center of the plate. We have not identified the origin of this phenomenon. Although the wave packets are overlapped, Excitelet is more prone to correctly map residual signals than DAS and MV, as it computes linear association between residual and analytical signals. Such linear association allows capturing differences in phase velocities of guided modes, while DAS and MV ignore them by mapping envelopes of residual signals.

As shown in Figure 3.15, inspection at 40 *kHz* leads to more accurate localization results for all the three imaging algorithms. Overall, Excitelet demonstrates the best statistical fit and the smallest variance for both predicted radius and angle regarding their reference values. However, observations located beyond 80 *mm* from the center of the plate are progressively underestimated by Excitelet.

The analysis of GWI results at 60 *kHz* reveals that the defect localization results start degrading for all the three imaging algorithms. At this frequency, the  $A_0$  mode excitability has decreased in comparison with 20 *kHz* and 40 *kHz*, see Figure 3.13b. It has been demonstrated that GW-defect interaction is followed by a guided mode conversion phenomenon [123] so that residual signals contain wave packets of diffracted and converted guided modes. While at 20 *kHz* and 40 *kHz* converted  $S_0 \rightarrow A_0$  and  $A_0 \rightarrow S_0$  guided modes have small amplitudes due to the low excitability of  $S_0$  mode, at 60 *kHz* they are more noticeable. Therefore, a part of the residual signal, which corresponds to the defect-free location, contains wave packets that are not taken into account by a single mode imaging procedure.

At 60 *kHz*, DAS and MV are more prone to localization errors as they map energy of converted modes to defect-free locations. Excitelet still demonstrates the best performance, but its variance has grown in comparison with 40 *kHz*. In Excitelet computation, linear association between analytically propagated  $A_0$  mode and experimental  $S_0$  mode in the residual signal provides a small magnitude, but a non-negligible coefficient of correlation. Hence, converted  $S_0 \rightarrow A_0$  modes are the primary source of defect localization errors as they interfere with the analytically propagated  $A_0$  mode.

Absolute Localization Error (ALE) is obtained by computing the Euclidean distance, i.e.,  $L_1$  norm, between reference and observed defect locations. Their distributions and corresponding experimental Probability Density Functions (PDFs) are presented in Figure 3.16.

The Kernel Density Estimate (KDE) [124] method has been used to determine underlying probability density distributions of localization errors. The advantage of the KDE approach is that it yields an empirical estimate of a true PDF without assuming any form of underlying density function. It can be deduced from Figure 3.16 that at 20 *kHz* and 40 *kHz* all error distributions have two distinct peaks, i.e., local maxima, in the probability density function. Such bimodal distributions were not anticipated, as the central limit theorem claims that for a given large number of observations, the corresponding error distribution should comply with the normal distribution.

The Gaussian Mixture Model (GMM) [125] is selected to analyze localization error distri-

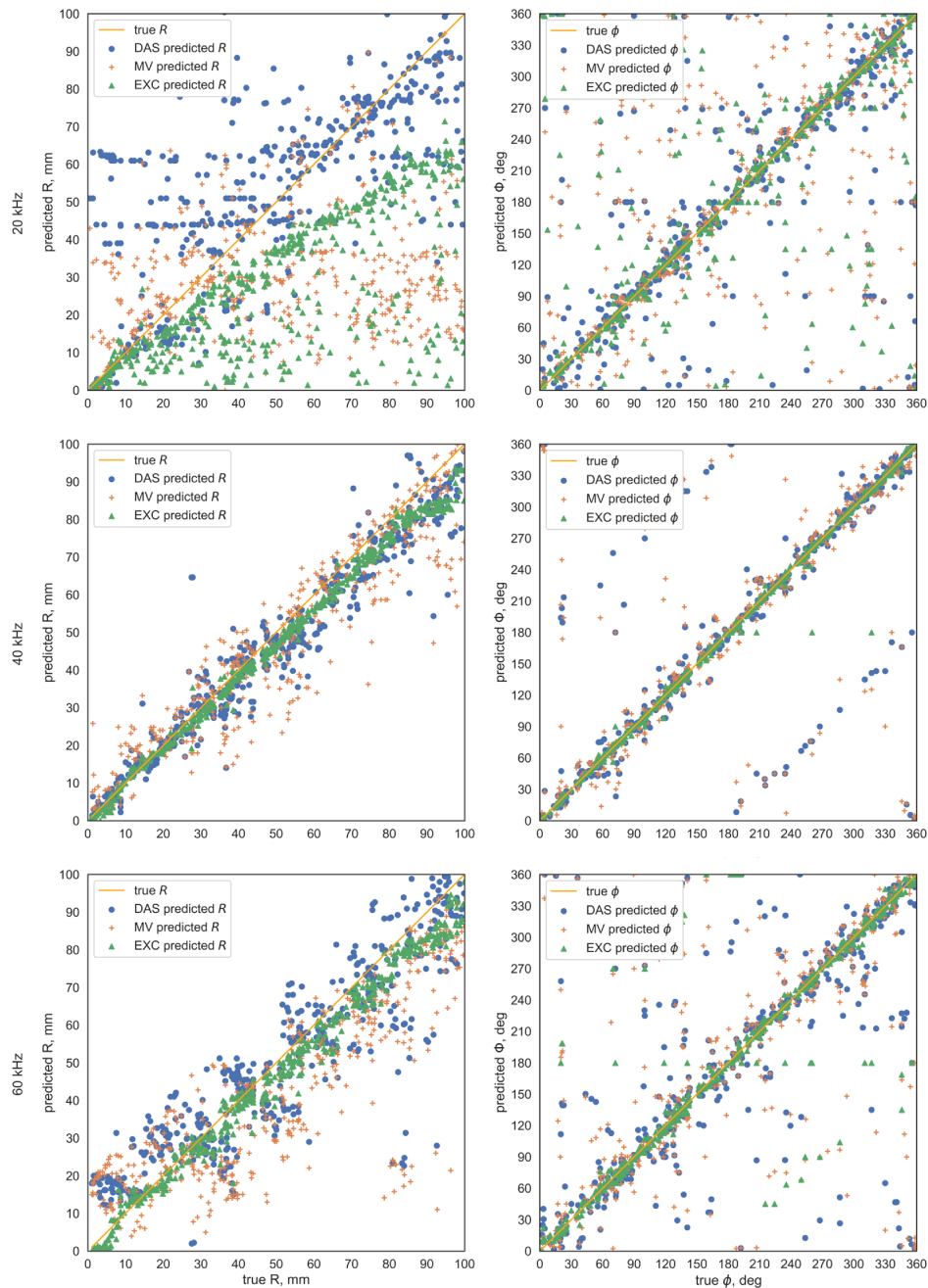


Figure 3.15 – Defect location predictions in a polar coordinate system that is originated at the center of a plate. Observations and reference values of  $\rho$  and  $\phi$  are plotted in left and right columns respectively. The imaging results are obtained at 20 kHz, 40 kHz, and 60 kHz and are shown in this order from the top to the bottom row.

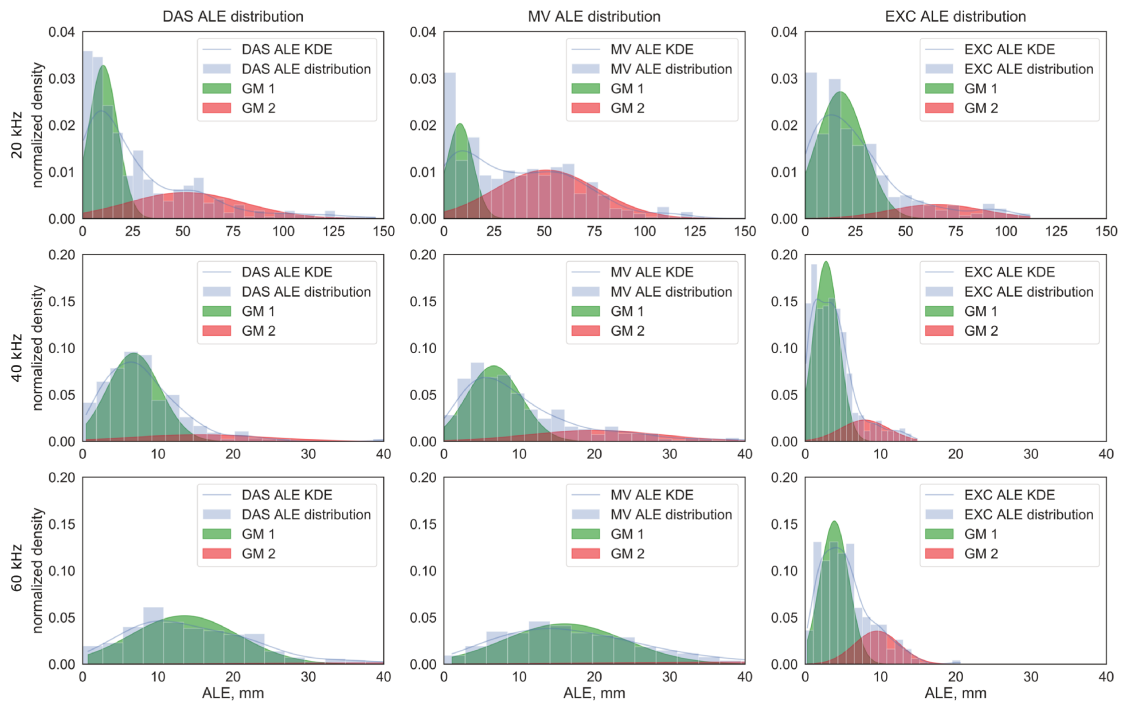


Figure 3.16 – Distributions and corresponding localization absolute errors obtained with DAS, MV, and Excitelet imaging algorithms.

butions. GMM is a probabilistic model assuming that all the data samples are generated from a mixture of Gaussian distributions. Therefore, it is possible to define normally distributed sub-populations within an overall dataset. Each family of localization errors is analyzed in order to determine underlying Gaussian Models (GMs), as shown in Figure 3.16. At 20 kHz, the corresponding PDFs can be decomposed into two Gaussian populations. The first one, denoted by GM1, corresponds to small localization errors (typically smaller than 20 mm), while the second one, denoted by GM2, represents the population of large localization errors. Further analysis of GWI samples that belong to either group allows concluding that the first group is represented by correctly computed images with certain uncertainty, and the second one mostly consists of erroneous GWI samples, where defect imaging algorithms failed to compute defect maps accurately. Visually, the failed images are characterized by multiple incoherent peaks, and the DI values distribution at the defect location does not comply with Gaussian distribution. Therefore, the damage location is deduced incorrectly by searching for the maximum of the image.

Similarly, at 40 kHz, the GM1 model represents small localization errors, and GM2 model describes relatively large errors imputable to the near-field effects. The localization error PDFs of all the three imaging algorithms are narrower due to the smaller wavelength of the inspecting mode. Nevertheless, both Gaussian models GM1 and GM2 describe error families similar to those at 20 kHz. At 60 kHz, PDFs bimodal behavior can still be observed. However, the GM1 model dominates over the GM2 model in terms of probability occurrence for localization errors obtained with both MV and DAS algorithms. For this wavelength, defect localization errors

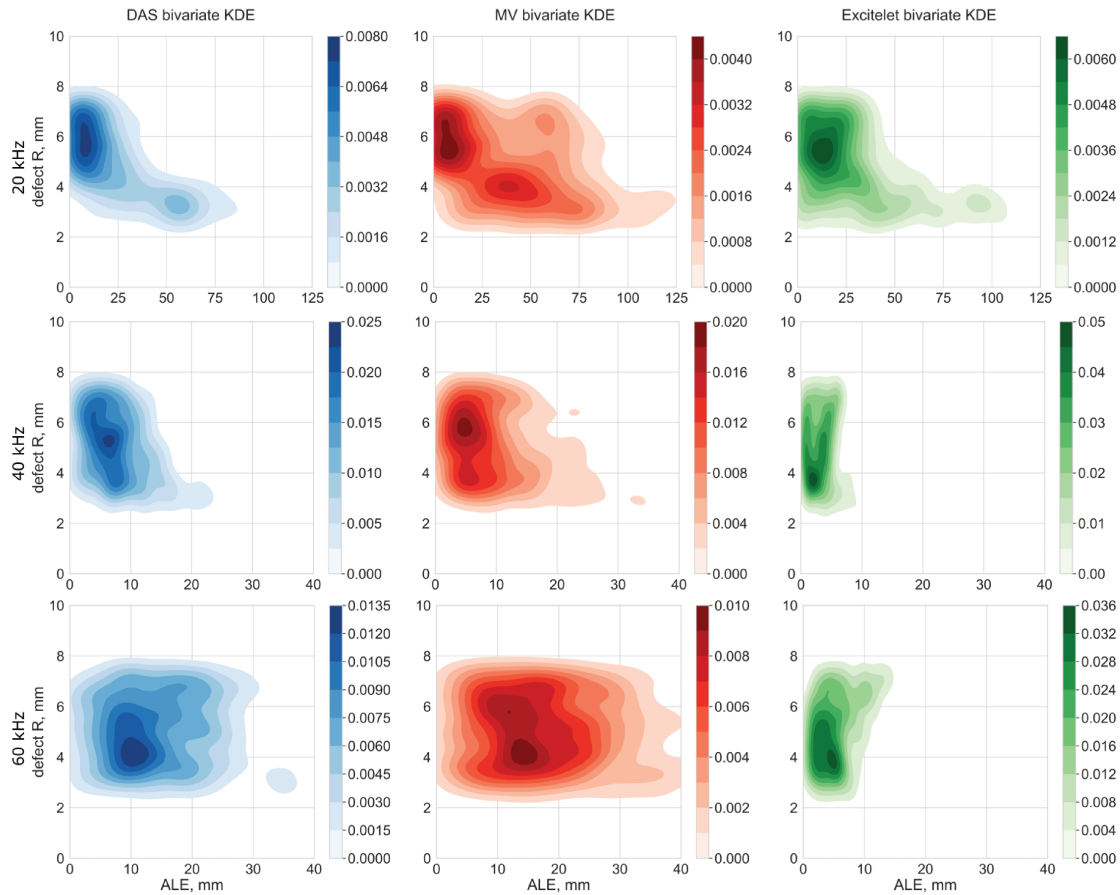


Figure 3.17 – Bivariate kernel density estimate of defect localization absolute error obtained with DAS, MV, and Excitelet imaging algorithms (from left to right column).

appear due to converted guided modes, so DAS and MV are prone to map the corresponding residual energy to defect-free locations. Excitelet is more robust to this phenomenon. The general tendency demonstrates better localization performance of Excitelet in comparison with DAS and MV algorithms for all studied frequencies. Corresponding localization ALE PDFs are narrower and have a smaller side pick, which means that the probability of significant errors is small. Moreover, at 40 kHz and 60 kHz, the probability of experiencing a localization error higher than defect size is negligible.

Furthermore, the statistical inference about localization errors probability distribution regarding the defect size can be deduced from their joint occurrence. A bivariate kernel density estimation with a radial basis function kernel is selected to evaluate an underlying probability density function for all families of localization errors. The corresponding results are presented in Figure 3.17.

At 20 kHz, all the algorithms are less accurate for the localization of small defects. The ALE can reach 150 mm, while the wavelength of an inspecting mode is of about 38 mm. At 40 kHz, localization errors are less significant. This frequency can be considered as optimal to search for

Algorithm	20 kHz			40 kHz			60 kHz		
	DAS	MV	EXC	DAS	MV	EXC	DAS	MV	EXC
STD, <i>mm</i>	28.05	29.39	<b>23.53</b>	5.91	8.14	<b>2.86</b>	11.14	13.67	<b>3.38</b>
RMSE, <i>mm</i>	38.93	47.09	<b>35.05</b>	10.14	13.04	<b>4.68</b>	19.09	23.73	<b>6.36</b>
MAE, <i>mm</i>	27.01	36.79	<b>25.97</b>	8.24	10.19	<b>3.71</b>	15.49	19.39	<b>5.39</b>
CoC	0.68	0.44	<b>0.71</b>	0.86	0.82	<b>0.99</b>	0.79	0.70	<b>0.95</b>
$P(ALE > 15, mm)$	<b>56.2 %</b>	70.2 %	61.7%	9.9 %	21.4 %	<b>0.15 %</b>	44.3 %	57.0 %	<b>1.0 %</b>

Table 3.1 – Performance metrics summary for Excitelet, DAS and MV defect imaging algorithms. Results for 20 kHz, 40 kHz and 60 kHz are grouped central inspection frequency.

defects in a given GWI configuration. The most frequent ALE is 7 *mm*, 5 *mm*, and 3 *mm* for DAS, MV, and Excitelet algorithms, respectively.

Excitelet demonstrates the most frequent absolute localization error of about 3 *mm*. Moreover, the probability of ALE higher than 10 *mm* is extremely small, while the defect size varies from 5 *mm* to 15 *mm*. At the same frequency, DAS and MV demonstrate the most probable error of about 8 *mm* because they do not account GWs dispersion phenomena. In addition, MV occasionally suffers from large localization errors due to the assumption of an omnidirectional defect diffraction pattern.

In practice, the probability of experiencing ALE larger than maximum tolerable error is required. In the present study, the maximum tolerable error is arbitrarily fixed at 15 *mm* corresponding to the largest transverse hole, and the probability of having ALE larger than maximum tolerable error  $P(ALE > 15, mm)$  can be evaluated by integrating the PDF between the corresponding bounds. Other maximum tolerable error could be defined depending on the application. At 20 kHz, the  $P(ALE > 15, mm)$  are quite high and equal 56.2 %, 70.2 % and 61.7 % for DAS, MV and EXC algorithms. Consequently, GWI results obtained at this frequency cannot be considered as reliable. On the other hand, at 40 kHz the corresponding results are 9.9 %, 21.4 % and 0.15 %, and at 60 kHz  $P(ALE > 15, mm)$  are 44.3 %, 57.0 % and 1.0 %, respectively. Note that  $P(ALE > 15, mm) = 1\%$  means that the probability of accurate localization is 99%. It is worth noting that the performance of Excitelet algorithm is more remarkable than of the two other algorithms, while the structure is inspected for all the three excitation frequencies.

General practice in model verification is to determine the alignment of model predictions with true values. It typically involves computing a set of performance metrics in order to capture all aspects of model behavior, reflecting statistical similarities and differences between true values and experimental observations.

A Mean Absolute Error (MAE) measures the average magnitude of errors over the dataset without considering their directions. In our case, it is computed as the average of absolute differences between the maxima of images and the corresponding reference coordinates, where all individual differences have equal weight. A Root Mean Square Error (RMSE) represents a quadratic mean of model deviations from reference values. Each RMSE component is proportional to a squared error which makes this metric highly sensitive to the presence of significant deviations, emphasizes the inability of an imaging algorithm to compute an image correctly. The Standard Deviation (STD) is a statistic that evaluates dataset dispersion. STD of model errors provides insights on the incertitude experienced by the imaging algorithm. For example, the spread of predictions at 20 kHz, shown in Figure 3.15, generally happens when defect imaging algorithms fail to reconstruct images. Finally, the product-momentum Coefficient of Correlation (CoC) is used for determining the strength of linear statistical relationship between observations and their reference values, where the perfect alignment of both leads to  $CoC = 1$ , and the absence of linear relationship results in  $CoC = 0$ .

The performance metrics of all the three defect imaging algorithms are collected and summarized in Table (3.1) in order to estimate a degree of correspondence between imaging algorithms outputs and reference values. In this table, STD, RMSE, MAE, and CoC are grouped by excitation frequencies for all the three imaging algorithms, so the merits of competing imaging algorithms and excitation frequencies can be determined for a given GWI configuration. From the analysis of Table (3.1), it can be deduced that the best defect localization accuracy is achieved when the structure is monitored at 40 kHz and imaged with Excitelet algorithm. Such a GWs imaging configuration allows obtaining  $CoC_{EXC}^{40kHz} \approx 0.99$  predictions, while RMSE and MAE are approximately equal to 4.86 mm and 3.71 mm, respectively. Such low and close by magnitude RMSE and MAE errors indicate that Excitelet algorithm does not fail in image reconstruction. The STD, which indicates how the data is distributed around the mean value, estimates model's uncertainty with respect to the reference data. For all the three excitation frequencies, Excitelet is the least uncertain, and MV is the most volatile in localizing defects.

Excitelet shows the best performance in terms of RMSE, MAE and MAE localization error metrics for all the three studied frequencies and reaches its peak while monitoring the structure at 40 kHz. The same conclusion holds for the CoC while measuring linear model alignment with reference values and searching for the best prediction accuracy.

This section presents statistical studies on localization performance of three state-of-art defect imaging algorithms for a GW-based SHM system. The study is conducted using a numerically generated database of GWI results. The statistical advantage of using the Excitelet algorithm in comparison with DAS and MV is demonstrated. Excitelet requires the comprehensive knowledge of GWs propagation in the structure for analytical signal computation, it provides smaller localization errors. Lower performances of DAS and MV are due to the neglect of GWs dispersion which has to be taken into consideration for accurate localization. The three algorithms suffer from mode conversion phenomena, emphasizing the need to adequately choose the inspection frequency to guarantee the best performances. For this specific configuration, this study leads to the conclusion that the best defect localization performance is achieved when the structure is monitored at 40 kHz, and imaging is performed using Excitelet algorithm. One of the main reasons that GWI results are better at 40 kHz for this plate is the diameter of piezoelectric transducers. This is a driving factor that influence the modal excitability. For this configuration, it is chosen to favor the  $A_0$  generation so that the accurate localization of the defect is obtained for 99% of the cases.

More generally, the presented methodology can contribute to SHM system optimization and reliability evaluation. It allows quantifying the performance gain, but it has to be repeated for each constituent and configuration. ALE probability distributions can also contribute to reliability and associated risks estimation; it can be determined by a variety of methods, including Monte Carlo simulations. For future work, authors plan to investigate defect localization and sizing accuracy in composite plates for various GWI configurations and include it into the performance demonstration of a SHM system as a whole.

### 3.5 Sparse defect imaging

Regardless of the choice of a defect imaging algorithm, the DI value has to be evaluated for each pixel of the image that represents the integrity of the structure. Computational complexity depends on the employed GWI method, and has been a subject of intensive research [63] in order to deploy a GW-based SHM system on large structures. Various techniques, such as parallelization and vectorization, have been used to speed up calculations. They allow decreasing significantly the computation time, but the pixel-wise evaluation process is remained.

Therefore, certain methods such as RAPID, which computes a correlation between damaged and pristine states in the vicinity of a GWs path, become computationally efficient, but others such as Excitelet, which for each pixel computes the theoretical signal and then correlates it with the experimental one, are still time and computationally demanding. The reasons to use Excitelet were statistically proven and presented in Section 3.4. It has a clear advantage in comparison with DAS and MV, but for real-life large structures defect imaging risks to last long, while a short time window is usually given for monitoring.

In this section, a procedure for sparse imaging is proposed. It is based on an adaptive sampling procedure, and relies on the Bayesian optimization of Gaussian process regressor (BO-GPR).

#### 3.5.1 Bayesian optimization of Gaussian process for sparse defect imaging

The Gaussian process, presented in section 2.4.1.2, has been proven efficient for regression tasks. In the presented approach, it is used to model an image that represents the integrity of a structure, i.e., the objective function. In comparison with other regression methods, GP provides probabilistic inferences that can be used in optimization procedure.

The GP is configured by its kernel that describes relationships between elements of the model. Historically, the square exponential and rational quadratic kernels [98] became default ones as they are universal. They can be integrated against most functions, and every function in their prior has infinitely many derivatives [126]. The rational quadratic kernel is used in this work. It is equivalent to adding together many square exponential kernels with different lengthscales, and is expressed as follows:

$$K_{RQ}(x, x') = \sigma^2 \left( 1 + \frac{(x - x')^2}{2\alpha l} \right)^{-\alpha}, \quad (3.14)$$

where  $\sigma^2$  is the output variance,  $\alpha$  determines the relative weighting of large-scale and small-scale variations, and  $l$  is the lengthscale determining the length of interpolation. GP priors with this kernel expect to see functions that vary smoothly across many lengthscales, and allow modeling data that vary at multiple scales.

Bayesian optimization is a method aimed at reducing the number of sampling points while maximizing the information gain they provide to the objective function. The presence of a defect and corresponding characterization is drawn from the analysis of spatial intensity distribution in the image. Thus, more attention is paid to the flawed zones where DI values are high and comply with Gaussian distribution.

Consider a reference image, i.e., pixel-wise computed image. It can be approximated by the objective function  $f$  with a corresponding prior. Iteratively, the Bayesian optimization uses a prior belief about  $f$  to evaluate an acquisition function. Searching for a maximum of the acquisition function allows determining points of maximal information gain for the function  $f$ . The prior belief is then updated with samples drawn from  $f$  to obtain a posterior that better approximates the objective function.

The acquisition function plays a key role in Bayesian optimization. It proposes sampling points in the search space so that the best improvement of the objective function can be achieved. The basic principle of this function is a trade off between exploitation and exploration. The exploitation means sampling in the areas where a surrogate model has a high objective, whereas the exploration means sampling at locations where the prediction uncertainty is high. Several acquisition functions have been developed and presented in the literature, including the probability of improvement, expected improvement, and upper/lower confidence bounds. Taking into account recent advances in the field of Bayesian optimization, the expected improvement function is used. It can be formulated as follows:

$$A(x) = \begin{cases} (\mu(x) - f(x_t) - \zeta)\Phi(Z) + \sigma(x)\phi(z), & \text{if } \sigma > 0 \\ 0, & \text{if } \sigma = 0, \end{cases} \quad (3.15)$$

with

$$Z = \begin{cases} \frac{\mu(x) - f(x_t) - \zeta}{\sigma(x)}, & \text{if } \sigma > 0 \\ 0, & \text{if } \sigma = 0, \end{cases} \quad (3.16)$$

where  $\phi(x)$  and  $\Phi(x)$  denote a probability density function (PDF) and a cumulative distribution function (CDF), respectively. The mean and the standard deviation of the GP posterior evaluated at  $x$  are denoted by  $\mu(x)$  and  $\sigma(x)$ . The parameter  $\zeta$  is responsible for the trade off between exploration and exploitation, it is often varied during the optimization procedure to promote exploration at early stage and exploitation later.

With respect to the Bayesian optimization formulation given above, a GWI sample is considered as an objective function, which can be evaluated using any defect imaging algorithm presented in the section 3.2. The acquisition function maximization allows selecting the next point at which to compute the DI value.

In addition, a GPR model can be tolerant to the acquisition noise, so that the integrity image can be denoised using this approach. It allows reconstructing the image itself while neglecting GWI artifacts. In the next chapter, where a defect sizing problem is considered, this property will be used to pull together simulated and experimental GWI databases.

### 3.5.2 Sparse imaging results

Aluminum plate  $600 \text{ mm} \times 600 \text{ mm} \times 3 \text{ mm}$  is chosen for this study. It is instrumented with eight PZT transducers  $18 \text{ mm}$  in diameter and  $0.5 \text{ mm}$  thick. The structural damage is a transverse hole  $10 \text{ mm}$  in diameter, and the GWI is performed by means of BO-GPR optimization of Excitelet algorithm using  $A_0$  mode for imaging.

Figure 3.18 presents GWI results obtained by using 20, 40 and 80 sampling points as well as corresponding uncertainty maps. The parameter  $\zeta$  is tuned to balance the exploration/exploitation ratio of the reconstruction process so that defect-free regions are sampled in more sparse manner than flawed zones. Indeed, observing Figures 3.18b 3.18d and 3.18f it can be seen that the BO-GPR model correctly identifies flawed region and has a high level of confidence about corresponding DI values. The associated STD is below 0.1 in comparison with the DI values that are of about 24, e.g., the through defect DI values are reconstructed precisely. The model is less confident in defect-free regions, where the STD is of about 0.7, but these regions do not provide any information on structural defects.

Obviously, the reconstruction precision depends on the number of sampling points. If it is too low the image reconstruction is not precise and flawed area might have distorted shape, as shown in Figure 3.18b. On the contrary, if the number of sampling points is too large, BO-GPR

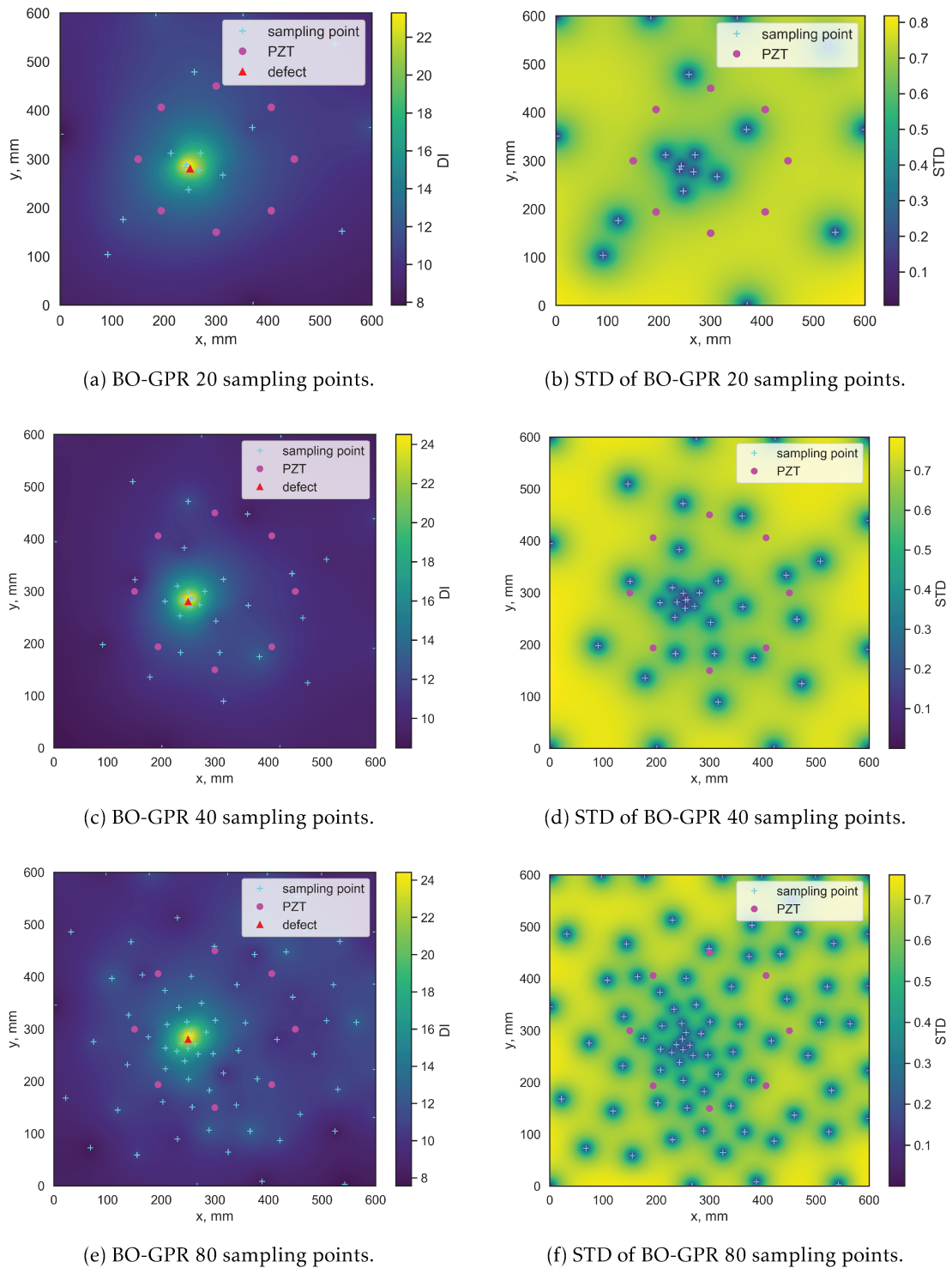
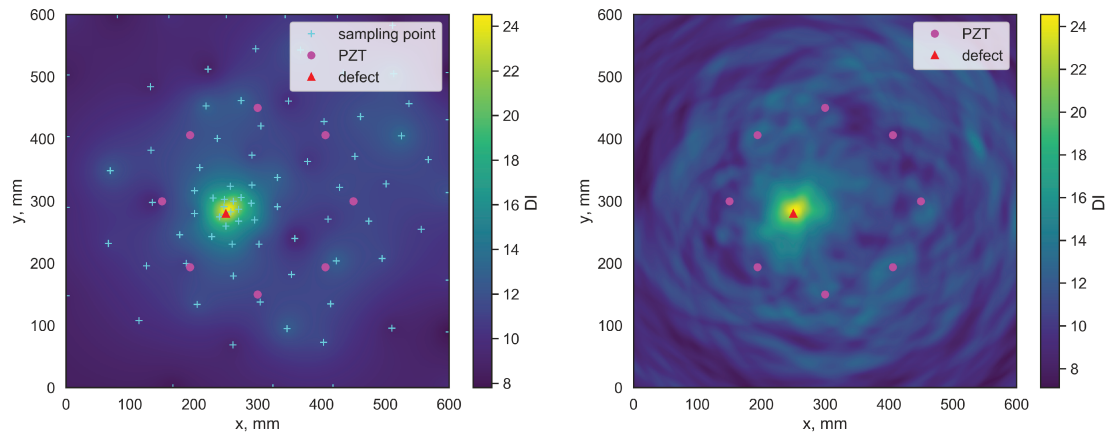
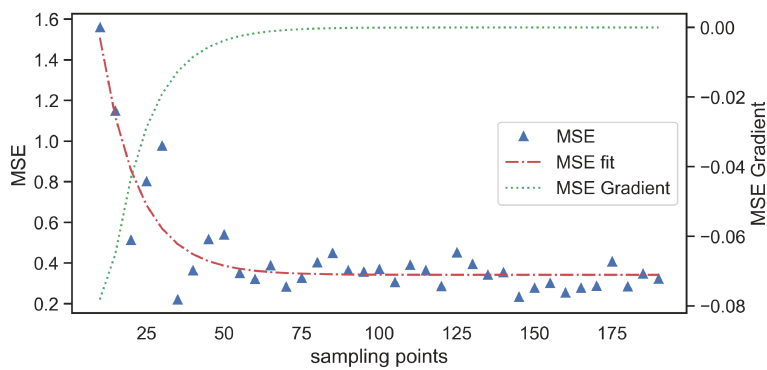


Figure 3.18 – BO-GPR reconstruction of transverse hole imaging in aluminum plate at 60 kHz using Excitelet.



(a) GWI by means of BO-GPR Excitelet using 90 sampling points.

(b) True cartography  $600 \times 600$  pixels.



(c) MSE and its gradient versus the number of sampling points used for image reconstruction.

Figure 3.19 – BO-GPR optimization of Excitelet algorithm.

model approximates correctly the image and starts additionally to approximate imaging artifacts because not much new information is learned. Figure 3.19a and Figure 3.19b demonstrate the case where the model uses too many sampling points and as a result it started to approximate artifacts in addition to the noise-free image. Therefore, an optimum number has to be identified in order to achieve the best efficiency of the model.

Each new sampling point introduces a certain improvement to the reconstructed image to the different extent. At the beginning, when the number of sampling points is low, each new point introduces a significant amelioration to the BO-GPR model, but as this number grows the improvement stagnates. In order to quantify such improvement a reconstructed image can be compared to the previous result by computing a mean square error (MSE) between two images, and the rate of change in relative MSE will indicate a stagnation point so that the optimum number of sampling points can be determined. Relative MSE versus a number of sampling points is shown in Figure 3.19c. These errors are fitted to the curve using a least square regression, in order to obtain the improvement function. The rate of change is then computed as a gradient of this function, and is shown by a green curve in the same figure. It can be observed that it grows promptly when the number of sampling points is smaller than 50, and saturates afterwards. Therefore, for a given GWI configuration, an optimum value of sampling points can be defined as 60.

Fortunately, the BO-GPR optimization of GWI can be performed using artificial defects such as an attached mass, so the new structure of interest has not to be damaged.

## 3.6 Chapter summary

This chapter reports on defect detection and localization in three different structures, namely an aluminum plate, a multilayered CFRP plate and HCSS. As such, they are often used in aerospace industry, e.g., for aircraft fuselages or wind skins, and also constitute the building blocks of more complex structures such as IFS of the aircraft nacelle. These structures are exposed to harsh operational conditions so such defects as fracture, corrosion, delamination or disbonding may appear due to impact forces or thermo-mechanical aging.

The defect detection and localization are performed by means of GWI due to its relative robustness to the corruption of GWs signals. The sparse array of embedded transducers distributed over the surface is typically used to excite and measure GWs signals in the structure. The GWI implements GWs signals processing methods to compute an image that represents the integrity of the structure. Each pixel of this image contains a DI value, and the spatial distribution of these values can be translated into the probability of structural flaw. Among various defect imaging algorithms presented in the literature, DAS, MV and Excitelet were selected to detect and locate three types of defects, namely a simulated defect, a transverse hole and delamination. To a different extent, these algorithms rely on GWs propagational characteristics, such as a directional group velocity and the 3D Green's function. These properties can be obtained using various simulation and experimental methods, including methods presented in Chapter 2.

Defect imaging algorithm constitutes an essential part of a SHM system, and its localization performance has to be evaluated before the system deployment. This chapter presents the methodology and results on defect localization performance of DAS, MV and Excitelet algorithms using statistical analysis of an extensive database of GWI specimens. It is demonstrated that among the three imaging methods Excitelet is statistically the most performing.

Taking into consideration that for large real-life structures pixel-wise computation of the image can be time-consuming, a novel approach for the sparse defect imaging was developed. It is implemented in the Bayesian framework, where the Gaussian process models the structural integrity image. Following the Bayesian optimization routine, a joint problem of an acquisition function is formulated so that the choice of sampling points is driven by maximizing the former. For example,  $600 \times 600$  pixels image can be reconstructed using 40 sampling points so that the sampling rate is reduced by four order of magnitude.

The GWI algorithms' sensitivity to the damage size is also demonstrated. While the damage presence and location can be directly deduced from the spatial intensity distribution of a GWI sample, the defect sizing is not straightforward and might require sophisticated solvers based on machine learning-based regressors. The next chapter formulates the defect sizing problem as an inverse problem and seeks a solution using regression methods.



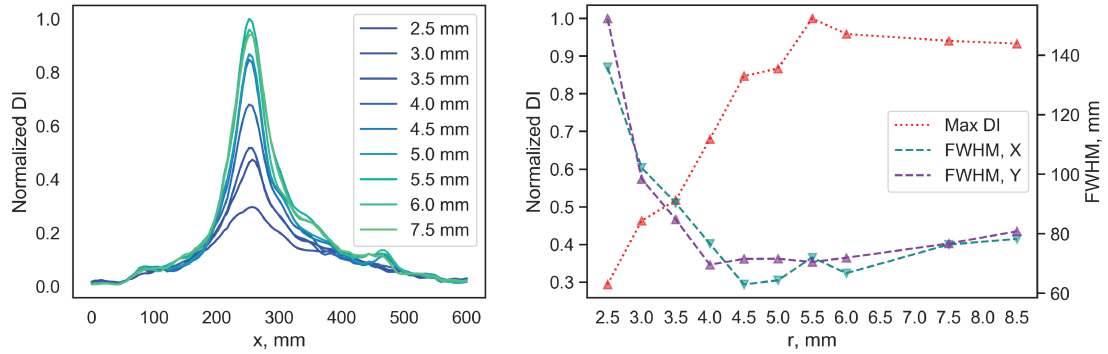
# Data driven approach for defect sizing using Guided Wave Imaging

## Outline of the current chapter

<b>4.1 Inversion problem formulation</b>	<b>82</b>
<b>4.2 Machine learning for defect sizing</b>	<b>84</b>
4.2.1 Supervised learning approach . . . . .	84
4.2.2 Defect sizing using Deep Learning . . . . .	84
4.2.2.1 Introduction to CNN . . . . .	85
4.2.2.2 Database generation . . . . .	87
4.2.2.3 Inversion of simulation results . . . . .	88
4.2.2.4 Inversion of experimental results . . . . .	92
4.2.2.5 Inversion model interpretation . . . . .	93
<b>4.3 Chapter summary</b>	<b>95</b>

The effectiveness of GWI for SHM systems has been demonstrated in the previous chapter. GWI relies on the knowledge of GWs propagation and allows computing images that represent the integrity of a structure. These images can be visually analyzed in order to detect and locate a defect, but defect characterization is a more complicated problem that might require application of sophisticated solvers.

This chapter presents a data-driven approach for defect size evaluation. Firstly, an inverse problem is formulated. Then, an extensive database of simulated GWI results is generated and processed using a deep convolution neural network in order to construct an inversion model capable of determining the size of a defect from images. Finally, an inversion model is validated on experimental GWI results.



(a) Normalized through defect DI values profiles. (b) Normalized Max-DI and FWHM versus hole radius.

Figure 4.1 – Demonstration of GWI sensitivity to the damage size at 45 kHz.

## 4.1 Inversion problem formulation

GWI as such is an effective method and a natural choice for a GWs-based SHM system. It allows computing an image representing the integrity of the structure, where each pixel is mapped to the elementary portion of the studied specimen. Defect imaging algorithms such as Excitelet can be used to compute DI values over the ROI. While the single DI value does not provide sufficient information about the integrity of the structure, the spatial distribution of DI values can be interpreted for determining the presence of the defect, its location and size. As demonstrated in Chapter 3, damage detection and localization are straightforward from the analysis of the intensity distribution in GWI results, whereas damage sizing is a more complex problem that might require sophisticated solvers.

Consider the same GWI configuration as in Section 3.4.2. Note that this is an aluminum plate  $600 \text{ mm} \times 600 \text{ mm} \times 3 \text{ mm}$  in dimension that is equipped with eight PZT transducers  $18 \text{ mm}$  in diameter. The SFE method (presented in Section 3.4.1) is used to simulate GWs propagation and GWs-defect interaction in the plate. The structural damage is represented by a transverse hole located at  $(X : 250, Y : 280, \text{ mm})$  that progressively grows from  $2.5 \text{ mm}$  to  $8.5 \text{ mm}$  in radius with increment of  $0.5 \text{ mm}$ . The plate is excited at  $45 \text{ kHz}$  with two-cycle Hanning modulated tone burst, and the defect imaging is performed by Excitelet algorithm using  $A_0$  mode where  $\lambda_{A_0}^{45\text{kHz}} = 24.85, \text{ mm}$ .

Corresponding GWI results are normalized with respect to the highest DI value, and DI profiles through the flawed region are shown in Figure 4.1a. It can be observed that for small defects ( $R \in [2.5, 5.5], \text{ mm}$ ) DI values increase progressively and sharpen with the radius of the hole, but for larger ones they saturate and decrease in magnitude.

As mentioned in Section 3.4.3, the DI distribution complies with the bivariate Gaussian distribution. Therefore, the maximum DI (max-DI) values and corresponding through defect Full Width Half Maximum (FWHM) in both  $X$  and  $Y$  directions can be collected for the sake of demonstration of GWI sensitivity to the defect size, see Figure 4.1b. It is worth noting that there are regions where dependence is almost linear ( $DI \in [2.5, 4.5], \text{ mm}$  and  $DI \in [6.0, 8.5], \text{ mm}$ ) but, in total, these variations are non-linear in both height and width. More details on the max-DI and FWHM parameters determination as well as corresponding illustrations are provided in Appendix A.

It should also be pointed out that DI values distribution is not spatially homogeneous,

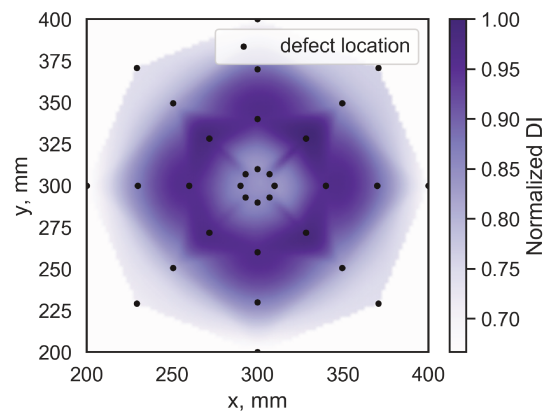


Figure 4.2 – Max-DI values distribution over the plate for defects 5 mm in radius.

meaning that DI values differ for the same size defects located at various positions. Thirty two SFE simulations representing transverse holes 5 mm in radius at different locations are run and post-processed by means of Excitelet algorithm in order to confirm the previous statement. The maxima of DI values are then collected for corresponding locations and interpolated using 3<sup>rd</sup> order polynomial interpolation in order to construct DI map for the current defect, see Figure 4.2. It can be observed that DI values' distribution is conditioned by the geometry of the structure and transducers' arrangement due to the GWs border reflections, which interfere with a theoretical signal in Excitelet computations. Taking into account such a non-linear behavior of DI values distribution regarding the defect location and size variations, the analytical solution for a defect sizing problem using GWI results is not evident.

Therefore, a data-driven approach is proposed to search for a solution to this problem as, under certain conditions, it is capable of approximating such complex non-linear functions.

Consider a data set of  $N$  elements  $D \equiv \{x_i, y_i\}_{i=1}^N$ , where  $x$  and  $y$  denote GWI results and corresponding defect sizes. The data-driven approach is aimed at learning structural relations in  $D$  in order to derive an image inversion model  $f(x)$  so that this model would be capable of determining a defect size  $y_*$  by processing any new image  $x_*$  for a given GWI configuration. More formally, it can be expressed as:

$$y = f(x) + \epsilon, \quad (4.1)$$

where  $f(x)$  is the model that maps images  $x$  to the corresponding size  $y$  and  $\epsilon$  represents the independent noise. The approximation of the model  $f(x)$  can be obtained using machine learning methods and is presented in the following section.

## 4.2 Machine learning for defect sizing

Recently, machine learning (ML) has revolutionized different fields of research, especially, image and signal processing [127], and, therefore, it has become of particular interest to the NDT and SHM communities [128–130]. ML methods are often considered as promising tools for completing challenging tasks such as automatic classification and regression as they are capable of finding an approximate solution for the problems where analytical solving is not obvious or even impossible.

### 4.2.1 Supervised learning approach

In general, ML can be divided into two categories: supervised learning and unsupervised learning [131]. The supervised ML consists in determining relationships in the input data that allow producing effectively the output data. The unsupervised learning, in contrast, lies in determining the inherent structure of the data without using explicitly-provided labels.

ML methods are data-driven. Therefore, the performance of these methods is heavily dependent on the choice of data representation, i.e., data features [132]. For this reason, many efforts are concentrated on the data preprocessing and transformation, so that the data representation can support effective ML. These procedures, often called feature engineering, are essential but labor-intensive. They allow taking advantage of human ingenuity and prior knowledge about the studied physical process.

In this work, the supervised ML is used to build an inversion model that is capable of determining a defect size from GWI results. Within this framework, the input and output data are simultaneously given to the ML algorithm, and the model is obtained by minimizing the error between actual predictions and reference values. The GWI results are considered as input parameters and the reference structural defect sizes as output parameters, respectively. Obviously, a model's performance depends on the choice of the ML algorithm. Many supervised ML algorithms are available, and each one has its strengths and weaknesses. Unfortunately, there is no a single guideline for selecting a supervised ML algorithm that would demonstrate the best performance. Therefore, a user has to follow the *No free lunch in search and optimization* [133] theorem in order to select the most convenient approach for the specific problem.

Once the ML algorithm is chosen, the collection of inputs and outputs can be used to build an inversion model. This preliminary and potentially computationally expensive phase is known as the training phase. However, once the model is trained, the ML algorithm enables a real-time prediction of forthcoming inputs and, therefore, fits perfectly into the SHM paradigm.

### 4.2.2 Defect sizing using Deep Learning

Nowadays, deep learning (DL) is of great interest in many fields. This is a subfield of ML that uses multi-layered artificial neural networks (ANNs) for completing challenging tasks such as image processing, object detection, speech recognition, language translation and many others [127]. Its recent success can be largely attributed to the strong emphasis on modeling multiple levels of abstractions with the depth of the DL model: from low-level features to higher-order representations using multiple, and usually non-linear, transformations. Convolution Neural Network [134] is one of the many possible DL architectures that have been proven particularly effective for image analysis, and, therefore, has been selected for GWI result processing.

### 4.2.2.1 Introduction to Convolution Neural Network

Convolution neural network (CNN) is a major breakthrough in the field of deep learning. Numerous practical machine learning tasks, such as image classification, object recognition, control-policy learning for autonomous ground and aerial vehicles [135, 136] or the board game Go are successfully solved using CNNs. The spectacular success of CNNs is not limited to image processing; they also perform well in natural language processing and speech analysis. However, standard, and arguably the most popular, application of these networks is for image processing.

Biological studies of visual cortex inspired the origination of CNNs [137]. The former has small regions of neural cells that are sensitive to specific patterns in the visual field. Hubel and Wiesel [138] demonstrated that some individual neural cells in the brain respond only to edges of specific orientation. Some neurons are activated when exposed to vertical edges, and some respond on horizontal or vertical edges. Together they are organized in columnar architecture that is capable of delivering visual perception. The idea of visual cortex imitation, i.e., of having specialized components in the system that are searching for specific patterns in the visual field, is the one that is basically implemented in computer vision and is the basis behind CNNs.

This type of ANNs searches for patterns in images, determines relevant features for the current problem and consequently adapts persecutors. CNNs are typically composed of multiple aggregated layers, each computes convolution transforms, applies non-linear activations and pooling operators as it goes deep [139, 140]. Aggregated layers are sequentially stacked and connected to fully connected layers, as schematically demonstrated in Figure 4.3.

A set of convolution operators, also called kernels, forms a convolution layer. For a given position, a kernel outputs a high value if the convolution feature is present in that position, otherwise the output is low. More precisely, the kernel's output can be computed as follows:

$$h_{i,j} = \sum_{k=1}^m \sum_{l=1}^m w_{k,l} x_{i+k-1,j+l-1} \quad (4.2)$$

where  $h$  is a convolution output,  $w$  is a convolution kernel of the width and height  $m$ , and  $x$  is a convolution layer input. Convolution operations can be considered as image transformations that result in different effects, such as extracting edges, blurring, sharpening, denoising etc. The main purpose of convolution kernels is to capture spatially dependent information, i.e. features, in the input. It is worth noting that a convolution layer typically may consist of dozens and even hundreds of kernels.

Convolution operators are followed by the application of an activation function. In general, non-linear activation functions are used as they allow generalizing and adapting a model to the complex data. Perhaps, the most prominent and effective activation function for CNNs is a Leaky Rectified Linear Unit (l-ReLU) [141]. It is computed as follows:

$$f(x) = \begin{cases} x, & \text{if } x > 0 \\ \alpha x, & \text{if } x < 0, \end{cases} \quad (4.3)$$

where  $f(x)$  denotes l-ReLU,  $x$  is input and  $\alpha$  is a constant with typical values:  $\alpha \in [0,1]$ . This activation function is biologically plausible [142] and allows overcoming efficiently the vanishing gradient problem [143]. The output of an activation function is called an activation map. By analogy with visual cortex, high values of the activation map correspond to the locations where a particular feature is present.

The last operator of an aggregated convolution layer is a pooling, i.e. subsampling, operator [144]. It is mainly used to decrease the variance and reduce computational complexity of the activation map. There are two different pooling mechanisms that are used in practice: max-

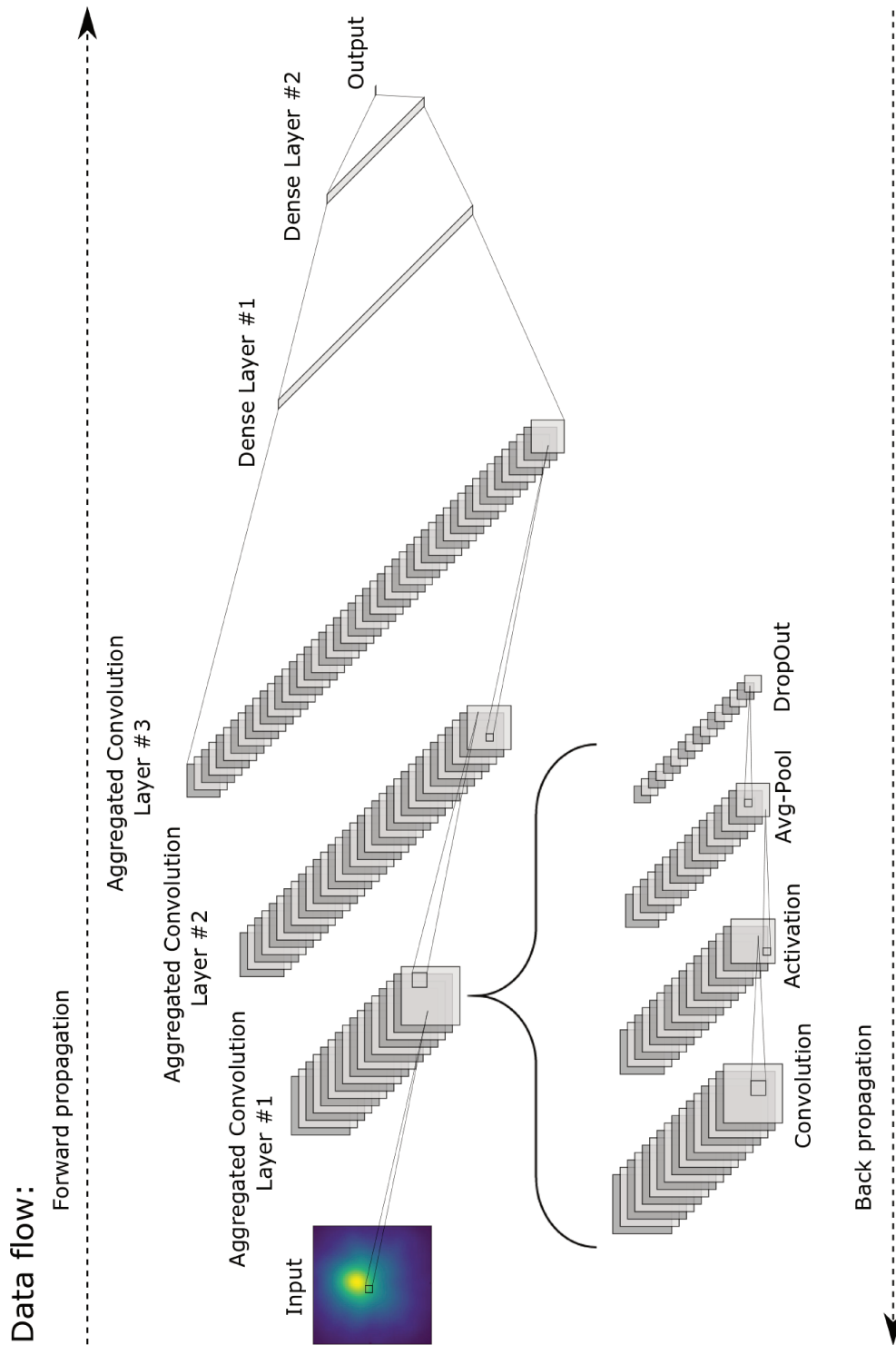


Figure 4.3 – Schematic representation of CNN architecture.

pooling and average-pooling. In this work, the average pooling is used as it allows extracting smooth features, whereas the max-pooling is rather oriented towards extreme features such as edges. The average-pooling operator can be expressed as follows:

$$p_{i,j} = \text{avg}(x_{i+k-1,j+l-1}), \forall 1 \leq k \leq m, \text{ and } 1 \leq l \leq m \quad (4.4)$$

where  $p_{i,j}$  is output of the average-pooling operator,  $x$  is input and  $m$  denotes pooling kernel width and height.

Aggregated convolution layers (note that each consists of convolution, activation and pooling operators) are connected to fully-connected layers. The term “fully-connected” implies that each neuron in the previous layer is connected to every neuron in the next layer. Therefore, high-level features of the input image learned by previous convolutional and pooling layers can be combined so that the network can build the global representation of the entire image [145]. Neurons in these layers are activated if a number of various convolution features are present, and together they produce different activation patterns based on the image content.

Adding several layers to the neural network allows learning features in hierarchical order, and their level of abstraction progressively grows with the depth of the model. In general, the performance of a neural network increases with the number of layers, but deeper models are more difficult to train and require a larger amount of data.

If the network is differentiable, the network training, i.e., kernel tuning, can be performed using the back propagation algorithm [144]. The overall training process of the neural network may be summarized as follows:

1. Initialize all the kernels and network parameters with random values.
2. Apply a forward propagation step for a batch of training images.
3. Compute an error metric using the network output and reference values.
4. Apply a back propagation algorithm to evaluate gradients of the error with respect to all weights in the network.
5. Use a gradient descent method to update kernels with values that minimize the output error.

The back propagation method allows adjusting kernels proportionally to their contribution to the total output error. The network architecture remains fixed during the training process - only the kernels’ values, neurons’ weight in fully connected layers and connection weights are updated. It is worth noting that CNNs can be used for regression and classification tasks as well as stand-alone feature extractors. Further details on CNNs operation, layer functions and effects can be found in many related works including the following: [144, 146].

#### 4.2.2.2 Database generation

In general, data-driven methods, and CNN in particular, require a large amount of data to construct an accurate model. Indeed, an experimental database is desired because it is fully representative and reproduces operational noise, which is inherent to the GW-based SHM process. However, the generation cost of the experimental database is prohibitive as a large number of samples are required. Therefore, a SFE simulation method [116, 120] is used in this work to generate a dataset of GWI samples.

The GWI configuration is the same as in the previous section: an aluminum plate  $600 \times 600 \times 3 \text{ mm}$  equipped with eight PZT transducers  $18 \text{ mm}$  in diameter. Each simulated sample

contains a transverse hole of varying size and position. Holes are distributed within the circle of  $100\text{ mm}$  in radius with the origin at the center of the plate. Damage radii vary from  $2.5\text{ mm}$  to  $7.5\text{ mm}$  and comply with random uniform distribution. Excitation functions are two-cycle Hanning modulated tone bursts centered at  $25$ ,  $35$  and  $45\text{ kHz}$ . In total,  $917$  SFEM simulations are run to generate a dataset of GWs signals, and Excitelet algorithm is then applied to produce a GWI database.

Each image in a GWI dataset is normalized and then cropped in order to preserve only the inner circle area, as shown in Figure 4.4. Afterwards, the dataset is randomly shuffled and split into two parts: training and testing sub-sets. The first one contains  $779$  images and the second one consists of  $139$  images. As the name suggests, the first sub-set is used for training a CNN model, whereas the second one is used alongside for testing CNN on the unseen samples in order to evaluate its accuracy. It is worth noting that images in a training sub-set are arranged in randomly shuffled batches, each contains  $32$  GWI samples due to computational reasons. In total,  $1000$  training epochs are run during the training phase and the performing model is selected among the proposed candidates. From now on, GWI samples are denoted as inputs and reference defect radii as outputs or target values, respectively.

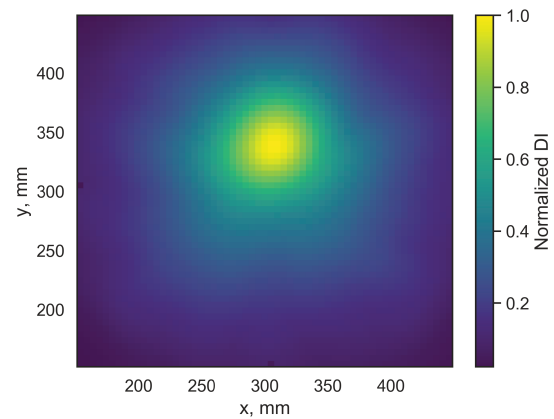


Figure 4.4 – GWI example.

#### 4.2.2.3 Inversion of simulation results

In this work, CNN's architecture has been manually tuned and regularized to achieve the best performance and to find a balance between overfitting and underfitting. It is worth noting that automatic search and reasoning for the best ANN architecture is currently under research by many entities [147, 148], but, for now, the common practice in model parameterization is to rely on human expertise.

Thereby, the CNN is constructed as follows. It consists of three aggregated convolution layers, each contains  $16$ ,  $32$  and  $64$  ( $3 \times 3$ ) convolution kernels that slide over the image with the stride  $1$ . The activation function is l-ReLU with  $\alpha = 0.3$  and the average-polling kernels are of the size ( $2 \times 2$ ). Aggregated convolution layers are connected to two sequential fully connected layers that allow combining all the learned patterns. The first fully connected layer contains  $128$  neurons and the second one -  $64$ . The CNN architecture is schematically shown in Figure 4.3.

Here, the CNN is used to build a defect size inversion model from the non-linear regression perspective. Therefore, the root mean square (RMS) metric is used to evaluate a model's accuracy during training and testing phases. Neuron weights are updated using Adaptive Moment Estimation (ADAM) optimizer [149]. It is more advanced in comparison with conventional optimization methods such as a stochastic gradient descent, an adaptive gradient algorithm and root mean square propagation [150]. ADAM implements per-parameter learning rates. More specifically, this algorithm computes an exponential moving average of an error gradient instead of a gradient itself and a squared error gradient to scale the learning rates.

Transverse hole sizing results are presented in Figure 4.5, where the blue dashed line denotes

	25, kHz	35, kHz	45, kHz	25, 35 and 45, kHz
MAE, mm	0.27	0.32	0.32	<b>0.24</b>
STD, mm	<b>0.23</b>	0.28	0.3	<b>0.23</b>
R2 score	<b>0.94</b>	0.91	0.89	<b>0.94</b>
Max ASE, mm	<b>1.11</b>	1.67	1.65	1.24

Table 4.1 – Performances of inversion models.

reference values, red dots represent inversion results of simulated GWI samples, and green triangles represent experimental transverse hole inversion results. Accuracy metrics such as mean absolute error (MAE), standard deviation (STD), maximum absolute sizing error (max-ASE) and R2-score are evaluated in order to estimate the performance of the CNN. The first two metrics were presented in Section 3.4.3, max-ASE is straightforward from the term, and R-squared (R2 score) describes the fraction by which the variance of ASEs is less than the variance of reference defect radii, where the best possible value of R2 score is one.

It is worth noting that the testing sub-set contains GWI samples computed for different defect sizes at various locations, therefore, performance metrics evaluated on the testing dataset can be generalized and considered as fully representative for the current inversion model.

Defect sizing results are presented in Figure 4.5. For all the three excitation frequencies, CNN demonstrates relatively good performance in determining radii of defects from simulated GWI results. The performance metrics are summarized in the Table 4.1.

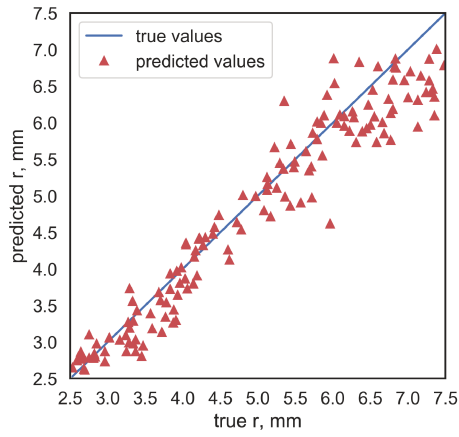
At 25 kHz, inversion MAE is equal to 0.27 mm, which is 2.7% of median defect size. Corresponding STD of defect radii prediction errors is equal to 0.23 mm, but uncertainty increases with the defect size, as shown in Figure 4.5a. It can be explained by the fact that as these frequency DI values vary much more for small defects than for large ones, as demonstrated in Figure 4.1a. For small defects, the energy scattered pattern varies to a greater extent than for large defects and, consequently, the inversion model is more precise. The R2 score, i.e. the coefficient of determination, is 0.94 and the maximum ASE equals 1.1 mm.

Inversion results at 35 kHz are shown in Figure 4.5b. It can be observed that the accuracy of predictions is degraded a little due to smaller variation of DI values, but still remains satisfactory. The MAE and STD of defect radii estimations are equal to 0.32 mm and 0.3 mm, respectively. The coefficient of determination equals 0.91 and the maximum ASE is 1.67 mm.

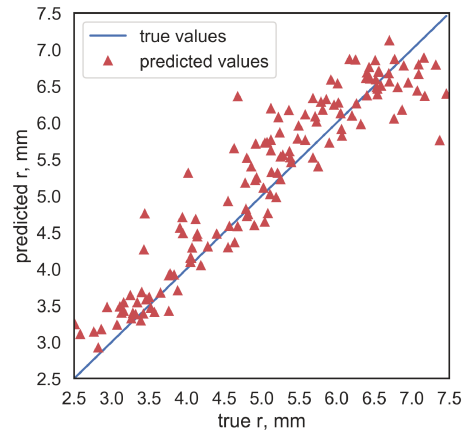
In general, the increase in excitation frequency leads to the decrease in the accuracy of inversion results. For example, at 45 kHz, the STD increased to 0.3 mm, R2 score decreased to 0.89 mm, as shown in Figure 4.5c. It is worth noting that MAE remains the same at 35 kHz, and the maximum ASE even decreased to 1.65 mm, but the model as a whole is less certain in predictions.

Defect imaging is not limited to the use of a single frequency. The proposed inversion model on the basis of CNN can also process simultaneously multi-frequency GWI results. For this reason, GWI samples corresponding to the same defect size and location but computed at different frequencies are combined into the GWI tensor of the following shape ( $n_x \times n_y \times n_f$ ), and GWI results are normalized with respect to the largest DI values in the tensor<sup>1</sup>. Corresponding inversion results are presented in Figure 4.5d. It can be observed that, in general, prediction accuracy increased but not that much. The MAE is equal to 0.24 mm while the model's uncertainty equals 0.23 mm. It is worth noting that the coefficient of determination is 0.94 (the same as at 25

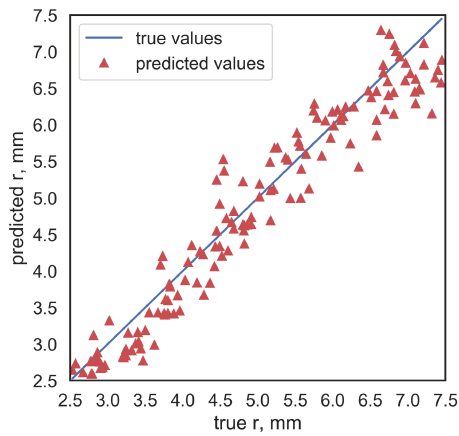
<sup>1</sup>It is worth noting that multi-frequency defect sizing requires a minor modification of CNN architecture in order to enable processing of imaging tensors. The network itself has also to be trained with consideration of multi-frequency data.



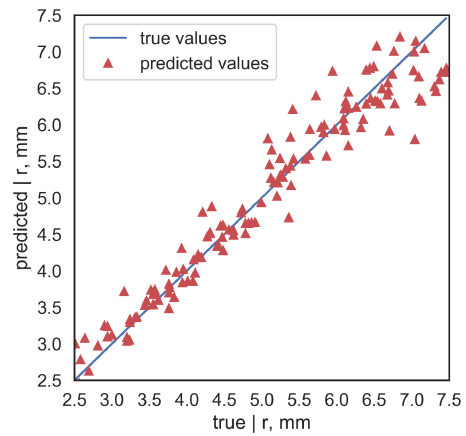
(a) Defect sizing at 25 kHz.



(b) Defect sizing at 35 kHz.



(c) Defect sizing at 45 kHz.



(d) Defect sizing using multi-frequency GWI results.

Figure 4.5 – Performances of CNN inversion models using simulated GWI results.

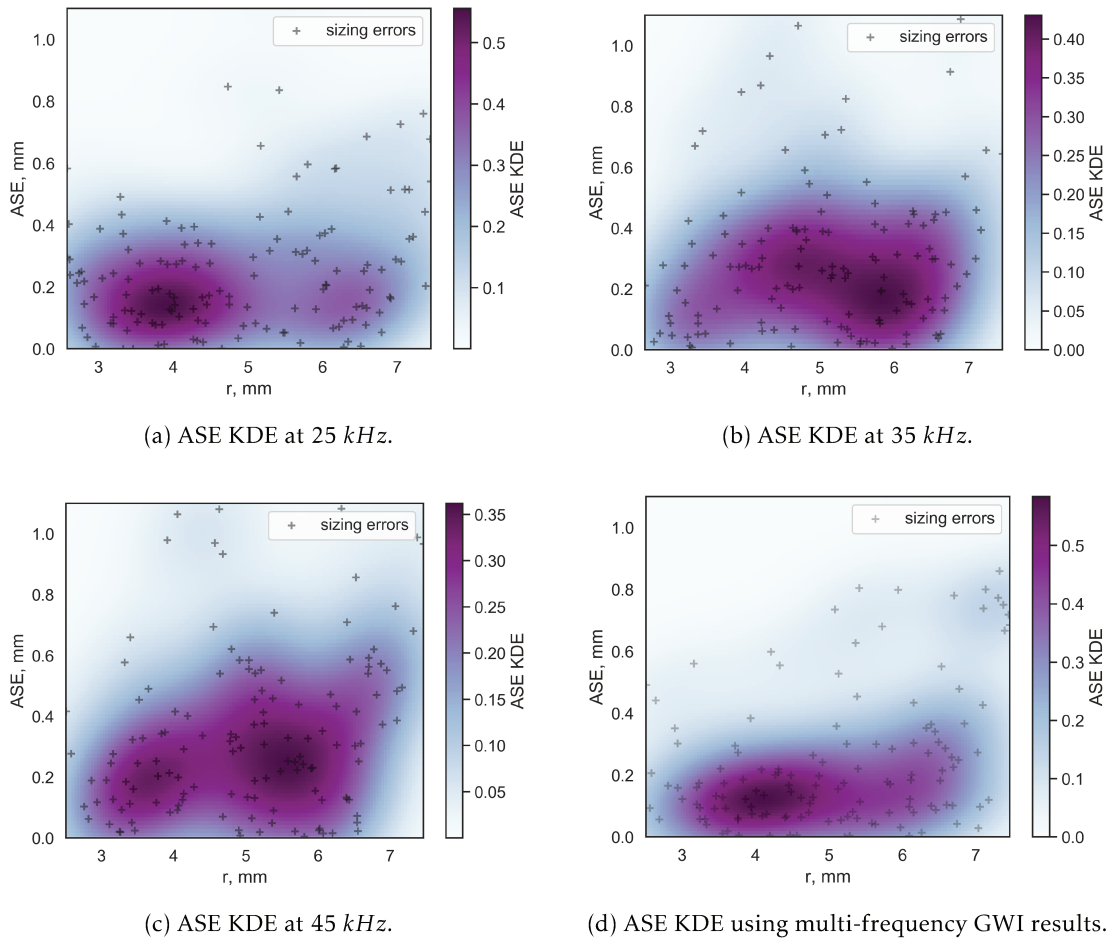


Figure 4.6 – Performances of CNN inversion models using simulated GWI results.

kHz), and the max-ASE is equal to 1.24 mm.

As previously mentioned in Section 3.4, KDE is used to evaluate the underlying probability density function of the data. Figure 4.6 presents bivariate KDE of ASEs versus transverse hole radii. If a maximum tolerable sizing error (max-TSE) is defined, then the probability of having a sizing error larger than max-TSE can be evaluated by integrating a corresponding part of the underlying KDE. For example, consider max-TSE that is equal to 0.25 mm, then for all the defects imaged at 25 kHz, 35 kHz, 45 kHz and multi-frequency the  $P(ASE > 0.25, mm)$  approximately equals 49%, 52%, 54% and 39%, respectively. It can be observed that in all cases ASE distributions are not homogeneous and depend heavily on the size of a defect. Suppose that a user is intended to determine the probability of ASE larger than max-TSE for two groups of defects: the first group comprises holes from 5 mm to 10 mm and the second one consists of defects from 7.5 mm to 15 mm in diameter.

For the first group of defects, probabilities  $P(ASE > 0.25, mm | \emptyset \in [5, 10], mm)$  are equal to 20%, 18%, 17%, 12% for 25 kHz, 35 kHz, 45 kHz and multi-frequency imaging. Similarly, for the second group of defects, corresponding probabilities are equal to 28%, 33%, 35%, 26%,

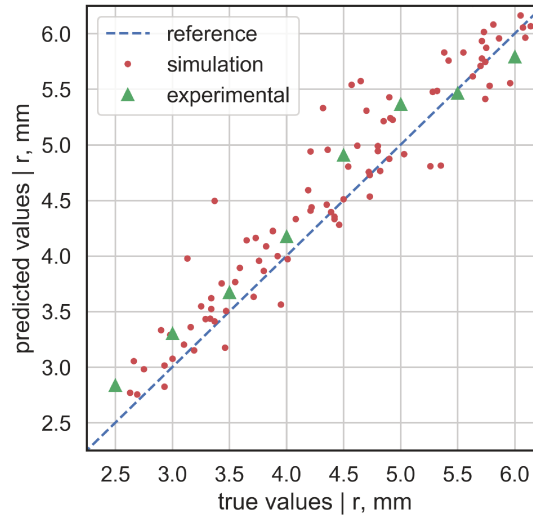


Figure 4.7 – Inversion of experimental GWI results at 45 kHz.

respectively. It can be deduced that multi-frequency imaging provides the best overall inversion result. However, among single-frequency imaging modes, the first group of defects is better resolved at 45 kHz, while the second one - at 25 kHz. Such inversion results can be related to the wavelength of the  $A_0$  guided mode that is used for imaging. At 25 kHz the corresponding wavelength is superior to the one at 45 kHz, so that the  $A_0$  mode is more sensitive to large defects.

#### 4.2.2.4 Inversion of experimental results

The same GWI configuration has been implemented experimentally in order to validate the inversion model. Transverse holes have been drilled at ( $X : 250, Y : 280, mm$ ) taking into consideration that the database does not contain corresponding simulated GWI samples. Holes radii vary from 1.5 mm to 6 mm with increment of 0.5 mm.

Defect radius inversion results are better at 25 kHz, but their accuracy does not vary with frequency as much as localization accuracy. As stated in Section 3.4.3, at 25 kHz, mean absolute localization errors and uncertainty are much higher than at 45 kHz and 60 kHz. Corresponding KDE of localization errors is considerably extended, and it leads to the high probability of inaccurate localization.

Therefore, 45 kHz excitation frequency has been selected as optimal to balance accurate defect localization and size inversion, and to construct a complete GWs-based SHM pipeline that includes defect detection, localization and sizing.

Inversion results of experimental GWI samples are presented in Figure 4.7. GWI results were only normalized, meaning that no filtering or preprocessing have been applied - they are used as such. Defect size inversion results are plotted against their reference values and overall CNN predictions from other defect locations. It can be seen that radii predictions of experimental defects are accurately estimated by the model and their spread remains in the limits of the model's uncertainty.

It is worth mentioning that submillimeter defect sizing accuracy for both simulated and experimental GWI results is achieved using images computed with spatial step of 5 mm, where

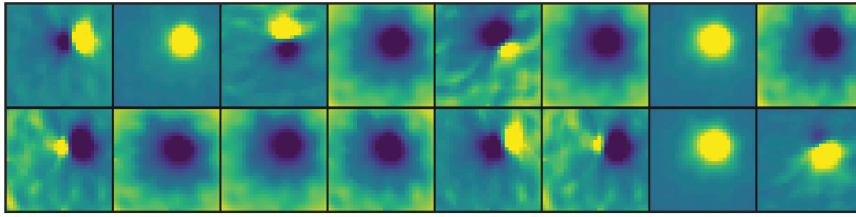


Figure 4.8 – Activation map of first aggregated convolution layer.

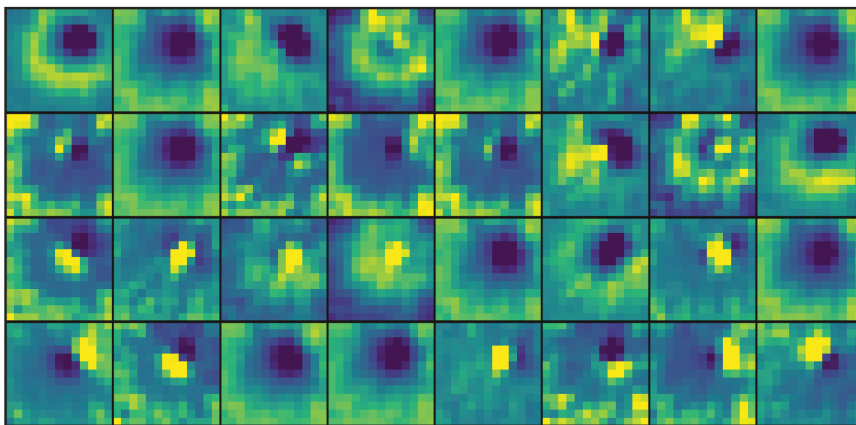


Figure 4.9 – Activation map of second aggregated convolution layer.

the wavelength of the  $A_0$  mode at 45 kHz is of about 25 mm. One of the driving factors of such precision is that the CNN is capable of perceiving not only single DI values but their mutual spatial distribution.

#### 4.2.2.5 Inversion model interpretation

Despite the encouraging performance of CNNs, there is a little insight into internal operations of these complex models. Without clear understanding of how the learning process goes and how kernels respond to different inputs, the development of better models is somewhat limited and can be even reduced to a trial-and-error approach. Therefore, several approaches for understanding and visualizing CNNs have been developed [151, 152], but the most part of them concerns classification problems.

Perhaps, the most straightforward visualization technique, which can be applied to regression problems, is to observe activation maps of the network during the forward pass. This technique allows revealing muted activation maps that correspond to dead kernels. The latter can be generally interpreted as a consequence of high learning rates. In this case, the network is no longer capable of adjusting kernel weights with respect to the loss gradient so that the learning process starts stagnating quickly after several epochs and never reaches the minimum of the loss.

Activation maps of the first aggregated convolution layer are presented in Figure 4.8. It can be observed that the first layer is arguably retains almost all the information present in the initial

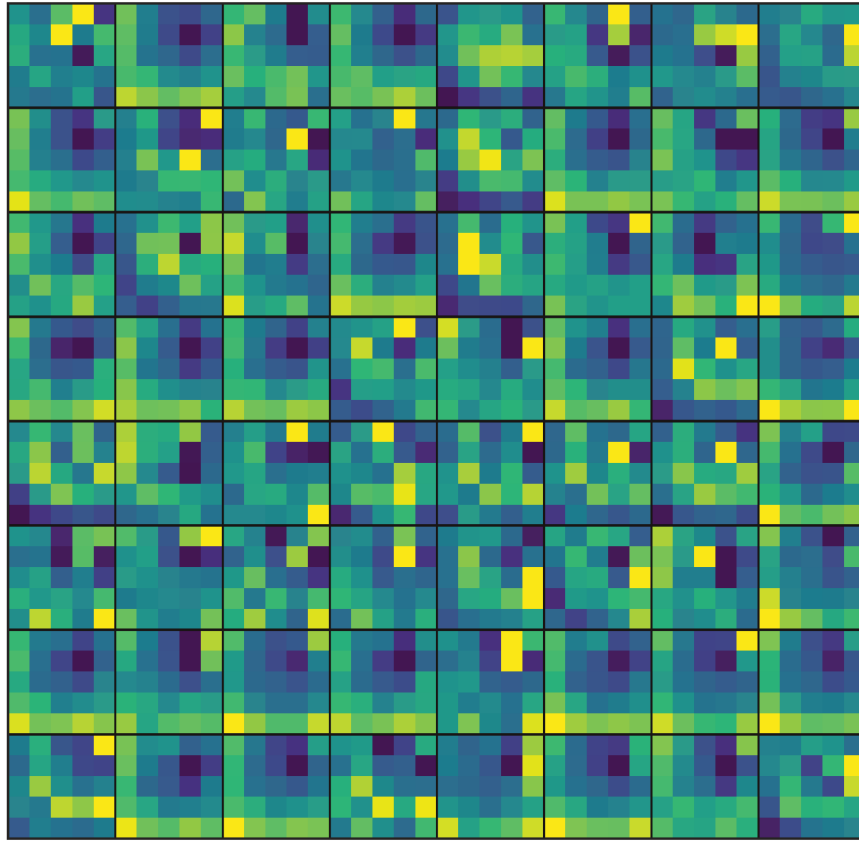


Figure 4.10 – Activation map of third aggregated convolution layer.

image. However, convolution filters are trying to split it by searching for circular patterns: some kernels pay more attention to a flawed region, while others process defect-free regions.

As the network depth increases, the activation maps become increasingly abstract and less visually interpretable, see Figure 4.9 where the activation maps of the second convolution layer are presented. Corresponding kernels start encoding local higher-level concepts such as summits, lune-shape and circular profiles, as shown in Figure 4.9. Unfortunately, the third aggregated convolution layer, shown in Figure 4.10, does not contain interpretable activation maps because such a high presentation carries increasingly less information about the visual content of the image, and increasingly more transformed information related to the size of the defect. Corresponding activation maps are shown in Figure 4.10.

Such a visualization procedure allows getting a small insight into the model so that the network architecture and hyper-parameters selection can be optimized better.

### 4.3 Chapter summary

This chapter presents an approach for the defects' size evaluation using GWI results. GWI is a robust and effective method for GWs signals processing that allows computing images representing the integrity of the structure. Defect detection and localization are straightforward from the analysis of these images, but defect sizing is a more complex problem. There are two main difficulties associated with this problem. First, the spatial intensity distribution of these images for the defects of different sizes that are located at the same position varies in non-linear manner. Second, the spatial intensity distribution depends on the location for defects of the same size. Therefore, a data-driven approach is proposed for defect sizing as it allows determining an approximate solution for complex problems, including the above mentioned one.

The proposed approach is based on the use of a convolution neural network. Among different data-driven approaches, this one is particularly interesting as it allows capturing both local and global spatial relations between the pixels of the image. The flexibility of the model and the degree of abstraction of learned patterns are controlled by the depth and width of the model, whereas the balance between overfitting and underfitting is kept by the regularization.

As the name suggests, any data-driven method, including this one, requires a large amount of data to build a well performing model. The SFE method and Excitelet algorithm are used for generating an extensive database of GWI samples. This dataset is created for a specific GWI configuration but represents defects of different sizes at various locations. Each GWI sample is normalized in order to unify simulated and experimental results that are used for validation. It is worth noting that the simulated dataset does not contain a GWI sample corresponding to the experiment.

The developed defect sizing model is validated on both unseen simulated and experimental GWI results and demonstrates a relatively good performance. The proposed approach allows completing the GW-based SHM system pipeline so that the defect detection, localization and characterization are possible. However, baseline-demanding GWI methods are vulnerable to the environmental influence and operational conditions. For example, GWs propagation and transducers' dynamics can be affected by temperature variations so that the baseline subtraction from the current state leads to the appearance of imaging artifacts. The next chapter presents methods for environmental effects compensation in order to increase the robustness of a GW-based SHM system.



# Robustness of GWs-based SHM

## Outline of the current chapter

<b>5.1 Effects of temperature variations on GWI</b>	<b>98</b>
5.1.1 Temperature effect on GWs propagation . . . . .	98
5.1.2 Defect detection under temperature variations . . . . .	99
5.1.2.1 Database generation . . . . .	101
5.1.2.2 Damage detection model . . . . .	101
<b>5.2 Methods for temperature effect compensation</b>	<b>105</b>
5.2.1 Conventional approach for baseline correction . . . . .	105
5.2.1.1 Optimal Baseline Selection . . . . .	105
5.2.1.2 Baseline Signal Stretch . . . . .	105
5.2.2 Dynamic Time Warping for baseline correction . . . . .	106
5.2.3 Defect imaging results under varying temperature . . . . .	109
<b>5.3 Chapter summary</b>	<b>118</b>

With a number of benefits, GWI is standing out among other methods for GWs-based SHM systems as an efficient technique for defect detection, localization and sizing. As previously stated, GWI methods rely on physical properties of GWs propagation and interaction with defects in order to compute an image representing the integrity of a structure.

In this work, baseline GWI methods are used as they allow discriminating the defect response better. These methods are efficient under stationary operational conditions but vulnerable to environmental effects. The primary source of GWs propagation disturbance is the temperature variation: a small temperature difference between baseline and current measurements is sufficient to deteriorate GWI results and other GW based SHM approaches.

This chapter reports on the effects of temperature on GWs propagation and GWI. A robust classification model is proposed for damage detection in the monitored structure even if GWI results are deteriorated. Then, strategies for temperature difference compensation are presented. Finally, GWI is performed under varying temperatures for both simulated and experimental cases.

## 5.1 Effects of temperature variations on GWI

### 5.1.1 Temperature effect on Guided Waves propagation

Despite of being effective under stationary operational conditions, baseline GWI techniques may be less efficient in real-world applications because all the baseline methods are adversely affected by environmental effects [153, 154]. In general, this is due to GWs signals modifications induced by temperature and humidity variations, ambient noise, accumulated stress etc [42]. These environmental effects change local and/or global elastic parameters of constitutive materials, and, consequently, modify transducer's dynamics and GWs propagation characteristics [155]. Since the temperature is the most significant effect that can highly distort GWs signals, further discussion is oriented towards the influence of this environmental phenomenon [156].

The primary effect of temperature variation on GWs signals is a time shift, whereas the secondary one consists in the distortion of waveforms. Croxford et al. [157] demonstrated that under the assumption of a single propagating guided mode the time shift between two signals measured at different temperatures can be expressed as follows:

$$\delta t = \frac{d}{v_{ph}} \left( \alpha - \frac{\gamma}{v_{ph}} \right) \delta T, \quad (5.1)$$

where  $\delta T$  denotes a temperature change,  $v_{ph}$  is the phase velocity,  $\gamma$  is the coefficient of change in the phase velocity with temperature,  $\alpha$  is the coefficient of thermal expansion of the material,  $d$  denotes the propagation distance and  $\delta t$  is the time shift induced by temperature variation.

In the simplest form, where GWs signals can be represented by time-delayed Hanning-modulated wavepackets, the difference between two signals measured at different temperatures can be expressed as follows:

$$|u(t, T) - u(t, T + \delta T)| = U_0 (\sin(\omega(t + \delta t)) - \sin(\omega t)), \quad (5.2)$$

where  $U_0$  denotes initial amplitude,  $\omega$  is angular frequency and  $t$  is time. For the small values of time shift a maximum difference amplitude can, therefore, be approximated as follows [42]:

$$|u(t, T) - u(t, T + \delta T)|_{max} \approx 2\pi f U_0 \delta t = 2\pi \frac{d}{\lambda} U_0 (\alpha - \gamma) \delta T, \quad (5.3)$$

where  $\lambda$  denotes the wavelength of the guided mode.

It can be observed that the level of temperature-induced residue in a difference signal is directly proportional to the propagation distance and inversely proportional to the wavelength of the guided mode. Therefore, in the low frequency range, where only two fundamental modes  $A_0$  and  $S_0$  are excited, it might be more advantageous to maximize the  $S_0/A_0$  ratio in order to resist this thermal effects. The  $A_0$  mode has smaller wavelengths than  $S_0$ , therefore, GWs signal will be less affected by temperature variations in comparison with the case where  $S_0$  mode is dominant.

For the sake of demonstration, GWs signals recorded in a CFRP plate at 1°C and 20°C are shown in Figure 5.1. It can be observed that phase mismatch increases with the time of observation, i.e. with the propagating distance of GWs, while the amplitude variations remain approximately constant. Although both signals are recorded when the structure is defect-free, the difference signal demonstrates some type of residual artificial waveforms.

Several practical approaches have been developed in order to limit and even reduce these effects, but, unfortunately, they cannot be entirely suppressed. For example, the adhesive for bonding transducers and transducers themselves can be carefully selected to minimize the

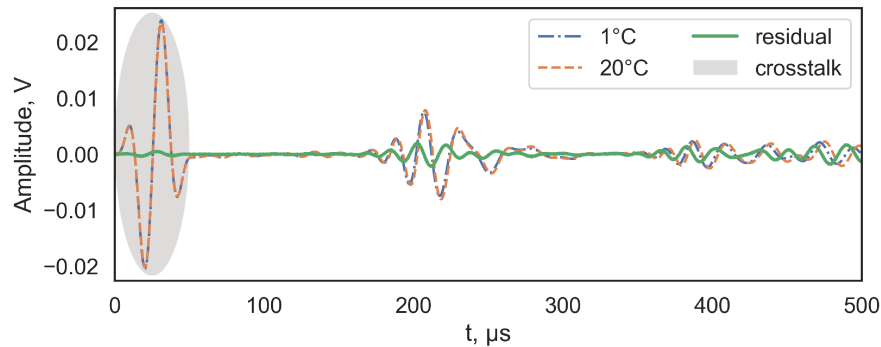


Figure 5.1 – Temperature-induced effect on GWs propagation in CFRP plate.

influence of temperature variations, but properties of the constitutive material of the structure, i.e. stiffness, density etc., cannot be manipulated. In general, elastic moduli decrease with the temperature while the elastic attenuation increases. Therefore, GWs phase and group velocities as well as amplitude decrease with the temperature and vice versa. It is worth noting that for composite materials including CFRP, GFRP and HCSS the temperature effects can be directionally dependent due to anisotropy of these structures so that advanced signal preprocessing tools might be required in order to develop a robust GWs-based SHM system.

### 5.1.2 Defect detection under temperature variations

As mentioned above, the performance of a GWs-based SHM system can be decreased due to thermal variation as it can introduce temperature-induced waveforms into residual signals. The significance of such temperature-induced waveforms increases with the temperature difference and can result in false alarms of a GWs-based SHM system regardless the state of the structure. In case of structural damage, a defect's response can be obscured by temperature-induced waveforms so that the residual signals become less interpretable. Consequently, defect imaging quality may degrade as these waveforms adversely interfere in GWI computations.

For example, experimental GWI results computed for an aluminum plate  $600\text{ mm} \times 600\text{ mm} \times 3\text{ mm}$  in dimension with different temperature between damaged and pristine states are presented in Figure 5.2. The plate is instrumented with six PZT transducers, each  $20\text{ mm}$  in diameter and  $0.5\text{ mm}$  thick, and the structural damage is represented by transverse hole  $10\text{ mm}$  in diameter. It can be observed that the imaging quality degrades with the temperature difference in comparison with the reference image. For small temperature differences, the image is noisy but still interpretable, however, as the difference increases the defect is increasingly concealed. It can be observed that when the temperature difference reaches  $10^\circ\text{C}$ , the defect is no longer detectable.

Such consequences are highly undesirable as the GWs-based SHM system may report a false negative (FN) alarm while the structure is actually damaged. This can intensify structural integrity deterioration and reduce useful residual service time. Similarly, the GWs-based SHM system can report false positive (FP) alarm, meaning that the structure has been evaluated as damaged while its integrity is still satisfactory. In this case, the structure will be withdrawn from the normal operation and significant effort might be wasted while searching for inexistent damage.

Therefore, a defect detection model capable of analyzing deteriorated GWI samples is

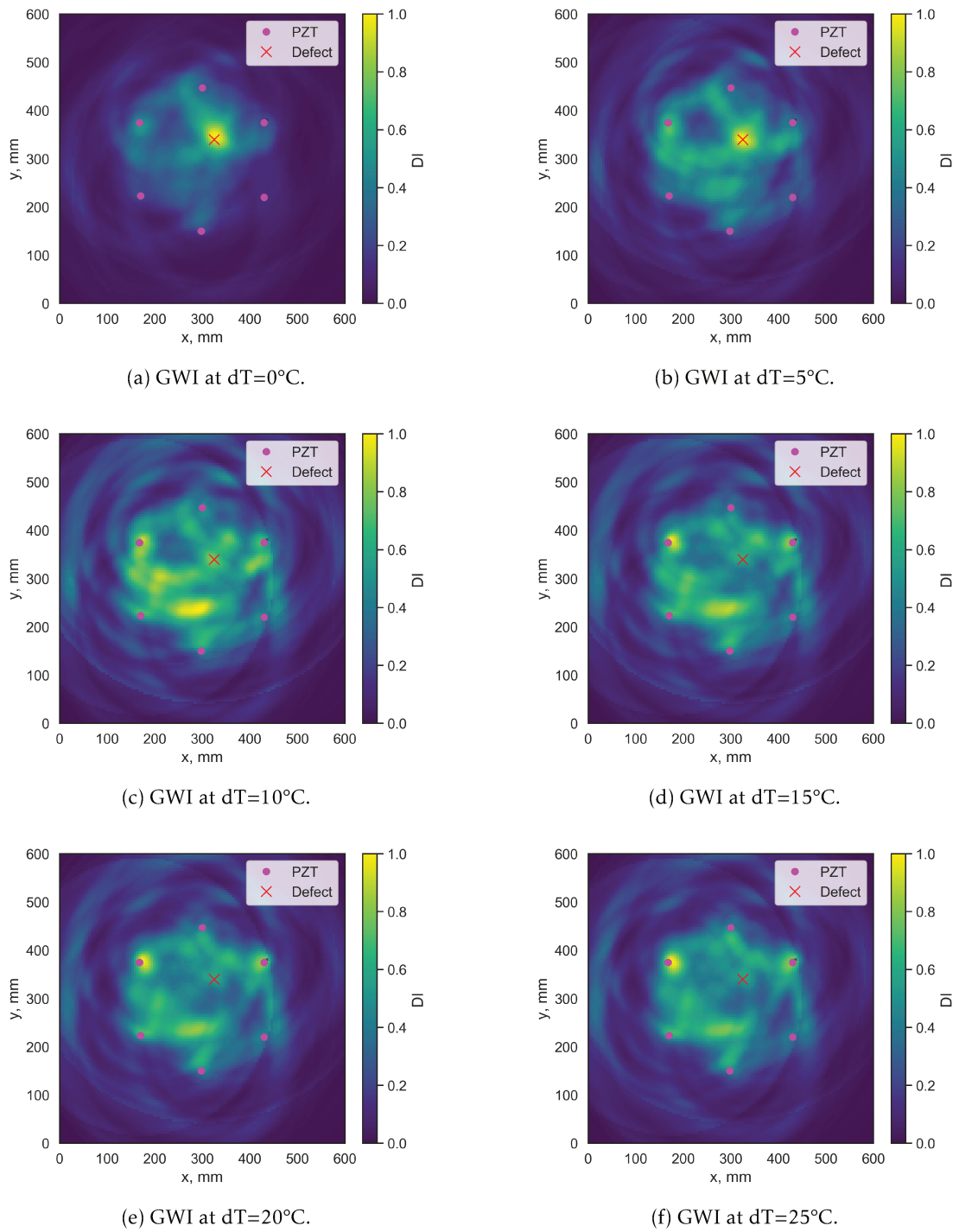


Figure 5.2 – Experimental transverse hole imaging at varying temperature in aluminum plate. Defect imaging is performed at 40 kHz by means of Excitelet algorithm using  $A_0$  mode.

required. Both FP and FN alarm rates have to be also evaluated in order to determine robustness of the corresponding GWs-based SHM system. Both FP and FN rates can be estimated by means of a discriminative classification model, which takes deteriorated GWI samples as input and determines whether this image represents a damaged structure or pristine. In general, such a type of classification tasks is solved using machine learning methods that require a significant database of representative samples.

### 5.1.2.1 Database generation

As previously mentioned, GWs signals modifications primarily concern the modal amplitude and changes of group and phase velocities. They are conditioned by various thermal effects, including material expansion and change in stiffness as well as change in piezoelectricity of transducers and their bounding [158]. It has been demonstrated that GWs signals can be numerically manipulated with respect to these phenomena in order to imitate variations in environmental effects and operational conditions [159]. This model implies degraded signals computation as follows:

$$S(t)_{degraded} = \alpha S(t(1 + \beta)) + \epsilon, \quad (5.4)$$

where  $\alpha$  represents amplitude variation,  $\beta$  GWs signal stretching due to thermal effects and  $\epsilon$  represents noise. On the basis of experimental results, all the three degradation parameters are supposed to vary in following ranges complying with random uniform distributions:  $\alpha \in [0.875, 1.125]$ ,  $\beta \in [-0.0005, 0.0005]$  and  $\epsilon = 0.05$ . They were selected to approximately cover a degradation range of GWI results that were observed experimentally while performing defect imaging under varying temperature with  $|dT_{max}| \approx 20^\circ\text{C}$ . More details on the GWs degradation model can be found in the following work [159].

Distorted GWs signals are then used to generate a database of corrupted GWI samples for training a classification model. This dataset contains two types of images: the first one represents GWI samples with false alarms while the structure remains pristine and the second type consists of noisy images that represent damaged structures. In total, 1000 GWI samples have been generated using a synthetic degradation model, where pristine and flawed structures are represented in equal proportion.

For example, several GWI samples of degraded GWI database are presented in Figure 5.3. The left column demonstrates images representing flawless data, while the right column presents GWI samples of damaged structures. It might be difficult to discern with the naked eye images corresponding to either class of data due to high deterioration rate, but this task can be efficiently performed using machine learning models.

### 5.1.2.2 Damage detection model

Among many other methods for image analysis, Convolutional Neural Networks (CNNs) are standing out as they are effective in learning both local and global patterns. General architecture and basic principles of operation of CNN have been presented in Section 4.2.2. Here, the architecture of CNN is similar to the one of the defect sizing model, see in Figure 4.3. However, the current model has several distinctions that mainly concern an activation function of the last layer of the network and a loss function that is used for training. Preceding layers of the network are responsible for learning spatial features and patterns in GWI samples that can be used for both tasks: regression and classification. Hence, the architecture of these layers remains unchanged.

The last layer of the current network is activated using the Softmax function [144]. It is often used in models that have to make a choice among a set of mutually exclusive options as it allows

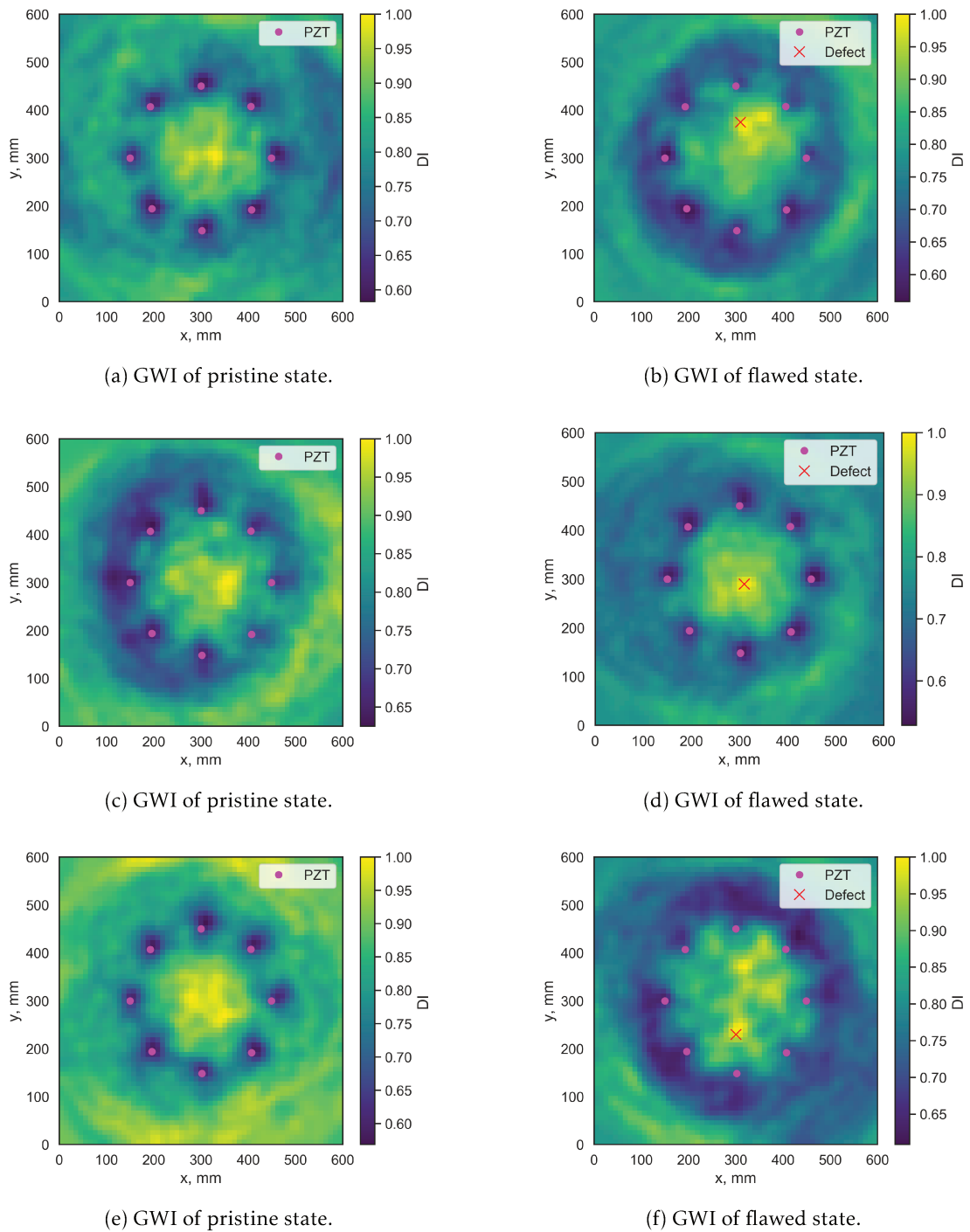


Figure 5.3 – Examples images in the corrupted GWI database. Left column represent degraded GWI results while the structures remain pristine, and the right column represents degraded GWI results of the flawed.

	Accuracy	Precision	Recall	AUC	Support <sup>a</sup>
Damaged	0.95	0.88	0.97	0.966	72
Pristine		0.97	0.87		78

Table 5.1 – Performances of inversion models.

transforming the output of the network into the probability distribution. It can be expressed as follows:

$$p_i = \frac{\exp x_i}{\sum_{j=0}^k \exp x_j}, i = 0, 1, 2...k, \quad (5.5)$$

where  $x_i$  is an evidence computed by CNN. The output probability distribution is of interest mainly for two reasons. First, for a given GWI sample it allows computing the probability of belonging to either class. Second, the categorical discrimination in the model can be trained using the cross-entropy loss function, which demonstrates better than standard MSE metric performance in classification tasks. For the binary classification problem, the model's performance can be evaluated as follows:

$$C = p_0 \log(1/q_0) + (1 - p_0) \log(1/(1 - q_0)), \quad (5.6)$$

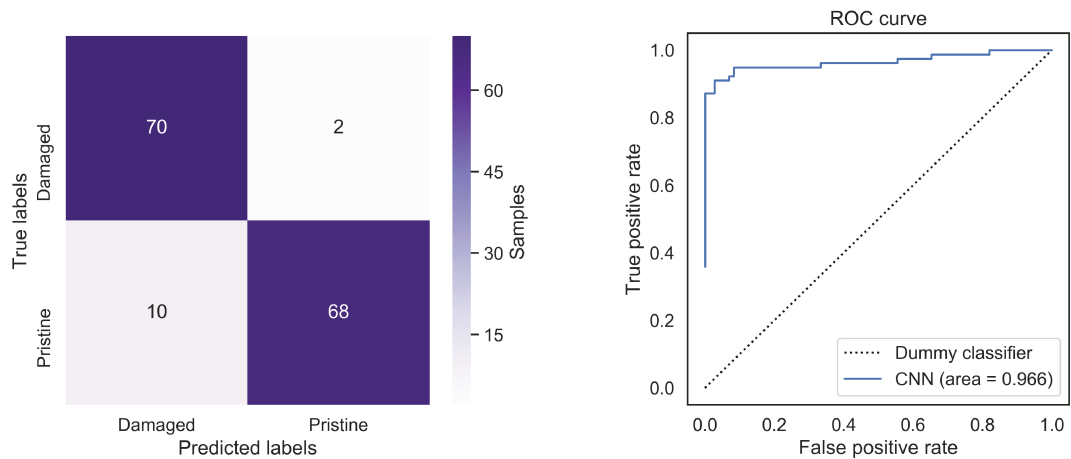
where  $p_0$  is the ground truth probability distribution and  $q_0$  is the current computed probability distribution.

Here, the CNN is used to build a classification model which determines whether forthcoming GWI samples represent a damaged structure. All the images in the database are normalized, then shuffled and split into two subsets that are used for training and testing. The training subset contains 850 images while the testing one consists of 150 GWI samples. As in the previous case, this network is trained using an ADAM optimizer that allows adaptive learning (its initial value is 0.03). Following the standard training routine presented in Section 4.2.2.1, the network is optimized using the back-propagation algorithm that allows adjusting kernels proportionally to their contribution to the total output error. In total, 500 training epochs were conducted in order to achieve an accurate classification model.

The classification model's performance can be consistently summarized using a confusion matrix, see Figure 5.4a, where true positives (TP), true negatives (TN), false positives (FP) and false negatives (FN) predictions are presented. These values allow determining other performance metrics such as *accuracy*, *precision*, *recall* and *F1-score* that are presented in Table 5.1. The accuracy score is straightforward and easy to understand as it represents a rate of correct classification. For the current model, this metric is equal to 0.95, where the perfect classifier would demonstrate accuracy equal to 1. Precision and recall are two other important model evaluation metrics. Precision refers to the percentage of correct predictions i.e.,  $(TP/(TP + FP))$ . For this model, it is equal to 0.88 and 0.97 while classifying pristine and damaged states, respectively. Recall represents the percentage of total relevant results correctly classified by the model  $(TP/(TP + FN))$ , and it is equal to 0.97 for pristine and 0.88 for damaged states of the structure.

Receiving Operator Characteristic (ROC) can provide more insight on the model's performance as it summarizes the performance of a classifier over all possible probability thresholds. It can be generated by plotting the TP rate against the FP rate as the probability threshold for assigning prediction to a certain class varies. The area under the ROC curve can be integrated

<sup>a</sup>Support denotes a number of samples per class in the testing dataset.



(a) Confusion matrix of classification model computed over the probability threshold equal to 0.5.

(b) ROC curve of the classification model.

Figure 5.4 – Performances of CNN inversion models using simulated GWI results.

and serves as a global quantitative metric of the classifier performance in the following manner: the larger the value, the better the classifier. In a more detail, a perfect classifier demonstrates the Area Under Curve (AUC) equal to 1. For  $AUC > 0.9$  the classifier can be considered to be very good and for  $0.8 < AUC < 0.9$  it is considered good, for  $0.7 < AUC < 0.8$  it is a decent one. For  $0.6 < AUC < 0.7$  values, a classifier is not well performing, and the random classifier provides AUC approximately equal to 0.5. The ROC curve of the current model is shown in Figure 5.4b, and the corresponding AUC is equal to 0.966.

It can be seen that, in general, this model is very accurate in determining whether GWI samples correspond to damaged structures, but it is less accurate in analyzing pristine states. This is due to imaging artifacts that sometimes have spatial intensity distributions similar to real defects DI values.

It is noteworthy that even if the damaged state of the structure can be correctly identified with high probability, it might be difficult to distinguish a correct number of present defects and their locations. The accurate defect size determination might also be barely possible. Therefore, temperature compensation techniques have to be applied in order to increase robustness of the GWs-based SHM system.

## 5.2 Methods for temperature effect compensation

As discussed above, all baseline methods are adversely affected by environmental effects and operational conditions. Though transducers' adhesives and transducers themselves can be carefully selected to reduce environmental effects, they cannot be completely suppressed so that the accurate residual signal computation is constrained to small temperature variations and low excitation frequencies, which is limiting for structural health monitoring in realistic operational environment. Therefore, several methods for GWs signal preprocessing have been developed, some of them are presented below.

### 5.2.1 Conventional approach for baseline correction

Recently, two temperature compensation strategies have been developed to increase robustness of GWs-based SHM systems and to promote them in real-life applications: Optimal Baseline Selection [160] and Baseline Signal Stretch [153]. These methods are often coupled together and applied sequentially. They rely on numeric optimization procedures in order to reduce GWs signal changes induced by temperature variations.

#### 5.2.1.1 Optimal Baseline Selection

As the name suggests, the Optimal Baseline Selection (OBS) [161] method consists in selecting the best possible baseline from the dictionary of baseline signals. This method assumes that the pristine structure of interest is first subjected to multiple environmental configurations that imitate variations of operational conditions including a temperature change.

Therefore, baseline measurements are collected with fine discretization over the set of environmental configurations, and the optimal baseline can be selected relying on the root-mean-square (RMS) metric. More specifically, signals in baselines' dictionary are subtracted in turn from the current measurement, and the RMS metric is computed to quantify the level of residue. Then, the optimal baseline can be determined as follows:

$$s(t)_{baseline}^{opt} = \underset{j}{\operatorname{argmin}} \left( \left[ \sum_{i=1}^N (s(t_i) - s(t_i)_{BL_1}^2) \dots \sum_{i=1}^N (s(t_i) - s(t_i)_{BL_j}^2) \right] \right), \quad (5.7)$$

where  $s(t)$  denotes current GWs measurements consisting of  $N$  timesteps,  $s(t_i)_{BL}$  is a dictionary of  $j$  baseline measurements and  $S(t)_{baseline}^{opt}$  is an optimal baseline.

Although this method allows selecting the best possible baseline from the dictionary, in reality, it is barely possible to collect baselines over the whole range of interest of temperature variations due to practical reasons especially for large structures.

#### 5.2.1.2 Baseline Signal Stretch

As stated above, it may be impossible to collect a baseline dataset that comprises all plausible environmental configurations. In practice, such a dataset is collected discreetly over the limited range of temperature variations of interest. Therefore, once the OBS method is applied, there is still a residual environmental effect to mitigate. In order to overcome this limitation and improve temperature compensation results, a Baseline Signal Stretch (BSS) technique has been proposed [153].

Consider a small temperature variation, the single mode GWs signal is then modified as follows:

$$u(t, T + \delta T) = \sum_{i=1}^N U_i s_i(t - t_i \beta(\delta T)), \quad (5.8)$$

with

$$\beta = 1 - \frac{v_{gr} k_{ph}}{v_{ph}^2} \delta T, \quad (5.9)$$

where  $\delta T$  is a temperature variation,  $U_i$  and  $s_i$  represent a modal amplitude and a corresponding waveform respectfully,  $t_i$  is arrival time, and  $\beta$  is a fractional change in arrival time of the wavepacket.

Therefore, the BSS method consists in stretching the time-axis of the baseline signal  $u(t, T_0)$  by the factor  $\hat{\beta}$  that satisfies the following relation:

$$\hat{u}(t, T_0, \hat{\beta}) = u(t/\hat{\beta}, T_0) = \sum_{i=1}^N U_i s_i(t/\hat{\beta} - t_i), \quad (5.10)$$

It can be deduced that if  $\hat{\beta}$  is equal to  $\beta$ , the stretched signal (5.10) will match the signal (5.8). It is worth noting that such time-axis stretching alters the frequency content of the GWs signals, therefore, it has to be resampled at a different sampling frequency.

In practice, this method is usually implemented in the frequency domain. The stretching parameter  $\hat{\beta}$  is typically determined from the joint optimization problem. The first sub-problem is to minimize the mean-square deviation between the measured signal and the baseline. More formally, it can be expressed as follows:

$$\hat{\beta}_{ms} = \operatorname{argmin} \left( \sum_{i=1}^N (u(t, T) - \hat{u}(t, T_0 \hat{\beta}))^2 \right) \quad (5.11)$$

The second sub-problem consists in the minimization of the maximum residual amplitude, which can be expressed as follows:

$$\hat{\beta}_{mr} = \operatorname{argmin} (\max(|u(t, T) - \hat{u}(t, T_0 \hat{\beta})|)) \quad (5.12)$$

It should be mentioned that this optimization problem can be solved iteratively using conventional optimizers such as ADAM (see Section 4.2.2.3). More information on the theoretical background and implementation details can be found in following work [153].

OBS and BSS methods are often coupled together in order to increase the robustness of the GWs-based SHM system. Both temperature compensation methods are intuitive and simple for implementing but they remain effective only for small temperature variations and short propagation distances. Therefore, baselines have to be collected over the temperature range of interest with high discrimination, which is not feasible for large engineering structures such as IFS.

## 5.2.2 Dynamic Time Warping for baseline correction

Stretch-based methods rely on the approximate physical model of temperature impact on the GWs signals. These methods are aimed at determining scalar stretching factors in order to realign the baseline with the current measurement. However, they are accurate only for

relatively small temperature variations due to the assumption of a small misalignment angle [153] made for deriving a factor of stretching. This assumption is no longer valid for significant temperature variations, high frequency measurements and large distances of GWs propagation, i.e. distances between transducers. It is worth noting that these limitations are fairly restrictive for implementing an efficient GWs-based SHM system. Therefore, Dynamic Time Warping (DTW) has been proposed [55] as a promising solution for overcoming these limitations. Unlike conventional stretching methods, it is not constrained by linear stretching approximations, does not require a supportive database of baseline measurements and reasonably flexible in signals' alignment.

The DTW was initially developed for speech recognition tasks, namely for discriminating two similar time series [162]. This algorithm measures some kind of distance between two temporal sequences that may vary in speed and amplitude. For instance, the same word pronounced by two different persons can be detected using DTW despite the pronunciation accent and the speech accelerations/deceleration. In the context of GWs signals under temperature variations, DTW can be used to overcome challenges inherent to stretch-based methods by determining an optimal mapping (that can be non-linear) between the samples of two temporal sequences [55].

Let us assume that  $X := [x_1, x_2, \dots, x_N]$  of length  $N \in \mathbb{N}$  and  $Y := [y_1, y_2, \dots, y_M]$  of length  $M \in \mathbb{N}$  represent two GW signals sampled at different temperatures. The objective of DTW consists in comparing these time series and determining the optimal warping path that maximizes the alignment of two signals. For the sake of understanding and visualization, the same GWs signals as in Section 5.1.1, i.e. measured at 1°C and 20°C are processed alongside the DTW algorithm explication; they are denoted as  $X$  and  $Y$ , respectively.

First, the 2D feature space  $F$  consisting of two signal's samples (i.e.  $x_n, y_m \in F$  for  $n \in [1 : N]$  and  $m \in [1 : M]$ ) is constructed. Then, the local cost matrix  $C_{loc}$  is constructed in order to compare features that belong to  $F$ . The  $C_{loc}$  matrix stores the cost of mapping single temporal sample  $n$  from the baseline signal  $X$  to each element  $m$  of the current signal  $Y$ . It can be expressed as follows:

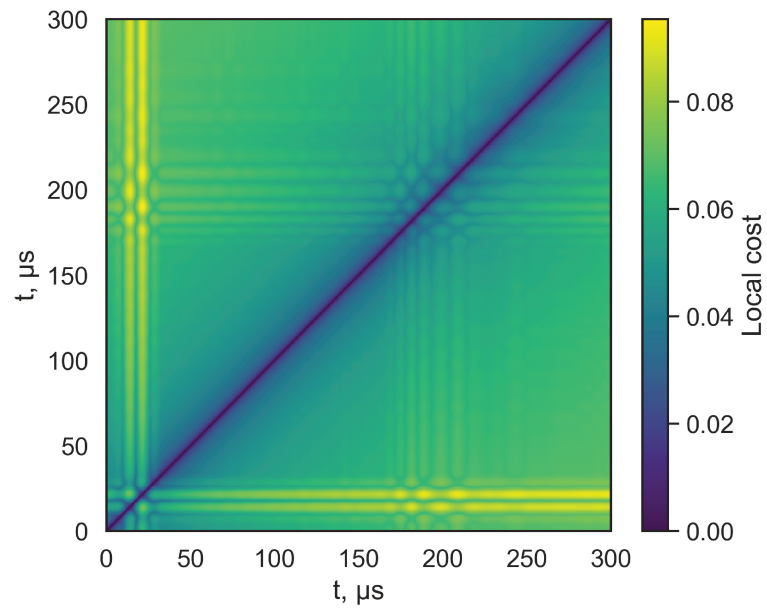
$$C_{loc_{n,m}} = d(x_n, y_m), \quad (5.13)$$

where the local cost is computed element-wise. As presented in literature, it can be obtained in multiple ways including  $L1$ ,  $L2$  norms and the similarity metric [55, 162]. However, in this work a novel metric is proposed. It imposes additional constraints on the signals compression/stretching in order to avoid GWs signals flattening and cropping (see Figure A.3 where these effects are shown). It can be expressed as follows:

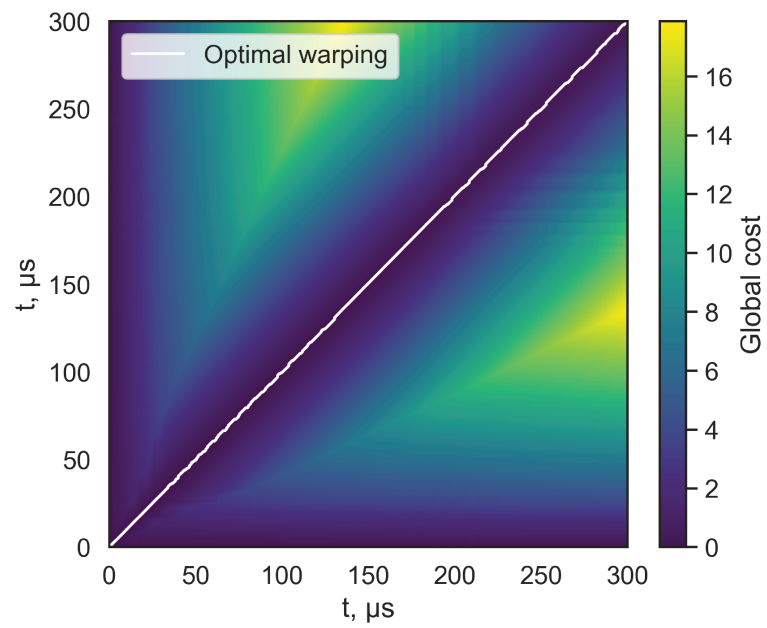
$$d(x_n, y_m) = |x_n - y_m| + \begin{cases} \frac{|n-m|}{\sum_{i=1}^N |x_i - y_i|} \log(|n-m|), & \text{if } |m-n| > 0 \\ 0, & \text{if } |m-n| = 0, \end{cases} \quad (5.14)$$

The local cost matrix for the current pair of GWs signals is shown in Figure 5.5a. It can be seen that the largest element-wise cost is around 200  $\mu s$  which corresponds to the time of arrival of  $A_0$  mode wavepacket. Such a high cost in this region is mainly due to the time shift that was manifested by Equation (5.1).

The next step consists in constructing the global cost matrix  $C_{glob}$  using values of the local cost matrix. Each element of the global cost matrix contains a total cost of signals' mapping across the local cost matrix, i.e. signal's warping paths. Note that total mapping costs for global cost matrix are performed respecting alignment monotonicity, unitary step size and boundary condition. The first two constraints ensure that the samples remain in the same order and that the next sample can be chosen from the adjacent temporal samples. In the context of GWs



(a) Local cost matrix.



(b) Global cost matrix.

Figure 5.5 – DTW local and global cost matrices computed for GWs signals measured in CFRP plate at 1°C and 20°C.

signals, the boundary condition is applicable only for the first elements  $(m_1; n_1) = (1; 1)$ , while for the last samples it can be relaxed, in other words, the final sample of the baseline signal  $X$  can be aligned with any sample of the current signal  $Y$ .

The computational complexity of such formulation for every warping path is exponential in  $N$ , and, therefore, it can be computationally prohibitive for long length GWs signals. For the sake of overcoming this limitation, Muller [163] proposed an iterative optimization strategy also known as dynamic programming. This method allows reducing computational complexity from  $O(N^N)$  to  $O(N^2)$ <sup>1</sup> so that  $C_{glob}$  can be determined more efficiently by removing suboptimal solutions. Therefore, the global cost matrix can be determined as follows:

$$C_{glob_{ij}} = C_{loc_{ij}} + \min_{n,m} (C_{glob_{i-n,j-m}}), \quad (5.15)$$

where

$$m := [0, 1], n := [0, 1] \mid i - n > 0, j - m > 0 \quad (5.16)$$

This algorithm computes recursively the elements of  $C_{glob}$  relying on the neighboring warping global costs. Once the global cost matrix is computed, the optimal warping path of two signals  $(X, Y)$  can be determined as follows:

$$DTW(X, Y) = \min(C_{glob}(X, Y)) \quad (5.17)$$

The back propagating algorithm is usually used for computing the optimal warping path. It starts at the minimum of the global cost measure that satisfies the boundary conditions and repetitively inspects each adjacent mapping in order to find the minimum global cost of signals' alignment.

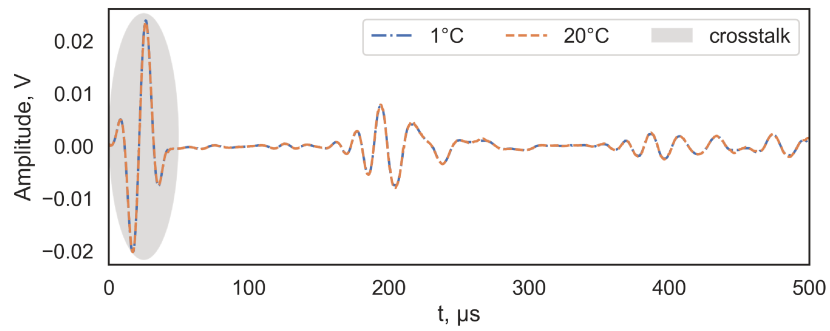
Figure 5.5b presents the global cost matrix for the studied signals as well as an optimal warping path. The latter is used to align two GWs signals of interest, see Figure 5.6a. It can be seen that thanks to DTW compensation the amplitude of the difference signal between two GWs measurements has significantly decreased in comparison with the original residue shown in Figure 5.1.

The DTW can be successfully applied to compensate temperature variations, namely to remove artificial wavepackets that appear due to the time shift and waveforms distortion in GWs signals. It is worth noting that in spite of the initial development of the DTW algorithm for the speech recognition tasks, its operational principle is similar to BSS. Perhaps, DTW should be considered as an advanced version of the former as it applies the same by means temporal shifting, stretching and compression manipulations. Obviously, these manipulations can be non-linear providing a significant alignment advantage in comparison with its competitor, which is constrained to linear modifications. However, the optimal warping path is derived relying only on mathematical principles and constraints ignoring the knowledge of GWs propagation.

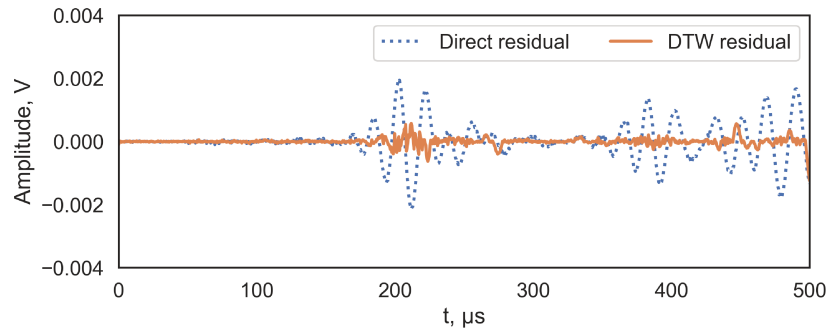
### 5.2.3 Defect imaging results under varying temperature

An experimental stand used in studies of temperature effects on GWs propagation is shown in Figure 5.7. It consists of a thermal chamber capable of generating a wide range of temperatures and the GWs acquisition system. Two structures are selected for this experiment, see Figure 5.7b. The first is an aluminum plate  $600 \text{ mm} \times 600 \text{ mm} \times 3 \text{ mm}$  in dimension. It is instrumented with six PZT transducers, each  $18 \text{ mm}$  in diameter and  $0.5 \text{ mm}$  thick. The second structure is a CFRP

<sup>1</sup>Computational complexity reduce from exponential to quadratic is a huge improvement, but quadratic complexity is still far from being optimal. Therefore, it is advised to use GWs signals containing less than  $2e^3$  samples.

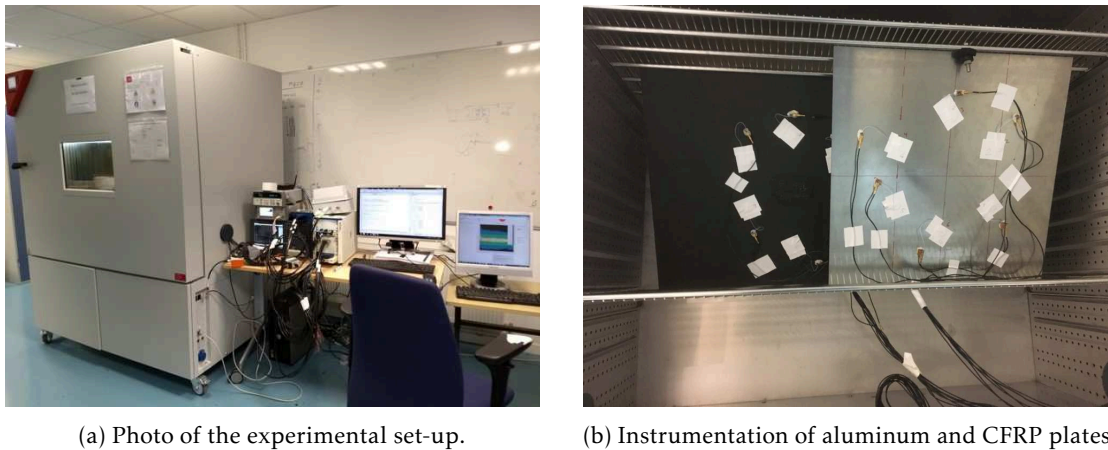


(a) Temperature-induced modifications correction in baseline signals by means of DTW.



(b) Comparison of direct and DTW corrected difference signals.

Figure 5.6 – DTW for temperature-induced GWs modification compensation in CFRP plate.



(a) Photo of the experimental set-up.

(b) Instrumentation of aluminum and CFRP plates.

Figure 5.7 – Experimental stand used in temperature effects studies.

plate  $1000\text{ mm} \times 600\text{ mm} \times 2.2\text{ mm}$  in dimension. It consists of eight orthotropic lamina, each  $0.275\text{ mm}$  thick. All the plies are oriented in  $0^\circ$  direction with respect to the fiber placement. This plate is instrumented with ten PZT transducers, each  $18\text{ mm}$  in diameter and  $0.5\text{ mm}$  thick.

The preliminary study of temperature compensation for GWI consists in simulated defect imaging under varying temperature in the CFRP plate. The defect is simulated by the mass attached to the surface of the plate. The pristine state of the structure is measured at  $20^\circ\text{C}$  while the damaged state at  $0^\circ\text{C}$ . Corresponding defect imaging results are presented in Figure 5.8.

The reference image, shown in Figure 5.8a, is computed when both pristine and damaged states were measured at  $20^\circ\text{C}$ . When the temperature difference occurs, the GWI result becomes noisy and the defect imaging resolution deteriorates in comparison with the reference image. In addition, imaging artifact right next to the defect location can be also observed. However, the application of the DTW algorithm allows decreasing the influence of the temperature on GWs propagation so that the residual signal computation becomes more accurate. Consequently, GWI quality is increased as the number and magnitude of imaging artifacts decreased, see Figure 5.8c. It is worth noting that simulated by an attached mass defect has a simple response: it scatters primary  $A_0$  mode and does not modify incident wavepackets. Therefore, baseline signals can be aligned with current measurements carrying simulated defect response more accurately than with measurements carrying a realistic damage response such as transverse hole that modifies GWs signals to greater extent.

The next study consists in determining operational limits of DTW for compensating temperature difference in aluminum and CFRP plates. For both plates structural damage is represented by drilled transverse holes  $10\text{ mm}$  in diameter. The same experimental stand, shown in Figure 5.7, is used for subjecting these plates to the wide temperature range  $T \subset [-40^\circ\text{C}, 85^\circ\text{C}]$  and for measuring propagating GWs. The excitation function is a two-cycle Hanning modulated tone burst centered at  $40\text{ kHz}$ .

Temperature induced GWs modification are compensated by DTW algorithm. Figure 5.9 provides more insight into the DTW results and demonstrates its effectiveness for compensating  $20^\circ\text{C}$  of temperature difference in the aluminum plate. The reference residual signal (denoted by blue dotted line) is plotted against direct residual signal (represented by orange solid line) and DTW corrected residual signal (shown by green solid line). The direct residual was obtained by subtracting the baseline from damaged state signal neglecting temperature-induced modifi-

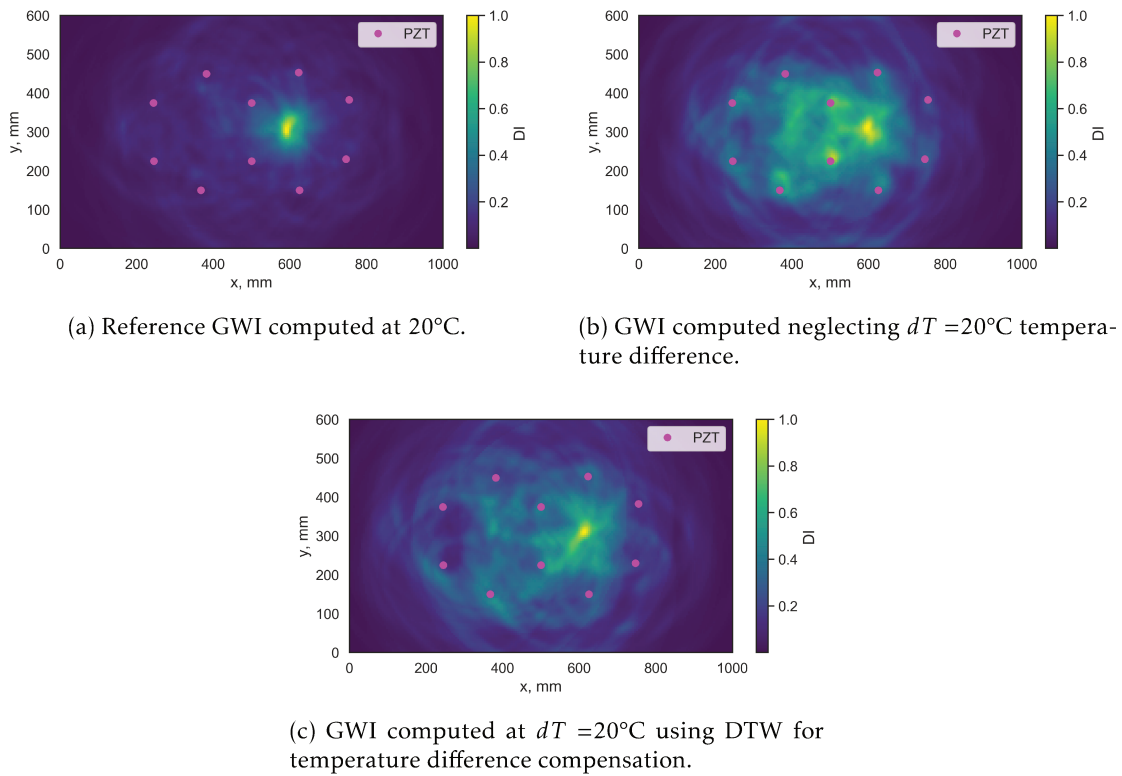


Figure 5.8 – Defect imaging results of an attached mass under temperature variation. The GWI is performed at  $40\text{kHz}$  by means of Excitelet algorithm using  $A_0$  mode.

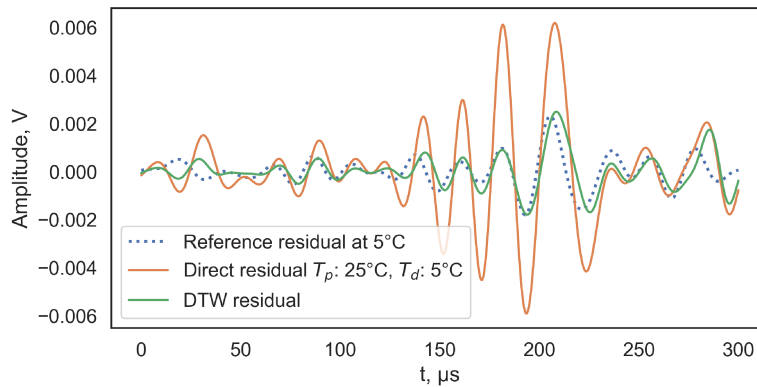


Figure 5.9 – Temperature difference compensation using DTW.

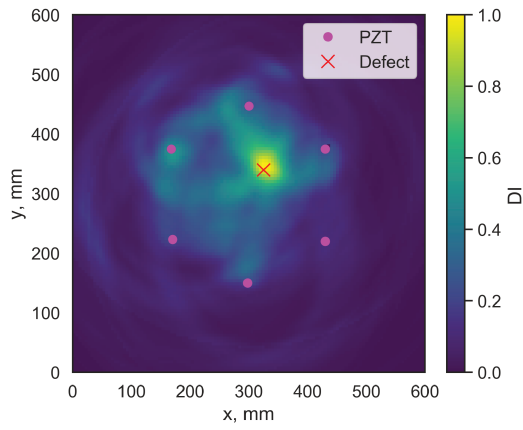
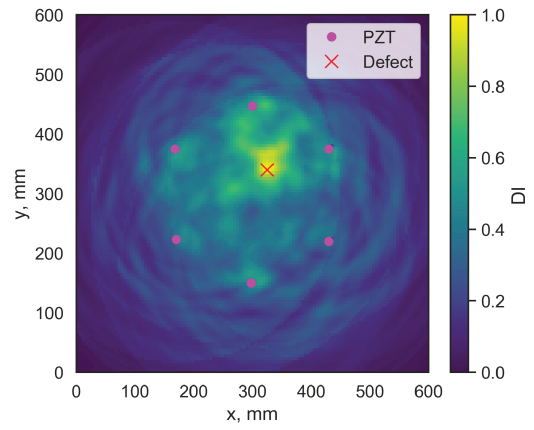
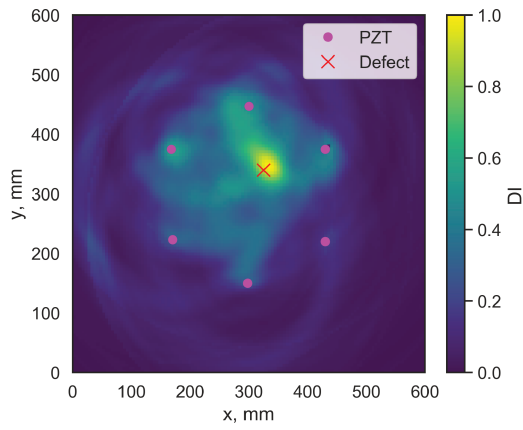
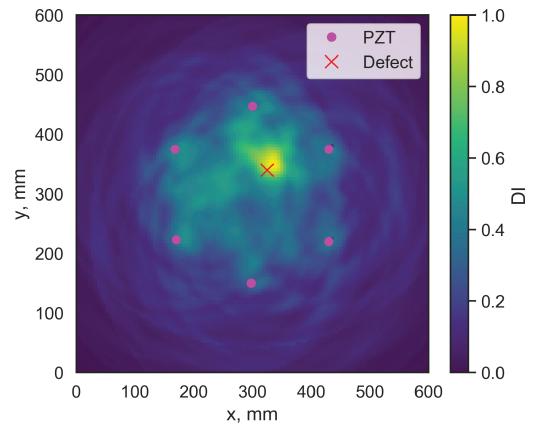
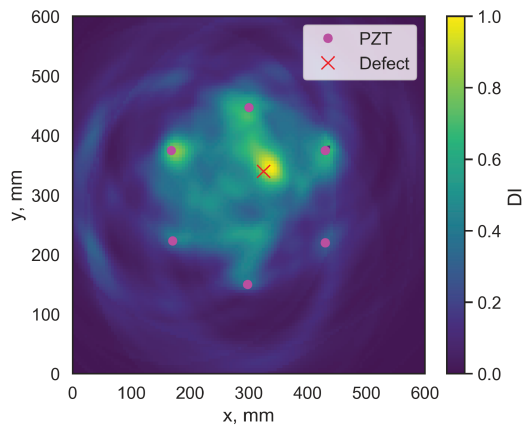
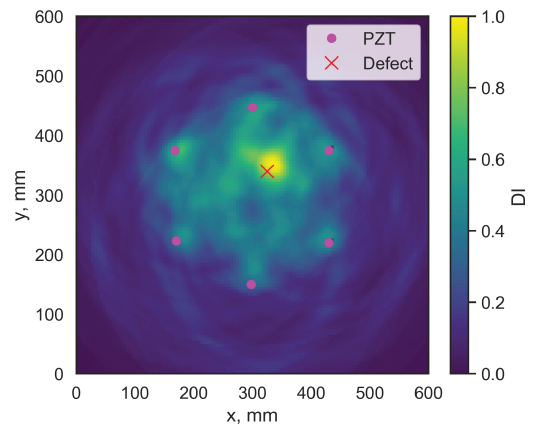
cations. It can be observed that temperature variation introduces additional waveform due to the GWs signals mismatch that can provide imaging artifacts. The application of DTW allows compensating efficiently but not completely temperature induced waveforms and, therefore, defect imaging quality can be increased.

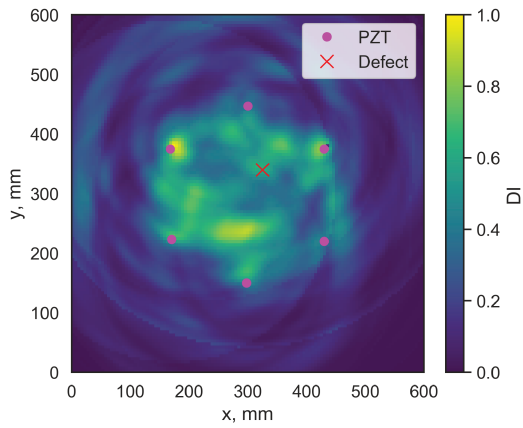
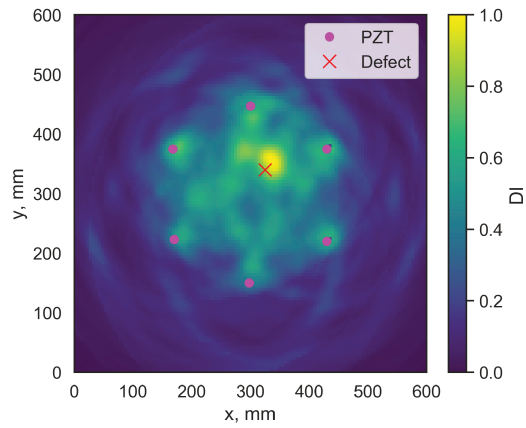
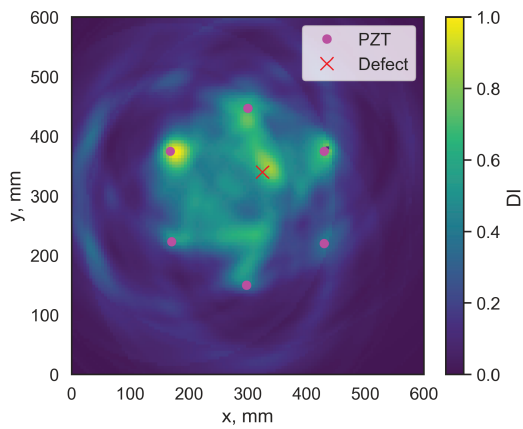
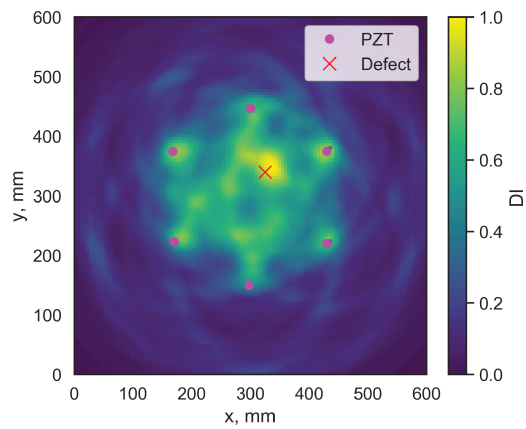
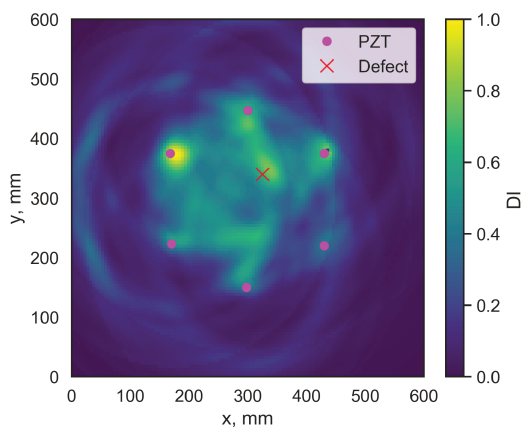
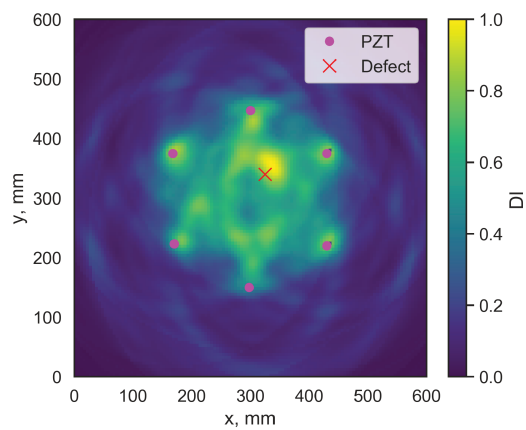
For the sake of comparison, GWI imaging is then performed using both direct and DTW corrected residual signals. Images are computed by means of Excitelet algorithm using  $A_0$  mode and are shown in Figure 5.10: the left column demonstrates GWI samples computed neglecting temperature differences while the right one presents GWI results obtained using DTW compensated signals. For both columns GWI samples are arranged in the temperature difference incrementing order.

It can be observed that for temperature difference from  $0^\circ\text{C}$  to  $5^\circ\text{C}$  the Excitelet algorithm is capable of accurate structural integrity image computation. For this temperature variation range, application of DTW is not necessary and can be even considered as adversarial because temperature induced perturbations are lesser than GWs signal modifications due to the defect. In this case, GWs phase velocity change is small so that the DTW algorithm rather obscures defect response in attempt to minimize GWs signals modifications likely coming from defect but not from GWs phase mismatch. Consequently, GWI results obtained by using DTW are more noisy than those that were computed neglecting such temperature difference.

However, for larger temperature differences, the primary source of GWs signals perturbation are thermal effects. In this case, DTW searches for the best possible alignment between the baseline and current measurements by minimizing thermal effects and not the defect response. Therefore, DTW residual contains less errors than the one obtained by direct subtraction, as shown in Figure 5.9. It can be observed that DTW is efficient for compensating temperature differences from  $10^\circ\text{C}$  to  $25^\circ\text{C}$ . Corresponding, GWI results computed neglecting the temperature difference provide false alarms and are not capable of correct defect detection and location. Application of DTW, in contrast, allows an accurate image computation but, for the given GWI configuration, effective temperature compensation range is limited to  $\delta T \approx 25^\circ\text{C}$ .

The following study consists in application of DTW algorithm for temperature-induced GWs modification compensation in CFRP plate. In spite of being efficient for aluminum plate, this method in the proposed configuration has not been confirmed yet effective for temperature difference compensation in the CFRP plate. Figures 5.11a and 5.11b provides a comparison between GWs signals collected at  $20^\circ\text{C}$  and those measured with the difference of  $5^\circ\text{C}$ . It can be observed that in CFRP plate GWs signals modification due to the transverse hole are

(a) GWI computed at  $dT = 0^\circ\text{C}$ .(b) GWI computed at  $dT = 0^\circ\text{C}$  using DTW.(c) GWI computed at  $dT = 5^\circ\text{C}$ .(d) GWI computed at  $dT = 5^\circ\text{C}$  using DTW.(e) GWI computed at  $dT = 10^\circ\text{C}$ .(f) GWI computed at  $dT = 10^\circ\text{C}$  using DTW.

(g) GWI computed at  $dT = 15^\circ\text{C}$ .(h) GWI computed at  $dT = 15^\circ\text{C}$  using DTW.(i) GWI computed at  $dT = 20^\circ\text{C}$ .(j) GWI computed at  $dT = 20^\circ\text{C}$  using DTW.(k) GWI computed at  $dT = 25^\circ\text{C}$ .(l) GWI computed at  $dT = 25^\circ\text{C}$  using DTW.

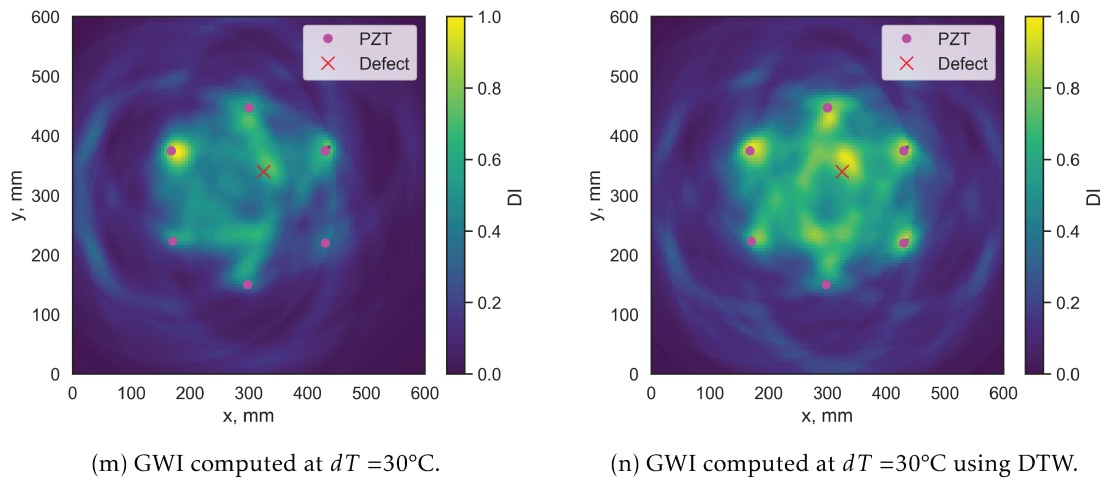
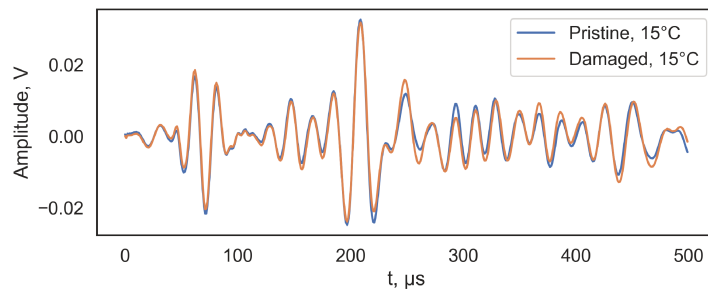
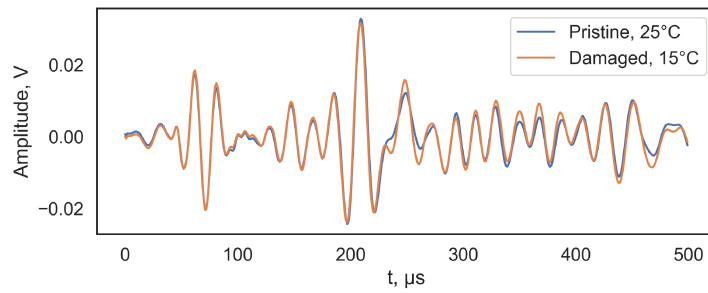
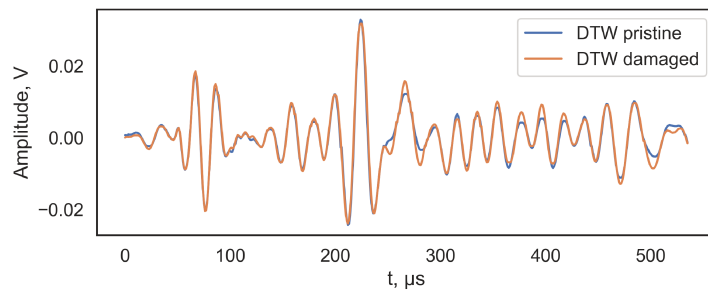
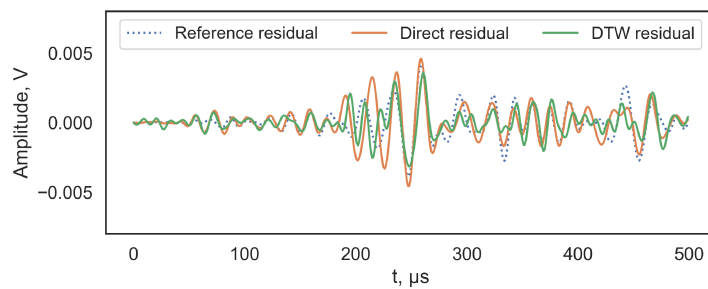


Figure 5.10 – Transverse hole imaging in aluminum plate under varying temperatures. GWI is performed at  $40\text{ kHz}$  by means of Excitelet algorithm using  $A_0$  mode. The hole is  $10\text{ mm}$  in diameter and is located at  $(X : 325, Y : 340, \text{mm})$ .

stronger than the temperature-induced variations. Therefore, aligning baseline and current GWs signals DTW is rather prone to compensate damage-induced perturbations so that the GWs residual signals are deteriorated, as shown in Figure 5.11c and 5.11d. Such a decrease in DTW performance is due to the absence of physical knowledge of defect response. Hence, future improvement of this method might comprise local and global costs matrices modification in order to introduce physical constraints of defect response that will allow to differentiate it from thermal effects. Furthermore, local cost matrix can be projected onto orthogonal basis for the sake of differentiating temperature-induced and defect-induced GWs modifications by means of PCA or kernel-PCA (if the kernel can be confirmed by physical meaning).



(a) GWs signals measured 15°C.

(b) GWs signals measured with  $dT = 10^\circ\text{C}$ .(c) GWs signals alignment using DTW to compensate  $dT = 10^\circ\text{C}$ .

(d) GWs residuals signal comparison.

Figure 5.11 – Temperature difference compensation in CFRP plate by means of DTW.

### 5.3 Chapter summary

This chapter reports on the studies conducted to estimate and increase the robustness of a GWs-based SHM system. It has been demonstrated that the baseline-demanding GWI methods, and Excitelet in particular, are vulnerable to temperature variations because GWs propagation as well as dynamics of transducers and their adhesion are affected by thermal effects. Namely, changes in modal amplitudes, group and phase velocities of GWs are the primary sources of disturbance. They lead to the appearance of temperature-induced waveforms in residual signals that can obscure defect's response. These waveforms can be mapped by GWI algorithms to the defect free locations introducing imaging artifacts that might result in false alarms of the GWs-based SHM system.

The first study of this chapter consisted in developing a classification model capable of analyzing corrupted GWI results in order to determine whether they represent damaged or pristine structure. This work has been conducted using the database of simulated GWI samples that were corrupted using a GWs signals deterioration model, which simulates temperature effects and operational noise. This model has been tuned in such a way that corrupted GWI samples would represent possible deteriorations due to operational conditions of aeronautic structures. A developed classifier demonstrates good performance: corresponding accuracy and AUC are equal to 0.95 and 0.966, respectively. However, in spite of a good defect detection accuracy the further analysis of a GWI sample might be difficult, namely defect localization might be confusing and defect's sizing might be impossible.

In order to overcome this limitation, existing temperature compensation approaches have been reviewed and adapted for GWI applications. More precisely, DTW algorithm is used to align two GWs signals measured at different temperature. This algorithm searches for the optimal warping path that allows minimizing the corresponding difference and the accurate GWs subtraction becomes possible. This method has been successfully applied for simulated defect imaging in CFRP plate while the temperature difference between pristine and damaged states is 19°C. DTW was also effectively applied to provide effective transverse hole imaging while the temperature difference can reach up to 25 °C. However, this algorithm in the proposed configuration was not effective for transverse hole imaging in CFRP plate under varying temperature. This is due to the complex defect response in anisotropic plate that is similar to the temperature-induced deteriorations so that the DTW algorithm compensated both types of modifications. This is preliminary work on adaptation of DTW algorithm for GWI applications to compensate thermal effects, therefore, more advances are required to achieve better performance.

This is the final chapter of the thesis, and it completes the pipeline of the GWs-based SHM system that allows efficient defect detection, localization and sizing in aeronautic structures. Conclusions and perspectives of this work are provided in the following.

# Conclusions

Different industries, and the aerospace in particular, use lightweight and high-performance materials, e.g. aluminum alloys and composites as well as their derivatives, such as HCSS, in order to reduce weight and to increase the reliability and profitability of engineering structures. However, in spite of excellent mechanical properties, defects, such as corrosion, plies fracture, delamination and debonding, might occur as these structures are often subjected to harsh environmental and operational conditions. These defects decrease structural integrity and, therefore, reduce remaining useful time or, even worse, might lead to structural failure.

The research topic of this work is aimed at developing a GWs-based SHM system for damage detection, localization, and characterization in plate-like structures made of aforementioned materials that could be eventually translated to complex composite structures, such as an aircraft nacelle. This work was conducted with respect to the imposed objectives and contains five chapters responding to research questions as follows.

The first chapter provided an introduction to the field of GWs based-SHM starting with motivation and basic concepts of structural integrity evaluation. It describes constitutive parts and an operational principle of a GWs-based SHM system and also provides a brief literature review highlighting advantages and challenges of such systems.

The second chapter presented general properties and principles of GWs actuation, propagation, defect interaction and sensing. Taking into account that GWs can be expressed in terms of the elastodynamic 3D Green's function, a SAFE modeling method coupled to a modal expansion method has been used to compute the 3D Green's functions in aluminum and monolithic composite plates. The homogenization model has been applied to replace a honeycomb layer with an equivalent orthotropic plate in order to extend a modeling framework to HCSS. This method provides correct modeling results only for low frequencies range but it is sufficient for targeted applications. These simulation tools are limited to ideal plate-like structures but, in reality, such structures are often equipped with rivets and other structural features that modify the elastodynamic 3D Green's function. For the sake of overcoming these limitations, a probabilistic data-driven approach has been developed. It is based on the use of probabilistic model and allows determining modal components of the 3D Green's function from the measured GWs wavefield. This method has been tested on an aluminum plate, CFRP plate and HCSS panel, and demonstrated a good agreement with modeling methods.

The third chapter presented GWI methodology and methods for GWs signals processing that are used for damage detection and localization in both isotropic and anisotropic structures. These methods rely on the knowledge of GWs propagation characteristics that can be determined using simulation or data-driven methods presented in the previous chapter. Both simulated and experimental defect imaging results are demonstrated in aluminum plates, CFRP plates and HCSS. Defect localization performance has been evaluated for several algorithms presented in literature DAS, MV and Excitelet algorithm by means of a statistical analysis of an extensive database of GWI specimens that was generated using the SHM module of CIVA software based

on Spectral Finite Element Modelling. Excitelet algorithm is the most accurate as it demonstrates both the lowest average localization error and the narrowest localization error probability distribution function. Taking into consideration that for large real-life structures pixel-wise image computation can be time-consuming, a novel approach for the sparse defect imaging was developed. It is implemented in the Bayesian framework, where the Gaussian process models the structural integrity image. Following the Bayesian optimization routine, a joint problem consisting in acquisition function maximization is formulated so that the forthcoming sampling points can be determined by maximizing the former. In addition, Excitelet's sensitivity to the damage size has been also demonstrated. While the defect presence and location are straightforward from image analysis, the defect sizing is not obvious due to non-linear dependencies in both location and size of the defect.

The fourth chapter presented an approach for the defect size evaluation using GWI results. It is based on the use of a convolution neural network that allows capturing both local and global spatial relations between pixels of the image. The flexibility of the model and the degree of abstraction of learned patterns is controlled and by architecture of the model, whereas the balance between overfitting and underfitting is reached by model regularization. This data-driven method requires a large amount of data, therefore, SHM module of CIVA software has been used again to generate an extensive dataset of GWI samples. This dataset is created for a specific GWI configuration but represents defects of different sizes at various locations. The developed defect sizing model has been validated on both unseen simulated and experimental GWI results and demonstrated a relatively good performance. The proposed approach allows completing the GW-based SHM system pipeline so that the defect detection, localization and characterization are possible.

Finally, chapter five presented studies conducted for the sake of increasing the robustnesses of a GWs-based SHM system. It has been demonstrated that baseline methods are adversely affected by environmental effects, where the primary effect is a temperature variation. The first study of this chapter consists in developing a defect detection model on the basis of CNN classifier that is capable of analyzing corrupted GWI samples in order to determine whether they represent a damaged or pristine structure. This work has been conducted using the database of simulated GWI samples that was adversely modified by means of GWs signals deterioration model. A proposed classifier demonstrates good performance with accuracy equal to 0.95. However, in spite of a good defect detection accuracy, defect localization and sizing are barely possible on the basis of deteriorated GWI results. To overcome this limitation, existing temperature compensation approaches have been reviewed and modified for current GWI applications. More precisely, DTW algorithm has been used to align GWs signals measured at different temperatures. This algorithm searches for the optimal warping path that minimizes temperature-induced difference so that the accurate GWs subtraction becomes possible. This method has been successfully applied for simulated defect imaging in CFRP plate while the temperature difference between pristine and damaged states is 19°C. DTW also demonstrated its efficiency for transverse hole imaging in aluminum plate under varying temperature up to  $\delta T \approx 25^\circ\text{C}$ . However, this algorithm in the proposed configuration has not yet been proven effective for transverse hole imaging in CFRP plate under varying temperature. This limitation might be due to a complex defect response in anisotropic plates. It is worth noting that this is a preliminary work on adaptation of DTW algorithm for GWI applications that started at the end of this thesis. Therefore, more studies are required to fully understand the physical phenomena involved in the unsuccessful application of DTW in CFRP plates and to achieve a better performance in thermal effect compensation.

This work concerns multiple research questions that were solved to a different extent in order to develop an efficient and reliable GWs-based SHM system for rapid integrity screening

---

in isotropic and anisotropic plate-like structures. However, as many other academic studies, this research work generates new challenges and perspectives that might advance the field of GWs-based SHM.



# Recommendation for future work

Despite the fact that this thesis has explored a wide range of research topics in the field of GWs-based SHM for composite structures, there are still several issues worthy of consideration for further advance. They can be formulated as follows:

- Transducers represent an important field where the progress is needed. As discussed earlier, the majority of reviewed works and this thesis in particular, are based on the use of PZT transducers. This is a mature and reliable technology for GWs signals excitation and sensing, but it is somewhat limiting for real-life aeronautical applications. The major limitation is not due to transducers themselves but rather due to the cabling necessary for connecting each of them to the SHM system. In light of this, FBG technology is standing out as a promising solution for replacing an entire PZT cell with a single optical fiber containing multiple FBG that can be integrated into the structure during the fabrication process. Such fibers can be used for GWs sensing and would allow the significant reduction of the number of PZT required for structure excitation. Minor modifications of GWI methodology are required to adapt FBG technology, but a significant effort has to be applied to develop supportive electronics that can be installed on the aircraft.
- The next proposal for future work consists in the improvement of simulation methods for the 3D Green's function computation in HCSS. As previously mentioned, the developed method provides accurate results only for the low frequencies range, where wavelengths are larger than a honeycomb cell size, and deviates rapidly when frequency increases. Therefore, further improvement can be focused on coupling the SAFE method with Bloch's function formulation to overcome limitations of HC homogenization model allowing accurate and rapid 3D Green's function computation while taking into consideration GWs-HC meso-scale interactions.
- The data-driven approach for the 3D Green's function determination can be also improved by developing a more robust spectral filtering technique capable of resolving complex modal trajectories that can come close and cross each other. This would allow extracting modal components of the 3D Green's function at high frequencies where multiple guided modes are present. For example, deep auto-encoding modes could be of great use for developing such filters as they allow efficient semantic segmentation of the data.
- GWI methods, and Excitelet algorithm in particular, can be improved to different extent by replacing a perfect reflector defect model with a more realistic one that would consider guided modes conversion, a directional pattern of GWs scattering and GWs energy trapping. Therefore, a theoretical signal can be computed more accurately, and this will allow the increase of imaging quality by reducing the number of artifacts and noise. In addition, multiple GWI configurations, including different types of plates, the number of transducers, excitation frequencies, the number and type of defects etc., have to be studied

by means of statistical analysis for the sake of accurate and comprehensive performance quantification of imaging algorithms.

- The defect size determination model has demonstrated a good performance but it is limited to image analysis corresponding to the specific GWI configuration and defect type. Therefore, an extensive and comprehensive database of GWI results has to be generated in order to comprise different materials, the varying number of defects as well as their types and locations, multiple transducers' configurations etc. This would allow training a more powerful and efficient defect sizing model. It is noteworthy that SHM module of CIVA software is a rapid and accurate tool for database generation but that certain advancements have to be introduced in order to simulate complex composite structures such as HCSS, to provide a more precise transducers model and to enable different possible structural geometries.
- As previously reported, baseline GWI techniques are effective under stationary operational conditions but they are adversely affected by thermal variations. The proposed method for temperature difference compensation is based on the use of the DTW algorithm. It has been validated for aluminum but not yet for composite plates due to the complexity of GWs modification. Therefore, further improvements of this approach might concern cost function determination that would allow differentiating temperature-induced GWs signals modification and defect response. Matrices decomposition techniques such as PCA or kernel-PCA might be useful for decoupling these phenomena.

# References

- [1] C. Florens. “Modeling of the viscoelastic honeycomb panel equipped with piezoelectric patches in view of vibroacoustic active control design”. PhD thesis. Ecole Central Paris, Jan. 2010.
- [2] C. Boller, F.K. Chang, and Y. Fujino. *Encyclopedia of Structural Health Monitoring*. Willey, 2009.
- [3] J. L. Rose. *Ultrasonic Guided Waves in Solid Media*. Cambridge University Press, 2014.
- [4] J. L. Rose and L. Soley. “Ultrasonic guided waves for the detection of anomalies in aircraft components”. In: *Materials Evaluation* 46 (9) (2000), pp. 1080–1086.
- [5] K. Diamanti and C. Soutis. “Structural health monitoring techniques for aircraft composite structures”. In: *Progress in Aerospace Sciences* 46 (8) (2010), pp. 342–352.
- [6] P. Cawley. “Structural health monitoring: Closing the gap between research and industrial deployment”. In: *Structural Health Monitoring* 17 (5) (2018), pp. 1225–1244.
- [7] H. Sohn, C. R. Farrar, N. F. Hunter, and K. Worden. “Structural health monitoring using statistical pattern recognition techniques”. In: *Journal of dynamic systems, measurement, and control* 123 (4) (2001), pp. 706–711.
- [8] V. Giurgiutiu. *Structural Health Monitoring with Piezoelectric Wafer Active Sensors*. Elsevier Academic Press, 2014.
- [9] C. R. Farrar and K. Worden. “An introduction to structural health monitoring”. In: *Philosophical Transactions of the Royal Society A: Mathematical, Physical and Engineering Sciences*. Vol. 365. 1851. 2006.
- [10] W.J. Staszewski, S. Mahzan, and R. Traynor. “Health monitoring of aerospace composite structures – Active and passive approach”. In: *Composites Science and Technology* 69 (2009), pp. 1678–1685.
- [11] A. Raghavan. “Guided wave Structural Health Monitoring”. PhD thesis. University of Michigan, 2007.
- [12] D. Roach. “Real time crack detection using mountable comparative and vacuum monitoring sensors”. In: *Smart Structures and Systems* 5 (4) (2009), pp. 317–328.
- [13] T. Dong and N. H. Kim. “Cost-Effectiveness of Structural Health Monitoring in Fuselage Maintenance of the Civil Aviation Industry”. In: *Aerospace* 5 (87) (2018).
- [14] M. Wishaw and D. P. Barton. “Comparative Vacuum Monitoring: a New Method of In-Situ Real Time Crack Detection and Monitoring”. In: *10th Asia-Pacific Conference on Non-Destructive Testing*. 2001.

- [15] D. Roach, J. Kollgaard, and S. Emery. "Application and certification of comparative vacuum monitoring sensors for in-situ crack detection". In: *Air Transport Assoc. Nondestructive Testing Forum*. 2006.
- [16] X. P. Qing, R. Ikegami, S. J. Beard, D. Zhang, S. Das, S. Banerjee, and F. K. Chang. "Multifunctional Sensor Network for Structural State Sensing and Structural Health Monitoring". In: *Sensors and Smart Structures Technologies for Civil, Mechanical, and Aerospace Systems* 7647 (2010).
- [17] J. J. Scholey, P. D. Wilcox, C. K. Lee, M. I. Friswell, and M. R. Wisnom. "Acoustic Emission in Wide Composite Specimens". In: *Acoustic Emission Testing*. Vol. 13. Trans Tech Publications, 2006, pp. 325–332.
- [18] N. Meyendorf, B. Frankenstein, D. Hentschel, and L. Schubert. "Acoustic techniques for structural health monitoring". In: *IV Conferencia Panamericana de END Buenos Aires*. 2007.
- [19] M. Lin, X. Qing, A. Kumar, S. Beard, and Acellent. "Smart layer and smart suitcase for structural health monitoring applications". In: 2006.
- [20] C. Hu, Z. Yu, and Anbo Wang. "An all fiber-optic multi-parameter structure health monitoring system". In: *Optics Express* 24 (18) (2016), pp. 20287–20296.
- [21] K. Worden and D. J. Inman. *Modal Vibration Methods in Structural Health Monitoring*. American Cancer Society, 2010.
- [22] R. Yan and X. Chen. *Structural Health Monitoring: An Advanced Signal Processing Perspective*. Ed. by S. C. Mukhopadhyay. Springer, 2017.
- [23] R. Rolfes, S. Zerbst, G. Haake, J. Reetz, and J. P. Lynch. "Integral SHM-system for offshore wind turbines using smart wireless sensors". In: *Proceedings of the 6th International Workshop on Structural Health Monitoring*. DEStech Publications Inc. Stanford, CA, USA. 2007, pp. 11–13.
- [24] G. C. Kahandawa, J. Epaarachchi, H. Wang, and K. T. Lau. "Use of FBG Sensors for SHM in Aerospace Structures". In: *Photonic Sensors* 2 (3) (2012), pp. 203–214.
- [25] J. Smitharda, P. Normana, S. Van-Der-Veldena, I. Powlesland, G. Junga, N. Rajica, and Steve Galeaa. "The Acousto Ultrasonic Structural health monitoring Array Module (AUSAM+) for Damage Detection in Structures". In: *APWSHM: 6th Asia Pacific Workshop on Structural Health Monitoring* 188 (2017), pp. 448–455.
- [26] K. R. Holford, R. Pullin, S. L. Evans, M. J. Eaton, J. Hensman, and K. Worden. "Acoustic emission for monitoring aircraft structures". In: *Proceedings of the Institution of Mechanical Engineers, Part G: Journal of Aerospace Engineering* 223 (5) (2009), pp. 525–532.
- [27] C. Barile, C. Casavola, G. Pappalettera, and P. K. Vimalathithan. "Acousto-ultrasonic evaluation of interlaminar strength on CFRP laminates". In: *Composite Structures* 208 (2019), pp. 796–805. ISSN: 0263-8223.
- [28] Z. Su, L. Ye, and Y. Lu. "Guided Lamb waves for identification of damage in composite structures: A review". In: *Journal of Sound and Vibration* 295 (3-5) (2006), pp. 753–780.
- [29] W. Ostachowicz and M. Radzienski. "Structural health monitoring by means of elastic wave propagation". In: *Modern Practice in Stress and Vibration Analysis*. Vol. 382. 012003. 2012.
- [30] J. L. Rose. *Health Monitoring of Composite Structures Using Guided Waves*. Tech. rep. FA9550-08-1-0311. Penn State University, 2012.

- [31] H. Soejima, T. Ogisu, H. Yoneda, Y. Okabe, N. Takeda, and Y. Koshioka. "Demonstration of detectability of SHM system with FBG/PZT hybrid system in composite wing box structure". In: *Sensors and Smart Structures Technologies for Civil, Mechanical, and Aerospace Systems*. 6932. International Society for Optics and Photonics. 2008.
- [32] A. J. Croxford, P. D. Wilcox, and B. W. Drinkwater. "Guided wave SHM with a distributed sensor network". In: *Proceedings of SPIE: Health Monitoring of Structural and Biological Systems* 6935 (2008), pp. 1–9.
- [33] D. C. Worlton. "Experimental confirmation of lamb waves at megacycle frequencies". In: *Journal of Applied Physics* 32 (6) (1961), pp. 967–971.
- [34] M.J.S. Lowe, D.N. Alleyne, and P. Cawley. "Defect detection in pipes using guided waves". In: *Ultrasonics* 36 (1) (1998). Ultrasonics International 1997, pp. 147–154. ISSN: 0041-624X.
- [35] D. N. Alleyne, B. Pavlakovic, M. J. S. Lowe, and P. Cawley. "Rapid, long range inspection of chemical plant pipework using guided waves". In: *AIP Conference Proceedings* 557 (180) (2001).
- [36] B. Chapuis, N. Terrien, and Daniel Royer. "Excitation and focusing of Lamb waves in a multilayered anisotropic plate". In: *Journal of the Acoustical Society of America* 127 (198) (2010).
- [37] A. Kulakovskiy, B. Chapuis, O. Mesnil, N.-R. Bedreddine, O. d'Almeida, and A. Lhémy. "Defect imaging on CFRP and honeycomb composite structures by guided waves generated and detected by a sparse PZT array". In: *Proceedings of the 11th International Workshop on Structural Health Monitoring*. 2017.
- [38] D. N. Alleyne and P. Cawley. "The interaction of Lamb waves with defects". In: *IEEE Transactions on Ultrasonics, Ferroelectrics, and Frequency Control* 39 (3) (1992), pp. 381–397.
- [39] B. Chapuis. "Contrôle Santé Intégré par méthode ultrasonore des réparations composites collées sur des structures métalliques". PhD thesis. Université Paris Diderot, 2010.
- [40] T. Windisch, B. Köhler, and N. Meyendorf. "Comparison of guided wave sensors for SHM sensor networks". In: *SPIE: Smart Sensor Phenomena, Technology, Networks, and Systems*. 7648. 2010.
- [41] L. Yu, G. Santoni-Bottai, B. Xu, W. Liu, and V. Giurgiutiu. "Piezoelectric wafer active sensors for in situ ultrasonic-guided wave SHM". In: *Fatigue & Fracture of Engineering Materials & Structures* 31 (2008), pp. 611–628.
- [42] T. Clarke and P. Cawle. "Enhancing the defect localization capability of a guided wave SHM system applied to a complex structure". In: *Structural Health Monitoring* 10 (3) (2010), pp. 247–259.
- [43] T. Druet, B. Chapuis, J. Manfred, G. Laffont, and E. Moulin. "Passive SHM System for Corrosion Detection by Guided Wave Tomography". In: *Sensors, Algorithms and Applications for Structural Health Monitoring: IIW Seminar on SHM, 2015*. Ed. by Bastien Chapuis and Eric Sjerve. Cham: Springer International Publishing, 2017, pp. 21–29. ISBN: 978-3-319-69233-3.
- [44] D. Alleyne and P. Cawley. "A two-dimensional Fourier transform method for the measurement of propagating multimode signals". In: *Journal of the Acoustical Society of America* 89 (3) (1991), pp. 1159–1168.

- [45] J. E. Michaels, A. C. Cobb, and T. E. Michaels. "A comparison of feature-based classifiers for ultrasonic structural health monitoring". In: *Proceedings of SPIE: Health Monitoring and Smart Nondestructive Evaluation of Structural and Biological Systems III*. Vol. 5394. 2004, pp. 363–374.
- [46] J. E. Michaels and T. E. Michaels. "Detection of structural damage from the local temporal coherence of diffuse ultrasonic signals". In: *IEEE Transactions on Ultrasonics, Ferroelectrics, and Frequency Control* 52 (10) (2005), pp. 1769–1782.
- [47] H. Xu, C. Xu, and S. Zhou. "A new ultrasonic guided wave signal processing method for UNDE of laminated composite material". In: *International Conference on Mechanic Automation and Control Engineering*. 2010, pp. 2542–2545.
- [48] J. Chen, J. Rostami, P. W. Tse, and X. Wan. "The design of a novel mother wavelet that is tailor-made for continuous wavelet transform in extracting defect-related features from reflected guided wave signals". In: *Measurement* 110 (2017), pp. 176–191. issn: 0263-2241.
- [49] D. Samaratunga, R. Jha, and S. Gopalakrishnan. "Wave propagation analysis in laminated composite plates with transverse cracks using the wavelet spectral finite element method". In: *Finite Elements in Analysis and Design* 89 (2014), pp. 19–32.
- [50] M. Ghrib, M. Rébillat, G. Vermot des Roches, and N. Mechbal. "Automatic damage type classification and severity quantification using signal based and nonlinear model based damage sensitive features". In: *Journal of Process Control* (2018).
- [51] G. Dib, O. Karpenko, E. Koricho, A. Khomenko, M. Haq, and L. Udpa. "Ensembles of novelty detection classifiers for structural health monitoring using guided waves". In: *Smart Materials and Structures* 27 (01) (2018), p. 1361.
- [52] Z. Su and L. Ye. *Identification of Damage Using Lamb Waves*. 978-1-84882-784-4. Springer, 2009.
- [53] J. Dobson and P. Cawley. "Independent Component Analysis for Improved Defect Detection in Guided Wave Monitoring". In: *Proceedings of the IEEE* 104 (8) (2016), pp. 1620–1631.
- [54] J. Quiroga, J. M. Párraga Quiroga, L. E. Mujica, R. Villamizar, M. Ruiz, and I. E. Mujica. "Temperature Robust PCA Based Stress Monitoring Approach". In: *Trans. Tech. Publications*. Vol. 713. 2016, pp. 288–292.
- [55] Alexander C. S. Douglass and Joel B. Harley. "Dynamic time warping temperature compensation for guided wave structural health monitoring". In: *IEEE Transactions on Ultrasonics, Ferroelectrics, and Frequency Control* 65 (5) (2018), pp. 851–861.
- [56] Y. Ren, L. Qiu, S. Yuan, and F. Fang. "Gaussian mixture model-based path-synthesis accumulation imaging of guided wave for damage monitoring of aircraft composite structures under temperature variation". In: *Structural Health Monitoring* 18 (1) (2018), pp. 284–302.
- [57] U. Dackermann, Y. Yu, E. Niederleithinger, J. Li, and H. Wiggenhauser. "Condition Assessment of Foundation Piles and Utility Poles Based on Guided Wave Propagation Using a Network of Tactile Transducers and Support Vector Machines". In: *Sensors* 17 (12) (2017), p. 2938.
- [58] V. Memmolo, L. Maio, N. D. Boffa, E. Monaco, and F. Ricci. "Damage detection tomography based on guided waves in composite structures using a distributed sensor network". In: *Optical Engineering* 55 (1) (2015), p. 011007.

- [59] T. Druet, J. L. Tastet, B. Chapuis, and E. Moulin. "Guided Wave Tomography for Corrosion Monitoring in Planar Structures". In: *Proceedings of IWSHM*. 2017.
- [60] C. H. Wang, J. T. Rose, and F.-K. Chang. "A synthetic time-reversal imaging method for structural health monitoring". In: *Smart Materials and Structures* 13 (2) (2004), p. 415.
- [61] J. E. Michaels and T. E. Michaels. "Guided wave signal processing and image fusion for in situ damage localization in plates". In: *Wave Motion* 44 (6) (2007), pp. 482–492.
- [62] J. E. Michaels. "Detection, localization and characterization of damage in plates with an in situ array of spatially distributed ultrasonic sensors". In: *Smart Materials and Structures* 17 (035035) (2008).
- [63] J. S. Hall and J. E. Michaels. "Computational Efficiency of Ultrasonic Guided Wave Imaging Algorithms". In: *IEEE Transactions on Ultrasonics, Ferroelectrics, and Frequency Control* 58 (1) (2011), pp. 244–248.
- [64] J. S. Hall and J. E. Michaels. "Minimum variance ultrasonic imaging applied to an in situ sparse guided wave array". In: *IEEE Transactions on Ultrasonics, Ferroelectrics, and Frequency Control* 57 (10) (2010), pp. 2311–2323.
- [65] J. S. Hall and J. E. Michaels. "Multipath ultrasonic guided wave imaging in complex structures". In: *Structural Health Monitoring* 14 (4) (2015), pp. 345–358.
- [66] N. Quaegebeur, P. Micheau, P. Masson, and A. Maslouhi. "Structural health monitoring strategy for detection of interlaminar delamination in composite plates". In: *Smart Materials and Structures* 19 (085005) (2010).
- [67] N. Quaegebeur, P. Masson, D. Langlois-Demers, and P. Micheau. "Dispersion-based imaging for structural health monitoring using sparse and compact arrays". In: *Smart Materials and Structures* 20 (025005) (2011).
- [68] A. Perelli, L. De Marchi, L. Flamigni, A. Marzani, and G. Masetti. "Best basis compressive sensing of guided waves in structural health monitoring". In: *Digital Signal Processing* 42 (2015), pp. 35–42.
- [69] Joel B. Harley and Jose M. F. Moura. "Sparse recovery of the multimodal and dispersive characteristics of Lamb waves". In: *The Journal of the Acoustical Society of America* 133 (5) (2013), pp. 2732–2745.
- [70] W. Zhao, M. Li, J. B. Harley, Y. Jin, J. M. F. Moura, and J. Zhu. "Reconstruction of Lamb wave dispersion curves by sparse representation with continuity constraints". In: *The Journal of the Acoustical Society of America* 141 (2) (2017), pp. 749–763.
- [71] Joel B. Harley and Jose M. F. Moura. "Data-driven matched field processing for Lamb wave structural health monitoring". In: *The Journal of the Acoustical Society of America* 135 (3) (2014), pp. 1231–1244.
- [72] O. Mesnil and M. Ruzzene. "Sparse wavefield reconstruction and source detection using Compressed Sensing". In: *Ultrasonics* 67 (2016), pp. 94–104.
- [73] H. Lamb. "On waves in an elastic plate". In: *Proceedings of the Royal Society of London A: Mathematical, Physical and Engineering Sciences* 93 (648) (1917), pp. 114–128.
- [74] L. Wang and F.G. Yuan. "Group velocity and characteristic wave curves of Lamb waves in composites: Modeling and experiments". In: *Composites Science and Technology* 67 (2007), pp. 1370–1384.
- [75] B. S. Tang. "Lamb Wave Propagation in Laminated Composite Plates". PhD thesis. Virginia Polytechnic Institute and State University, 1988.

- [76] B. Hosten and M. Castaings. "FE modeling of Lamb mode diffraction by defects in anisotropic viscoelastic plates". In: *NDT & E International* 39 (3) (2006), pp. 195–204.
- [77] G. F. Roach. *Green's Functions*. 2nd. Cambridge University Press, 1982.
- [78] R. E. Diaz-Contreras and S. Nomura. "Green's function applied to solution of Mindlin plates". In: *Computers & Structures* 60 (1) (1996), pp. 41–48.
- [79] D. Duhamel. "Finite element computation of Green's functions". In: *Engineering Analysis with Boundary Elements* 31 (2007), pp. 919–930.
- [80] G. R. Liu and J. D. Achenbach. "A Strip Element Method for Stress Analysis of Anisotropic Linearly Elastic Solids". In: *Journal of Applied Mechanics* 61 (2) (1994), pp. 270–277.
- [81] M. Castaings and B. Hosten. "The propagation of guided waves in composite, sandwich-like structures and their use for NDT". In: *AIP Conference Proceedings* 557 (999) (2001).
- [82] A. Velichko and P. D. Wilcox. "Modelling the Excitation of Guided Waves in Generally Anisotropic Multi-layered Media". In: *Journal of the Acoustical Society of America* 121 (60) (2007).
- [83] M. Stévenin, A. Lhémery, and S. Grondel. "An efficient model to predict guided wave radiation by finite-sized sources in multilayered anisotropic plates with account of caustics". In: *Journal of Physics: Conference Series*. Vol. 684. 012004. 2016.
- [84] L. Yu, Z. Tian, X. Li, R. Zhu, and G. Huang. "Core–skin debonding detection in honeycomb sandwich structures through guided wave wavefield analysis". In: *Journal of Intelligent Material Systems and Structures* (2018).
- [85] L. Taupin, A. Lhémery, and G. Inquiété. "A detailed study of guided wave propagation in a viscoelastic multilayered anisotropic plate". In: *Journal of Physics: Conference Series*. Vol. 269. 1. 2011, p. 012002.
- [86] F. Song, G. L. Huang, and K. Hudson. "Guided wave propagation in honeycomb sandwich structures using a piezoelectric actuator/sensor system". In: *Smart Materials and Structures* 18 (125) (2009), p. 125007.
- [87] V. N. Smelyanskiy, V. Hafiychuk, D. G. Luchinsky, R. Tyson, J. Miller, and C. Banks. "Modeling wave propagation in Sandwich Composite Plates for Structural Health Monitoring". In: *Annual Conference of the Prognostics and Health Management Society*. Vol. 2. 2. 2011.
- [88] S. Sikdar and S. Banerjee. "Guided wave propagation in a honeycomb composite sandwich structure in presence of a high density core". In: *Ultrasonics* 71 (2016), pp. 86–97.
- [89] B. Tian. "Numerical simulation of elastic wave propagation in honeycomb core sandwich plates". PhD thesis. Ecole Centrale Paris, 2014.
- [90] L. J. Gibson and M. F. Ashby. *Cellular Solids: Structure and Properties*. 2nd ed. Cambridge University Press, 1997.
- [91] S. Malek and L. Gibson. "Effective elastic properties of periodic hexagonal honeycombs". In: *Mechanics of Materials* 91 (2016), pp. 226–240.
- [92] B. Tie, D. Aubry, A. S. Mouronvala, D. Solas, J. Thébault, and B. Y. Tian. "High Frequency Elastic Wave Propagation in Media with a Microstructure". In: *AIP Conference Proceedings* 1233 (299) (2010).
- [93] B. Tie, B. Y. Tian, and D. Aubry. "Theoretical and numerical modeling of membrane and bending elastic wave propagation in honeycomb thin layers and sandwiches". In: *Journal of Sound and Vibration* 382 (2016), pp. 100–121.

- [94] L. Taupin, A. Lhémy V. Baronian, and A. S. Bonnet-BenDhia. “Scattering of obliquely incident guided waves by a stiffener bonded to a plate”. In: *Journal of Physics: Conference Series*. Vol. 353. 012011. 2012.
- [95] A. Leleux, P. Micheau, and M. Castaings. “Long Range Detection of Defects in Composite Plates Using Lamb Waves Generated and Detected by Ultrasonic Phased Array Probes”. In: *Journal of Nondestructive Evaluation* 32 (2) (2013), pp. 200–214.
- [96] M. Lazaro-Gredilla, S. Van Vaerenbergh, and N. D. Lawrence. “Overlapping Mixtures of Gaussian Processes for the data association problem”. In: *Pattern Recognition* 45 (4) (2011), pp. 1386–1395.
- [97] M. N. Gibbs. “Bayesian Gaussian Processes for Regression and Classification”. PhD thesis. University of Cambridge, 1997.
- [98] C. E. Rasmussen and C. K. I. Williams. *Gaussian processes for machine learning*. MIT Press, 2006.
- [99] M. A. Alvarez, L. Rosasco, and N. D. Lawrence. *Kernels for Vector-Valued Functions: a Review*. Tech. rep. Computer Science and Artificial Intelligence Laboratory Technical Report, 2011.
- [100] M. J. S. Lowe. “Matrix Techniques and for Modeling and Ultrasonic Waves and in Multilayered and Media”. In: *IEEE Transactions on Ultrasonics, Ferroelectrics, and Frequency Control* 42 (4) (1995), pp. 525–542.
- [101] A. C. Arpaci-Dusseau. *Operating Systems: Three Easy Pieces*. Springer, 2014.
- [102] Lynda Chehami, E. Moulin, J. de Rosny, C. Prada, O. B. Matar, F. Benmeddour, and J. Assaad. “Detection and localization of a defect in a reverberant plate using acoustic field correlation”. In: *Journal of Applied Physics* 115 (104901) (2014).
- [103] H. Gao, Y. Shi, and J. L. Rose. “Guided Wave Tomography on an Aircraft Wing with Leave in Place Sensors”. In: *AIP Conference Proceedings* 760 (1788) (2005).
- [104] A. K. Mal, S. Banerjee, F. Riccio, E. Monacoc, and L. Lecce. “Autonomous health monitoring of a stiffened composite plate”. In: *Health Monitoring and Smart Nondestructive Evaluation of Structural and Biological Systems III*. 617701-1. 2006.
- [105] X. Zhao, H. Gao, G. Zhang, B. Ayhan, F. Yan, C. Kwan, and J. L. Rose. “Active health monitoring of an aircraft wing with embedded piezoelectric sensor/actuator network: I. Defect detection, localization and growth monitoring”. In: *Smart Materials and Structures* 16 (4) (2007), p. 1208.
- [106] W. B. Westin, T. E. Michaels, and J. E. Michaels. “Characterization of guided wave velocity and attenuation in anisotropic materials from wavefield measurements”. In: *AIP Conference Proceedings* 1706 (1) (2016).
- [107] P. C. Ostiguy. “Modélisation pour l’imagerie des composites par ondes guidées”. PhD thesis. Sherbrooke, 2016.
- [108] E. Kausel. “Wave propagation in anisotropic layered media”. In: *International Journal for Numerical Methods in Engineering* 23 (8) (1986), pp. 1567–1578.
- [109] M. Castaings and B. Hosten. “Delta operator technique to improve the Thomson–Haskell method stability for propagation in multilayered anisotropic absorbing plates”. In: *Journal of the Acoustical Society of America* 95 (1931) (1994).
- [110] O. Mesnil. “Sparse reconstruction and analysis of guided wavefields for damage detection”. PhD thesis. Georgia Institute of Technology, 2016.

- [111] Z. Sharif-Khodaei and M. H. Aliabadi. "Assessment of delay-and-sum algorithms for damage detection in aluminium and composite plates". In: *Smart Materials and Structures* 23 (075007) (2014).
- [112] J. C. Aldrin, E. A. Medina, E. A. Lingren, C. F. Buynak, and J. S. Knopp. *Protocol for Reliability Assessment of Structural Health Monitoring Systems Incorporating Model-assisted Probability of Detection (MAPOD) Approach*. Tech. rep. DTIC Document, 2011.
- [113] S. S. Kessler, E. B. Flynn, C. T. Dunn, and M. D. Todd. "A Structural Health Monitoring Software Tool for Optimization, Diagnostics and Prognostics". In: *Annual Conference of the Prognostics and Health Management Society*. 2011.
- [114] E. Etebu and M. Shafiee. "Reliability analysis of structural health monitoring systems". In: *ESREL Proceedings: Safety and Reliability – Safe Societies in a Changing World*. 2018.
- [115] C. M. Schubert-Kabban, B. M. Greenwell, M. P. DeSimio, and M. M. Derriso. "The probability of detection for structural health monitoring systems: Repeated measures data". In: *Structural Health Monitoring* 14 (3) (2015), pp. 252–264.
- [116] O. Mesnil, A. Imperiale, E. Demaldent, V. Baronian, and B. Chapuis. "Simulation tools for guided waves based structural health monitoring". In: *AIP Conference Proceedings*. 2018.
- [117] C. Willberg, S. Duczek, J. M. Vivar-Perez, and Z. A. B. Ahmad. "Simulation Methods for Guided Wave-Based Structural Health Monitoring: A Review". In: *Applied Mechanics Reviews* 67 (1) (2015), p. 010803.
- [118] C. Leckey, K. Wheeler, V. N. Hafiychuk, H. Hafiychuk, and D. Timucin. "Simulation of guided-wave ultrasound propagation in composite laminates: Benchmark comparisons of numerical codes and experiment". In: *Ultrasonics* 84 (2018), pp. 187–200.
- [119] G. Cohen. *Higher-Order Numerical Methods for Transient Wave Equations*. Springer: Scientific Computation, 2002.
- [120] O. Mesnil, A. Imperiale, E. Demaldent, and B. Chapuis. "Validation of spectral finite element simulation tools dedicated to structural health monitoring". In: *AIP Conference Proceedings*. 2018.
- [121] E. Fribourg-Blanc. "Thin film actuators for structural health monitoring : study of PZT and PMNT films". PhD thesis. University of Valenciennes, 2003.
- [122] J. Moriot, N. Quaegebeur, A. Le Duff, and P. Masson. "A model-based approach for statistical assessment of detection and localization performance of guided wave-based imaging techniques". In: *Structural Health Monitoring* 17 (6) (2017), pp. 1460–1472.
- [123] Y. Cho. "Estimation of ultrasonic guided wave mode conversion in a plate with thickness and variation". In: *IEEE Transactions on Ultrasonics, Ferroelectrics, and Frequency Control* 47 (3) (2000), pp. 591–603.
- [124] Y. Chen. "A Tutorial on Kernel Density Estimation and Recent Advances". In: *ArXiv: Methodology* eprint arXiv:1704.03924 (2017).
- [125] Z. Ju and H. Liu. "Fuzzy Gaussian Mixture Models". In: *Pattern Recognition* 45 (2012), pp. 1146–1158.
- [126] D. K. Duvenaud. "Automatic Model Construction with Gaussian Processes". PhD thesis. University of Cambridge, 2014.
- [127] Y. LeCun, Y. Bengio, and G. Hinton. "Deep learning". In: *Nature* 521 (7553) (2015), p. 521.

- [128] R Miorelli, A. Kulakovskiy, O. Mesnil, and O. d’Almeida. “Automatic defect localization and characterization through machine learning based inversion for guided wave imaging in SHM”. In: *QNDE Proceedings*. 2018.
- [129] P. Tamilselvan and W. Pingfeng. “Failure diagnosis using deep belief learning based health state classification”. In: *Reliability Engineering & System Safety*. 2013, pp. 124–135.
- [130] R. Zhao, R. Yan, Z. Chen, K. Mao, P. Wang, and R. X. Gao. “Deep learning and its applications to machine health monitoring: A survey”. In: *ArXiv: Machine Learning* (2016).
- [131] F. Pedregosa, G. Varoquaux, A. Gramfort, V. Micheland, G. B. Thirion, and B. O. Grisel. “Scikit-learn: Machine learning in Python”. In: *Journal of machine learning research* 12 (2011), pp. 2825–2830.
- [132] G. Isabelle and A. Elisseeff. “An introduction to feature extraction”. In: *Feature extraction*. Springer, 2006, pp. 1–25.
- [133] D. H. Wolpert and W. G. Macready. “No Free Lunch Theorems for Optimization”. In: *IEEE Transactions on Evolutionary Computation* 1 (1) (1997), pp. 67–82.
- [134] C. Szegedy, V. Vanhoucke, S. Ioffe, J. Shlens, and Z. Wojna. “Rethinking the Inception Architecture for Computer Vision”. In: *ArXiv: Computer Vision and Pattern Recognition* (2015).
- [135] H. R. Maei, C. Szepesvari, S. Bhatnagar, and R. S. Sutton. “Toward Off-Policy Learning Control with Function Approximation”. In: *ICML*. 2010.
- [136] T. Zhang, T. G. Kahn, S. Levine, and Pieter Abbeel. “Learning deep control policies for autonomous aerial vehicles with mpc-guided policy search”. In: *IEEE international conference on robotics and automation (ICRA)*. 2016, pp. 528–535.
- [137] D. Ciresan, M. Ueli, and S. Jürgen. “Multi-column deep neural networks for image classification”. In: *ArXiv: Computer Vision and Pattern Recognition* (2012).
- [138] D. H. Hubel and T. N. Wiesel. “Receptive field of single neurones in the cat’s striate cortex”. In: *Journal of Physiology* 148 (1959), pp. 574–591.
- [139] C. Szegedy, W. Liu, Y. Jia, P. Sermanet, S. Reed, D. Anguelov, D. Erhan, V. Vanhoucke, and A. Rabinovich. “Going deeper with convolutions”. In: *In Proceedings of the IEEE conference on computer vision and pattern recognition*. 2015, pp. 1–9.
- [140] T. Wiatowski and H. Bolcskei. “A Mathematical Theory of Deep Convolutional Neural Networks for Feature Extraction”. In: *IEEE Transactions on Information Theory* 64 (2018), pp. 1845–1866.
- [141] W. Shang, K. Sohn, D. Almenia, and H. Lee. “Understanding and Improving Convolutional Neural Networks via Concatenated Rectified Linear Units”. In: *International Conference on Machine Learning*. 2016, pp. 2217–2225.
- [142] I. Kuzovkin, R. Vicente, M. Petton, J.-P. Lachaux, M. Baciú, P. Kahane, and S. Rheims. “Activations of deep convolutional neural networks are aligned with gamma band activity of human visual cortex”. In: *Nature: Communications Biology* 1 (107) (2018).
- [143] A. Maas, H. Y. Awni, and A. Ng. “Rectifier nonlinearities improve neural network acoustic models”. In: *Proceedings of the 30-th International Conference on Machine Learning*. Vol. 28. 1. 2013, p. 3.

- [144] A. Krizhevsky, I. Sutskever, and G. E. Hinton. "ImageNet Classification with Deep Convolutional Neural Networks". In: *Advances in Neural Information Processing Systems*. Ed. by F. Pereira, C. J. C. Burges, L. Bottou, and K. Q. Weinberger. Curran Associates, Inc., 2012, pp. 1097–1105.
- [145] K. Simonyan and A. Zisserman. "Very deep convolutional networks for large-scale image recognition". In: *ArXiv: Computer Vision and Pattern Recognition* (2014).
- [146] I. Goodfellow, Y. Bengio, and A. Courville. *Deep Learning*. MIT Press, 2016.
- [147] P. P. Bonissone, Y.-T. Chen, K. Goebel, and P. S. Khedkar. "Hybrid soft computing systems: industrial and commercial applications". In: *Proceedings of the IEEE* 87 (9) (1999), pp. 1641–1667.
- [148] M. Saemi, M. Ahmadi, and A. Y. Varjani. "Design of neural networks using genetic algorithm for the permeability estimation of the reservoir". In: *Journal of Petroleum Science and Engineering* 59 (1-2) (2007), pp. 97–105.
- [149] D. P. Kingma and J. Ba. "Adam: A method for stochastic optimization". In: *ArXiv: Machine Learning* (2014).
- [150] I. Goodfellow, Y. Bengio, A. Courville, and Y. Bengio. *Deep learning*. Vol. 1. MIT press Cambridge, 2016.
- [151] M. D. Zeiler and R. Fergus. "Visualizing and understanding convolutional networks". In: *European conference on computer vision*. Springer. 2014, pp. 818–833.
- [152] J. Yosinski, J. Clune, A. Nguyen, T. Fuchs, and H. Lipson. "Understanding neural networks through deep visualization". In: *ArXiv: Computer Vision and Pattern Recognition* (2015).
- [153] A. J. Croxford, J. Moll, P. D. Wilcox, and J. E. Michaels. "Efficient temperature compensation strategies for guided wave structural health monitoring". In: *Ultrasonics* 50 (2010), pp. 517–528.
- [154] C. Fendzi, M. Rébillat, N. Mechbal, M. Guskov, and G. Coffignal. "A data-driven temperature compensation approach for Structural Health Monitoring using Lamb waves". In: *Structural Health Monitoring* 15 (5) (2015), pp. 525–540.
- [155] J. C. Dodson and D. J. Inman. "Thermal sensitivity of Lamb waves for structural health monitoring applications". In: *Ultrasonics* 53 (2013), pp. 677–685.
- [156] O. Putkis, R. P. Dalton, and A. J. Croxford. "The influence of temperature variations on ultrasonic guided waves in anisotropic CFRP plates". In: *Ultrasonics* 60 (2015), pp. 109–116.
- [157] A. J. Croxford, P. D. Wilcox, B. W. Drinkwater, and G. Konstantinidis. "Strategies for guided-wave structural health monitoring". In: *Proceedings of The Royal Society A Mathematical Physical and Engineering* 463 (2008), p. 2087.
- [158] S. Chaabene, F. Bouchoucha, M. N. Ichchou, and M. Haddar. "Wave mode diffusion and propagation in structural wave guide under Varying Temperature". In: *Applied Acoustics* 108 (2015), pp. 84–91.
- [159] R. Miorelli, A. Kulakovskiy, O. Mesnil, B. Chapuis, and O. d'Almeida. "Supervised learning strategy for classification and regression tasks applied to aeronautical structural health monitoring problems". In: *IEEE Transactions on Ultrasonics, Ferroelectrics, and Frequency Control* (Currently Under Review) (2019).
- [160] Z. Lu, S. J. Lee, J. E. Michaels, and T. E. Michaels. "On The Optimization Of Temperature Compensation For Guided Wave Structural Health Monitoring". In: *Review of Quantitative Nondestructive Evaluation*. Vol. 12. 11. 2010, p. 1860.

- 
- [161] Y. Lu and J.E. Michaels. "A methodology for structural health monitoring with diffuse ultrasonic waves in the presence of temperature variations". In: *Ultrasonics* 43 (2005), pp. 717–731.
- [162] R. J. Turetsky and D. P.W. Ellis. "Ground-Truth Transcriptions of Real Music from Force-Aligned MIDI Syntheses". In: *ISMIR*. 2003.
- [163] M. Müller. *Information Retrieval for Music and Motion*. Berlin, Heidelberg: Springer-Verlag, 2007.



# Appendix

## Outline of the current chapter

<a href="#">A.1 Maximum likelihood for the normal distribution</a>	137
<a href="#">A.2 GWI profiles</a>	139
<a href="#">A.3 DTW Local cost computation</a>	140
<a href="#">A.4 List of communications</a>	141

### A.1 Maximum likelihood for the normal distribution

This is a toy example to demonstrate how the parameters can be derived for the model complying with Gaussian distribution. Given the data  $x$ , and the probability distribution of the model can be expressed as follows:

$$P(x|\mu, \sigma) = \frac{1}{\sqrt{2\pi\sigma^2}} \exp \frac{-(x-\mu)^2}{2\sigma^2}, \quad (\text{A.1})$$

where parameters  $\mu$  and  $\sigma$  have to be derived from the data  $x$ .

As described in 2.26, the optimal parameters can be derived from the likelihood. For computational reasons, a logarithm of likelihood is computed as follows:

$$\begin{aligned} L(\mu, \sigma|x) &= \ln\left(\frac{1}{\sqrt{2\pi\sigma^2}} \exp \frac{-(x_1-\mu)^2}{2\sigma^2} \times \dots \times \frac{1}{\sqrt{2\pi\sigma^2}} \exp \frac{-(x_n-\mu)^2}{2\sigma^2}\right) \\ &= -\frac{n}{2} \ln(2\pi) - n \ln(\sigma) - \frac{-(x_1-\mu)^2}{2\sigma^2} - \dots - \frac{-(x_n-\mu)^2}{2\sigma^2} \end{aligned} \quad (\text{A.2})$$

The optimal parameters can be obtained the maximum of likelihood is achieved, i.e it derivative is equal to zero. Hence A.2 can be differentiated with respect to the  $\mu$  and  $\sigma$ . It gives the following:

$$\frac{\partial}{\partial \mu} \ln L(\mu, \sigma|x) = \frac{1}{\sigma^2} (x_1 + \dots + x_n), \quad (\text{A.3})$$

and

$$\frac{\partial}{\partial \mu} \ln L(\mu, \sigma | x) = -\frac{1}{\sigma} + \frac{1}{\sigma^3} ((x_1 - \mu)^2 + \dots + (x_n - \mu)^2). \quad (\text{A.4})$$

By setting this derivatives to zeros, optimal parameters values can be obtained for this model as follows:

$$\frac{\partial}{\partial \mu} \ln L(\mu, \sigma | x) = 0 \longrightarrow \mu = \frac{x_1 + \dots + x_n}{n}, \quad (\text{A.5})$$

$$\frac{\partial}{\partial \sigma} \ln L(\mu, \sigma | x) = 0 \longrightarrow \sigma = \sqrt{\frac{(x_1 - \mu)^2 + \dots + (x_n - \mu)^2}{n}}. \quad (\text{A.6})$$

Therefore, following the Bayesian framework, it is possible to derive optimal parameters  $\mu$  and  $\sigma$ . As expected, for Gaussian distribution the optimal  $\mu$  is a mean value, and optimal  $\sigma$  is a standard deviation.

## A.2 GWI profiles

Simulated GWI result of the transverse hole in aluminum plate  $600\text{ mm} \times 600\text{ mm} \times 3\text{ mm}$  in dimension is shown in Figure A.1. The image is computed by means of Excitelet algorithm using  $A_0$  for imaging while the excitation function is a two-cycle Hanning modulated tone burst centered at  $45\text{ kHz}$ .

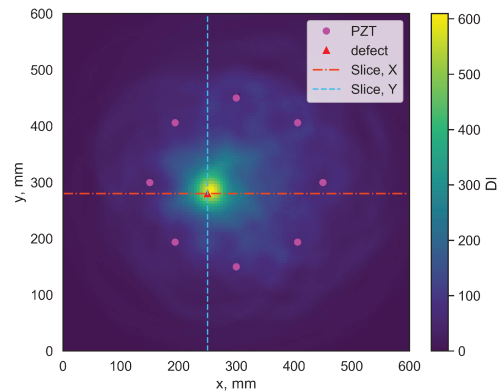


Figure A.1 – GWI of transverse hole in aluminum plate.

The cyan dashed line and dash-dotted line represent vertical and horizontal trough defect slices. These profiles allow determining corresponding Full Half Width Maximum (FWHM) metrics in both X and Y directions. These metrics can be, consequently, used to demonstrate the non-linearity of the defect inversion problem.

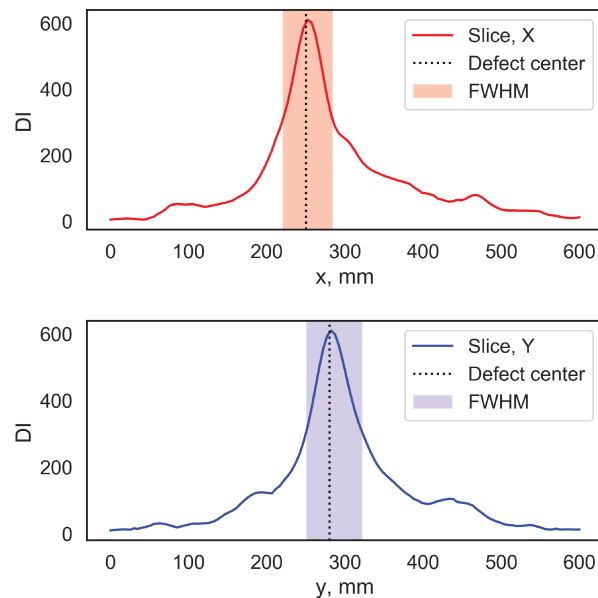
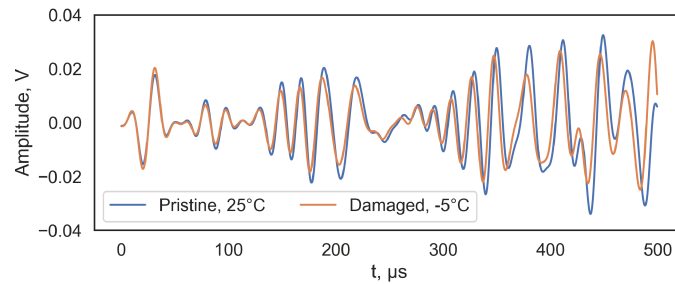


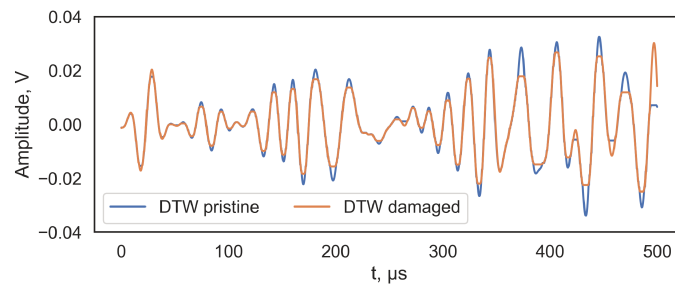
Figure A.2 – The through defect DI profiles and the corresponding FWHM.

### A.3 DTW Local cost computation

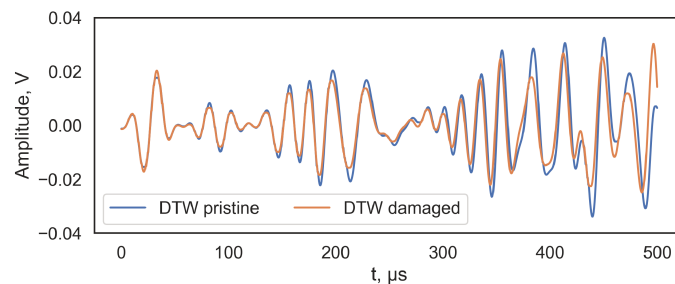
The  $L1$  norm is effectively used for measuring local distance between signals in typical speech recognition tasks but it can introduce waveform modifications while processing GWs signals. Therefore, a modified metric is proposed to compute local cost matrix. In addition to standard  $L1$  norm it introduces a regularization term that penalizes GWs signals flattening and cropping, as shown in Figure A.3.



(a) Temperature-induced modification on GWs propagation.



(b) DTW for GWs signals alignment using  $L1$  norm to compute local cost matrix.



(c) DTW for GWs signals alignment using proposed regularized metric.

Figure A.3 – DTW local and global cost matrices computed for GWs signals measured in CFRP plate at  $1^{\circ}\text{C}$  and  $20^{\circ}\text{C}$ .

## A.4 List of communications

The progress of this research work has been presented in the following conferences:

1. (EWSHM 2016) Development of an SHM system of sandwich composite panels using guided elastic waves.
2. (IWSHM 2017) Defect imaging on CFRP and honeycomb composite structures by guided waves generated and detected by a sparse PZT array.
3. (AFPAC 2018) Defect imaging in composite plates using the sparse piezo-electric transducers network.
4. (ACMA 2018) Defect imaging in CFRP and Honeycomb panels.
5. (COFREND 2018) Development of SHM system for sandwich composite panels using guided elastic waves.
6. (EWSHM 2018) Experimental determination of 3D Green's function in composite plates for defect imaging using guided waves.
7. (QNDE 2018) Automatic defect localization and characterization through machine learning based inversion for guided wave imaging in SHM.
8. (QNDE 2018) High-Resolution Defect Imaging In Laminate Composites And Honeycomb Structures.

In addition the following papers are currently under preparation:

1. (J.Smart.Mat.Struc) Statistical study on performances of guided wave imaging algorithms for structural health monitoring. (*submitted*)
2. (IEEE Trans. Ultrason., Ferroelectr., Freq. Control) Defect size inversion using machine learning tools for SHM.
3. (Ultrasonics) Deep convolutional neural networks for material elastic parameters estimation.



**Titre :** Développement d'un système SHM pour structures composite par ondes élastiques guidées

**Mots clés :** Structural Health Monitoring (SHM), Imagerie par Ondes Guidées, Excitelet, CNN, DTW

**Résumé :** Un système SHM par ondes guidées a pour but d'évaluer l'intégrité d'une grande variété de structures fines, telles que les fuselages d'avions, les tuyaux, les réservoirs, etc. Un tel système est basé sur un réseau de capteurs piézoélectriques pour l'excitation et la mesure des ondes guidées. Cette méthode de SHM par ondes guidées est prometteuse pour l'inspection de structures de grande taille, ces ondes se propageant sur de grandes distances avec peu d'atténuation, tout en étant sensibles aux défauts surfaciques et subsurfaciques.

Cette thèse présente les travaux menés dans le but de développer un système de SHM par ondes guidées capable de détecter, localiser et dimensionner efficacement les défauts dans des structures aéronautiques assimilables à des plaques, en matériaux composites ou en aluminium. Des simulations et des méthodes d'apprentissage sont utilisées pour déterminer les caractéristiques principales des ondes guidées propagées, notamment les vitesses de phase et de groupe ainsi que la fonction de Green 3D. Celles-ci sont ensuite utilisées pour traiter les signaux des ondes guidées afin de produire des images représentant l'intégrité des structures étudiées. Ce travail comprend également une étude approfondie des algorithmes d'imagerie DAS, MV et Excitelet, les plus prometteurs parmi ceux de la littérature, une évaluation de leurs

performances par analyse statistique sur une grande base de données de résultats de simulation d'imagerie par ondes guidées et propose une méthode d'imagerie parcimonieuse. Alors que la détection et la localisation des défauts à partir de l'analyse des images est aisée, le dimensionnement du défaut est un problème plus complexe en raison de sa forte dimensionnalité et de sa non-linéarité. Il est démontré que ce problème peut être résolu par des méthodes d'apprentissage automatique sur une grande base de données de résultats de simulation d'imagerie par ondes guidées. Ces méthodes d'imagerie nécessitent cependant une référence, mesurée sur la structure dans un état supposé sain. Elles sont efficaces dans des conditions opérationnelles stationnaires mais sont sensibles aux variations de l'environnement et notamment aux fluctuations de température. Ce travail présente donc l'étude de la robustesse face aux effets thermiques des méthodes d'imagerie par ondes guidées et propose un modèle de détection de défauts capable d'analyser des résultats d'imagerie détériorés. Plusieurs techniques de compensation des effets thermiques sont étudiées et des améliorations sont proposées. Leur efficacité est validée pour les plaques d'aluminium mais des améliorations supplémentaires sont nécessaires pour les étendre aux plaques de composites.

**Title :** Development of Structural Health Monitoring System for composite structures using guided elastic waves

**Keywords :** Structural Health Monitoring (SHM), Guided Wave Imaging, Excitelet, CNN, DTW

**Abstract :** A guided wave-based structural health monitoring (SHM) system aims at determining the integrity of a wide variety of plate-like structures, including aircraft fuselages, pipes, tanks etc. It relies on a sparse array of piezoelectric transducers for guided waves (GWs) excitation and sensing. With a number of benefits, these waves are standing out among other methods as a promising method for the inspection of large structures. They can propagate on significant distances with small attenuation while being sensitive to surface and subsurface defects.

This thesis presents studies conducted with the purpose of developing such a GWs-based SHM system that is capable of efficient defect detection, localization and sizing aeronautical plate-like structures made of aluminum and composite materials. Simulation and data-driven approaches are presented for determining principal characteristics of propagating GWs, namely modal group and phase velocities, 3D Green's functions etc. in structures of interest. They are then used for GWs signals processing in order to compute images representing the integrity of studied structures. This work also provides a comprehensive overview of DAS, MV

and Excitelet defect imaging algorithms, determines their performance using statistical analysis of an extensive dataset of simulated guided waves imaging (GWI) results and proposes a method for sparse defect imaging. While defect detection and localization are straightforward from the image analysis, the defect sizing is a more complex problem due to its high dimensionality and non-linearity. It is demonstrated that this problem can be solved by means of machine learning methods, relying on an extensive database of simulated GWI results. Aforementioned defect imaging methods are baseline demanding. They are efficient under stationary operational conditions but vulnerable to environmental variations, especially to the temperature fluctuation. Finally, this work presents studies on the robustness of GWI methods against thermal effects, and a defect detection model capable of analyzing deteriorated GWI results is proposed. Different techniques for thermal effects compensation are reviewed, and improvements are proposed. Their effectiveness is validated for aluminum plates but further improvements are required to translate these techniques to composite plates.



